Proceedings of the 13th CEReS Int'l Symposium on Remote Sensing
"Disaster Monitoring and Mitigation in Asia"

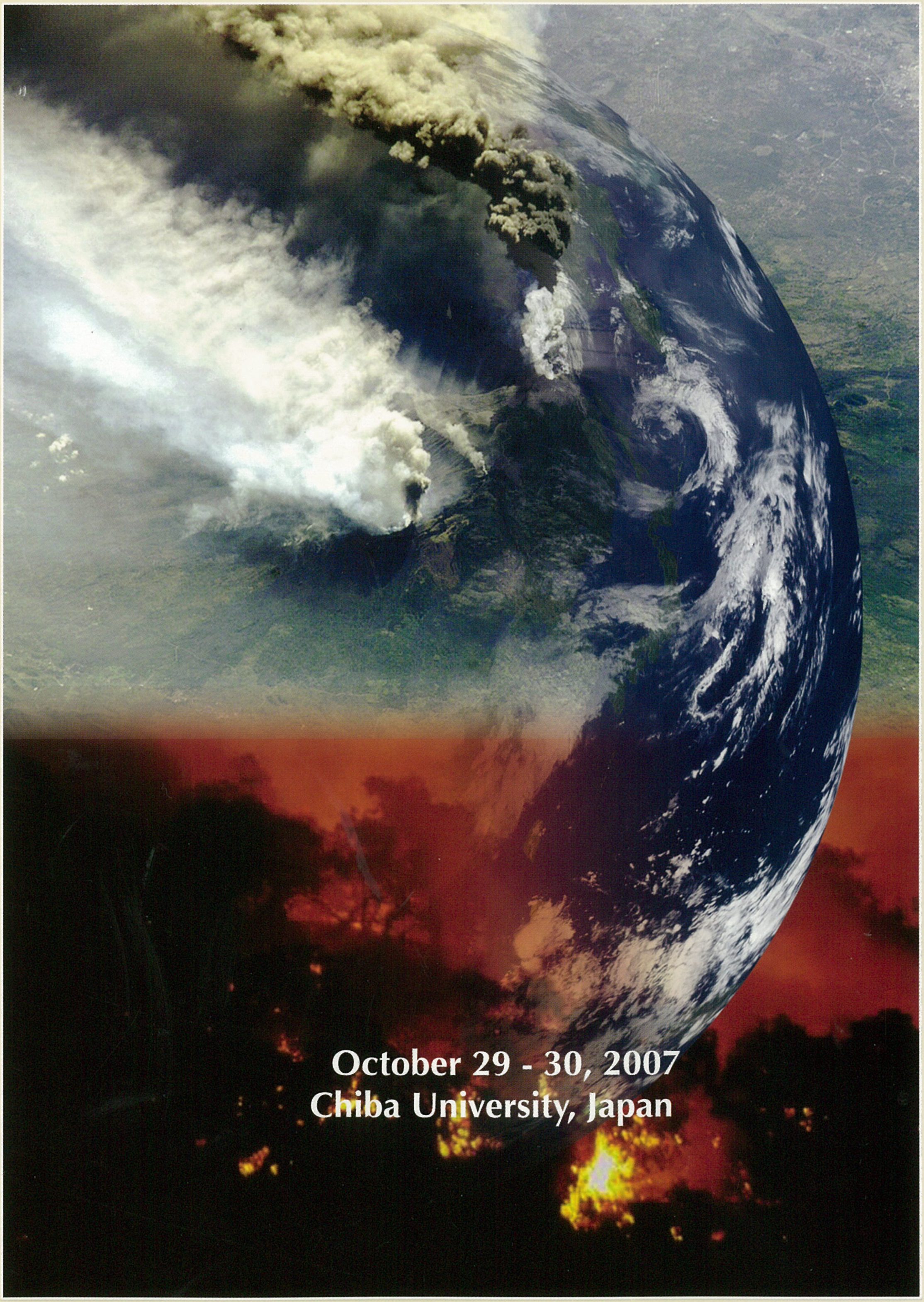

October 29 - 30, 2007
Chiba University, Japan

Published by
Center for Environmental Remote Sensing (CEReS),
Chiba University, Japan
1-33 Yayoi-cho, Inage, Chiba, 263-8522 Japan

Cover Designed by T. Ishiyama

Proceedings of The 13th CEReS Int'l Symposium on Remote Sensing

"Disaster Monitoring and Mitigation in Asia"

October 29 - 30, 2007

Organized by
Center for Environmental Remote Sensing (CEReS), Chiba University,
Japan

(Editors)
J. Tetuko S. S., T. Ishiyama and R. Tateishi

Contents

(Paper)

Contents

(Paper)

(Poster)

Using Remote Sensing to Monitor Floods in Indonesia

Eleonora RUNTUNUWU

Indonesian Agroclimate and Hydrology Research Institute
Email: runtunuwu2001@yahoo.com

Abstract

Flood is among the most devastating natural hazard in Indonesia, claiming more lives and causing more property damage than any other natural phenomena. Among the Asian countries, Indonesia is the third of the most frequently affected country by floods, after China and India. In February 2007, the flood has covered 60% of Jakarta and in some areas the water depth has reached more than 3 meters. Even during the dry season on 2007, there were hazardously floods in a number of provinces such as NTT, Central of Sulawesi, South Sulawesi, NAD Aceh Darussalam, and North Sulawesi. Remote sensing and Geographical Information (GIS) technologies are useful technologies in flood disaster monitoring. In this paper the use of remote sensing and GIS for floods disaster monitoring in Indonesia is discussed.

1. Introduction

In general flood is defined as any relatively high water flow that overtops the natural or artificial banks in any portion of a river or stream. When a bank is overtopped, the water spreads over the flood plain and generally becomes a hazard to society. When extreme meteorological events occur in areas characterized by a high degree of urbanization, the flooding can be extensive, resulting in a great amount of damage and loss of life. Heavy rain, snowmelt, or dam failures cause floods. The events deriving from slope dynamics gravitational phenomena) and fluvial dynamics (floods) are commonly triggered by the same factor: heavy rainfall. Especially in mountainous areas, analyzing flood risk is often impossible without considering all of the other phenomena associated with slope dynamics (erosion, slides, sediment transport, etc.) whereas in plains damages are caused by flood phenomena mainly controlled by water flow.

There have been many demonstrations of the operational use of the satellites for detailed monitoring and mapping of floods and post-flood damage assessment. Sandoz, *et al* (2007) purposed an operational methodology for inventory and monitoring of wetland habitats and wetland flooded duration in South of France; Aduah *et al.* (2006) compared and combined the optical and radar satellite images to map and monitor flooding system in Southern Zambia; Pham (2004) used remote sensing and GIS technologies for monitoring and assessment of flooding status at the Coastal Zone in Central Part of Vietnam; Sandholt *et al.* (2003) compared several different sensors (optical and radar) and validated against ground based surveys in Senegal river valley; and Choudhury (1994) monitored and forecasted of disasters using NOAA and GMS images in Bangladesh.

Following those research evidence, this paper reviewed the application of the remote sensing and GIS technologies in monitoring the flood events in Indonesia, which already done by several institutions such as Indonesian National Institute of Aeronautics and Space Agency (LAPAN), Ministry of Agriculture, Operations Centre, etc.

2. Recent Flood Events in Indonesia

Dutta and Herath (2004) founded out that that in Asia; floods are by far the most frequent and devastating compared to other natural disasters, like drought, earthquake, extreme-temperature, landslide, volcano, wild fire, and winds storm. There were on average about 10 flood events annually in 1970s, it become 30 in 1990s, and in the last three years it has increased to about 50 events per year. Among the Asian countries, the ten countries which the most frequently affected by floods are China, India, Indonesia, Philippines, Bangladesh, Iran, Thailand, Sri Lanka, Vietnam, and Pakistan in descending order. The 5-year average flood statistics of last 30 years show that flood frequency in increasing in the top ten flood affected countries in Asia. It is no debatably since the Intergovernmental Panel on Climate Change (IPCC) noted that number of heavy daily precipitation events that lead to flooding have increased due to the global climate change (IPCC, 2007).

In South East Asia (Figure 2) and Indonesia (3), flood also is the most frequent natural disaster (CRED, 2007). In period of 1960-2007, about 37% of all natural disasters is flood and occurred almost in all provinces of Indonesia, and it was increasing year by year (Figure 1 and Figure 3). The worst flood in Indonesia occurred in 2007, when 454,8 km^2 of Jakarta areas have covered by floods, and 590,000 people were forced to leave their domiciles (National Planning Board, 2007).

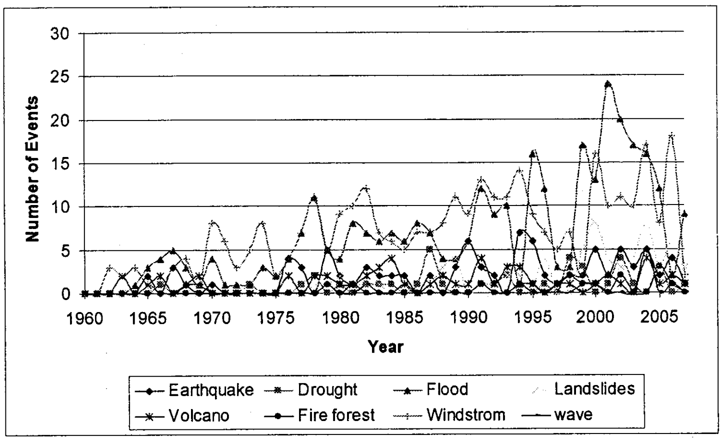

Figure 1. Flood trend in most frequently flood affected countries in South East Asia from 1960 to 2007.

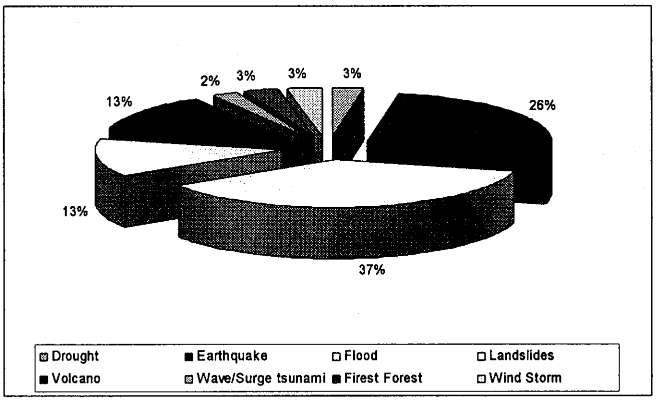

Figure 2. Flood disaster data in Indonesia compared to other natural disasters from 1960 to 2007.

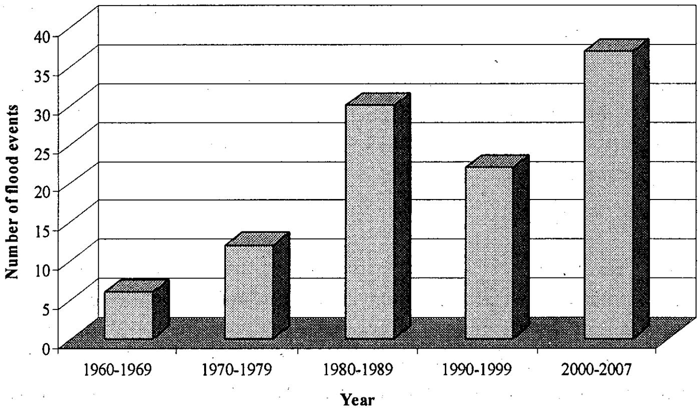

Figure 3. Flood disaster data in Indonesia from 1960-2007.

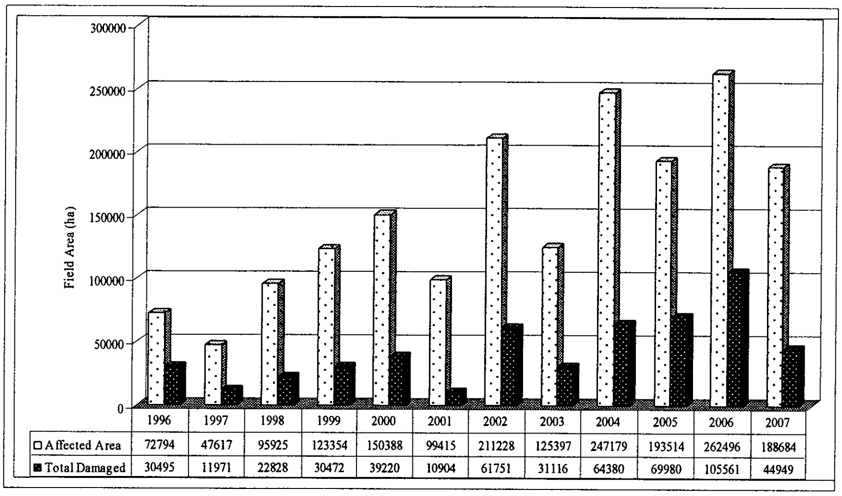

	1996	1997	1998	1999	2000	2001	2002	2003	2004	2005	2006	2007
☐ Affected Area	72794	47617	95925	123354	150388	99415	211228	125397	247179	193514	262496	188684
■ Total Damaged	30495	11971	22828	30472	39220	10904	61751	31116	64380	69980	105561	44949

Figure 4. Flood impacts on rice fields' period of 1996-2006, and Jan-July 2007. (Source: Directorate of Food Crop Protection, Ministry of Agricultural, 2007).

3. How Remote Sensing/GIS Technologies Could Contribute to Monitor Remote Sensing

Jeyaseelan *et al.* (2003) noted that the remote sensing and GIS technology significantly contributes in the activities of all the three major phases of flood management, *i.e.* (1). Preparedness Phase, where activities such as prediction and risk zone identification are taken up long before the event occurs, (2). Response Phase, where activities such as early warning/forecasting, monitoring and preparation of contingency plans are taken up just before or during the event and (3). Recovery/Mitigation Phase, where activities just after the event includes damage assessment and relief management.

3.1. Preparation phase

The preparation phase occurs prior to and in anticipation of a severe flood. In this phase, remote sensing may contribute to mapping of inundated areas, especially at the regional level based on the flood information and experience developed during the earlier floods. Flood risk zone map may consist of two types: (1) A detailed mapping approach, that is required for the production of hazard assessment for updating (and sometimes creating) risk maps. The maps contribute to the hazard and vulnerability aspects of flooding. (2) A larger scale approach that explores the general flood situation within a river catchment or coastal belt, with the aim of identifying areas that have greatest risk (Jeyaseelan, *et al.*, 2003).

3.2. Response phase

The response phase occurs prior to the onset of a flood and is based on weather reports and information from spotter groups. The response phase actins to be taken after the receipt of evidence indicating likely flooding (Gissing, 2003). Three kinds of contribution might be done by remote sensing in this phase, there are (1) Flood prone/Risk zone identification, (2) Flood monitoring, and (3) Flood forecasting.

3.3. Recovery/mitigation phase

The recovery phase usually overlaps the previous phase. The recovery phase may begin just after the flood and can last for several years. In this phase, the remote sensing might contributed on assessment of (1) Flood damage rehabilitation – immediately during flood, and (2) relief efforts – after the flood.

4. Example Of Remote Sensing Application For Flood Monitoring In Indonesia

4.1. Delineation of Flood Prone Paddy Fields Based on Landsat TM

Ministry of Agriculture (2002) delineated the flood prone in paddy field area of Java Island based on Landsat TM, land characteristics, and rainfall data. The divided into four level of flooding, *i.e* (1) the very vulnerable, (2) vulnerable, (3) less vulnerable, and (4) non vulnerable.

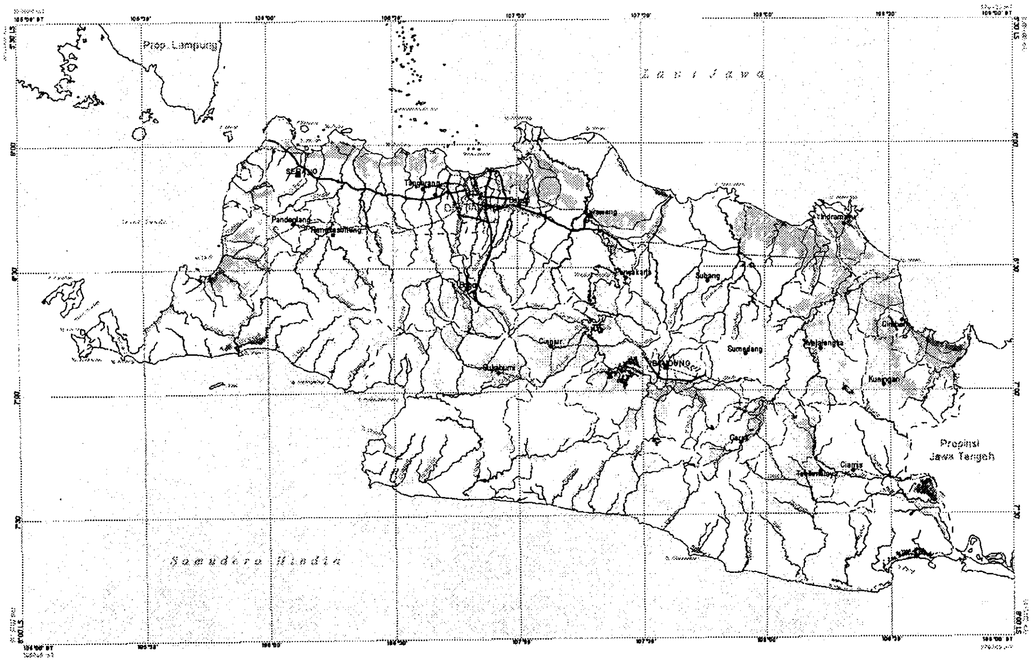

Figure 5. The paddy field area that influenced by flood. Red shown the very vulnerable, pink shown vulnerable, yellow shown less vulnerable, and green shown non vulnerable.

4.2. Delineation of Flood Prone Areas Based on Landsat TM (LAPAN, 2002)

Lapan is the one institution in Indonesia that has mandate to inventory remote sensing data and using it for multiple purposes. In 2002, Lapan delineated the floode prone area for whole Indonesia, as shown in Figure 6.

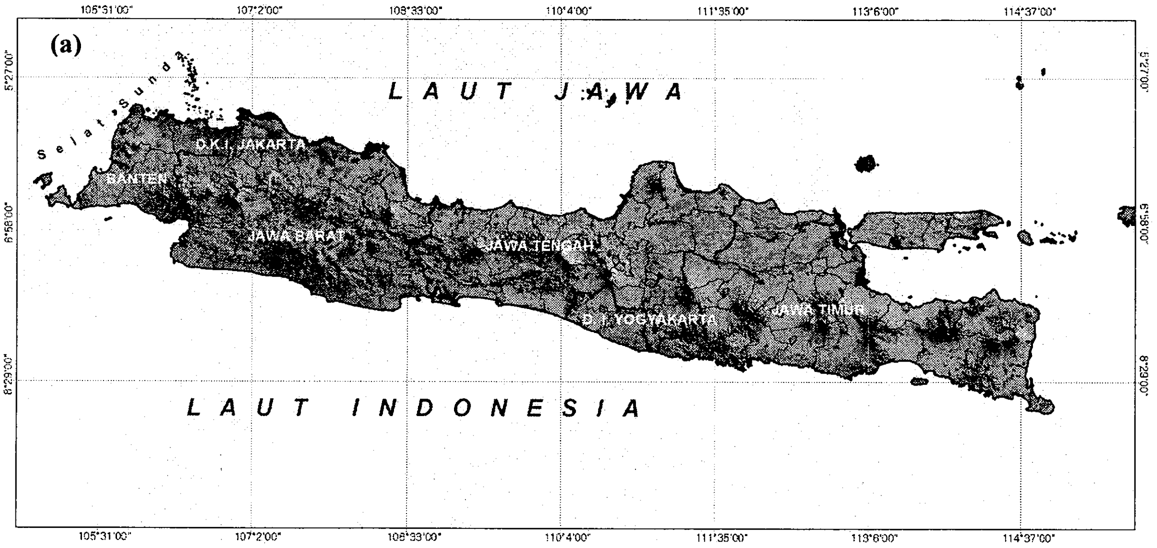

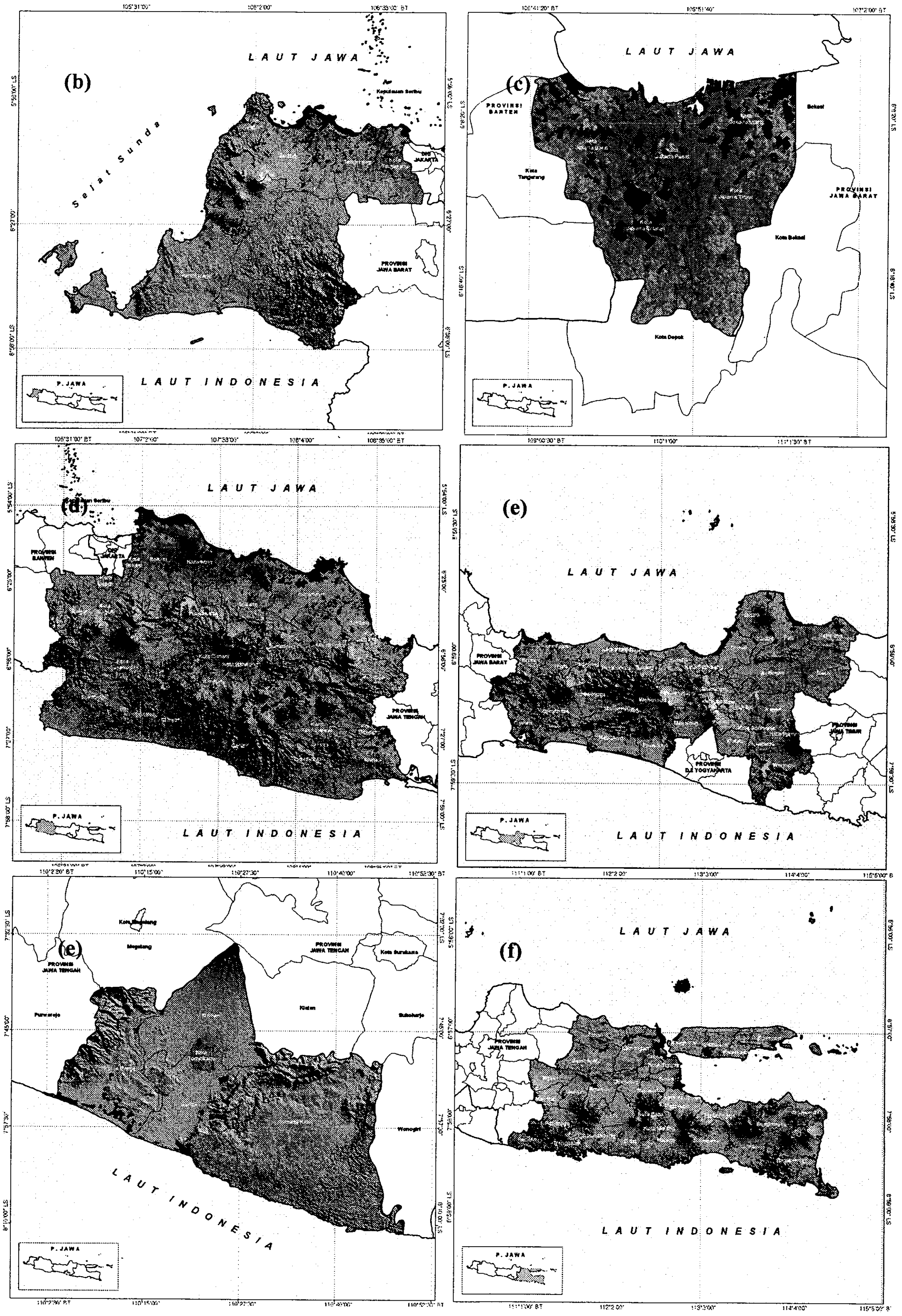

Figure 5. The flooded area delineated using LANDSAT TM (a) Java Island, the Province of: (b) Banten, (c) Jakarta, (d) West Java, (e) Center of Java, (f) Yogyakarta, and (g) East Java. (Source: Lapan, 2002).

4.3. Daily Potential Flooded Area (MTSAT) Information

LAPAN also used MTSAT-1R (Multifunction Transport Satellite - 1R) for monitoring the daily potential flooded area, as shown in Figure 6.

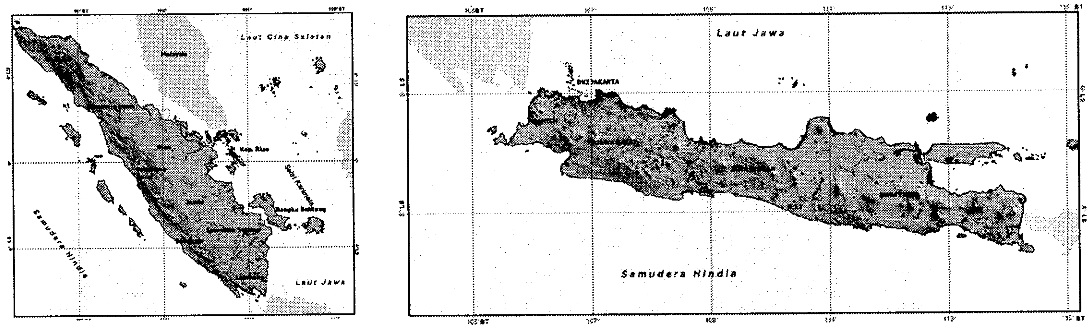

Figure 6. The flooded area delineated using MTSAT-1R of (a) Sumatera and (b) Java islands (Source: Lapan, 2007).

5. Conclusions

Flood is a recurrent problem in Indonesia. Application of the remote sensing technologies is necessary in the activities of the three major phases of flood management (preparation, prevention, and recovery phases). In this paper, brief review of remote sensing and GIS methods and its utilization for flood management in Indonesia are discussed.

References

Aduah M, B. Maathuis, and Y. A. Hussin. 2007. Synergetic Use of Optical and Radar Remote Sensing for Mapping and Monitoring Flooding System in Kafue Flats Wetland of Southern Zambia. The joint meeting of ISPRS Commission VII WG2 & WG7. Conference on Information Extraction from SAR and Optical Data, with Emphasis on Developing Countries. Istanbul, 16-18 May 2007 Istambul, Turkey. 6 p.

Choudhury A. M. 1994. Monitoring and Forecast of Disasters in Bangladesh Using Remote Sensing Technology. ACRS 1994.

CRED, 2007. International Disaster Database, Centre for Research on the Epidemiology of Disasters, Brussels, Belgium.

Dutta, D. and Herath, S. 2004. Trend of floods in Asia and Flood Risk Management with Integrated River Basin Approach. Proceedings of the 2nd International Conference of Asia-Pacific Hydrology and Water Resources Association, Singapore, Volume I, pp. 55-63.

Gissing A. 2003. Flood action plans – Making Loss Reduction More Effective in the Commercial Sector. The Australian Journal of emergency Management, Vol. 18 No. 3, August 2003.

IPCC, 2007. Climate Change 2007: Impacts, Adaptation and Vulnerability. Contribution of Working Group II to the Fourth Assessment Report of the Intergovernmental Panel on Climate Change, M.L. Parry, O.F. Canziani, J.P. Palutikof, P.J. van der Linden and C.E. Hanson, Eds., Cambridge University Press, Cambridge, UK.

Lapan (2002, 2007). http://www.lapan.rs.

Jeyaseelan A.T. (2003). Droughts and Floods Assessment and Monitoring Using Remote Sensing and GIS. Satellite Remote Sensing and GIS Applications in Agricultural Meteorology pp.291-313.

Pham Viet Hoa. 2004. Use of Remote Sensing and GIS Technology for Monitoring and Assessment of Flooding at the Coastal Zone in the Central Part of Vietnam. Presented in 3th Regional Conference, Jakarta, October 3-7, 2007.

Sandoz, A., P. Chauvelon, and M. Pichaud. 2007. Satellite Remotes Sensing Used for Wetland Flooding Duration and Habitats Monitoring. Geographical research Abstract, Vol 9, 09667. European Geosciences Union.

Sandholt I, L. Nyborg, B. Fog, M. Lô, O. Bocoum, K. Rasmussen. 2003. Remote Sensing Techniques for Flood Monitoring in the Senegal River Valley. Danish Journal of Geography 103(1): 71-81.

Urban Sprawl Phenomenon Detection Using Spectral Mixture Analysis (SMA) from Multitemporal Landsat Satellite Images: A case study in Bandung Basin, Indonesia

Ketut WIKANTIKA[1], Ivan PRATAMA[2], Akhmad RIQQI[2], Ibnu SYABRI[3], Y. Ihya ULUMUDDIN[1],
Syams NASHRRULLAH[1] and Firman HADI[1]
[1] Center for Remote Sensing, Institut Teknologi Bandung
[2] Geodetic and Geomatics Engineering, Institut Teknologi Bandung
[3]Urban and Regional Planning Engineering, Institut Teknologi Bandung
E-mail: wikantika@yahoo.com

Abstract

Bandung was a rapid developed city in Indonesia. However the development was unplanned and sporadic. It was urban sprawl phenomenon that was most found in developed countries. Our study was using Spectral Mixing Analysis (SMA) to detect the phenomenon using multitemporal Landsat satellite images. The most difficult process and crucial of the method was determination of end-member. The study could determine two end-member for one band of image and its were used to detect the urban sprawl phenomenon. The application of determined end-member could detect the urban sprawl and it shown that the pattern of residential land distribution is around primary road connecting Bandung and other cities around.

1. Introduction

Urban sprawl is defined as continues growth of urban areas, expanding to peripheral, sporadic and unplanned, and its always produce land use change from rural to urban use. The phenomenon emerges as response of spatial needs in rural for residential land, commercial and service areas, industrial areas, transportation, communication and utility land use and other public facility land use. Rapid population growth and urbanization were causes of sporadic and unplanned residential land development in rural areas. It is urban sprawl phenomenon that is found in Indonesia and other developed countries.

One of big cities that are rapidly developing in Indonesia is Bandung that has a unique magnetic power (Kompas, 2004). Bandung is one of center for mode in Indonesia. Textile and garment industries were spreading out in peripheral areas of Bandung City and it is supported by shop and store tourism for clothing and shoes. Culinary tourism is also supported the shop and store tourism. It could be unique magnetic power for tourists-most of them come from Jakarta-particularly after toll road Cikampek-Purwakarta-Padalarang corridor (connecting Jakarta and Bandung) has been opened. Not only it is making easy to access to Bandung from Jakarta, but also it could be magnetic effect for somebody, which is working in Jakarta, to live in Bandung and around. In addition, Bandung has many universities; there are three governmental universities and many non-governmental universities. Therefore many students from overall of Indonesia are interested in Bandung. All of them are making rapid urban growth in Bandung and it towards urban sprawl phenomenon.

Since 1970s, Bandung's decision-makers have known the phenomena mentioned-above. To solve the problem, Bandung and small cities around have been planned in "Bandung Raya Development" concept. But it is never being and to be far away from the concept; establishment of Cimahi City is the sign of the failure (Kompas, 2003). Unplanned urban growth is pictured on some spots such as Kopo, Setia Budhi, Ujungberung and Cimahi.

In our study will be investigated the using of multitemporal Landsat satellite images to detect width and distribution of residential land on the spots mentioned-above. Satellite images are time series data and it could be used for monitoring purposes. To achieve the aims of study, Landsat images (that has medium resolution in spatial) must be proceed by using particular methods. Thus the medium resolution satellite images could produce residential land map more accurately. Therefore Spectral Mixture Analysis will be developed in the investigation to produce the map.

2. Study area

The spots of residential land mentioned-above are in Bandung Basin. The areas include Bandung City, Kabupaten Bandung, Cimahi City and part of Kabupaten Garut and Sumedang. Fig. 1. is Bandung Basin map. :

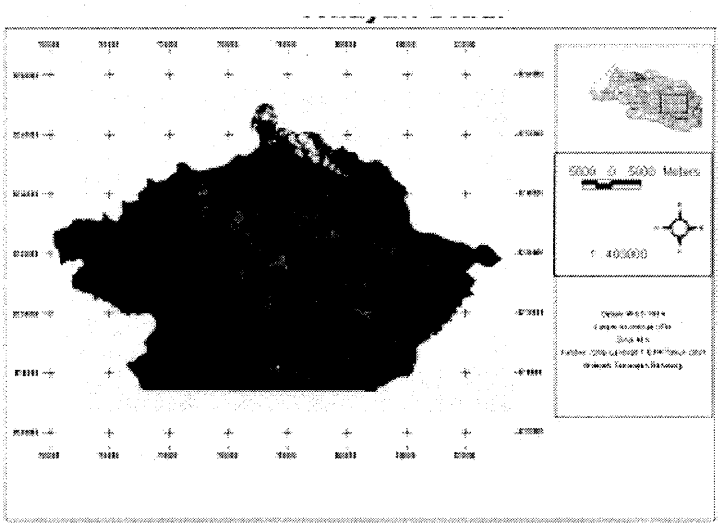

Figure 1. Bandung Basin

3. Data and Methodology

The study uses images of Landsat TM 1994, Landsat ETM 2001. The Landsat images are composite data, 6 bands (1-5 and 7). It is used WGS'84 for datum reference and SUTM 48 zone for projection system. The images are proceed through the stages which is shown in flowchart below:

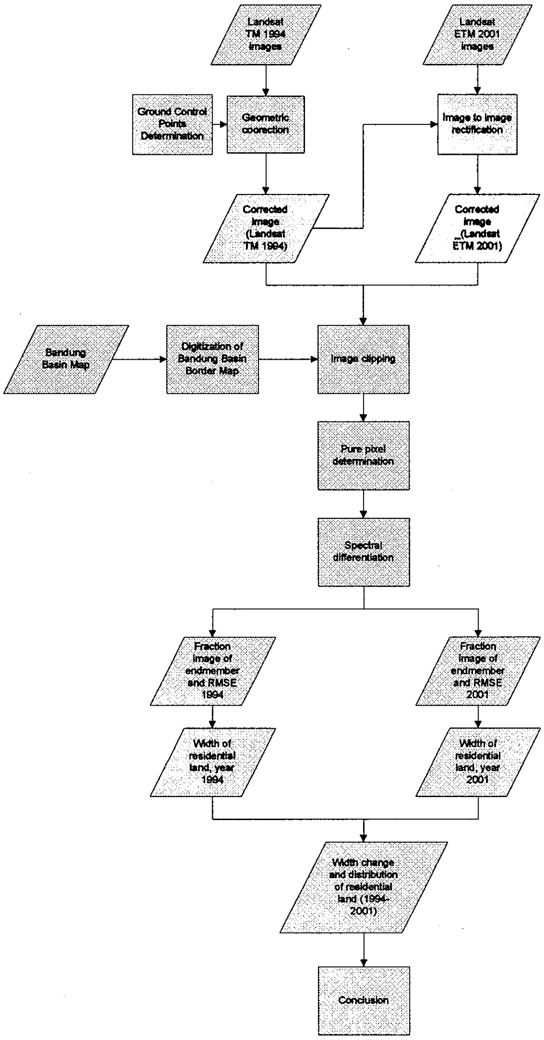

Figure 2. Flowchart of methodology

4. Spectral Mixture Analysis

Spectral Mixture Analysis (SMA) is a process or method to identify the different objects in one pixel of medium and low spatial resolution images. For example: Landsat and MODIS imagery respectively are 30x30 m and 250x250 m in spatial resolution. One pixel may contain more than one object, but one pixel has only one brightness value. By using SMA method, the proportion of the objects in one pixel can be identified and determined. Identified and determined the objects are defined as end-member.

The first process in SMA is determination of pure pixel. The pure pixel is pixel that contains brightness value of one object. Pure pixel determination is proceed through creating training sample end-member. The next process is calculation of each end-member fraction of images. The fraction of each end-member is inverse of matrix below (Peng and Uchida, 1999):

$$\begin{pmatrix} d_{i1} \\ d_{i2} \\ \cdots \\ d_{im} \end{pmatrix} = \begin{pmatrix} r_{11} & r_{12} & \cdots & r_{1p} \\ r_{21} & r_{22} & \cdots & r_{2p} \\ \cdots & \cdots & \cdots & \cdots \\ r_{m1} & r_{m2} & \cdots & r_{mp} \end{pmatrix} x \begin{pmatrix} f_{i1} \\ f_{i2} \\ \cdots \\ f_{ip} \end{pmatrix} \ldots\ldots\ldots\ldots\ldots\ldots\ldots\ldots (1)$$

or

$$D_i = R \text{ x } f_i \ldots\ldots\ldots\ldots\ldots\ldots\ldots\ldots\ldots\ldots\ldots\ldots (2)$$

where,

d_{im} = brightness value of pixel i and band m
r_{mp} = brightness value of end-member p and band m.
f_{ip} = fraction of end-member p and pixel i
n = pixel total of overall image

with requirements:

$f_{ik} \geq 0$, and
$f_{i1} + f_{i2} + f_{i3} + \ldots + f_{ik} = 1$, *where* $i = 1, 2, 3, \ldots, n$ ....(3)
and requirements of matrix to make its inverse matrix.

5. The Result of Spectral Mixture Analysis Application

According to the requirement of spectral differentiation matrix in eq (1), it was chose three cases for end-member determination, two end-member one band, three end-members two bands, and four end-members three bands. From three cases, two end-members one band was selected to detect residential land change in width and urban sprawl phenomena. The end-member determination is the most crucial process because probably pixels with the same brightness value (they have the same object) have different fraction magnitude. It can produce error in interpretation to define direction and magnitude of the changes. The result of selection of the cases is used to investigated urban sprawl phenomena on some spots in Bandung Basin: Kopo, Setia Budhi, Ujungberung and Cimahi.

5.1. *Urban Sprawl* in Kopo

Kopo areas are passed by Jalan Kopo as primary collector road collecting transportation from and to Bandung City (Fig 3). It is connecting Bandung hinterland around. It enhances the growth of residential land around Jalan Kopo (Kristiani, 2004).

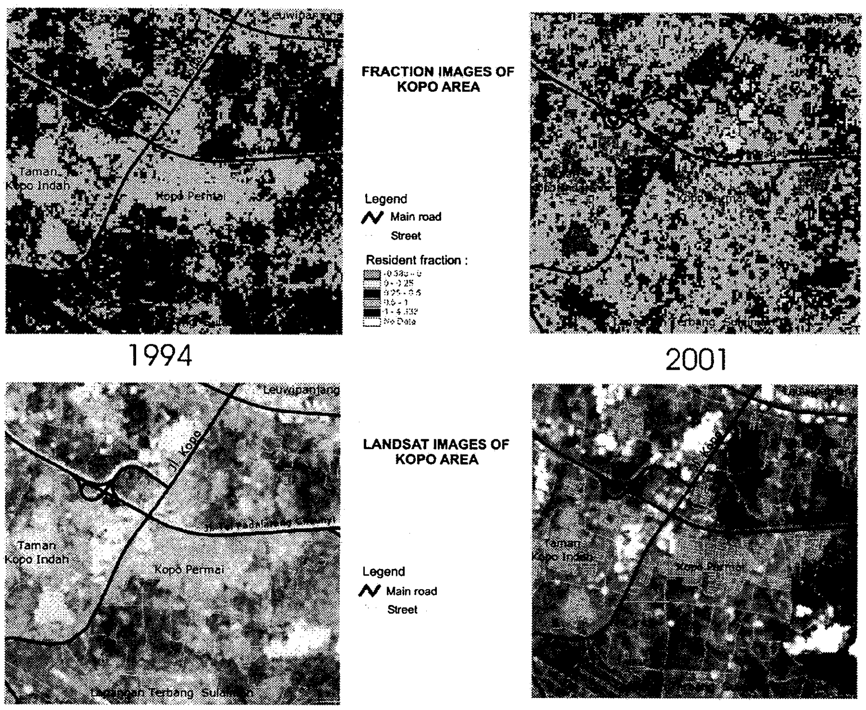

Figure 3. Fraction Images of Kopo Area

5.2. *Urban sprawl* in Ujungberung

Governmental Role number 16, 1987 (PP No. 16, 1987) gives a role of rural development in Bandung toward east. Unfortunately, residential land expansion is not only toward east but also toward west or center of Bandung City (Budianto, 2001). Residential land spreads out following primary road that the purpose of the road is as artery road connecting Bandung and others (Fig. 4).

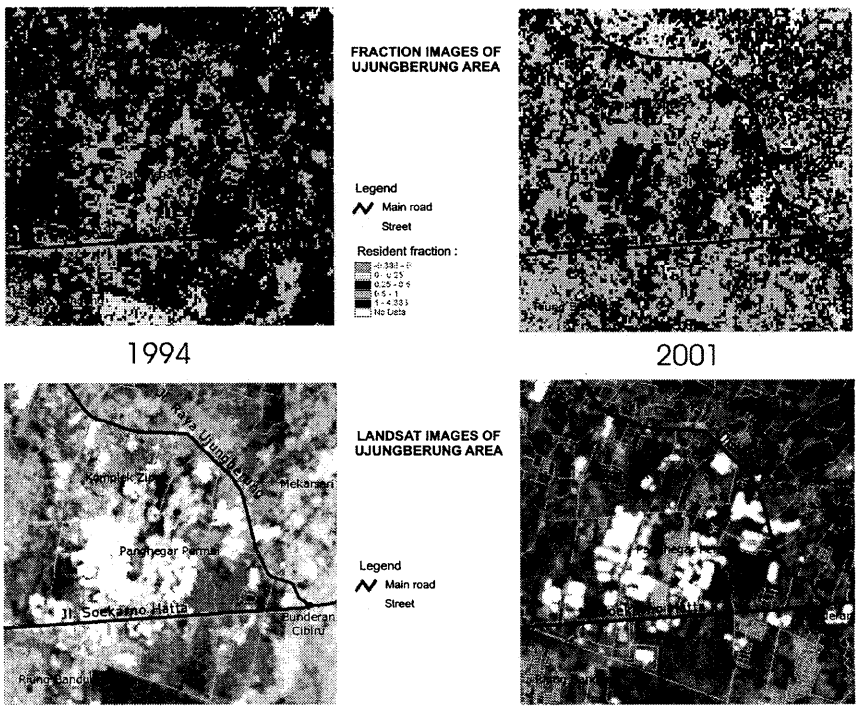

Figure 4. Fraction images of Ujungberung Area

5.3. *Urban sprawl* in Setia Budhi

The residential land of two spots above growths rapidly because it is supported by the road connected Bandung and others. Residential land expansion in Setia Budhi follows Jalan Setia Budhi, the easier access to governmental facilities and commercial and service facilities (Fig. 5). In addition, mountain air-fresh (ten years before) in Setia Budhi areas is one of reasons to build houses. Jalan Setia Budhi is also as primary road connected to tourism areas in Lembang and Kabupaten Subang.

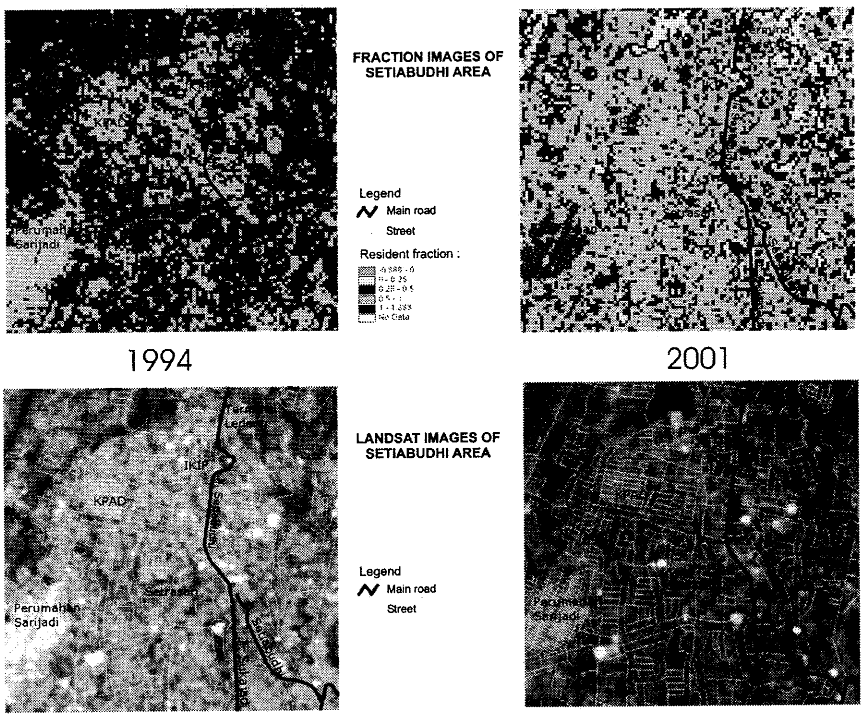

Figure 5. Fraction Images of Setia Budhi Area

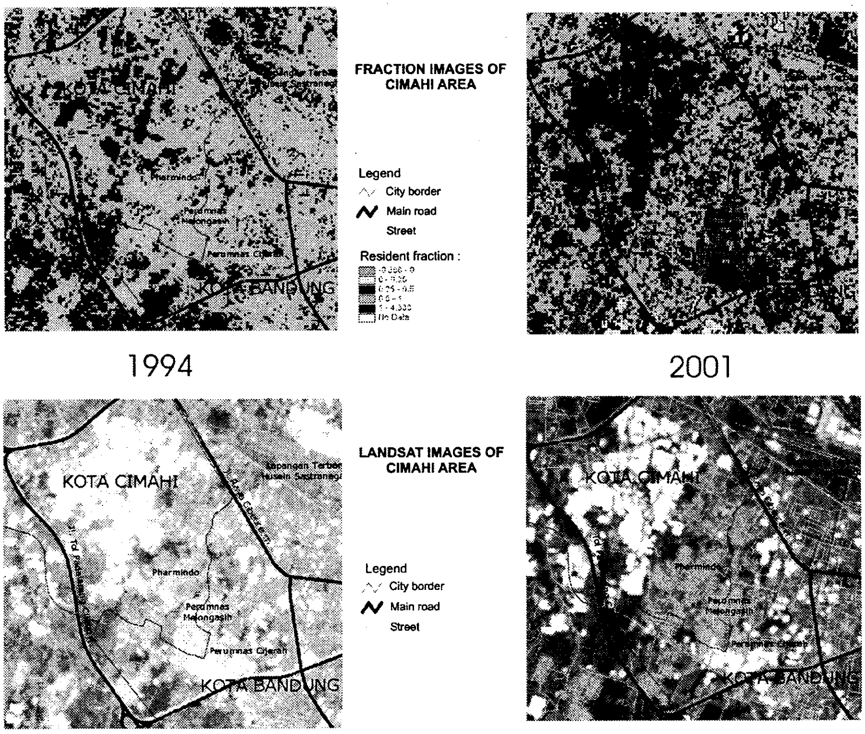

Figure 6. Fraction images of Cimahi Area

5.4. *Urban sprawl* in Cimahi

Different from three spots above, residential land expansion in Cimahi follows the rural growth as center for military training and education and industrial areas to improve the income of Kabupaten Bandung (before being Kota Cimahi). Residential land growth in the spot overlaps with the two activities. Population growth in Cimahi enhances development of commercial and service areas that its placement also overlaps with other land use. The development is enhanced by strategic position as a gate of Bandung City in the south (Fig. 6).

6. Conclusion

The use of Spectral Mixture Analysis method has difficulties on end-member determination. From three cases end-member determination, two end-members, one band was selected to detect residential land growth in Bandung Basin. In general, residential land growth on the spots investigated follows road development, particularly the roads connected to other city.

References

Budianto, F. 2001. Karakteristik Perjalanan Penghuni Perumahan Formal dan Pengaruhnya Terhadap Tingkat Pelayanan Jalan Raya Timur Bandung. Kasus Perumahan Formal di Kawasan Ujungberung Bandung. Departmen Teknik Planologi. Institut Teknologi Bandung. Bandung. Indonesia

Kristiani, L.A. 2004 Kajian Perubahan Tingkat Pelayanan Jalan Kopo Bandung dengan Pengelolaan Lalu Lintas. Skripsi. Departemen Teknik Planologi. Institut Teknologi Bandung. Bandung. Indonesia

Layuck, J. R. 2003. ___________________. Kompas, 30 November 2003. Jakarta. Indonesia

Suganda, H. 2004. Bandung Raya, Apakah masih relevan?. Kompas, 6 Desember 2004. Jakarta. Indonesia.

Peng, Y and Uchidas. S. *The Use of Linear Spectral Unmixing Model for Improving Estimation Accuracy of Winter Wheat Acreage – A Case Study in Shunyi County.* Beijing. China.

Long-Term Landcover Monitoring and Disaster Assessment in ShiMen Reservoir Watershed Using Satellite Images

Fuan TSAI[1] and Liang-Chien CHEN[2]
[1,2]Center for Space and Remote Sensing Research, National Central University, Taiwan
Email: {ftsai, lcchen}@csrsr.ncu.edu.tw

Abstract

ShiMen Reservoir is one of the largest and most important water resources in northern Taiwan. It supplies water to more than two million people as well as to high-tech industry and irrigations for agricultural development in the area. The watershed of ShiMen Reservoir covers an area of 764 km^2 with 3000m variations in elevation. Being a relatively young region in geology, the rock and soil formations in the watershed are fragile. Landslides are commonly triggered in the area by heavy rainfalls, typhoons and earthquakes. Consequently, it is necessary to continuously monitoring landcover/landuse changes to identify and further reduce the potential of landslides as well as to assess the damages after natural and man-made hazardous events for better watershed management. This project implemented an intensive long-term monitoring program using multi-temporal remote sensing images acquired from multiple satellite sensors. The monitoring program integrated remote sensing image analysis, geographic information systems (GIS) and other spatial information technologies to develop a sophisticated operational system. The developed system has been used for detecting landcover/landuse changes on a monthly basis and for dynamic disaster assessment as needed. It is also used for long-term monitoring of vegetation recoveries in previously damaged regions within the watershed. The program has been in effective for five years and proved to be a powerful mechanism for watershed management.

1. Introduction

Landuse management and post-disaster assessment are two important tasks in watershed administration. A timely and accurate update about landcover changes in a watershed can provide the authority not only helpful knowledge for the administration but also necessary support for decision making. When a natural disaster or man-made hazard happens, it is critical to have a complete and thorough evaluation of the areas and severity of damages in order to come up with effective remedy and prevention strategies. Traditionally, these tasks rely primarily on *in-situ* investigations, which are often expensive and time-consuming. Remote sensing, on the other hand, provides a more economical and effective alternative for investigating large-area ground coverage. Therefore, remote sensing can be a powerful tool for landcover monitoring and disaster assessment for watershed management.

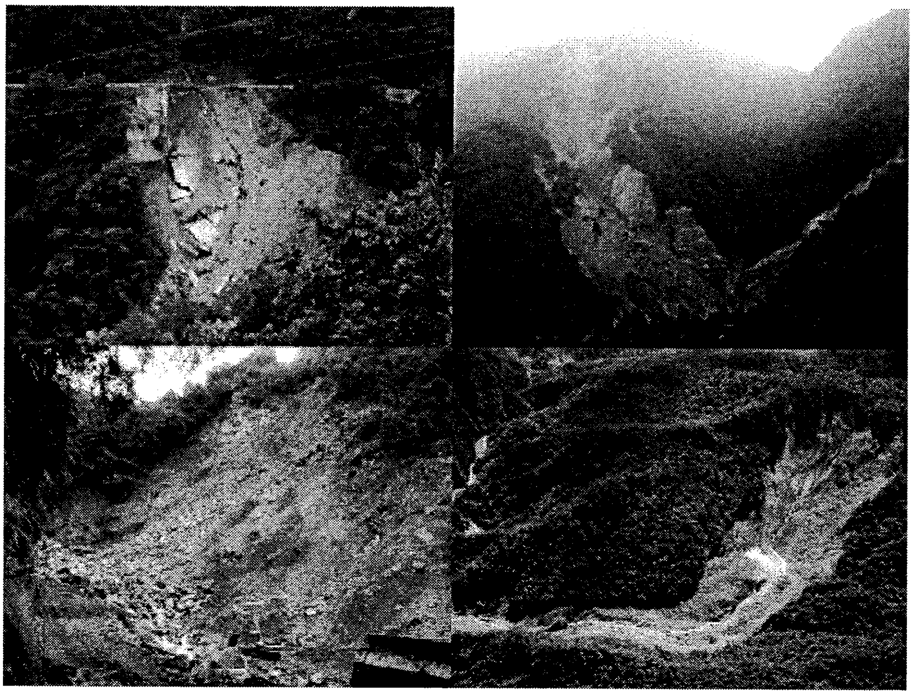

Fig. 1: Four landslides in ShiMen Reservoir watershed induced by Typhoon AERE in Oct. 2004.

ShiMen (stone gate, literally in Chinese) Reservoir is one of the largest water resources in Taiwan. Water supplies of more than two million people in Taipei and Taoyuan of northern Taiwan all depend on the reservoir. It also provide water to high-tech industry and irrigations for agricultural development in the area. The ShiMen Reservoir watershed covers an area of about 764 km^2. There are more than 3000m variations in elevation within the watershed. The geological conditions in the watershed are not very stable—fractural rock formations with mountainous joints and cleavages. Therefore, landslides are frequently triggered by earthquakes and heavy rainfalls. For example, the 1999 Chi-Chi Earthquake, which measured 7.3 in Richter Scale, had caused tens to hundreds of severe coseismic landslides in the watershed [1] and Typhoon AERE (Oct., 2004) also triggered serious landslides and mudslides (some examples are shown in Fig. 1). The debris of landslides were flushed into the reservoir, making the water too turbid and shutting down water supply for weeks to months.

In order to obtain accurate landcover information and disaster assessment in the ShiMen Reservoir watershed, a long-term satellite monitoring program was established in 2002. The purpose of this program is multifold. It ordinarily serves as a dynamic landcover change detection force. When a hazardous event occurs, the program will quickly perform a disaster assessment and provide valuable inputs for decision support.

2. Methodology

2.1 *Data Acquisition*

The primary data used in the monitoring program are SPOT series satellite imageries (including SPOT-2, 4, and 5) and FORMOSAT-2 data. SPOT series satellites are operated by SPOT Image [2]. SPOT-2 has two sensors, one for panchromatic (PAN, with 10m resolution) and the other for a three-band multispectral imaging (green, IR and NIR; with 20m resolution). SPOT-4 also has a PAN senor; however, its multispectral sensor has an additional short-wave IR (SWIR) channel. SPOT-5 was launched in 2002. The PAN data of SPOT-5 have 1 5m ground resolution and its multispectral data are similar to SPOT-4. In addition, SPOT-5 can also provide 2.5m resolution data (Super Mode) using image fusion technologies. FORMOSAT-2 (formerly ROCSAT-2) was launched in 2004. It is the first resource satellite of Taiwan. It has a unique daily revisit capability. FORMOSAT-2 data also come with a PAN band with 2m resolution and four multispectral band (blue, green, red, NIR) with 8m resolution [3]. Fig. 2 illustrate the data acquisition plans of SPOT and FORMOSAT-2 data over Taiwan and the sample images of the ShiMen Reservoir watershed. In ordinary time, both satellites maintain their regular acquisition schedule, allowing acquiring an image of the watershed every three days in average. When a hazardous event occurs, if the weather condition permits, an emergency acquisition plan will be activated, which uses the two sensors onboard of the SPOT satellites for acquiring multispectral data simultaneously to cover a 120km swath (Twin Mode). This will increase the SPOT coverage of the watershed to about two images in three days. In conjunction with the FORMOSAT-2 data, the objective is to targeting daily image acquisition.

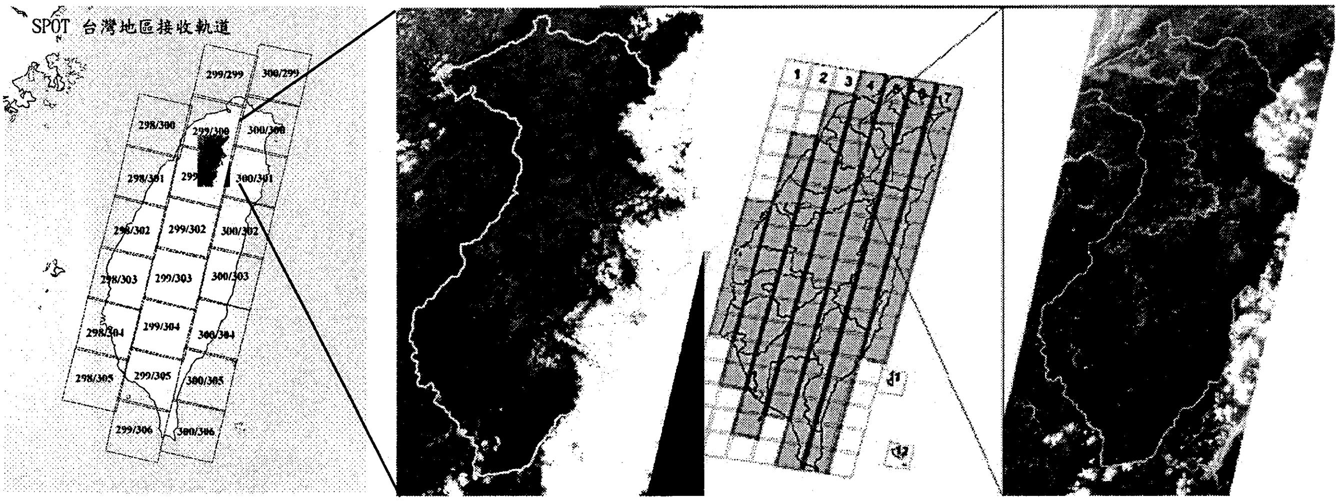

Fig. 2: Data acquisition plan for SPOT (left) and FORMOSAT-2 (right) images

2.2 Data Processing and Analysis

The acquired images are orthorectified with a multi-senor geocoding system (MSGPS) [4]. The system utilizes ground control points and rigorous sensor models for orbit adjustment and least-squares filtering [5]. A digital terrain model is also used for terrain relief corrections of the images.

The landcover change detection is performed using Normalized Difference Vegetation Index (NDVI) and Change Vector Analysis (CVA) [6]. CVA is a transformation for measuring the magnitudes of variations in multispectral and multi-temporal (spectral) vectors. Combining CVA and NDVI provides a more thorough landcover change detection mechanism because NDVI is insensitive to changes among non-vegetation types (e,g, from soil to buildings). For automatic change detection, an empirical threshold was used to identify changed regions so they could be vectorized for subsequent analysis. For NDVI analysis, the threshold is set as 0.3 after analyzing long-term (three years) detected results and comparing with in-situ verifications.

2.3 The Operational System

A sophisticated image processing and analysis system was developed to perform the long-term landcover monitoring and disaster assessment. The developed system integrates remote sensing image analysis, geographic information systems (GIS) and other spatial information technologies. It also provides user-friendly graphical user interfaces. Fig. 3 shows an example of the interfaces. The system can also overlay detected changed regions on 1/5000 or 1/10000 maps and output the results in high quality print-outs. Statistical reports for each detection will also be generated automatically. In case of disaster assessment, a special report will be generated for each hazard site along with regular change-detection maps.

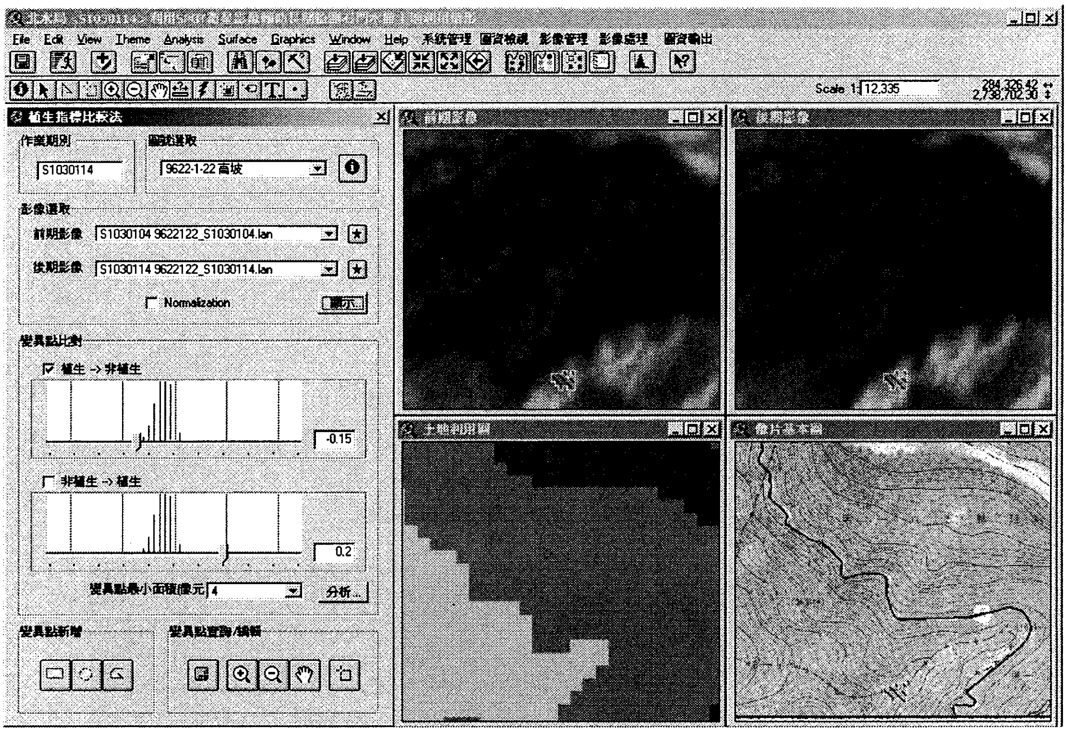

作業期別: S1030114

圖號選取: 9622-1-22 高坡

前期影像: S1030104 9622122_S1030104.lan

後期影像: S1030114 9622122_S1030114.lan

☐ Normalization

☑ 植生 -> 非植生: -0.15

☐ 非植生 -> 植生: 0.2

變異點最小面積(像元): 4

Fig. 3: User interface of the developed change detection system.

3. Results

As mentioned in 2.3, each detected change site will be overlaid onto maps and sent to the watershed administration for field investigation. Fig. 4 displays an example of a detected landslide after Typhoon SEPAT (Aug. 2007). The detection was made by comparing two SPOT images (July 19 and Aug. 28). In the region shown in the images there was already an old landslide. After the typhoon, the damaged area has extended further uphill as marked in green polygon. Similar maps were produced for each detected change regions and a statistical report was generated. The report listed all detected regions with assorted attributes, including coordinates, townships, areas and preliminary determination of change types.

For disaster assessment, in addition to the image maps, a special report was also created for each hazard site. The report also shows three-dimensional perspective view of the site. The 3D perspective view was created by draping satellite images onto digital terrain models (as shown in Fig. 5). These images, maps and reports were also sent to the watershed administration. Field investigators would then be dispatched for in-situ verification. If the change was caused by illegal land development or logging activities, the situation will be forwarded to appropriate authorities and proper causes would be enforced.

The field investigation results were fed back to the monitoring program to evaluate the detecting performance as well as to fine tune the analysis parameters. Since this program was in effect in 1993, the collected data of detected changed sites also provide valuable information. For example, Fig. 6 displays seasonal statistics of dynamic changes from 2003 to 2005. As can be seen from the figure, the primary sources of landcover changes were agricultural cultivations. However, the severe typhoon AERE in 2004 caused serious landslides in the watershed resulting in about 400 hectares of detected hazard sites, Typhoon MASA and Typhoon TALIM in 2005 also caused landslides, but there damages were less serious. The implemented program was also used to conduct thorough landuse map updates and monitoring the vegetation coverage changes (as shown in Fig. 7). These types of data and derived parameters have been prove to be valuable information to the watershed administration in developing viable strategies and policies for management and disaster mitigation and prevention plans.

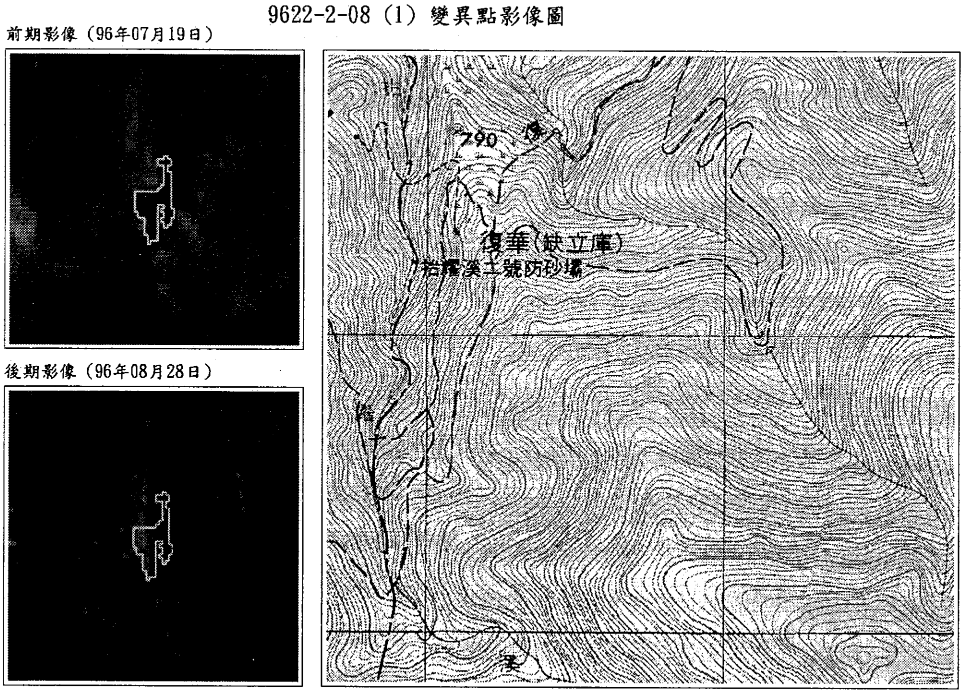

Fig. 4: Change detection example.

Fig. 5: 3D perspective view of landslide sites.

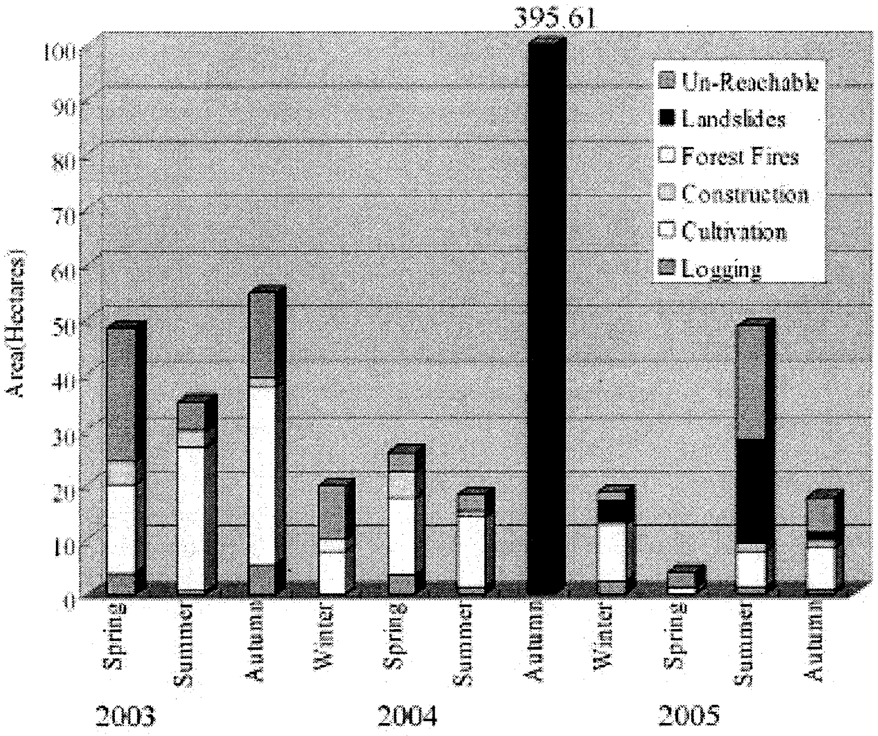

Fig.6: Seasonal statistics of detected dynamic changes from 2003 to 2005.

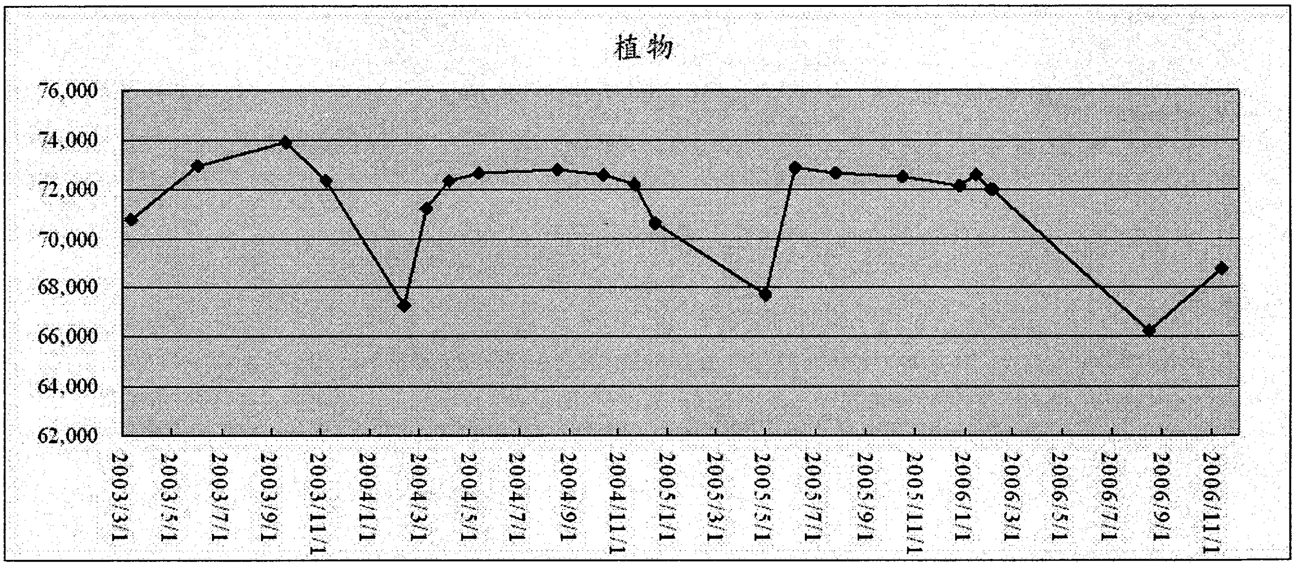

Fig.7: Vegetation coverage changes in ShiMen watershed from 2003 to 2006.

Another task of the implemented program is to continuously monitor the detected changed areas, especially those detected hazard sizes. This long-term monitoring was carried out by comparing NDVI values using multi-temporal and multi-senor data. However, in order to eliminate NDVI variations caused by illumination and atmospheric parameters over different time periods, NDVI data derived from individual images were further "normalized" or stretched using selected "evergreen spots" as references. The purpose of this type of monitoring is twofold. First, it serves as an evaluation of the natural vegetation recovery process in the watershed. Secondly, it is used as a reliable and subjective tool for monitoring the progress and comparing different man-made vegetation-recovery projects employed in several landslide sites. Fig. 8 demonstrates an example of the vegetation recovery monitoring. The landslide was induced by Typhoon AERE in Oct. 2004. The left image in Fig. 8 was acquired on Oct. 12, 2004, while the middle image was acquired on Oct. 20, 2006. Comparing these two images indicated that vegetation has been recovered in more than 14000 m^2 of the landslide site. The right image shown in Fig. 8 is a digital photograph of the same area taken in late May of 2006. From the picture, it can be seen that vegetation has gradually regained grounds of the slided hill.

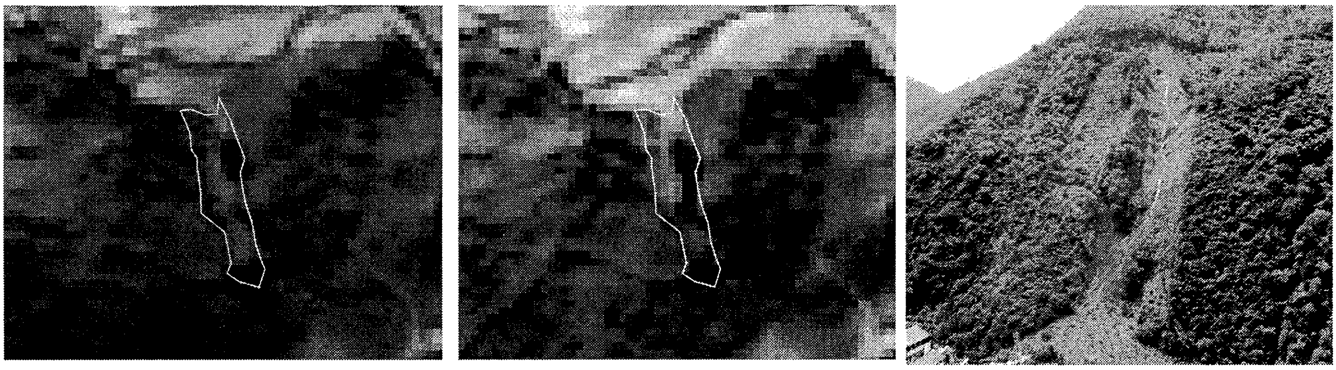

Fig. 8: Vegetation recovery of landslide sites.

4. Conclusions and Future Works

This project implemented an intensive long-term monitoring program in the ShiMen Reservoir watershed of northern Taiwan, using multi-temporal remote sensing images acquired from multiple satellite sensors. The primary objective was to continuously monitoring landcover/landuse changes to identify and further reduce the potential of landslides as well as to assess the damages after natural and man-made hazardous events for better watershed management. The monitoring program integrated remote sensing image analysis, geographic information systems (GIS) and other spatial information technologies to develop a sophisticated operational system. The developed system has been used for detecting landcover/landuse changes on a monthly basis and for dynamic disaster assessment as needed. It is also used for long-term monitoring of vegetation recoveries in previously damaged regions within the watershed. The program has been in effective for five years and proved to be a powerful mechanism for watershed management. The next phase of this project will be developing viable approaches for identifying and categorizing potential landslide sites based on spatial analysis and other related researches.

Acknowledgment

This project was funded by the North Region Water Resource Office (NRWRO), Water Resource Agency, Ministry of Economy, Taiwan. The authors would like to thank Dr. J. Y. Rau for his efforts in the development and execution of this project.

References

[1] Seismic Database, Sep. 21, 1999, Central Weather Bureau, Taipei, Taiwan. http://www.cwb.gov.tw/V5e/index.htm.

[2] SPOT Image. Http://www.spot.com.

[3] Wu, AM, 2003. “Qualification test of ROCSAT-2 image processing system”, Proc. *24th Asian Conference on Remote Sensing*, Busan, Korea, 2003, CD-ROM.

[4] Rau, J. Y., L. Y. Chang, T. A. Teo, K. Hsu, J. Y. Chen, L. C. Chen, AJ Chen and K. S. Chen, 2003. “An operational multi-sensor geocoded production system for earth resources satellite images”, *Proc. 5th Int'l Symp. RCSGSO*, Pasadena, CA USA. Jul. 8-11, 2003, CD-ROM.

[5] Chen, L. C., T. A. Teo and J. Y. Rau, 2003. “Fast orthorectification for satellite images using patch backprojection”, *Proc. IGARSS'03*, Toulouse, France, 2003.

[6] Lambin, E. F. and A. H. Strahler, 1994. “Change vector analysis in multi-temporal space: a tool to detect and categorize land-cover change process using multi-resolution satellite data”, *Remote Sensing Environ.*, 48(2), pp. 231-244.

Remote Sensing for Disaster Monitoring and Mitigation in Malaysia

CHUNG Boon Kuan
Centre for Applied Electromagnetics, Multimedia University
E-mail: bkchung@mmu.edu.my

Abstract

Remote sensing has been used widely for disaster management in terms of monitoring and mitigation operations. With advances in sensor technology and computation power, application of remote sensing has been enhanced with the availability of optical and radar images of the earth surface to complement the traditional black and white survey aerial photographs. Remote Sensing sensors are regularly flown on satellites such as European Remote Sensing (ERS), Japanese Environmental Resources Satellite (JERS), Radarsat, and SPOT. The image products may be ordered from the respective satellite operating agencies. However, the management of dynamic events such as natural disaster, search and rescue operations and surveillance requires real-time, on-demand, high resolution and all-weather data. Airborne sensors are vital to provide an effective disaster monitoring. In addition, it is important to have a central system for collecting, storing, processing, analyzing and disseminating value-added data and information to the relevant agencies in the management of major disasters in the country. This paper introduces the developments of remote sensing infrastructure and some of the research projects undertaken in Malaysia.

1. Introduction

The main aim of remote sensing is to develop techniques for the utilization of observations to derive information about the biophysical and geometrical properties of the targets without physical contact. Optical and microwave sensors are widely used to facilitate the research and development work.

The most important tools for remote sensing applications are the imaging sensors mounted on flying platform (aircraft or spacecraft) to produce pictures of the Earth surface. Optical sensors rely on the sun as the source of illumination. The intensity of reflected light or emitted infrared from the ground object depends on the time-of-day, direction of sunlight relative to the viewing angle, and cloud cover condition.

Microwave sensors operate based on the principle of radar. The main advantage of radar instruments is their ability to penetrate clouds, rain, tree canopies, and even dry soil surfaces depending on the operating frequencies. Objects below the forest canopy can be “seen” by the imaging radar. This leads to some interesting applications such as estimation of tree-trunk diameter, canopy biomass, and moisture content of leaves and soil. On the other hand, due to the persistent cloud cover in tropical climate, the use of microwave remote sensing technology is crucial and advantageous over optical technology in the tropics. In addition, since radar is an active instrument which provides its own illumination, it can operate in both day and night. The imaging outputs are more consistent because they are not affected by sunlight intensity or direction. Different polarizations of electromagnetic wave can be transmitted, therefore the multi-polarization backscattering responses can provide additional information of the ground objects.

The images produced by both optical and microwave sensors have shown many useful applications in natural resource management and environmental monitoring. These include agriculture, forestry, and range resources management; land use and mapping; Geology; water resources management; Oceanography; environmental management; and planning of infrastructure development and town. Disaster management is another very important remote sensing application. Nevertheless, it is very much related to the other applications mentioned above. For example, in the management of forest fire, one needs to know the crop types, crop acreage by species, biomass, moisture condition, and soil conditions in order to predict the spreading of the fire. After the disaster is over, land use map with detailed inventory information is needed to assess the damage and economic loss. In the management of landslide, one needs to know the land uses, mapping changes of major geologic units, delineation of unconsolidated rock and soils, and monitor modified slopes and deforestation in order to assess landslide risk and hazard and take the necessary proactive measures that will prevent the occurrence of major landslide or provide early warning to minimize loss of human lives. In flood monitoring and mitigation, one needs to know the normal water boundaries, channel networks of the terrain, mapping of floods and flood plains, and determine the water depth. It is also important to determine the effects of the natural disasters in terms of transportation disruption, economic loss, and epidemic proliferation. On needs to map and monitor water pollution and retrieve eddies and waves information from sensor images to assist in tracing of oil spills and other pollutants. One needs to process remote sensing data to detect haze and air pollution. Techniques are yet to be developed for remote sensing of tsunami. Real-time tsunami sensor network is normally use for early warning purposes. However, remote sensing techniques can be applied in mapping shoreline changes after the disaster.

Remote sensing research and development has seen many changes in the past few years. The disasters of tsunami in 2004 and hurricanes in 2005 have presented new challenges for geosciences and remote sensing scientists and engineers. Advanced applications can only be developed with the supporting research and development in sensor systems, theoretical modeling of wave-matter interaction, and controlled experiments. This article aims to give an overview of the developments of remote sensing infrastructure and some of the research projects undertaken in Malaysia.

2. Remote Sensing Development in Malaysia

A few groups of researchers have worked on remote sensing research for the past 30 years or so. The potential of remote sensing is enormous. The Malaysian Centre for Remote Sensing (MACRES) was established in 1988 by the government to intensify the R&D in remote sensing and to enhance the collaboration between the relevant agencies, universities and industry.

A National Resource and Environmental Management System (NAREM) was developed in 2001. It comprises three major components: NaSAT organizes remote sensing data into an integrated database; NaMOS consist of a collection of application packages employing model-based technique to support the various applications; and NaDES is a decision support system which provides the desired information to the data and application queries. NAREM application packages were developed through inter-agency collaboration involving natural resources agencies and universities for nine sectors, namely: agriculture, forestry, geology, marine, environmental management, hydrology, coastal, topography, and socio-economic, as well as the central planning authority of the government as the main user of the system. The applications include landslide hazard zoning, coastal sensitivity index, soil erosion, ground water potential, agro suitability zoning, and forest management. The system is also used to continuously monitor development activities on environmentally sensitive area in the country. Accordingly, reports are submitted on regular basis for activities affecting areas such as water catchments, highlands, forest reserves and wetlands.

Remote Sensing sensors are regularly flown on satellites such as European Remote Sensing (ERS), Japanese Environmental Resources Satellite (JERS), Radarsat, and SPOT. The image products may be ordered from the respective satellite operating agencies. However, the delivery of the image product on CD or tape may take substantial time. MACRES has established a ground receiving station (MGRS) at Temerloh to receive remote sensing data on real-time basis directly from the satellites of SPOT, Landsat, Radarsat and NOAA. The raw data can be converted to various levels of image products by the Data Processing System. The system was fully operational since 2002. It was later upgraded to receive MODIS data from Terra and Aqua satellites, and OCM data from Indian IPS-P4 satellite. With its 2500 km radius footprint coverage, the facility is capable of receiving satellite data of Malaysia, ASEAN countries, southern part of China and eastern part of India.

The MGRS will be upgraded to receive data from RazakSAT, the second remote sensing satellite of Malaysia. The payload of RazakSAT is a Medium Aperture Camera comprising 1 panchromantic-band sensor (2.5-m resolution) and 4 Multispectral sensors (5-m resolution). The small satellite will circulate on near-equatorial orbit (NEqO) at an altitude of 600-800 km and inclination of 7 – 9 degrees. Commercial LEO satellites that circle the earth on polar orbit will pass over the same spot along the equatorial belt around once every 21 days. The RazakSAT, being on NEqO, will see the same spot along the equatorial belt every 2 – 6 days but it will see Malaysia as many as 11 – 14 times a day. It will be able to provide timely data to its users in Malaysia as well as catering to the needs of countries located on the equatorial belt.

The management of dynamic events such as natural disaster, search and rescue operations and surveillance requires real-time, on-demand, high resolution and all-weather data. For this reason, MACRES is acquiring from China a Hyperspectral sensor (64 VIS/NIR, 2 SWIR, 1 MIR, 1 TIR; 3-m resolution at 1-km altitude) and an L-band Synthetic Aperture Radar (SAR, 3-m resolution), mounted on two different aircraft platforms. At the same time, Multimedia University (MMU) is collaborating with MACRES to develop a C-band airborne SAR. The prototype antenna, transceiver hardware and image reconstruction software have been implemented and tested [1]-[11].

Multi-temporal, multi-polarization, multi-look-angle, and multi-frequency SAR data are not readily available. Therefore, controlled experiments on natural targets are best conducted using a truck-mounted scatterometer. A C-band scatterometer [12] has been designed and constructed. It supports full-polarimetric measurements. The measured polarization responses for dihedral and trihedral corner reflectors show excellent match with the theoretical responses. The non-imaging sensor can be easily deployed to the measurement site such as a paddy field [13]. Measurement can be performed at various incident angles over the growth stages of the crop. The measurement results can be used to test the accuracy of theoretical models. An L-band scatterometer is being developed to complement the C-band system in future field measurements.

Theoretical modeling is important for understanding of the interaction between microwave and the earth terrain so that software algorithm can be developed to predict the radar returns from such medium. In order to validate the theory under controlled environment, measurements using anechoic chamber and scatterometer systems are conducted. A multipurpose anechoic chamber has been designed to operate over an extremely wide frequency range from 30 MHz through 18 GHz [14]. The geometry of the chamber is asymmetrical, consisting of a combination of rectangular and tapered volumes. The size of the chamber is 64' × 32' × 24' height. Less expensive absorbers can be used to obtain the required wideband performance made possible by the unique geometry. For Remote Sensing research, the chamber can facilitate both monostatic and bistatic microwave scattering measurements for a variety of incident/scattering angles and polarization configurations.

3. Disaster Monitoring and Mitigation Requirements

Remote sensing has been used widely for disaster management in terms of monitoring and mitigation operations. With advances in sensor technology and computation power, application of remote sensing has been enhanced with the availability of optical and radar images of the earth surface to complement the traditional black and white survey aerial photographs.

Data from both optical sensor (VIS and NIR) and SAR may complement each other to provide accurate detection of environmental hazard and monitoring of disaster. The required spatial resolution is in the range of 1 m – 20 m, while the required temporal resolution may be seasonal, daily, or event dependence. The revisit time of commercial remote sensing satellites is in the range of 5 – 24 days. They cannot provide timely data for disaster management applications. On the other hand, countries in the equatorial belt suffer from persistent cloud cover which severely hampers the application of optical satellite images. The use of microwave remote sensing technology is crucial and advantageous over the optical technology in tropical regions. Airborne SAR is particularly useful for disaster monitoring and mitigation operations.

In the event of a natural disaster, remote sensing processing system must be in place to monitor, model, and map natural hazards quickly and reliably. In addition, appropriate decision must be made for deployment of rescue teams to diminish possible threats to human safety and infrastructure. A national disaster monitoring and mitigation framework called NADDI has been developed to establish a central system for collecting, storing, processing, analyzing and disseminating value-added data and information to support the National Security Division and relevant agencies in the management of major disasters in the country. The system consists of three components: (i) Early Warning; (ii) Detection and Monitoring, and (iii) Mitigation and Relief.

The Early Warning component produces risk maps of areas that are susceptible to disasters. It also control a number of real-time alert systems installed at high risk area. The Detection and Monitoring component acquires remote sensing images from satellite-borne and airborne system as well as data from ground surveillance to provide near real time information on the exact locations and extent of the disaster to the disaster coordinating authority. The Mitigation and Relief component is an inter-agency activities carried out through a Disasters Management and Coordination Centre to mitigate and manage disasters. Disasters addressed by NADDI are flood, landslide, forest fire, oil spill and "hot-installations", and tsunami.

4. Remote Sensing Research at MMU

The research team at the Centre of Applied Electromagnetics of MMU has worked closely with MACRES for many years. The remote sensing research includes the development of Radar Sensors and Microwave Remote Sensing Applications. Theoretical models to study wave scattering mechanism (such as Renormalization Technique, Monte Carlo model, Dense Medium Phase and Amplitude Correction Technique, and Radiative Transfer Equation) have been developed and used in SAR image processing and analysis.

One of the research projects that the Centre is currently undertaking is modeling of landslide processes. Generally, landslide may be triggered by (i) Endogenic force – due to tectonic adjustment, usually the uplift processes that alters the surficial features of hill slopes; and (ii) Exogenic force - due to weather related phenomena such as storms, hurricanes, typhoons, sandstorms, and ground water depletions. The objectives of this project are to identify zones of landslide occurrence and the potential path(s) that the landslide will follow. Multiscale Mathematical Morphology techniques are used to produce multiscale Digital Elevation Models

(DEM) and extract ridge and channel networks of the terrain [15]-[17]. An example is shown in Fig. 1 and 2. Soil types, land use/land cover features, and mountain moist fields will be classified from airborne and space-borne remote sensing images. Certain models of landslide dynamics will be applied to multi-temporal remote sensing data to predict landslide risk and impact.

Fractal and multi-fractal based techniques are used in land use classification [18]. A Hybrid Entropy Decomposition and Support Vector Machine Method has shown promising results in agricultural crop types and growth stages classification from multi-polarization, multi-band, multi-temporal remote sensing data [19]. Fig. 3 shows the classification results of various techniques.

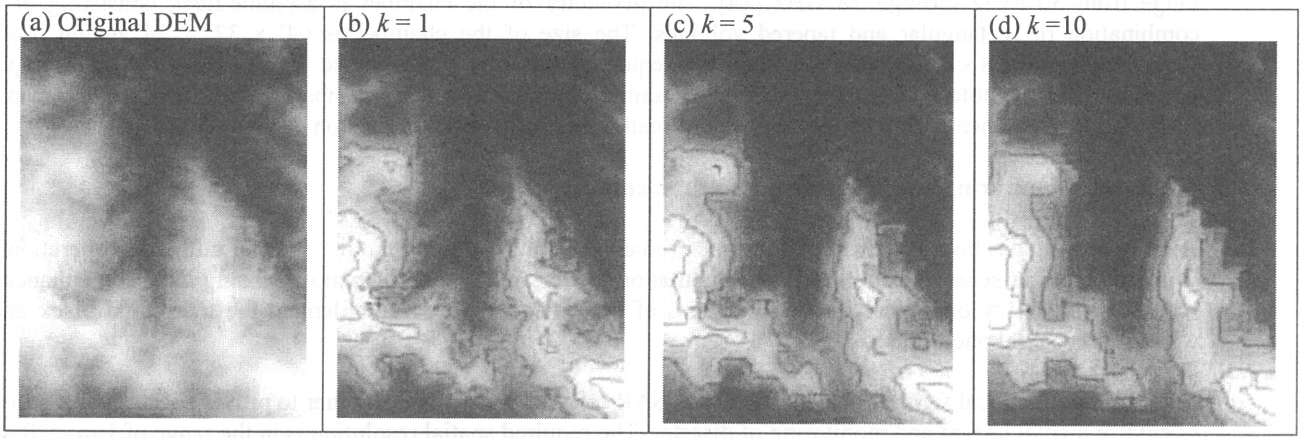
(a) Original DEM
(b) $k = 1$
(c) $k = 5$
(d) $k = 10$

Fig. 1: DEM of Cameron Highlands at multiple scales.

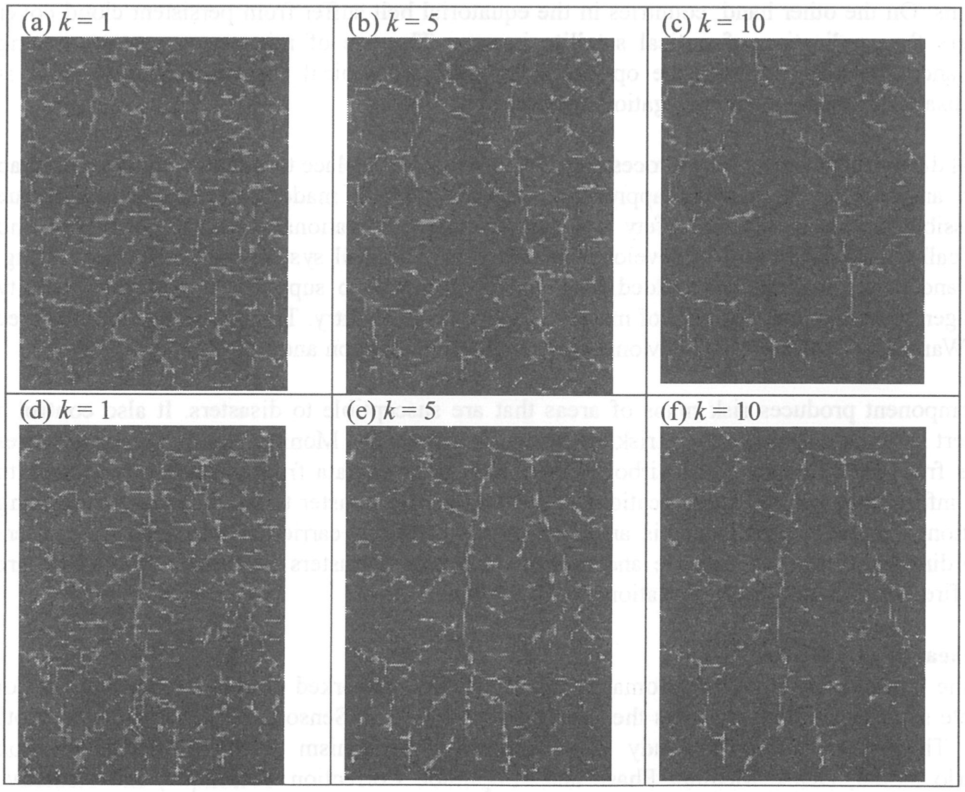
(a) $k = 1$
(b) $k = 5$
(c) $k = 10$
(d) $k = 1$
(e) $k = 5$
(f) $k = 10$

Fig. 2: (a-c) Multiscale ridge networks, and (d-f) multiscale channel networks extracted from the corresponding multiscale DEMs.

The Centre also participates in the Malaysian Antarctic Research Programme coordinated by the Academy of Sciences Malaysia (ASM) under a bilateral scientific cooperation between Malaysia and New Zealand. A multilayer model that represents the sea ice in terms of the wave-target interaction has been developed based on dense random medium modeling techniques [20]. The backscattering model take into account the sea ice thickness, dielectric constant, the brine and the bubble counts, and that the sea ice is covered by snow layer. Sea ice properties which affect the radar backscattering were investigated using remote sensing images and ground truth measurement data. The model is then used in the classification of sea ice at the Antarctic.

(a) ML (b) SVM

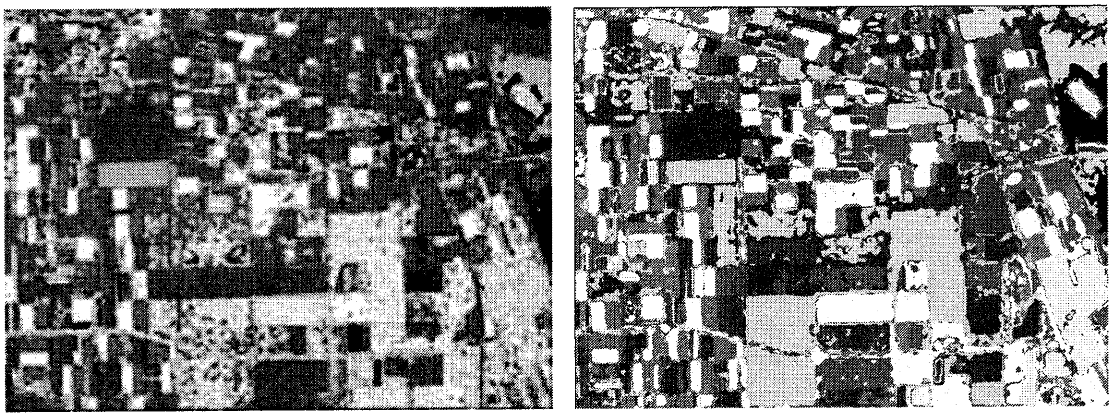

(c) EDML (d) EDSVM

Legend:

▨ Stem Bean
▨ Forest
▨ Wheat
▨ Bare Soil

▨ Beet
▨ Rape Seed
■ Water

□ Potato
▨ Lucerne

■ Pea
▨ Grass

Fig 3: Classification of agricultural crop types on Flevoland image with optimum window size (a) ML, (b) SVM, (c) EDML (d) EDSVM for optimized window size

5. Conclusion

Remote sensing is very useful for monitoring the state of the Earth, increase understanding of Earth processes, and enhance predication of the behavior of the Earth system. Disaster monitoring and mitigation applications must be supported by other remote sensing applications such as land use classification, terrain mapping, forest inventory, etc. The management of dynamic events such as natural disaster, search and rescue operations and surveillance requires real-time, high resolution and all-weather data. Airborne sensors are vital to provide an effective disaster monitoring. It is important to have a central system for collecting, storing, processing, analyzing and disseminating value-added information to the relevant agencies in the management of major disasters.

References

1. Y.K. Chan, B.K. Chung, and H.T. Chuah, Transmitter And Receiver Design of an Experimental Airborne

Synthetic Aperture Radar Sensor, Progress in Electromagnetics Research, vol. 49, page 203 –218, 2004

2. V.C. Koo, T.S. Lim, Rao M.V.C., H.T. Chuah, A GA-Based Autofocus Technique for Correcting High-Frequency SAR Phase Error, Journal of Electromagnetic Waves and Applications, vol. 18, no. 6, page 781-795, 2004
3. V.C. Koo, Y.K. Chan, Vetharatnam G., T.S. Lim, B.K. Chung, and H.T. Chuah, The MASAR Project: Design and Development, Progress in Electromagnetics Research, Vol. 50, page 279-298, 2005.
4. V.C. Koo, Y.K. Chan and H.T. Chuah, A New Autofocus Based on Sub-Aperture Approach, Journal of Electromagnetic Waves and Applications, vol. 19, no. 11, pp. 1547-1561, 2005
5. V.C. Koo, Y.K. Chan and H.T. Chuah, Multiple Phase Difference Method for Real-Time SAR Autofocus, Journal of Electromagnetic Waves and Applications, vol. 20, no. 3, pp. 375-388, 2006
6. Vetharatnam G., B.K. Chung, H.T. Chuah, Design of A Microstrip Patch Antenna Array for Airborne SAR Applications, Journal of Electromagnetic Waves and Applications, vol. 19, no. 12, page 1687-1701, 2005
7. Vetharatnam G., B.K. Chung, H.T. Chuah, Combined Feed Network for a Shared-Aperture Dual-Band Dual-Polarized Array, Antennas and Wireless Propagation Letters, vol. 4, page 297 - 299, 2005
8. T.S.Lim , Y.K.Chan, V.C.Koo, H.T.Ewe, H.T.Chuah, Synthetic Aperture Radar Calibration and Field Experiment Setup, Proceedings of Progress In Electromagnetics Research Symposium 2005 (PIERS 2005), Hangzhou, China, pp. 12-15, August 22-26, 2005.
9. V.C.Koo, T.S.Lim, H.T.Chuah, A Comparison of Autofocus Algorithms for SAR Imagery, Proceedings of Progress In Electromagnetics Research Symposium 2005 (PIERS 2005), Hangzhou, China, pg 16-19, August 22-26, 2005.
10. T.S.Lim, V.C.Koo, H.T.Ewe and H.T.Chuah, High-frequency Phase Error Reduction In SAR Using Particle Swarm Optimization, Journal of Electromagnetic waves and Applications, Volume 21, Number 6, pp. 795-810, 2007
11. V. C. Koo, Y. K. Chan, and T. S. Lim, A Real-time Hybrid Correlator for Synthetic Aperture Radar Signal Processing, Proceedings of Progress In Electromagnetics Research Symposium 2007 (PIERS 2007), Beijing, China, pg 1709-1712, March 26-30, 2007
12. Koo, V.C., B.K.Chung and H.T.Chuah, Development of A Ground-based Radar for Scattering Measurement, IEEE Antenna and Propagation Magazine, vol. 45, no. 2, April 2003.
13. H. Jamil, A. Ali, S. Yusof, Z. Ahmad, K.A. Mahmood, S.B. Abu Bakar, H. Aziz, N. Ibrahim, V.C. Koo, and K.S. Lim, Preliminary Results on Radar Measurement of Paddy Field Using C-Band Scatterometer System, The 24th Asian Conference on Remote Sensing (ACRS) & 2003 International Symposium on Remote Sensing (ISRS), Busan, Korea, Nov 2003.
14. B.K. Chung, H.T. Chuah, Design and Construction of A Multipurpose Anechoic Chamber, IEEE Antennas and Propagation Magazine, vol. 45, No. 6, pp. 41- 47, 2003.
15. Lea Tien Tay, B. S. Daya Sagar, and Chuah Hean Teik, Derivation of terrain roughness indicators via Granulometries, International Journal of Remote Sensing, vol. 26, no. 18, pp. 3901-3910, September 2005
16. Lea Tien Tay, B. S. Daya Sagar, and Chuah Hean Teik, Analysis of Geophysical Networks Derived from Multiscale Digital Elevation Models: A Morphological Approach, IEEE Geoscience and Remote Sensing Letters, vol. 2, no. 4, pp. 399-403, Oct 2005.
17. Lea Tien Tay, B. S. Daya Sagar, and Chuah Hean Teik, Allometric relationships between travel-time channel networks, convex hulls, and convexity measures, Water Resources Research, vol. 42, no. 6, W06502, doi:10.1029/2005WR004092, 2006
18. H.T. Teng, H.T. Ewe, S.L. Tan, C.P. Tan, H.T. Chuah, S. Bahari, "Landuse Classification by Multifractal Dimensions using AIRSAR Image", PacRim AIRSAR Significant Results Symposium, 26-28 June 2006, MACRES, Kuala Lumpur
19. C.P. Tan, J.Y. Koay, K.S. Lim, H.T. Ewe, H.T. Chuah, Classification of Multi-Temporal SAR Images for Rice Crops Using Combined Entropy Decomposition and Support Vector Machine Technique, Progress in Electromagnetics Research, PIER 71, page 19-39, 2007.
20. M.D. Albert, T.E. Tan, H.T. Ewe and H.T. Chuah, "A Theoretical and Measurement Study of Sea Ice and Ice Shelf in Antarctica as Electrically Dense Media", Journal of Electromagnetic Waves and Applications, volume 19, number 14, page 1973-1981, 2005

Detection of Speed of Moving Objects from Digital Aerial Camera and QuickBird Sensors

Fumio YAMAZAKI[1], Wen LIU[1], T. Thuy VU[2]

[1]Department of Urban Environment Systems, Graduate School of Engineering, Chiba University
1-33 Yayoi-cho, Inage-ku, Chiba 263-8522, Japan
yamazaki@tu.chiba-u.ac.jp, nanahachimizu@yahoo.co.jp,

[2]Grid Technology Research Center, National Institute of Advanced Industrial Science and Technology
1-1-1 Umezono, Tsukuba 305-8568, Japan. thuyvu@as.tu.chiba-u.ac.jp

Abstract

This paper highlights the method to detect moving objects and measure their speeds from high-resolution satellite images and airborne images. First using the images from Google Earth, "ghosts" of moving objects seen in pansharpened QuickBird images are demonstrated. The slight time lag (0.2 seconds) between panchromatic and multispectral sensors of QuickBird is responsible for the ghosts and they can be used to measure the speeds of moving objects using only one scene of QuickBird's "bundle product". However, due to limitation of the short time lag and the resolution (2.4 m for multispectral bands), high accuracy is expected only for high-speed large objects, e.g. airplanes. A method to detect the speed of vehicles is also proposed using a pair of aerial images. An object-oriented approach is employed to detect cars on an expressway automatically and the accuracy is examined comparing with visual extraction results.

Introduction

Satellite remote sensing and aerial photography have been used to capture still (snapshot) images of the earth surface. But if two images with a small time interval are taken, they can be utilized to detect moving objects, e.g. cars, and even to measure their speeds. If such data are available, many new applications can be considered such as observing highway traffic conditions.

From the images taken by high resolution satellites, e.g. QuickBird, we can observe small objects, like cars. It is known that panchromatic and multi-spectral sensors of QuickBird have a slight time lag, about 0.2 seconds, depending on the scanning mode of the instrument. Using this time lag between two sensors of one scene, the speed of moving objects can be detected (Etaya et al., 2004; Xiong and Zhang, 2006). In this study, using the pansharpened images of airports, trains, and expressways from Google Earth, the effect of the small time lag is demonstrated. Then the speed of running cars on a road is evaluated using a QuickBird scene (a bundle product of panchromatic and multi-spectral bands) of Bangkok, Thailand, as an example.

Another method to detect car speed is proposed using aerial photographs. Aerial photographs are often taken along a flight line with an overlap among adjacent scenes. If a moving object captured in a scene is also captured in an adjacent image, the speed of the object can be detected. A new object-based method is developed to extract the moving vehicles and subsequently detect their speeds from two consecutive aerial images automatically. Using a pair of digital aerial images of central Tokyo, the proposed automated extraction method is applied and the accuracy is examined comparing with visual extraction results.

Images of Moving Objects in Google Earth

Google Earth (http://earth.google.com/) recently provides high resolution optical images of urban areas, either from aerial photographs or pansharpened QuickBird (QB) images. For one scene, a pansharpened image can be produced by co-registering a panchromatic (PAN) image and a multispectral (MS) image. But due to the slight time lag (about 0.2 seconds) between a pair of PAN and MS images, the locations of moving objects displace after the short time interval. Even if the PAN and MS bands have been co-registered for still objects like roads and buildings, they cannot be co-registered for moving objects.

Figure 1 shows a part of Ninoy Aquino International Airport, Metro Manila, Philippines, from Google Earth. Two airplanes are seen on the runway. The right plane is just at the moment of landing and the left one is standing still and waiting for take-off. A “ghost” is only seen in front of the moving airplane. Similar ghosts were observed in several airports in the world such as Narita/Tokyo International (Japan), Bangkok International (Thailand), and Hong Kong International. These ghosts were produced due to the time lag between PAN and MS sensors of QB. The speed of the airplane in Fig. 1 is evaluated as 326 km/h assuming the time lag as 0.2 seconds.

This kind of ghosts are also seen in front of other moving objects, like trains, automobiles, ships, but due to limitation of the image resolution and short time lag, ghosts are not so clear as those for airplanes. We simulated a higher resolution pansharpened image of an expressway with 0.25 m resolution from an aerial photograph. By this resolution, the ghosts resulting from the time lag between PAN and MS sensors were clearly seen in front of moving vehicles.

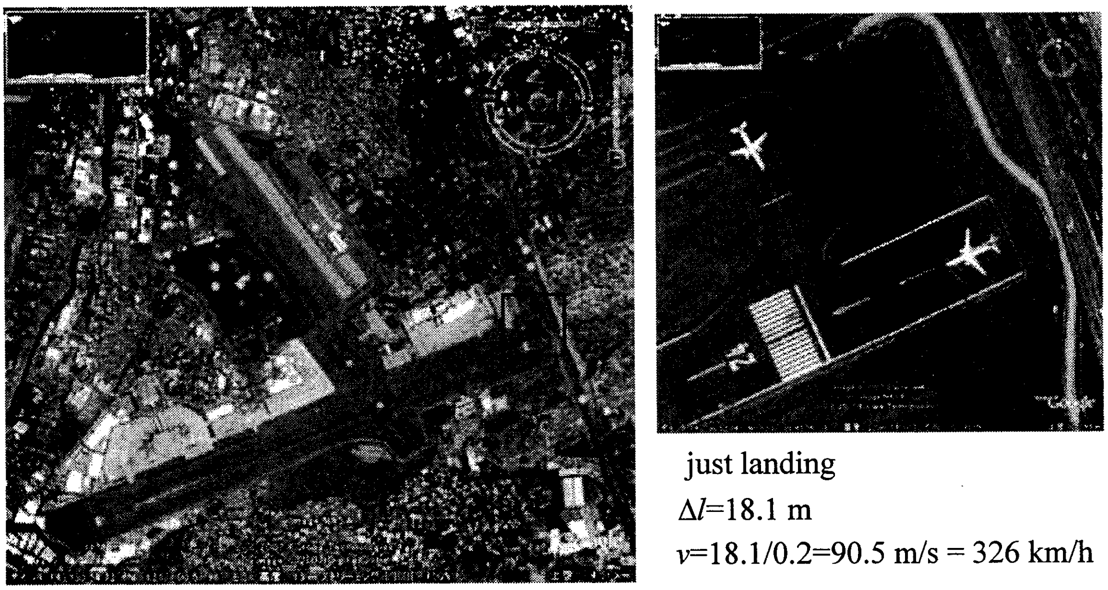

just landing

Δl=18.1 m

v=18.1/0.2=90.5 m/s = 326 km/h

Figure 1 Pansharpened QuickBird Image of Ninoy Aquino International Airport, Manila, Philippines, from Google Earth. A ghost is generated in front of the just landing airplane.

Detection of Car Speed from QuickBird Image

The time lag between PAN and MS sensors of QB was investigated using bundle products of QB. Figure 2 shows the time lag for 36 scenes which we have at hand. These images were taken for various parts of the world, e.g. Japan, USA, Peru, Thailand, Indonesia, Morocco, Iran, Turkey, Algeria, from March 2002 to July 2006. The time lag is either about 0.20 seconds or about 0.23 seconds, but we cannot find any rule to determine this time lag, as also stated by Etaya et al. (2004).

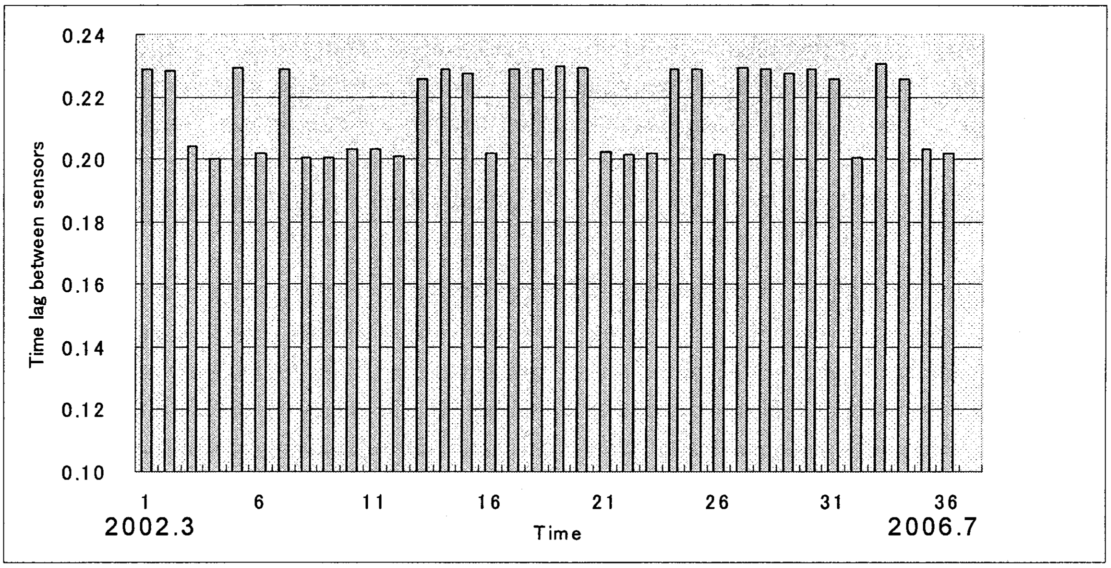

Figure 2 Time lag between PAN and MS sensors of QuickBird for 36 scenes in the world

Since the spatial resolution of QuickBird multi-spectral image is 2.4 m, rather coarse to figure out small cars, measuring the speed for smaller and slower objects is not so accurate. Figure 3 shows a QB image of central Bangkok, Thailand. Comparing the location of cars on the road in PAN and MS images with 0.20s time lag, the speed and moving direction of the cars can be evaluated as arrows in the figure. In this investigation, we encountered some difficulty to locate cars in MS images with 2.4 m resolution. Improvement of spatial resolution of satellite sensors is desired to detect the speed and moving direction of cars more accurately.

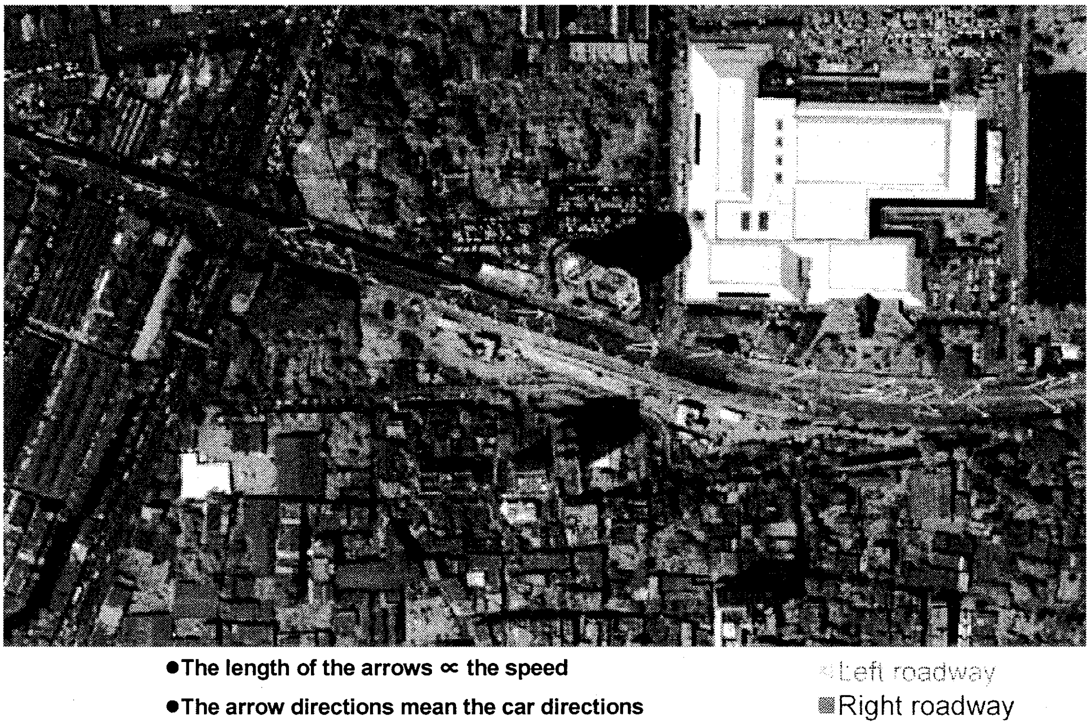

Figure 3 Result of visual detection of car speed from QB bundle product for central Bangkok, Thailand

Detection of Car Speed from Digital Aerial Images

Aerial images are often taken along a flight line with an overlap among adjacent images. If a moving object is captured in adjacent images, the speed of the object can be detected. Although conventional aerial photography with film has enough high spatial resolution to detect cars, recent digital aerial cameras can provide much higher radiometric resolution even though the spatial resolution is almost the same level. Hence to extract vehicles from an image visually or automatically becomes much easier.

A new object-based method was developed to extract the moving vehicles and subsequently detect their speeds from two consecutive digital aerial images automatically (liu et al., 2007). Several global and local parameters of gray values and sizes are examined to classify the objects in the image. The vehicles and their associated shadows can be discriminated by removing big objects such as the roads. To detect the speed, firstly vehicles and shadows are extracted from two consecutive images (Vu et al., 2005). The corresponding vehicles from these two images are then linked based on similarity in the shape, size and their distance within a threshold. Finally, using the distance between the corresponding vehicles and the time lag of the two images, we can detect the moving speed and moving azimuth angle. Our test shows a promising result of detecting the speed of moving vehicles. In addition, the speed detection process also helps to mitigate the errors generated in the vehicle extraction.

Figure 4 shows two consecutive images of central Tokyo taken by UltraCamD (Vexcel Corporation, 2007). The images are much clearer than those obtained by film cameras. Two other features of digital cameras help to measure the speed and azimuth direction of vehicles. One is very high overlapping ratio (80 % in this example) and another is very accurate acquisition time. These characteristics of digital aerial cameras enable us to calculate the speed and azimuth directions of moving objects very

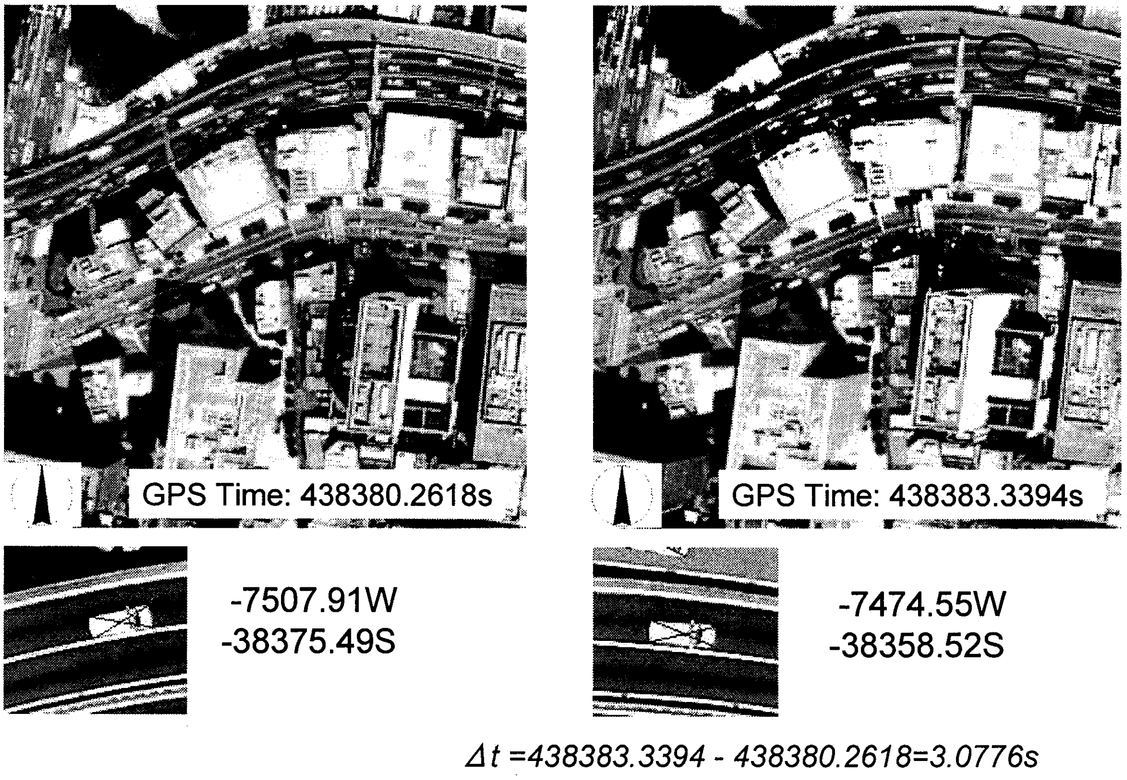

Figure 4 Two consecutive aerial images of central Tokyo having about 3.08 s time lag, taken by digital aerial camera. The images were provided by Geographical Survey Institute of Japan.

accurately.

The two images in Figure 4 were coregistered first by image-to-image matching using eight control points. The result of the automated car extraction and speed detection is shown in **Figure 5**. A total of 37 vehicles were detected in the pair of images and their speeds were evaluated. The average speed on the top lanes (east bound) is obtained as 39.7 km/h while that on the bottom lanes (west bound) as 19.0 km/h. These values well represent a heavy traffic condition of this segment of the urban expressway.

The proposed method does not need to deploy ground-based traffic sensors and can cover wide areas at a time. Hence it is expected to serve as a convenient tool to assess traffic conditions of urban areas.

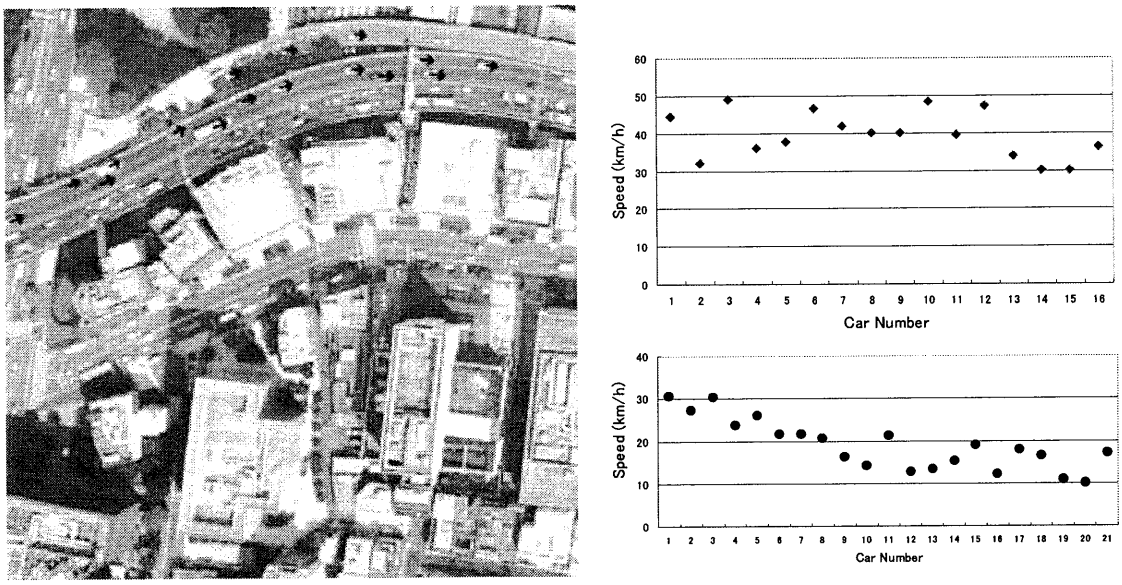

Figure 5 Result of detection of speed and azimuth direction of vehicles. The top graph shows car speed in east bound lanes and the bottom graph shows that in west bound lanes.

Conclusions

Methods to extract moving objects and measure their speeds from high-resolution satellite images and airborne images were highlighted. First using the images from Google Earth, "ghosts" of moving objects in pansharpened QuickBird images were demonstrated. The slight time lag, about 0.2 seconds, between panchromatic and multispectral sensors of QuickBird was shown to be responsible for the ghosts and they can be used to measure the speeds of moving objects using only one scene of QuickBird's "bundle product". Due to limitation of the short time lag and the resolution (2.4 m for multispectral bands), however, high accuracy is expected only for high-speed large objects, e.g. airplanes. An example of visual detection of speed and azimuth direction of cars was provided using a QB image of central Bangkok, Thailand.

A method to detect the speed of vehicles is also proposed using a pair of overlapped aerial images. An object-oriented approach is employed to detect cars on an expressway automatically. The method was applied to two adjacent images of central Tokyo. Comparing the location of extracted corresponding vehicles in the image pair, the speed and azimuth direction of moving vehicles were obtained with high accuracy. The proposed method may be used in assessing traffic conditions of wide urban areas without using ground-based traffic sensors.

Acknowledgement

The digital aerial images used in this study were provided from Geographical Survey Institute of Japan.

References

Etaya, M., Sakata, T., Shimoda, H., Matsumae, Y. (2004). An experiment on detecting moving objects using a single scene of QuickBird data, *Journal of the Remote Sensing Society of Japan*, Vol. 24, No. 4, pp. 357-366.

Leberl, F., Gruber1, M. (2003). Economical large format aerial digital camera, *GIM International.*

Liu, W., Yamazaki, F., Vu, T.T., Maruyama, Y. (2007). Speed detection of vehicles from aerial photographs, *Proc. 27th Asian Conference on Remote Sensing* (submitted).

Vexcel Corporation (2007). http://www.vexcel.com/products/photogram/ultracam/index.html

Vu, T.T., Matsuoka, M., Yamazaki, F. (2005.) Preliminary results in development of an object-based image analysis method for earthquake damage assessment. *Proc. of 3rd International Workshop Remote Sensing for Post-Disaster Response*, Chiba, Japan.

Xiong, Z., Zhang, Y. (2006) An initial study of moving target detection based on a single set of high spatial resolution satellite imagery, *Proc. ASPRS 2006 Annual Conference*, Reno, Nevada, May 1-5, 2006.

Measuring land displacement in Boso Peninsula Japan by Differential Interferometry SAR Technique

Ashar Muda Lubis[1, 2], and Nobuhiro Isezaki[2]
Graduate School of Science and Technology Chiba University[1]
Laboratory of Geophysics, Faculty of Science, Chiba university[2]
1-33, Yayoi-cho, Inage-ku, Chiba-shi, Chiba, 263-8522, Japan
Tel: +81-43-290-2854, Fax: +81-43-290-2859
E-mail: asharml@graduate.chiba-u.jp

Abstract

The Philippine Sea plate is subducting beneath the Boso peninsula, central Japan, with the Pacific plate underlying the Philippine Sea plate and the complicated tectonic setting is occurred here, followed by numerous seismic events. In order to detect the temporal and spatial pattern of surface deformation in this area, we use the benefit tool of Interferometric Synthetic Aperture Radar (InSAR) method. The raw SAR data which is from 2 C-band acquired by the ERS-1 SAR satellite from 1992 to 1996 are analyzed by using GAMMA, EarthView-3 software commercial software and SIGMA_SAR software respectively. We explored the ability for producing the best interferogram between them. In SIGMA_SAR software, by using Goldstein-Wagner filter, we are successfully increasing Signal Noise Ratio (SNR) on the interferogram image. The DEM 50 m Japan is used to remove the topography effects from InSAR fringes. Our InSAR mapping suggests that subsidence occurs around Mobara region (at the center InSAR image), and the uplift area was detected both in northeast and in Chiba city extending to the northwest of its city. We estimated that our InSAR image has peak amplitude of ~ 5 to 8 cm in line of sight (LOS) direction during 1992-1996 time period. To compare our result, we also analyzed 3 interferograms of JERS-1 data from 6 scenes L band SAR data (1993-1996). Even though the coherency of ERS-1 interferogram is higher than JERS-1 data pair, in general, we got almost the same pattern displacement from both ERS-1 and JERS-1 data. We also present evidence of the subsidence area from leveling data which recorded during 1993-1997. The radar observations of land subsidence are in good agreement with leveling data. However, the radar data provides a more detailed mapping of both the amplitude and spatial extent of land subsidence.

Key words: Boso Peninsula, InSAR, subsidence, leveling

1. INTRODUCTION

The Philippine Sea plate is subducting beneath the Boso peninsula, central Japan, with the Pacific plate underlying the Philippine Sea plate (see Fig. 1). Because of the complicated tectonic setting, shown in figure 1, seismic events are numerous off the coast of the Boso peninsula. The coupling rate off the east coast of the Boso peninsula is estimated at between 1 and 2 cm/year with the southern part showing a higher coupling rate between the Philippine Sea plate and the overriding North American plate **(Sagiya T., 1997.)** There were several earthquakes that have been reported off the Boso peninsula such as slow slip event in May 1996 which has peak GPS displacement of 15 mm **(Ozawa *et al.,* 2003,** and **Sagiya, 2004)** , October 2002 and recently earthquake on August 27, 2007. Moreover, the rapidly subsiding areas north of Tokyo and in the eastern part of the Boso peninsula have also reported due to the product of ground water pumping and natural gas extraction, respectively **(Geographical Survey Institute, 1999).**

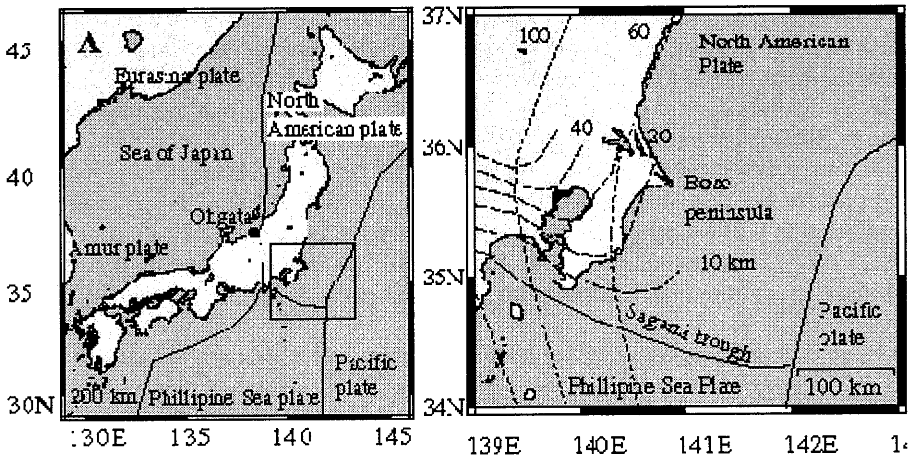

Figure 1. Tectonic map in and around the Boso peninsula, central Japan

Investigating of land displacement associated with either earthquake or aseismic activity can be detected by Global Positioning System, leveling data and Interferometry Synthetic Aperture Radar (InSAR) method. Permanent GPS observation sites (GEONET) set up by the Geographical Survey Institute of Japan (GSI) have been in operation since 1994. Unfortunately there was few GPS receiver around Boso peninsula (only 3 sites). As a result, measurement land displacement using GPS observation in large spatial area could not be performed. Therefore we use the benefit InSAR method to estimate land displacement during 1992 – 1996 period in Boso peninsula area.

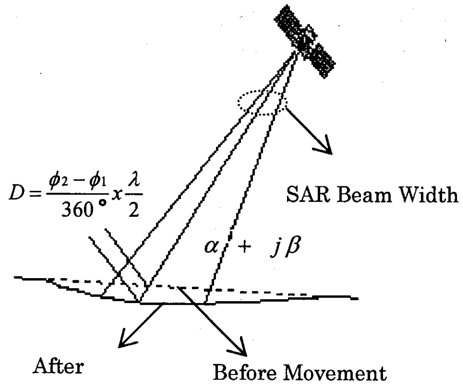

Figure 2. Image acquisition geometry of SAR. φ_1 and φ_2 are the phase differences obtained from the two image scenes related to slant range change D and λ is the wavelength. $\alpha+j\beta$ is the Cartesian representation of amplitude and phase recorded by the SAR

Spaceborne radars on the ERS and JERS-1 satellites have been successfully used for surface deformation studies, including coseismic deformation associated with earthquakes **(Massonnet *et al.*, 1993; Zebker *et al.*, 1994; Murakami *et al.*, 1996)**, volcanic deflation **(Massonnet *et al.*, 1995; Rosen *et al.*, 1996)**, and glacier motion **(Goldstein *et al.*, 1993)** with centimeter- to millimeter-scale precision, and this became a key result to promote many studies on InSAR application for disaster monitoring due to earthquakes or volcanic eruptions.

A single SAR image does not contain enough information to say anything about the movement or relative height change of the imaged scene **(Soren, N.M, H.A. Zebker, and J.Martin, 1992)**. InSAR combines two complex and co-registered images of the same scene from almost identical perspectives into a so-called interferogram. The phase difference for each picture element (pixel) in the interferogram is a measure of relative change in distance between the ground (scatterer) and the SAR antenna as shown in Figure 2.

In general, the phases corresponding to differential range change in the interferogram will contain topographical information as well as movement information. Thus, there is a need for two interferometric pairs (4 images), so that the first two images can be used to generate an accurate topographical model or Digital Elevation Model (DEM) and then this model can be used to remove the topographical phases from the subsequent pair to obtain movement information. This technique is called differential interferometry. In principle, phase relating to range change can be written as

$$\Delta\varphi = \Delta(\varphi Topography) + \Delta(\varphi displacement) + \Delta(\varphi error) \qquad (1)$$

The two interferometric pairs (4 images) are required to generate the movement-only interferogram, assuming there is no other way to get the topographical information of the scene **(Gabriel, A.K., R.M. Goldstein, and H.A. Zebker, 1989)**. If the external Digital Elevation Model (DEM) is exist, only one pair interferometry (2 images) is needed to measure ground deformation between image acquisition times.

Although the principle of InSAR for detecting land displacement is very simple as shown above, the actual procedure is much complicated because it is necessary to remove the first and third fringe components (equation 1) from the original fringe patterns perfectly. For the second one, conventional digital elevation data (DEM) are usually used because it is rather easy to remove the second one (topographic fringe) by simulating precise topographic fringe patterns by using DEM and, in addition, the sensitivity of topographic fringe for the height differences is much lower than that for land displacement.

Another problem is that phase unwrapping is finally necessary to obtain absolute displacement values and this phase unwrapping is much sensitive to phase noises and easily fails in degraded phase patterns. The phase noises are generated by incomplete interferometry, which is brought by spatial and temporal decorrelation of SAR signals. The former is brought by large baseline length and therefore the data pairs with baseline length as short as possible are preferable for interferometric analysis. The latter is actually the most significant factor to achieve InSAR successfully for displacement detection especially for C-band SAR data, because the temporal decorrelation is bigger for shorter wavelength than the longer one. The temporal decorrelation is also much affected by land cover types. It is large for vegetated land covers and small for non-vegetated, because the surface of vegetation is unstable in the scale of wavelength order of SAR signal. Therefore, the result of InSAR using C-band SAR is much affected by land cover types, and forest and agricultural areas are difficult to apply C-band InSAR in general.

2. DATA AND RESULT

In this study we use ascending C band ERS-1 SAR data which acquired on March 3, 1992 as master data and November 11, 1996 as slave data. The perpendicular baseline of two SAR data is 20 m. In order to compare InSAR image derived from ERS-1 data, we use also SAR data from two passes of JERS-1 which launched on February 11, 1992. The data were provided by National Space Development Agency of Japan (NASDA). The JERS-1 revolves on circular orbit with 568 km in altitude, illuminating the Earth surface with L band radar which microwave frequency is 1275 MHz. The orbit is Sun synchronous and sub recurrent, with a repeating period of 44 days. **(Mukarami., M., *et. al.* 1996)**

Table 1. SAR data used for monitoring land displacement in Boso peninsula region

Pair	Master	Slave	Baseline (m)	Perpendicular Baseline (m)	Period (days)
Pair 1	1993/02/22	1996/05/25	1168.42	1037.83	1188
Pair 2	1993/02/22	1996/08/21	594.04	389152	1276
Pair 3	1993/02/22	1996/11/17	389.93	387.88	1364
Pair 4	1993/04/07	1996/11/17	1758.80	1368.53	1320

Figure 3 shows a location map of these interferograms. The Synthetic Aperture Radar pair covers a larger area in rectangular box. Table 1 summarizes the JERS-1 data pairs and spatial baselines relevant to region interferometry.

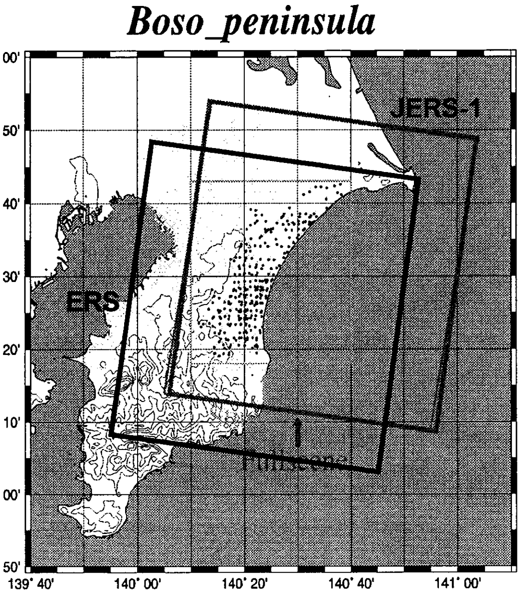

Figure 3. Map location research area.

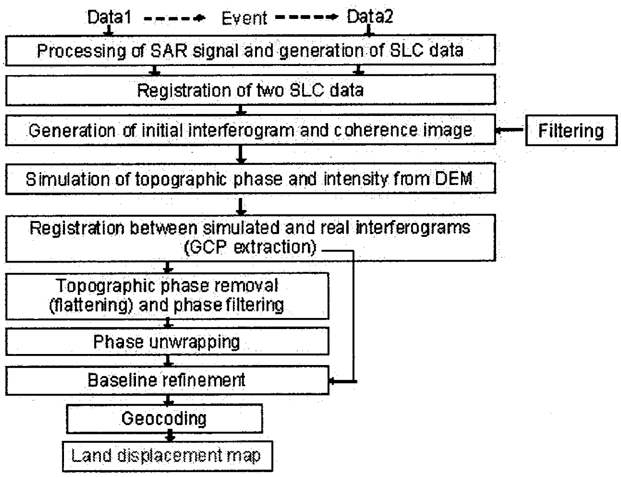

Figure 4. Flow chart for two-pass differential interferometry to detect land displacement patterns

The ERS-1 data, we processed with commercial GAMMA software, EarthView software and SIGMA_SAR packed software made by JAXA Japan. The procedure, called two-pass differential interferometry, to obtain land displacement patterns is shown by figure 4. Mainly, data processing was started from single look complex (SLC), which then continued by resampling SLC (co-registration), creating interferograms and image coherency, filtering, unwrapping interferogram and geocoding process.

In order to remove fringe related to topographic effect we use digital elevation data from Geographical Survey Institute (GSI) with resolution 50 m. We improved signal to- noise ratio of each differential interferogram using a weighted power spectrum filter as discussed in **Goldstein and Werner (1998)**.

The result of InSAR application by ERS-1 data for Boso Peninsula region for monitoring land displacement can be seen in Figure 6a-6c. In this figure, the fringe patterns are detected very clearly in Chiba city extending to northwest direction and in the eastern of Boso (Mobara region) region where in this area water pumping and natural gas extraction were intensively done **(Geographical Survey Institute, 1999)**. Figure 6a, 6b and 6c were processed by commercial GAMMA software, SIGMA_SAR software and EartView respectively. The interferograms reveal that the spatial pattern of subsidence almost does not change. However, the map displacement which had processed by EarthView a little bit noisily even the subsidence can be detected.

The dominant signal in the interferograms is a bowl-shaped pattern of apparent line-of-sight (LOS) displacements in the Mobara region. We interpret the cycle elliptical-shaped fringes in Figure 6a-6c as indicating land subsidence in Mobara region.

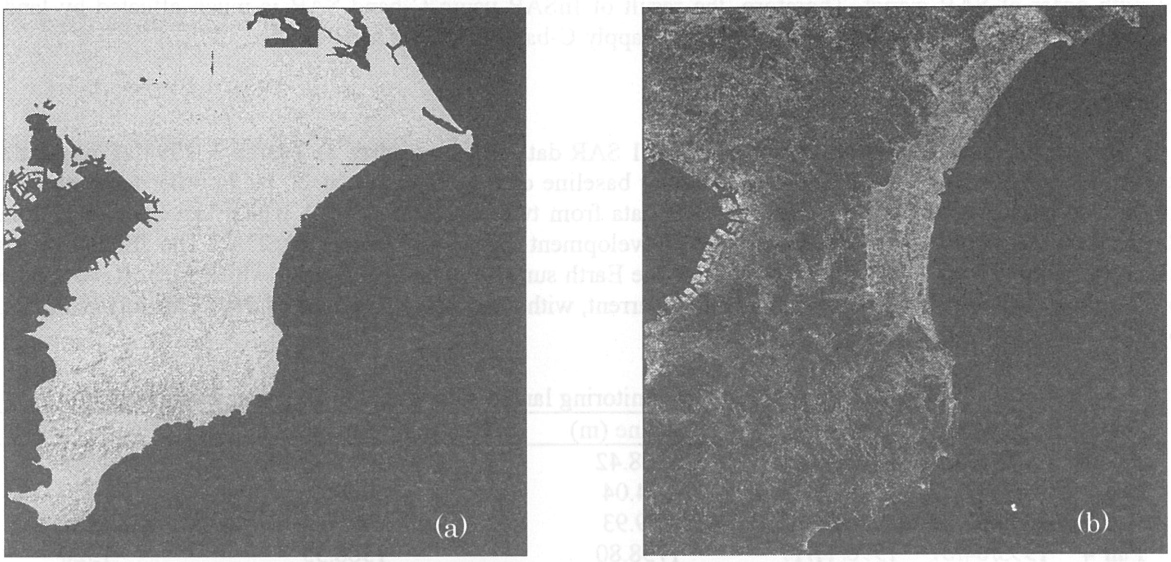

Figure 5. (a) GSI DEM with 50m resolution (b) Topographic phase from simulated DEM, one cycle equal to 160 m

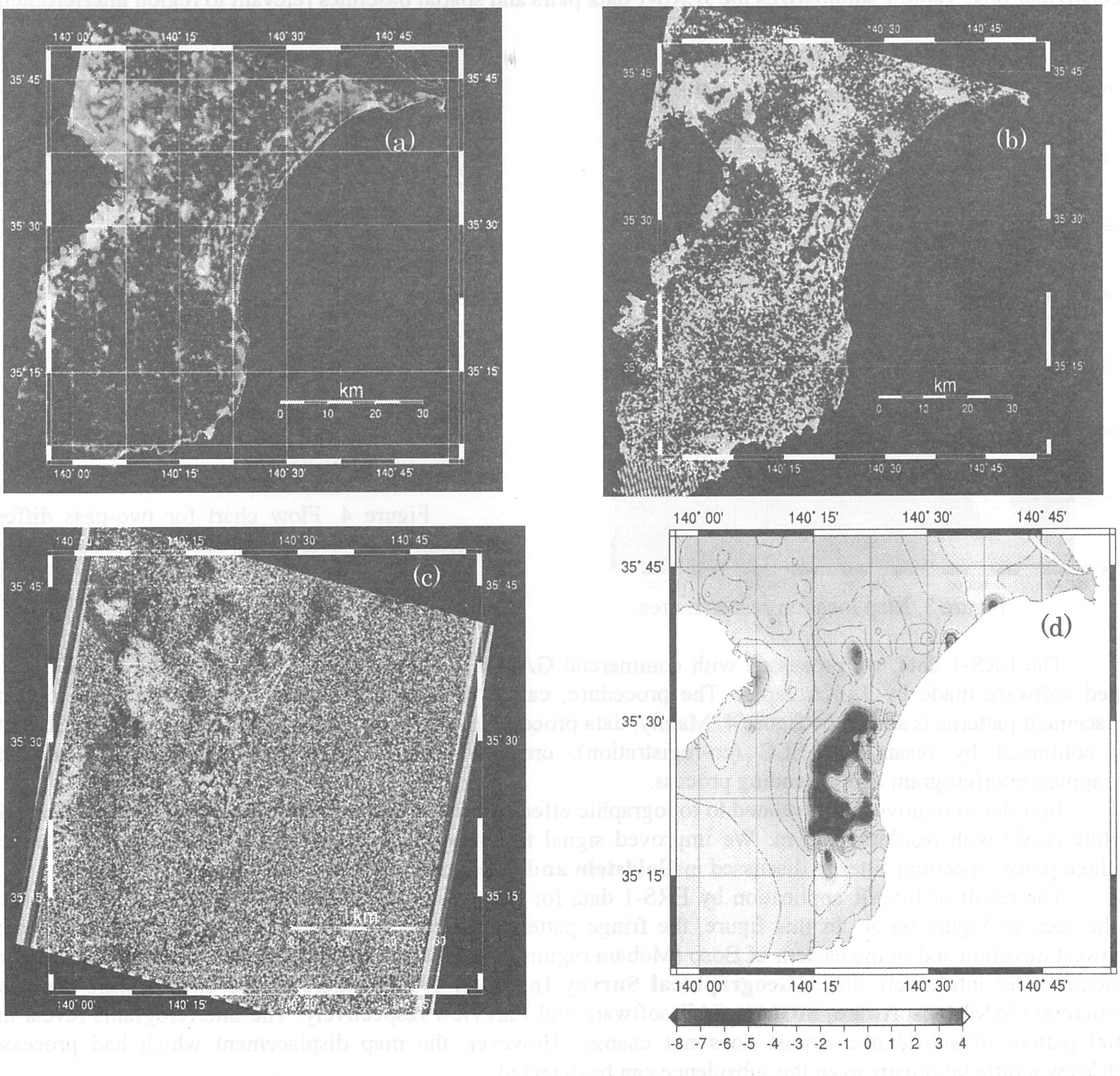

Figure 6. Result of land displacement patterns detected by ERS-1. (a) Land displacement derived by GAMMA software. (b) Land displacement processed by SIGMA_SAR software. (c) Land displacement using EarthView software, one palette scale is equal to 2.58 cm. (d) Map of leveling data, scale in cm

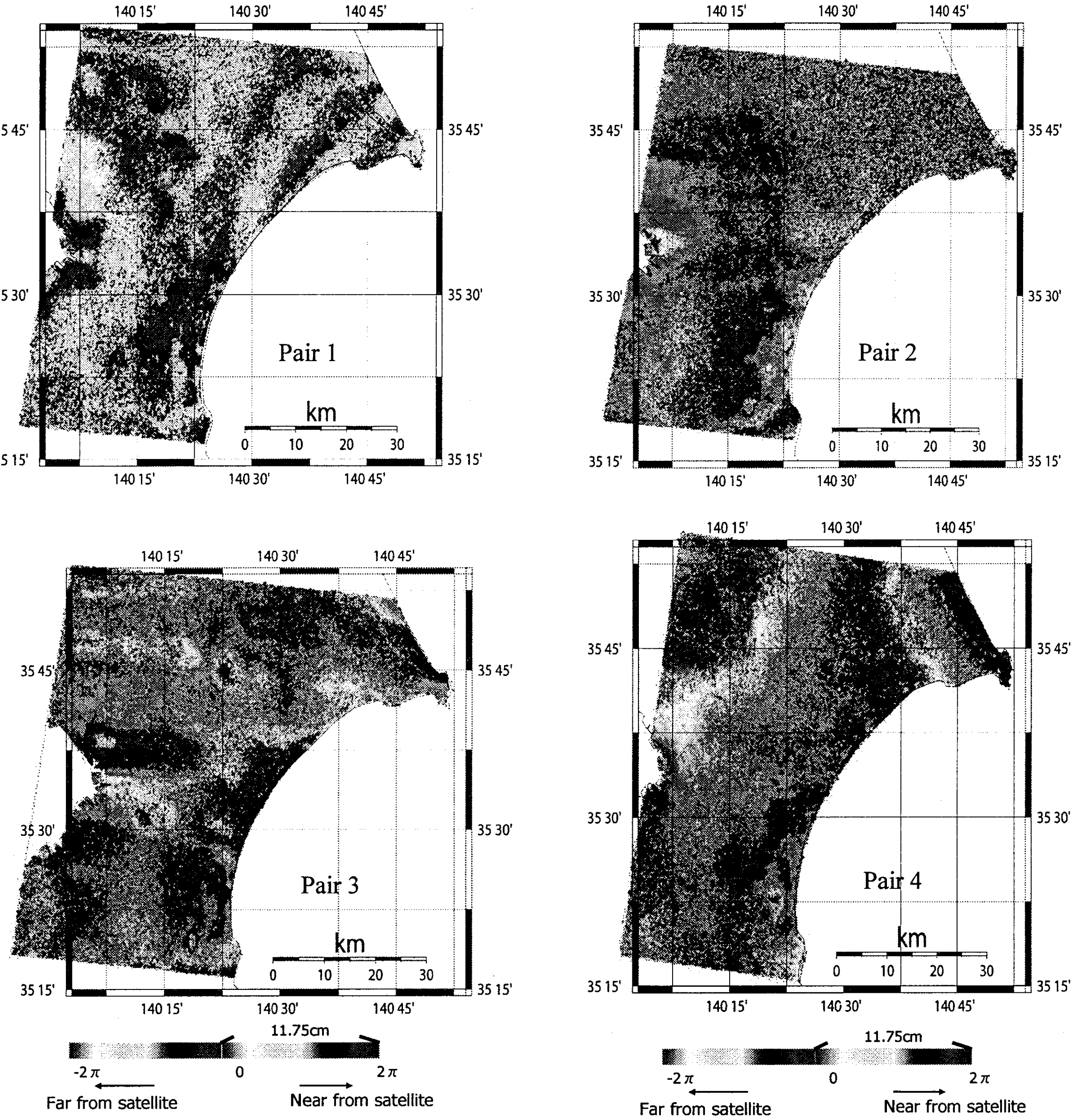

Figure 7. Result of land displacement patterns detected by JERS-1

In general the correlation of pair ERS-1 data is higher than pair JERS-1 data. Though the time interval for our first interferogram is about four years, the coherence value is still very high and the interferometric fringes are very clear. Phase unwrapping was uncritical. The correlation of InSAR data depends on several factor, i.e. local slope (steep slope), properties of surface being imaged (vegetated or moving surface such as ice glacier) and baseline between master and slave SAR data. Our JERS-1 data have baseline more than 300 m, so we note that this phenomenon leads poor correlation in comparison to ERS-1 data. The problem in data processing is the inaccuracy of the ERS-1 orbit parameters. In addition, the passes in the illumination interval, usually about 16 s, are not exactly parallel to each other. To solve this problem, we attempted DEFLT precision orbital data records in GAMMA software to refine orbit parameter.

Figure 7, pair 1, pair 2, pair 3 and pair 4, illustrates the land displacement in Boso peninsula from JERS-1 data. In all of pairs, the dominant signal in the interferograms is a bowl-shaped pattern of apparent line-of-sight (LOS) displacements in the Mobara region. The same fringe pattern can be traced in all of the interferometric pairs even covering different time interval. Due to the loss of coherent signal, it is difficult to assess exactly the maximum amount of subsidence in the long-term interferograms, but the data suggest that the subsidence for this time interval is approximately has amplitude 5 - 7 cm in LOS direction. The instability interferogram was detected in interferogram of pair 1 and pair 4 which may be caused long baseline master and slave of both pair interferograms. The interferogram pair 2, there is loss phase detected in northeast of Boso peninsula due to low signal noise ration in this region .In general, four interferograms which have been constructed from Table 1, there is no significant seasonal variation is observed in the InSAR measurements during the 1993-1996 time interval.

Since in this region there was no available GPS data in 1992 and GEONET was initiated in 1994 with 3 sites in the region, we could not make comparison to validity our result using GPS data. We present evidence of the subsidence area from leveling data which recorded during 1993-1997 (Figure 6d). The radar observations of land displacement are in good agreement with leveling data. However, the radar data provides a more detailed mapping of both the amplitude and spatial extent of land subsidence.

3. CONCLUSIONS

We have applied Interferometric Synthetic Aperture Radar (InSAR) for monitoring land displacement in Boso Peninsula. We estimated that during 1992-1996 the land displacement in Boso peninsula region has amplitude of ~ 5 to 8 cm in line of sight (LOS) direction. For both ERS-1 and JERS-1 data, even though the coherency of ERS-1 interferogram is higher than JERS-1 data pair, the same pattern of displacement from both ERS-1 and JERS-1 data was obtained. Our results also match well with in situ, leveling data observation. Finally, from radar measurement we can calculate accurately land displacement around Boso Peninsula. In 2006, the new satellite, DAICHI (Advanced Land Observing Satellite: ALOS) was launched by Japan Aerospace Exploration Agency (JAXA), so for the next future we can easy to conduct disaster monitoring in Boso Peninsula due availability data around the world.

ACKNOWLEDGMENT

We are thankful to Dr Manabu Shimada in Japan Aerospace Exploration Agency (JAXA) for providing SIGMA SAR software packed. Some of figures were made by using GMT (Paul Wessel and Walter H.F Smith, 1998).

REFERENCES

[1] Gabriel, A.K., R.M. Goldstein, and H.A. Zebker, 1989, Mapping small elevation changes over large areas: differential radar interferometry, J.Geophys.Res., 94(B7), 9183-9191

[2] Geographical Survey Institute, 1999, Report on survey and investigation of land subsidence in the Kanto region (in Japanese), *Technical Rep. Geograph. Surv. Inst.*, B.7-F-No16, 23 pp.

[3] Goldstein R M, Werner C L, 1998, Radar Interferogram Filtering for Geophysical Applications. *Geophysical Research Letters*, 25(21): 4035-4038.

[4] Goldstein, R. M., H. Engelhardt, B. Kamb, and R. M. Frolich, 1993, Satellite radar interferometry for monitoring ice sheet motion: Application to an Antarctic ice stream, *Science*, 262, 1525–1530

[5] Mukarami M, Tobita M, Fujiwara S, Saito T, and Masaru H, 1996, Coseismic crustal deformation of 1994 Northridge, California earthquake detected by interferometric JERS-1 Synthetic Aperture Radar, *Journal of Geophysical Research*, 101, 8605-8614,

[6] Massonnet, D., P. Briole, and A. Arnaud, 1995, Deflation of Mount Etna monitored by spaceborne radar interferometry, *Nature*, 375, 567–570

[7] Massonnet, D., M. Rossi, C. Carmona, F. Adragna, G. Peltzer, K. Fiegl, and T. Rabaue, 1993, The displacement field of the Landers earthquake mapped by radar interferometry, *Nature*, 264, 138–142

[8] Rosen, P. A., S. Hensley, H. A. Zebker, F. H. Webb, and E. J. Fielding, 1996, Surface deformation and coherence measurements of Kilauea Volcano,Hawaii, from SIR-C radar interferometry, *J. Geophys. Res.*, 101,23109–2312

[9] Sagiya, T., 1997, Boso Peninsula silent earthquake of May 1996, *Eos Trans.*, 78, F165

[10] Sagiya, T., 2004, Interplate coupling in the Kanto district, central Japan, and the Boso Peninsula silent earthquake in May 1996, *Pure Appl. Geophys.*, 161, 2327-2342.

[11] Soren, N.M, H.A. Zebker, and J.Martin, 1992, Topographic mapping using radar interferometric processing techniques, IEEE Trans. Geosci. Remote. Sens., 30(3),560-567

[12] Ozawa, S., S. Miyazaki, Y. Hatanaka, T. Imakiire, M. Kaidzu, and M. Murakami, 2003, Characteristic silent earthquakes in the eastern part of the Boso peninsula, Central Japan, *Geophys. Res. Let.*, *30*, 1283, doi:10.1029/2002GL016665.

[13] Wessel, P., and W. H. F. Smith, 1998, New improved version of the Generic Mapping Tools Released, *EOS Trans. AGU*, *79*, 579

[14] Zebker, H. A., P. A. Rosen, R. M. Goldstein, A. Gabriel, and C. L. Werner, 1994, On the derivation of coseismic displacement fields using differential radar interferometry: The Landers earthquake, *J. Geophys. Res.*, 99, 19617–19634

Study of relationship between ENSO/IODM and NDVI in Western Pacific regions

○Bannu, Josaphat Tetuko Sri Sumantyo, Hiroaki Kuze
Center for Environmental Remote Sensing (CEReS), Chiba University,
1-33 Yayoi-cho, Inage-ku, Chiba 263-8522, Japan
E-mail : bannu@graduate.chiba-u.jp

Abstract: We examine the correlation between the Niño-3,4/IODM indices that describe the SST anomalies on a global scale and the regional NDVI index in the Western Pacific including Indonesia. An approach is adopted that enhances NDVI anomalies relative to the long-term climatology on the global and regional scales. We find a negative NDVI anomaly for most of the region during the El Niño/IODM events, whereas for the non-El Nino/IODM events, positive NDVI anomalies are observed over most regions. Also we identify the possible factors that may play a role in the different NDVI responses to the different El Niño/IODM case. Especially the response of vegetation may depend upon the climate conditions prior to the El Niño/IODM events. In this context, droughts are particularly well suited to early warning systems because the disasters have a slow onset.

Keywords: El Niño, IODM, Rainfall, NDVI, cloud pattern

1. Introduction

Modeling studies (Miller et al., 1992) and observations (McBride et al., 2003) have indicated that small changes in the SST within the Indonesian Maritime Continent can result in significant changes in rainfall patterns across the Indo-Pacific region. On the planetary scale, it is expected that Indonesian rainfall is strongly affected by both the El Niño-Southern Oscillation (ENSO) and the Indian Ocean Dipole (IODM) phenomena. The ENSO and IODM events, in turn, are strongly influenced by radiative and cloud processes in the Tropical Western Pacific (TWP). It is expected that variability of cloud pattern may lead to variability of other climate indicators such as precipitation, evaporation and ocean stream flow.

Satellite information has contributed to improving our understanding of the spatial variability of hydro-climatology. Vegetation activity is tightly coupled with climate and it controls water budget in basins on a wide range of space–time scales. The purpose of the present paper is to elucidate the temporal and spatial relations between El Niño/IODM indices with the cloud pattern, precipitation, and vegetation conditions in Indonesia and related areas.

2. Data and Methodology

The normalized difference vegetation index (NDVI) is defined as NDVI = $(\rho_2-\rho_1) / (\rho_2+\rho_1)$, where, ρ_1 and ρ_2 are the reflectance in the visible (VIS) and the near infrared (IR) band, respectively. The dataset provided by the Global Inventory Monitoring and Modeling Systems (GIMMS) group is based on a 23-year (1981–2003) satellite record of bi-monthly changes in terrestrial vegetation. Its new features include reduced NDVI variations arising from calibration, view geometry, volcanic aerosols, and other effects not related to actual vegetation change (Anyamba et al., 2001). The original GIMMS dataset consists of compositions during 15 days. In order to extract more genuine NDVI variations, first, twice monthly images were averaged to produce one image per month. Second, monthly climatology images were constructed by averaging the monthly data for 23 years. Third, NDVI anomaly or NDVI deviations from the climatology images are calculated for all months from 1981 to 2003. Negative NDVI deviation values indicate lower than average greenness, while positive deviations indicate more green conditions

The Geostationary Meteorological Satellites (GMS-5) captured the hourly cloud pattern over the TWP. We analyze hourly 1-km visible image (0.55-0.90 μm), 5-km infrared-1 (IR1; 10.5-11.5 μm), infrared-2 (IR2; 11.5-12.5 μm) and infrared-3 (Water Vapor; 6.5-7.0 μm) radiance images using the Atmospheric Window Method (AWM), a method proposed by Meteorological Satellite Center of Japan Meteorological Agency (MSC, 2002).

3. Results and Discussion

3.1 Sea Surface Temperature (SST) pattern

The occurrence of El Niño and/or La Niña conditions is represented by the SST anomalies Here we retrieve the SST from the ERSST v2 dataset (Smith & Reynolds, 2005). Figure 1 shows the monthly-average SST during the El Niño/La Niña event of September 1997/September 1998. The El Niño case (Fig. 1a) shows cold areas around the Indonesian region, though relatively warm SSTs are found in the Central Pacific and Indian Oceans.

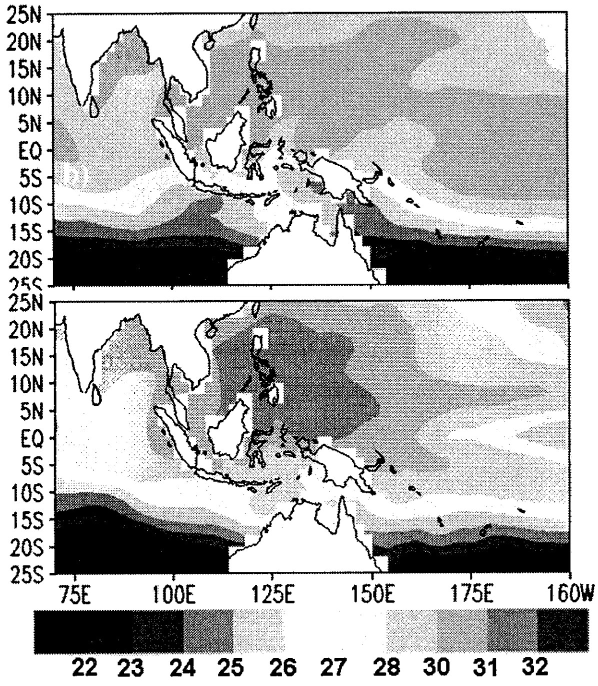

Figure 1 Monthly SST (°C) obtained from ERSST v2 reanalysis dataset (Smith & Reynolds, 2005) surrounding Indonesian region during: a) the El Niño event (September 1, 1997), and b) the La Niña event (September 1, 1998).

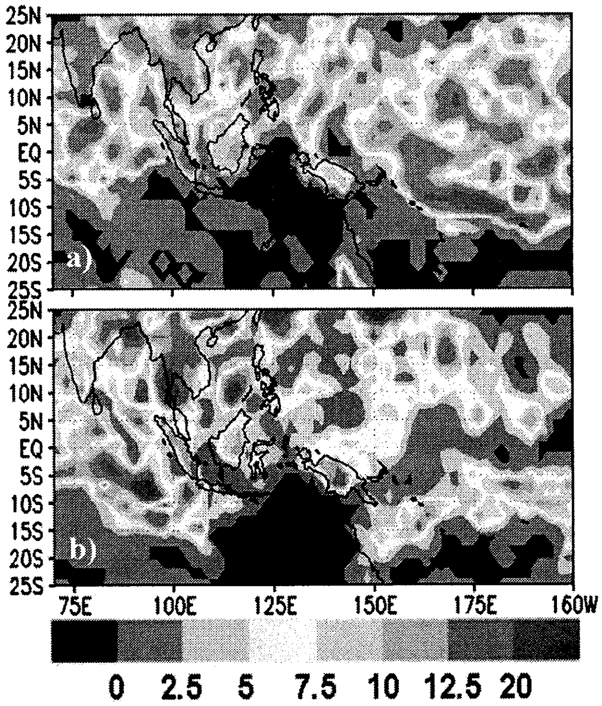

Figure 2 Daily rainfall (mm/day) obtained from NCEP/NCAR reanalysis dataset (Kalnay et al, 1996) during: a) the El Niño event (September 1, 1997), and b) the La Niña event (September 1, 1998).

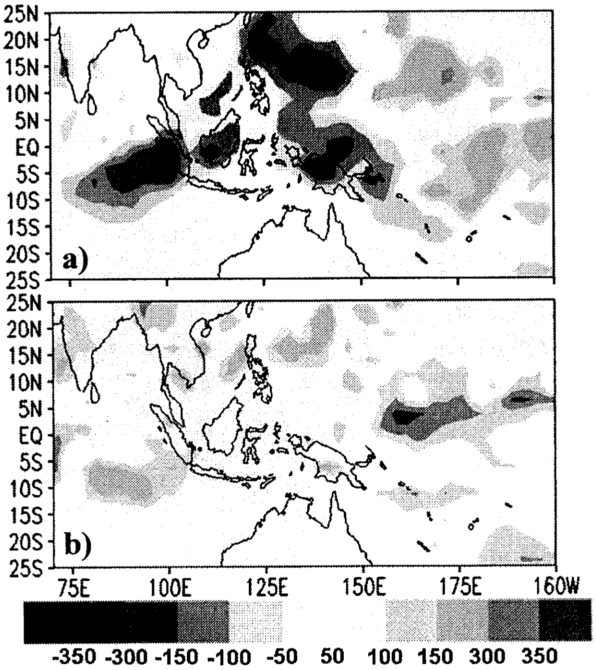

Figure 3 Monthly rainfall anomaly (mm/month) obtained from GCPC v2 dataset (Adler et al, 2003) during: a) the El Niño event (September 1997), and b) the La Niña event (September 1998).

The opposite condition appears in the La Niña condition (Fig. 1b).

The corresponding daily rainfall (non-anomaly) and the monthly rainfall anomalies in the region are depicted in Figs. 2 and 3, respectively. Warm SSTs around the islands of the Maritime Continent lead to vast amounts of evaporation and deep convective cells over the region. The anomaly plot in Fig. 3 well characterizes the influence of El Niño/La Niña conditions on the convective activity.

3.2 Cloud pattern

Figure 4 illustrates the cloud distributions over tropics for the 1997 El Niño (a) and 1998 La Niña (b) conditions derived from the differential IR images of GMS-5. At 00UTC on September 1, 2007 (Fig. 4a), a high cloud fraction is seen over equatorial central Pacific area with a low coverage over the Indonesian region, associated with the dry conditions there. The apparent cloud increase over Kalimantan and Sumatra is presumably due to smoke clouds caused by forest fire events.

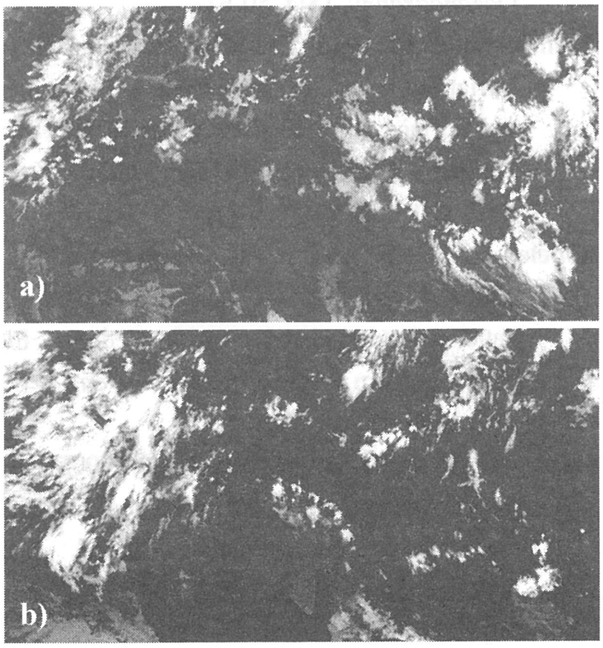

Figure 4 Hourly convective cloud patterns using Infrared differential image taken by GMS-5 at 00UTC on: a) September 1, 1997 (El Niño) and b) September 1, 1998 (La Niña).

The patterns in Fig. 4 also indicate that over the Indonesian region, there is less convection and fewer cold clouds during the El Niño (September 1997) as compared to the La Niña (September 1998) conditions. Nevertheless, in the Western Pacific, there is a greater spatial extent of cold temperatures during the El Niño of 1997 compared to the La Niña conditions of 1998. It is possible that these differences are due to the very cold cloud tops associated with the very intense deep convection prevalent over the ocean in comparison to the weaker, less intense deep convection over the land. Further studies on the diurnal cycle will be useful for the understanding of this cloud behavior.

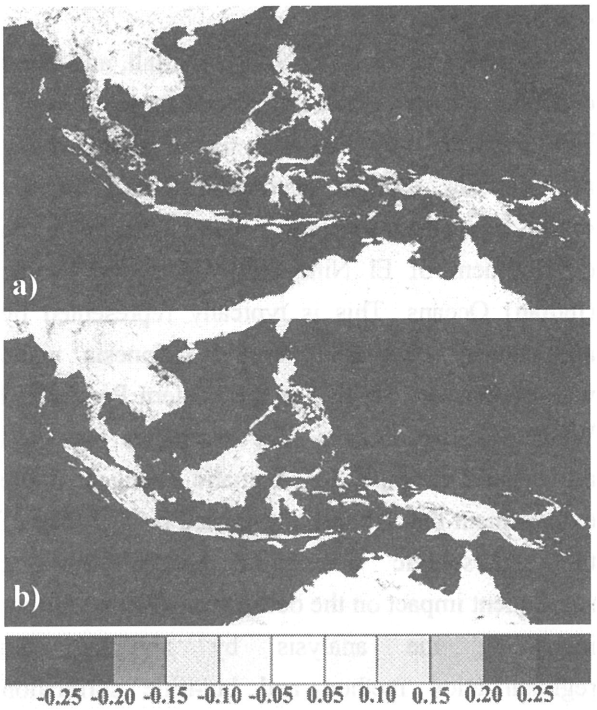

Figure 5 Monthly AVHRR-NDVI anomaly images of Indonesia region during: a) the El Niño event (September 1997) and the La Niña event (September 1998).

3.3 NDVI anomaly

Monthly NDVI anomalies for the El Niño (September 1997) and La Niña (September 1998) events are shown in Fig. 5. Changes in rainfall patterns induced by the El Niño and IODM conditions exert significant effects on biomass production of Indonesia area. This effect can be revealed by NDVI anomaly patterns, particularly in equatorial western part of Indonesia (Kalimantan and Sumatera) where the ENSO–rainfall linkage is most pronounced. A reversal was found in the NDVI response from negative during the El Niño event in 1997/98 to positive during the La Niña event in 1998/99. This reversal can partly be attributed to the east–west reversal in SST gradients in the Pacific Ocean, but more significantly to the changes in the SST anomaly patterns in the equatorial western Indian Ocean. The results of the lag-correlation analysis between the NDVI anomalies and the ENSO/IODM indices will be given in the presentation.

4. Conclusion

Changes in the SST, NDVI, rainfall, and cloud coverage clearly indicate the occurrence of an El Niño event in 1997. Our analysis has indicated that in Indonesia, drought conditions during the dry season typically take place in conjunction with the development of El Niño (IODM) in the Pacific (Indian) Oceans. This is typically represented by anomalously cold SST around Indonesia while warm anomalies develop in the Eastern Pacific and Western Indian Oceans. The anomalies presented are a good example for dramatic changes of the environment that are initially caused by a change of the atmospheric circulation pattern and its subsequent impact on the ocean state. We are further improving the analysis by applying the regionalization method and lag-time correlation analysis (Bannu et al, 2007) among the relevant parameters of climatological importance.

References:

Adler, et al, (2003): The version 2 Global Precipitation Climatology Project (GPCP) monthly precipitation analysis (1979-Present). *J. Hydrometeor*, **4,** 1147-1167.

Anyamba, et al, (2001): NDVI anomaly patterns over Africa during the 1997/98 ENSO warm event. *Int. J. Remote Sensing*, **22,**1847–1859.

Bannu, et al (2007): Influence of El Niño and Indian Ocean dipole mode on the regional rainfall in Indonesia, *J.Clim.*, (submitted).

Hendon, H.H, (2003): Indonesian rainfall variability: impacts of ENSO and local air-sea interaction. *J. Climate*, **16**, 1775-1790.

Kalnay, E., and coauthors, 1996: The NCEP/NCAR 40-year reanalysis project. *Bull. Amer. Meteor. Soc.*, **77**, 437-471.

Miller et al., 1992: The sensitivity of the ECMWF model to the parameterization of evaporation from the tropical oceans. *J. Climate*, **5**, 418–434.

McBride, J. L, et al, (2003): Relationships between the Maritime Continent Heat Source and the El Niño-Southern Oscillation Phenomenon. *J. Clim*, **16**, 2905-2914.

MSC, (2002): Analysis and use of meteorological satellite images, Japan Meteorological Agency.

Qu, T. et al, (2005): Sea surface temperature and its variability in the Indonesian region, *Oceanography*, **18:4**, 50-61.

Rasmusson, E.M., and T.H. Carpenter, (1982): Variations in tropical sea surface temperature and surface wind fields associated with the Southern Oscillation/El Niño. *Mon. Wea. Rev.*, **110**, 354-384.

Ropelewski, C. F. and M. S. Halpert, (1987): Global and regional scale precipitation patterns associated with the El Niño/Southern Oscillation. *Mon. Wea. Rev.*, **115,** 1606–1626.

Smith, T. M., and R. W. Reynolds (2005), A global merged land air and sea surface temperature reconstruction based on historical observations (1880-1997). *J. Clim.*, **18**, 2021-2036.

Saji, et al, (1999): A dipole mode in the tropical Indian ocean, *Nature*, **401**, 360-363.

ESTIMATION AND EVALUATION OF SOIL EROSION USING MULTITEMPORAL SPATIAL DATA

Study case West Java-Indonesia

Darmawan S.[1,2)], Wikantika K.[1,3)], Hirano A.[2)], Uchida S.[2)], and Firman H.[1)]

1) Center for Remote Sensing, Institute Technology Bandung
Ganesha No. 10 Bandung 40132, Indonesia
2) Japan International Research Center for Agricultural Sciences (JIRCAS)
1-1 Ohwashi, Tsukuba, Ibaraki 305-8686 Japan
3) Geodesy and Geomatic Study program, Faculty of Earth Sciences and Technology
Institute Technology Bandung, Ganesha 10 Bandung 40132, Indonesia

Corresponding Author : soni@crs.itb.ac.id soni_darmawan@yahoo.com, soni@jircas.affrc.go.jp

Abstract

Rapid economic and population growth in West Java has been accompanied by significant land use change. This condition has been effected soil erosion. Soil erosion appears to be one of the most significant environmental problems. Soil erosion is a big problem because physically effect can be decrease turbidity, change water temperature and fish habitat and spawning patterns and chemically effect can transport nutrients such as phosphorus and nitrogen, heavy metals, degrade water quality and degrade land quality. To estimate soil erosion value can use USLE (Universal Soil Loss Equation). USLE is most widely used method for estimating soil erosion although originally developed for agricultural purpose; its use has been extended to catchments area with other land uses. Remote sensing and GIS technology used to estimate and to evaluate distribution of soil erosion. This technology can be easy to collect, to process and to analyze multitemporal spatial data. Data collected such land use, rainfall, soil erodibility, slope and others data in 1994, 1997, 2001 and 2005. Image processing and spatial analyze can using commercial and open source software. To integrate their software using virtual machine but unfortunately data in windows can be "read-only" only, therefore data exchange is done with other interface medium. Most big Soil erosion distribution based on river basin area in 1994 – 2005 is Ciujung, Cisanggarung, Cimandur and Cibareno. Soil erosion was very big occurs in Cibareno river basin because changes of forest to agricultural area and agricultural area to palawija fields as well. Based on administrative area most big soil erosion distribution in 1994 – 2005 are Majalengka, Kuningan, Bandung, Bogor and Sukabumi. Big soil erosion occurs in 2001 because of rainfall extreme, in Majalengka and Kuningan while small rainfall exchange will impact on big soil erosion because of steep slope.

Key words: land use change, USLE, GIS, distribution of soil erosion

1. Introduction

Soil is a natural body of solids, liquid, and gases, with either horizons, or layers or the ability to support rooted plants. Plant can not live without soil. Soil fertilizer very helpful for growth plant. Not only for plant soil function for regulating and partitioning water and solute flow, filtering, buffering, degrading, immobilizing, and detoxifying, sustaining plant and animal life below and above the surface, Storing and cycling nutrients (NRCS-USDA). Human activity on the land will effect soil condition. Other activity which effect soil condition is wind and water. Soil is naturally removed by the action of water and wind. Soil which removed by water and wind is soil erosion. Soil erosion effect can occurs soil degradation, environmental disaster, agricultural production decrease and capital income decrease.

Land use majority in West Java used agricultural. Paddy, tea and coffee provided more production better other province. Rapid economic, population growth, urbanization in West Java has been accompanied by significant land use change (CRS-ITB, 2006). During the past few years not only soil erosion but environmental disaster like landslide, floods and dryness occurs in West Java. This condition will effect to agricultural product and regional income.

Scientific planning for soil and water conservation requires knowledge of he relations between those factors that cause erosion of soil and water and those that help to reduce such losses. The USLE (Universal Soil Loss Equation) is an erosion model designed to predict the longtime average soil losses in runoff from specific areas in specific cropping and management systems. Widespread field use has substantiated its usefulness and validity for this purpose. It is also applicable for such non-agricultural conditions as construction sites (Walter H et.al, 1972). The USLE model is expressed as follows:

$$\mathbf{A = R \times K \times Ls \times C \times P} \ldots\ldots\ldots\ldots\ldots\ldots (1)$$

A	is the computed soil loss per unit area
R	the rainfall and runoff factor.
K	the soil erodibility factor.
LS	the slope length-gradient factor.
C	the crop/vegetation and management factor.
P	the support practice factor.

Soil erosion tolerance rate (Robert P., 2000):

Table 1. soil erosion tolerance rate

Soil erosion class	Potential soil erosion (tons/acre/year)
Very low	< 3
Low	3 - 5
Moderate	5 - 10
High	10 - 15
Severe	> 15

To estimate soil erosion in large area can use spatial data. To implement can use integration commercial software based on windows and open source software based on Linux. Open source software can use GRASS (Graphical Resource Analys Support System) as a tool (Darmawan, 2007).

2. Study Area

West Java provinces in geodetics position are extending longitudes $104^0\ 48'$ - $108^0\ 48'$ E and latitude $5^0\ 50'$ - $7^0\ 50'$ S (figure 1). It has large area 4.709.528 ha there is 25 districts, 437 sub districts, and 5738 village. Population in West Java around 37 million and people work in agricultural around 30%. Paddy field and tea plantation is more product than other province. Paddy field area growth around north West Java such Kerawang, Subang, Purwakarta dan indramayu. Tea plantation growth around south West Java such Bandung, Garut, Subang and Cianjur. West Java is buffering province for capital city of Indonesia. If big rainfall in part of West Java like in Bogor, will provide flood in Jakarta. West Java have three dams for irrigation and Citarum is a big river basin in West Java.

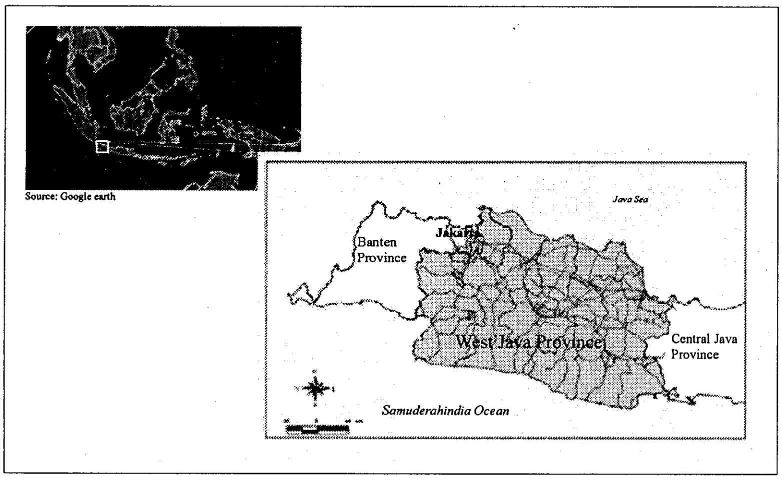

Figure 1. Study site in West Java Province

3. Data and Instrument Preparation

The supplementary data was acquired like land use, contour topographic, soil erodibility, rainfall and support practice. Land use data had been generated from LANDSAT in 1994, 1997, 2001 and 2005 published by West Java Planning Agency. Contour topographic had been generated from topographic map at scale 1:25.000 published by Bakosurtanal. Soil erodibility was provided by soil institute and rainfalls were provided by meteorology agency in 1994, 1997, 2001 and 2005. Parameter of conservation factor, support practice factor, rainfall factor, soil erodibility factor and support practice factor for USLE model can get from soil institute. Tools to image processing and to spatial analyze using integration commercial and open source software such GRASS. For integrate commercial and open source software can use virtual machine.

4. Method

General method to estimate and to evaluate soil erosion using spatial data was provided spatial data for USLE model. Data for USLE model are vegetation and management factor (C factor), rainfall factor (R factor), soil erodibility factor (S factor), slope-length factor (Ls factor) and support practice factor (P factor) can see figure 2.

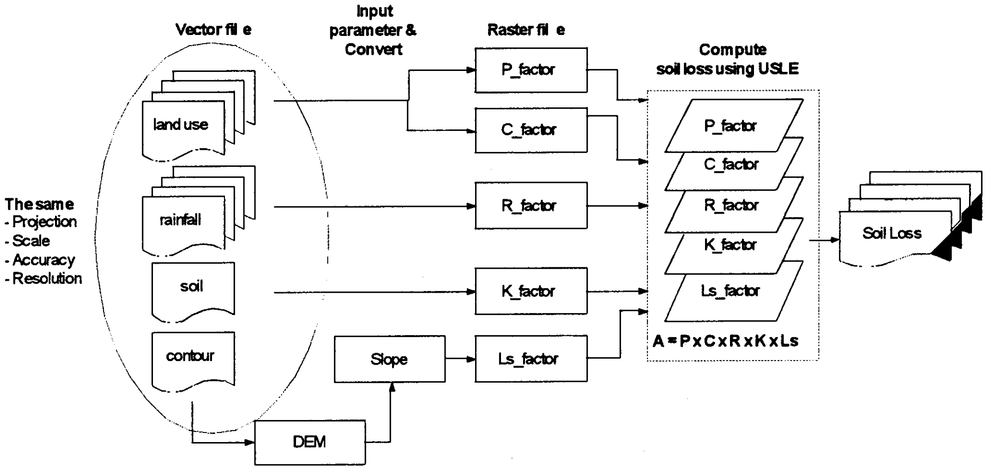

Figure 2 method for compute soil erosion

To create vegetation and management factor and support practice can input vegetation and management factor and support practice to land use map in 1994, 1997, 2001, 2005 and convert to grid format. To create soil erodibility factor, can input soil erodibility factor to soil map and convert to grid format. To create rainfall factor can generate rainfall map from rainfall tabular in 1994, 1997, 2001 and 2005, input rainfall factor to rainfall map in 1994, 1997, 2001 2005 and convert to grid format. To create slope-length factor can generate DEM from contour scale 1:25.000 and next step generate slope from DEM, input slope length factor to slope and convert to grid format. In this case grid dimension 30x30 metres and slope length 30 metres. For distribution analysis of soil erosion used spatial analyze base on river basin and based on administrative boundary.

5. Result and Discusion

USLE is most widely used method for estimating soil erosion, soil erosion with USLE model very simple and familiar method used in Indonesia because it is easy to get parameters such land use, rainfall, slope, soil erodibility and supporting factor. Accuracy soil erosion using USLE model depends on dimension of data. This case, dimension of grid format is 30x30 metres and dimension of slop length is 30 metres for all area. Probabilities of soil erosion provided under estimate. To image processing and to spatial analyze using integration commercial and open source software such GRASS. For integrate commercial and open source software can use virtual machine. Virtual machine can be helpful for integration of windows to GRASS Linux, unfortunately data in windows can be "read-only" only, therefore data exchange is done with other interface medium

Land use map have been generated from LANDSAT in 1994, 1997, 2001 and 2005 that provided land use change information. This information about primery forest, secondary forest, paddy field and dike have been decrease. Brushwood, industry zone, urban area, agricultural are and mix agricultural have been increase. Exploration zone, grassland bare soil and wetland have been relative constant. Slope map have been generated from DEM, and DEM have been generated from contour topographic map at scale 1:25.000. Information provided about majority elevation in West Java 0–500 metres, and majority slope in West Java 0-16 %. Rainfall map have been generated from rainfall tabular that provided some information. Information provided about average rainfall in 1994 around 3000 mm/year, in 1997 around 2500 mm/year, in 2001 around 4000 mm/year and in 2005 around 3250 mm/year. Soil erodibility map have been generated from soil map that provided some information. Information provided about majority of soil erodibility indeks in West Java around 0.28. Soil erodibility indeks around 0,29 provide in north west java and soil erodibility indeks around 0.13 provide in south west java.

In 1994 average of soil erosion around 12.9 tons/acre/year, this is high soil erosion class. Ciujung and Cisanggarung river basin provided biggest soil erosion value and 14 river basins in severe of soil erosion class in 1994. If based on administrative boundary, Majalengka and Kuningan provided bigger soil erosion value than other district and 9 districts have severe of soil erosion class. In 1997 average of soil erosion around 9.79 tons/acre/year, this is moderate of soil erosion class. Ciujung and Cisanggarung river basin provided biggest soil erosion value and 8 river basins in severe of soil erosion class in 1997. If based on administrative boundary, Majalengka and Kuningan provided bigger soil erosion value than other district and 5 districts have severe of soil erosion class. In 2001 average of soil erosion around 23.74 tons/acre/year, this is severe of soil erosion class. Ciujung and Cimandur river basin provided biggest soil erosion value and 26 river basins in severe of soil erosion class in 2001. If based on administrative boundary, Majalengka and Kuningan provided bigger soil erosion value than other district and 16 districts have severe of soil erosion class. In 2005 average of soil erosion around 18.74 tons/acre/year, this is severe of soil erosion class. Ciujung and Cibareno river basin provided biggest soil erosion value and 20 river basins in severe of soil erosion class in 2005. If based on administrative boundary, Majalengka and Kuningan provided bigger soil erosion value than other district and 13 districts have severe of soil erosion class (figure 3 and figure 4).

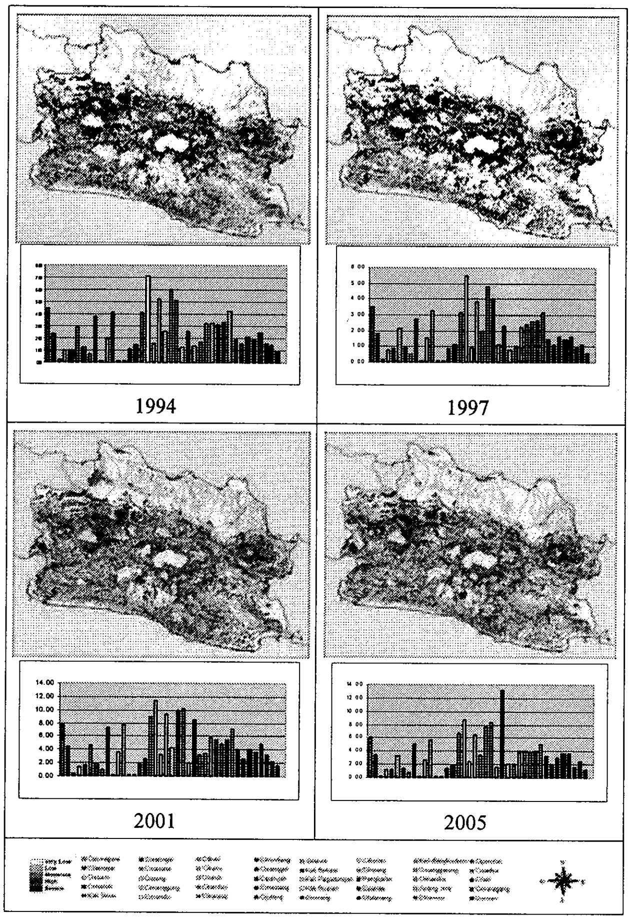

1994

1997

2001

2005

Figure 3. Distribution of soil erosion based on river basin

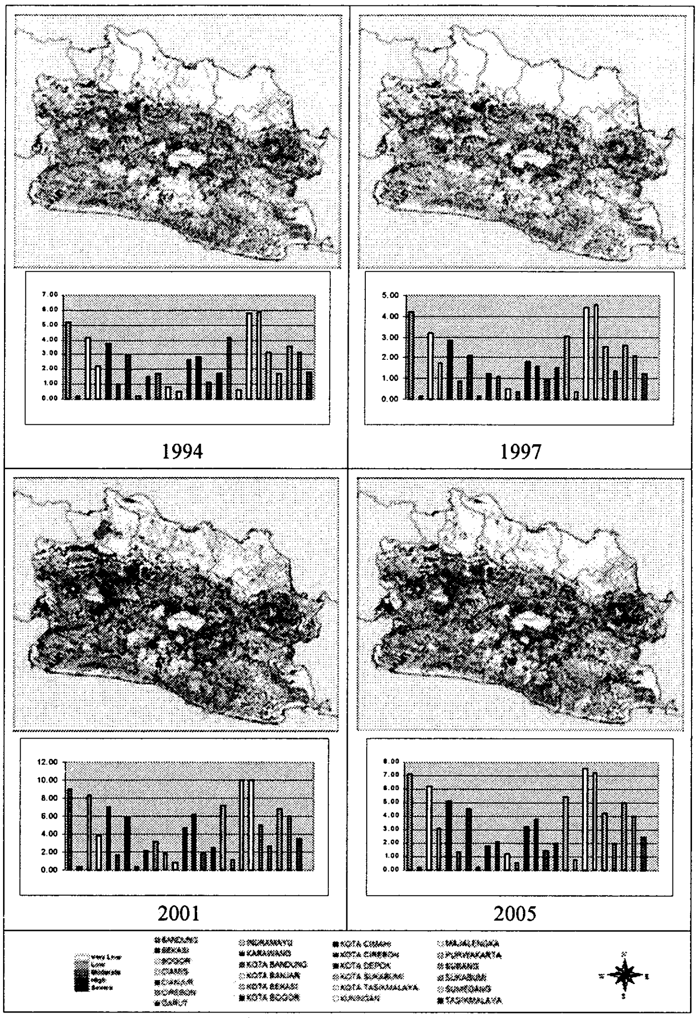

Figure 4. Distribution of soil erosion based on administrative boundary

Soil erosion value depend on rainfall every years, during 1994 – 2005 big soil erosion occurs in 1994 because rainfall extreme, next biger soil erosion in 2005, 1994 and 1997. In 2005 rainfall smaller than 2001 but soill erosion value in Cibareno river basin bigger than 2001 because changes of forest to agricultural area and agricultural area to palawija fields as well. The big five river basin provide soill erosion is Cibareno, Ciujung, Cimandur, Cisanggarung and Citarum. If depends on administrative boundary the big five district provide soil erosion is Majalengka, Kuningan, Bandung, Bogor and Sukabumi. In Majalengka and Sukabumi while small rainfall exchange will impact on big soil erosion because of steep slope (figure 5).

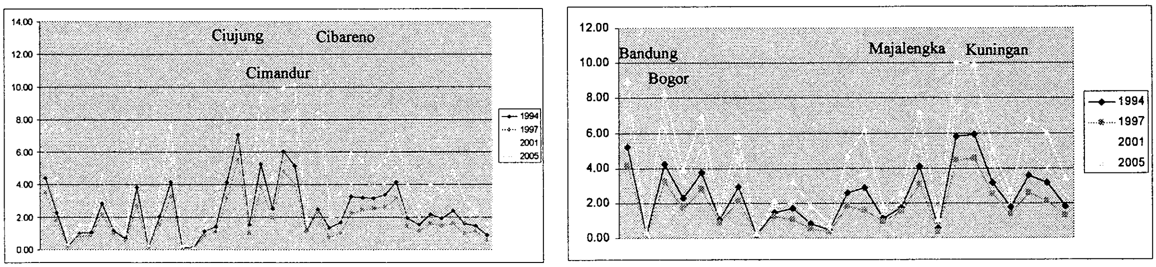

a

b

Figure 5. Soil erosion value based on river basin (a) and based on administrative boundary (b)

6. Conclusion

- Soil erosion with USLE model very simple and familiar method used in Indonesia because it is easy to get parameters such land use, rainfall, slope, soil erodibility and supporting factor. Accuracy soil erosion using USLE model depends on dimension of data.
- Virtual machine can be helpful for integration of windows to GRASS Linux, unfortunately data in windows can be "read-only" only, therefore data exchange is done with other interface medium.
- Most big Soil erosion distribution based on river basin area :
  - in 1994 : Ciujung, Cisanggarung, Cimandiri, Cimandur, Citarum
  - in 1997 : Ciujung, Cisanggarung, Cimandur, Cimandiri, Citarum
  - in 2001 : Ciujung, Cimandur, Cisanggarung, Cimandiri, Cisadane
  - in 2005 : Cibareno, Ciujung, Cimandur, Cimandiri, Cisadane
- Most big Soil erosion distribution based on administrative area : in 1994, 1997, 2001 and 2005: Majalengka, Kuningan, Bandung, Bogor and Sukabumi.
- Soil erosion was very big occurs in Cibareno river basin because changes of forest to agricultural area and agricultural area to palawija fields as well.
- Big soil erosion occurs in 2001 because of rainfall extreme, in Majalengka and Kuningan while small rainfall exchange will impact on big soil erosion because of steep slope .

References

1. Darmawan S., Hirano A., Uchida S., Wikantika K,. "Universal Soil Loss Equation (USLE) Spatial Modeling Using GRASS Virtual Machine" course material, Tsukuba 2007
2. Robert P. Stone "Universal Soil Loss Equation USLE" http://www.omafra.gov.on.ca/english/engineer/facts/00-001.htm, Ontario 2000
3. Walter H., Wishchmeier, Dwight D., "Predicting Rainfall-Erosion Losses from Cropland East of the Rocky Mountains" Guide for selection of practices for soil and water conversion. Agricultural Handbook No 357. Agricultural research service – US. Department of Agriculture in Corporation with Purdue Agricultural Experiment Station. Washington DC. 1972.
4. _______________Natural Resources Conservation Service-United States Departement of Agriculture (NRCS-USDA) http://www.nrcs.usda.gov
5. _______________Center for Remote Sensing Institute Technology Bandung (CRS-ITB) "Identify land use in West Java Using Remote Sensing" Progress report, Bandung 2006

ASTER time series image database dedicated to volcanoes

Minoru URAI
Geological Survey of Japan, AIST, Central 7, 1-1-1 Higashi, Tsukuba, Ibaraki, 305-8567 Japan.
Email : urai-minoru@aist.go.jp

Abstract

The Advanced Spaceborne Thermal Emission and Reflection Radiometer (ASTER), which was launched on Terra platform in 1999, has a high spatial resolution imaging spectro-radiometer in the visible to near-infrared, shortwave-infrared and thermal infrared regions. A global volcano monitoring plan by using ASTER data has started, in which over 900 volcanoes are monitored periodically. A web-based ASTER image database dedicated to volcanoes is developed and opened to the public (http://www.gsj.jp/database/vsidb/image/index-E.html). The database consists of Official Version and Prototype Version. The Official Version contains all ASTER images of 49 most active volcanoes that are mainly in East Asia. The Prototype Version contains a part of ASTER images over 900 active volcanoes.

1. Introduction

Satellite remote sensing is a powerful tool for volcano monitoring. The Advanced Spaceborne Thermal Emission and Reflection Radiometer (ASTER), which was launched on Terra platform in 1999, is a high spatial resolution imaging spectro-radiometer (Yamaguchi et al., 1998). The ASTER can be used for volcano observations in the context of 1) topographic and geologic analysis, 2) mapping volcanic products, 3) eruption plume analysis, 4) discolored sea water and crater lake monitoring, 5) generating digital elevation models, 6) surface temperature mapping and 7) sulfur dioxide emission analysis (Urai et al., 1999). The unique features of the ASTER instrument such as along track stereo imaging and multispectral thermal infrared radiometry allow additional information about volcanoes to be acquired.

The ASTER Science Team proposed the global volcano observation plan with ASTER (Urai et al., 1999) and a large number of volcanic ASTER scenes were acquired since June 2000 when the ASTER normal operation was started. We can retrieve ASTER data from the ASTER Ground Data System (GDS) by geographic location. However, we often do not know the exact geographic location of the volcano. The Geological Survey of Japan, AIST developed a prototype image database for volcanoes that we can retrieve ASTER data by the volcano name. In this paper, the author describes the global volcano observation plan with ASTER and the ASTER image database dedicated to volcanoes.

2. Overview of ASTER instruments

The ASTER consists of three separate optical subsystems: visible and near-infrared (VNIR) radiometer, shortwave-infrared (SWIR) radiometer, and thermal infrared (TIR) radiometer, as described in Table 1. The VNIR subsystem has four bands similar to JERS-1 OPS including along-track stereo capability with nadir (band 3N) and backward (band 3B) views. The SWIR subsystem has a band centered at 1.65 μm and five bands from 2.1 μm to 2.5 μm mainly for soil and mineral mapping. The Low Gain 2, which is the special gain setting available only for SWIR, is used for observation of high temperature targets such as lava flows and fumaroles. The TIR subsystem has five bands in the thermal infrared region mainly for precise temperature measurements and rock type discrimination. Further details can be found in Yamaguchi et al. (1998) and Fujisada et al. (1998).

3. Volcano monitoring with ASTER

Volcanic features such as craters, lava flows and faults can be interpreted from an ASTER image, particularly a VNIR image with a 15 m ground resolution for a 60 km swath. The acquisition of a stereo image pair makes geologic interpretation easier. The areas covered by fresh volcanic ash and pyroclastic flow deposits are observed as bright colors in the VNIR images. Lava flows are represented by dark colors in the VNIR and bright colors in the SWIR images.

Eruption plumes are observed by the ASTER as well as Landsat TM, SPOT HRV, JERS-1 OPS, MOS 1/2 MESSR and NOAA AVHRR (Kinoshita, 1996). Drift velocity and altitude of volcanic plumes can be obtained using an image pair taken by the ASTER VNIR along track stereo function (Urai, 2004). Discolored sea water, which is generated above a submarine volcano or along the shoreline of a volcano, are observed by the VNIR bands (Urai and Machida, 2005). Temperature changes of crater lakes are observed in the TIR bands. Digital elevation models generated by ASTER stereo image pairs have the accuracy better than 20 m and 50 m in the vertical and horizontal directions, respectively, without GCP correction (Fujisada et al., 2005). The ASTER GDS provides digital elevation models as one of the standard data products. The TIR instrument is designed for surface temperature and emissivity mapping. Surface temperature up to 300 K are observed by the TIR. Pieri and Abrams (2005) found pre-eruption thermal anomalies at Chikurachki volcano, Russia, using TIR.

Radiance from active lava flows, lava lakes, pyroclastic flows and high temperature fumaroles may saturate the TIR detectors. These high temperature targets are observed by the SWIR bands, which have a special gain mode : Low Gain 2. The ASTER allows continuous temperature measurements ranging from the prevailing temperature to 460 °C and from 670 °C to 910 °C.

Sulfur dioxide is one of the major constituents of volcanic gases. Sulfur dioxide has a strong absorption spectrum in the thermal infrared region, where the ASTER TIR has five bands. Realmuto et al. (1994) pointed out that the ASTER TIR could be used to make an estimation of the sulfur dioxide content of a volcanic plume. Urai (2004) estimated the sulfur dioxide flux from the Oyama volcano in Miyakejima, Japan using ASTER.

Subsystem	Band no.	Spectral range(μm)	Spatial resolution
VNIR	1	0.52-0.60	15m
	2	0.63-0.69	
	3N, 3B	0.78-0.86	
SWIR	4	1.600-1.700	30m
	5	2.145-2.185	
	6	2.185-2.225	
	7	2.235-2.285	
	8	2.295-2.365	
	9	2.360-2.430	
TIR	10	8.125-8.475	90m
	11	8.475-8.825	
	12	8.925-9.275	
	13	10.25-10.95	
	14	10.95-11.65	

Stereo Base-to-Height ratio	0.6
Swath width	60km
Total Coverage in Cross-Track Direction by Pointing	232km
Distance between adjacent orbit	172km
Repeat cycle	16days

Table 1 ASTER base line performance requirements (modified from Yamaguchi et al., 1998)

4. Global volcano monitoring plan with ASTER

Urai et al. (1999) proposed a global volcano monitoring plan using ASTER data. Over 900 volcanoes are monitored periodically (Figure 1). Observing strategies for individual volcanoes will vary according to their volcanic activity. The volcanoes to be monitored are selected from Simkin and Siebert (1994) and the Japan Meteorological Agency (1991). They are divided into three classes, A, B and C as shown in Table 2. Volcanoes of Class A, which have several eruption records during the last 10 years, are observed every 48 days in the daytime and every 32 days at night. Volcanoes of Class B have several eruption records during the last 100 years and are observed every three months in the daytime and at night. The other volcanoes classified as Class C are observed every six months in the daytime and at night.

Class	Number of volcano	Observation interval in day time (day)	Observation interval in night time (day)
A	102	48	32
B	222	91	91
C	182	182	182

Table 2 Observation intervals for the Global Volcano Monitoring (Urai et al., 1999).

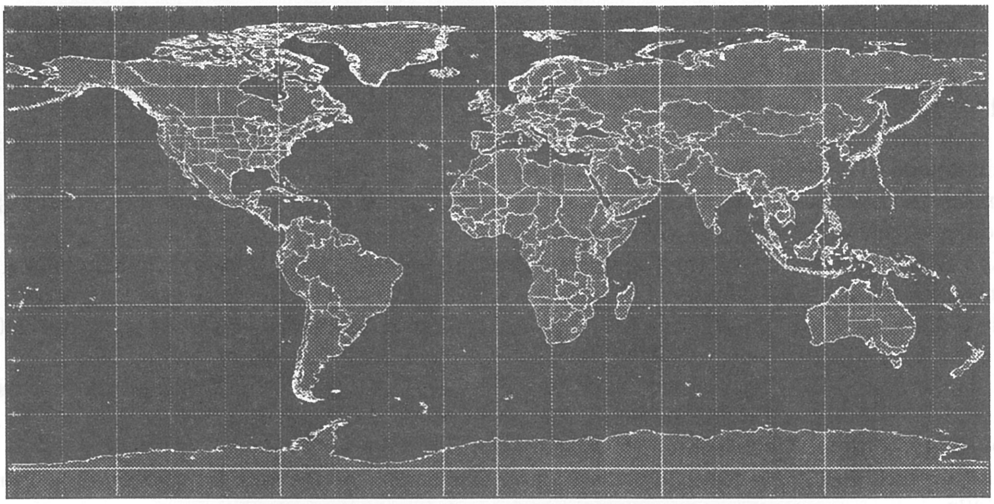

Figure 1 Volcano locations monitored by ASTER.

5. ASTER image database dedicated to volcanoes

A web-based ASTER image database dedicated to volcanoes is developed and opened to the public (http://www.gsj.jp/database/vsidb/image/index-E.html). The database consists of Official Version and Prototype Version. The Official Version contains all ASTER images of 49 most active volcanoes that are mainly in East Asia. The Prototype Version contains a part of ASTER images over 900 active volcanoes. All newly acquired ASTER images of the volcanoes in the Official Version are added to the database every month. However, some ASTER images of the volcanoes in the Prototype Version may not be added to the database. About 60 most active volcanoes other than in East Asia will be added to the Official Version within several months.

Figure 2a shows the web-based image database dedicated to volcanoes. You can choose a volcano from the menu displayed on the left hand side. Clicking a volcano name, you can see thumbnail ASTER images that are sorted by the data acquisition date. You can get a full resolution image by clicking a thumbnail as shown in Figure 2b.

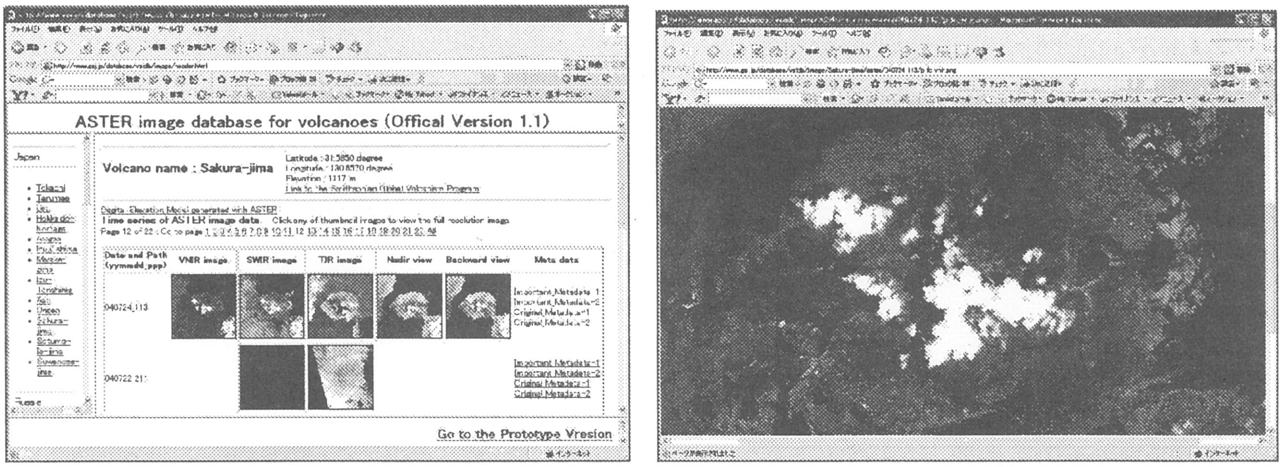

ASTER image database for volcanoes (Offical Version 1.1)

Japan

Volcano name : Sakura-jima

Latitude : 31.5850 degree
Longitude : 130.6570 degree
Elevation : 1117 m
Link to the Smithsonian Global Volcanism Program

Digital Elevation Model generated with ASTER

Time series of ASTER image data. Click any of thumbnail images to view the full resolution image.

Date and Path (yymmdd_ppp)	VNIR image	SWIR image	TIR image	Nadir view	Backward view	Meta data
040724_113						Important_Metadata-1 Important_Metadata-2 Original_Metadata-1 Original_Metadata-2
040722_21						Important_Metadata-1 Important_Metadata-2 Original_Metadata-1 Original_Metadata-2

Go to the Prototype Vresion

(a) (b)

Figure 2 Web based ASTER image database dedicated to volcanoes.
(a) : Initial menu of the Official Version. (b) : Full resolution image display.

6. Conclusions

The ASTER can be used for volcano observations in the context of 1) topographic and geologic analysis, 2) mapping volcanic products, 3) eruption plume analysis, 4) discolored sea water and crater lake monitoring, 5) generating digital elevation models, 6) surface temperature mapping and 7) sulfur dioxide emission analysis. The ASTER observation is complementary to those from existing satellite sensors as well as with the MODIS instrument that is flying on the same platform. The global volcano monitoring has started using the ASTER. Over 900 volcanoes are monitored periodically according to the level of their volcanic activity. A web-based ASTER image database dedicated to volcanoes is developed and opened to the public. ASTER instrument is a powerful tool for monitoring of active volcanoes because ASTER has a wide spectral range, stereo imaging allowing DEM generation, thermal anomaly detection capability and the ability to classify land cover characteristics.

Acknowledgments

The author is grateful to the ASTER Science Team members for their helpful discussions.

References

Fujisada, H., Sakuma, F., Ono, A. and Kudoh, M. (1998) Design and Preflight Performance of ASTER Instrument Protoflight Model. IEEE Transactions on Geoscience and Remote Sensing, 36, no.4, 1152-1160.

Fujisada, H., Bailey, G. B., Kelly, G., Hara, S. and Abrams, M. J. (2005). ASTER DEM Performance. IEEE Transactions on Geoscience and Remote Sensing, 43, no.12, 2707-2714.

Japan Meteorological Agency (1991) National catalogue of the active volcanoes in Japan (Second edition). Japan Meteorological Agency, Tokyo, p.483. (in Japanese)

Kinoshita, K. (1996) Observation of flow and dispersion of volcanic clouds from Mt. Sakurajima. Atmospheric Environment, 30, no.16, 2831-2837.

Pieri, D. and Abrams, M. J. (2005) ASTER observations of thermal anomalies preceding the April 2003 eruption of Chikurachki volcano, Kurile Islands, Russia. Remote Sensing of Environment, 99, no.1/2, 84-94.

Realmuto, V. J., Abrams, M. J., Buongiorno, M. F. and Pieri, D. C. (1994) The use of multispectral thermal infrared image data to estimate the sulfur dioxide flux from volcanoes: A case study from Mount Etna, Sicily, July 29, 1986. Journal of Geophysical Research, 99, no.B1, 481-488.

Simkin, T. and Siebert, L. (1994) Smithonian Institution Volcanoes of the world (2nd edition). Geoscience Press, Tucson, 349p.

Urai, M. (2004) Sulfur dioxide flux estimation from volcanoes using Advanced Spaceborne Thermal Emission and Reflection Radiometer - A case study of Miyakejima volcano, Japan. Journal of Volcanology and Geothermal Research, 134, no.1-2, 1-13.

Urai, M. and Machida, S. (2005) Discolored seawater detection using ASTER Reflectance Products: a case study of Satsuma-Iwojima, Japan. Remote Sensing of Environment, 99, 95-104.

Urai, M., Fukui, K., Yamaguchi, Y. and Pieri, D. C. (1999) Volcano Observation Potential and Global Volcano Monitoring Plan with ASTER (in Japanese with Eng lish abstract). Bulletin of the Volcanological Society of Japan, 44, no.3, 131-141.

Yamaguchi, Y., Kahle, A. B., Tsu, H., Kawakami, T. and Pniel, M. (1998) Overview of Advanced Spaceborne Thermal Emission and Reflection Radiometer (ASTER). IEEE Transactions on Geoscience and Remote Sensing, 36, no.4, 1062-1071.

Disaster information acquisition system using multi-platform remote sensing technology

Takashi SHIBAYAMA[1], Takashi NONAKA[1], Susumu TAKAGISHI[1] and Tadashi SASAGAWA[1]
[1] PASCO Corporation Satellite Business Division
E-mail: takashi_shibayama@pasco.co.jp

Abstract

Japan is not only a country with frequent earthquakes, but also is located in the typhoon-prone zone with one of the most frequent severe rain storms and sediment disasters in the world. Despite those natural disasters, it is difficult to determine the extent of the disaster damage quickly and extensively. Facing this problem, it is necessary and effective to make the most use of remote sensing technology of satellite and airborne platform. Because of this situation, we are developing a disaster information service based on satellite and airborne sensors.

In this system, SAR (Synthetic Aperture Radar) satellite sensor acquires images of the areas of interest during normal phase, and they can be put in order as ready-to-use reference data. When a disaster happens, the quickest way of data acquisition, whether satellite or airplane, is to be done. In case of SAR satellite sensor, it is possible to extract changed areas between images acquired before and after the disaster. If more detail information is demanded, images acquired by airborne sensors are analyzed for mapping disaster-affected areas and will be provided. Moreover, acquiring images regularly after disaster, it is possible to monitor recovery and restoration status of the damaged areas.

1. Introduction

Japan, where about 10 percent of all volcanoes in the world are located, is not only a country with frequent earthquakes, but also is located in the typhoon-prone zone with one of the most frequent severe rain storms and sediment disasters in the world. Despite those natural disasters, it is difficult to determine the extent of the disaster damage quickly and extensively. Facing this problem, it is necessary and effective to make the most use of remote sensing technology of satellite and airplane platform.

Generally, comparing satellite images acquired before and right after the disaster makes it possible to retrieve the information of damage-hit areas. However, it is also difficult to prepare such information in advance of the disaster. Because of this situation, we are developing a system for acquiring disaster information based on spaceborne and airborne sensors.

2. Method

It is crucial to satellite images in every different phase of disaster occurrence: namely, pre-disaster phase, disaster phase, and recovery phase. Suppose that image data can be acquired with various sensors in a time of disaster, methods to integrate those images with periodically acquired images are discussed. Eventually, it is ideal that people can access and effectively use the information.

2.1 Pre-disaster phase

In this system, SAR (Synthetic Aperture Radar) satellite sensor acquires images of the areas of interest during pre-disaster phase, and they can be put in order as ready-to-use reference data. Also, image acquisition by optical sensors is necessary as a reference image. Bringing this system to realization, a database that includes satellite images and various kinds of geospatial information should be developed.

On the other hand, the combination of periodically acquired images is useful as basic data for making hazard maps and conducting an evacuation drill in the field of measures against disasters. This also can be utilized in maintenance of public infrastructure such as roads, rivers, and forests.

2.2 Disaster phase

In times of disaster, information is to be retrieved based on the following procedure.

1) Grasping the situation of the damage-hit areas with helicopter TV system and CCTV.

- CCTV (Closed-circuit Television) is set at where we would want to monitor in advance of disaster, so it can shoot movies of the site on regular basis.

- It is also possible to acquire the disaster information from websites of governmental organism and news reports from other media agencies.
- With all those things mentioned above, we can specify where the disaster occurs and consequently can send an order of image acquisition of the disaster area to the SAR satellite (*e.g.* TerraSAR-X).

2) Figuring out the disaster area extensively with SAR satellite images.

- Using TerraSAR-X, whose spatial resolution is high and revisit time is short.
- The maximum spatial resolution of the TerraSAR-X image is approximately 1 m.
- Its StripMap mode is capable of acquiring an image of large area (30km x 50km on the ground although the spatial resolution is 3 m with this mode).
- Although the repeat period of TerraSAR-X is 11 days, when it tries to cover the territory of Japan, it is possible to cover the whole territory within 3 days in a 80% of success rate.

3) Comprehending the area of disaster and the level of the damage by analysis of SAR images.

- Interpretation the acquired SAR image and comparing images before and after the disaster, one can know the center and the extent of the disaster.
- Consequent of this method, we can specify where we have to retrieve detail information such as aerial photos from with airborne sensors can be specified more.

4) Acquiring images of severely damaged areas with airborne (fixed-float) optical sensor intensively.

- Acquiring images of areas specified by SAR image analysis intensively.

5) Pinpointing the location of disaster sites by analysis and image interpretation of the optical images and creating a disaster map.

- With the result of analysis of the SAR satellite image and interpretation of the aerial photos, drawing the disaster areas on the map prepared in advance.
- Depending on the level of necessity, field work can be done if possible to make sure the accuracy of analysis.

When a disaster happens, the quickest way of data acquisition, whether satellite or airplane, is to be done. In case of SAR satellite sensor, it is possible to extract change areas between images acquired before and after the disaster.

3. Case study

We ran a simulation of the workflow described above taking the Chuetsu-oki earthquake on July 16th, 2007 as a case study. When the earthquake occurred, the weather condition was bad with dense cloud cover, and aerial photo acquisition of the earthquake site could not be done until 2 days after the disaster. On the other hand, checking the orbital path of TerraSAR-X at that time, we assume that image acquisition could have been done about 30 hours after the earthquake. If image analysis had been done a few hours after that, aerial photo acquisition session would have been planned more effectively. As a result, the extent of the earthquake damage could have been determined more rapidly so that it would greatly assist relief and rescue activities after the disaster.

If more detail information is demanded, images acquired by airborne sensors are analyzed for mapping disaster-affected areas and will be provided. Moreover, acquiring images regularly after disaster, it is possible to monitor recovery and restoration status of the damaged areas.

4. Discussion/Conclusion

In this study, a method to assess the situation of disaster rapidly and effectively with the use of data acquired with various satellite sensors such as SAR was introduced. To bring such a system into an operation in an actual disaster, it is necessary to construct the database based on a wide range of geospatial information ready to use as reference data. Making sure the data acquisition procedure of satellite sensors and data passing would be also an important issue.

At this point in time, considering the system realization in Japan, but if the issues discussed above are solved, there is a great possibility that the system operates as an effective way to minimize the extent of disaster damage.

Relationship between Lineament Density Extraction from Satellite Image and Earthquake Distribution of Taungtonelone Area, Myanmar

Myint Soe[a], **Krit Won-In**[b], **Isao Takashima**[b], **Punya Charusiri**[c]

a Graduate School of Engineering and Resource Science, Akita University, Akita 010-8502 JAPAN
b Center for Geo-Environmental Science, Akita University, 1-1 Tegatagakuen-cho, Akita 010-8502 Japan
c Department of Geology, Faculty of Science, Chulalongkorn University, Bangkok 10330, Thailand
* Corresponding author, E-mail: myintsoe68@gmail.com

Abstract:
We studied relationship between lineament density extraction from satellite image and earthquake distribution using remote sensing applications. The result of this study aim to set up a complete earthquake hazard Map. The selected area is located in the Taungtonelone area, northern Myanmar. Myanmar is an earth-quake-prone country. It lies in a major earthquake zone of the world called Mediterranean – Himalayan belt. As the major urban areas in Myanmar lie in earthquake prone zones, earthquake hazard reduction program is needed. Seismic monitoring and seismic database in Myanmar is in the early stage of developing. The current seismic hazard map of Myanmar is based on historical seismicity. Thus, there is a pressing need to prepare national seismic hazard maps for earthquake. Tectonic faults are often associated with characteristic geo-morphological features such as linear valleys, ridgelines and slope breaks that can be identified as lineaments in remotely sensed images of digital elevation models. A lineament map was prepared using stereo pair image of ASTER image, Landsat 7ETM+ image, SRTM DEM image. A variety of image processing techniques were used to highlight linear features of images. Known techniques such as color composite, Pseudo color DEM shade relief and 3D stereo anaglyph have been applied to enhance images for visual interpretation. The lineament reflects the geological structures such as faults or fractures. All lineament frequencies and lengths per unit area are calculated and combined to generate lineament density map. A grid system was used to obtain the data for lineament density values. This analysis produced a map showing concentrations of the lineaments over the area. The lineament density map can be used for the quantitative evaluation between lineaments and the earthquake risks monitoring for the future.

Key words: earthquake prone zones, image processing, lineaments, lineament density

1. Introduction

The study area of focus covers the Taungtonelone area, northern Myanmar. It is situated between latitudes 23° 30'N to 25° 30'N and longitudes 95° 00' E to 96° 30' E. Taungtonelone area were selected for the study because there have been active tectonic features such as fractures, folds, and active Sagaing fault zone. The total area is about 20000 km^2.

Myanmar has suffered from more than 16 large earthquakes (the magnitude (M> 7) during the last 170 years. Seismic monitoring and seismic zoning in Myanmar is in the early stage of developing. The current seismic hazard map of Myanmar is based on historical seismicity. As the major urban areas in Myanmar lie in earthquake prone zones. Thus, there is a pressing need to prepare national seismic hazard maps for earthquake.

According to geological data, Myanmar is an earth-quake-prone country. It lies in a major earthquake belt of the world called Mediterranean – Himalayan belt. There are three regions of earthquake epicenter concentrations in Myanmar. The first one lies along the eastern foothills of Rakhine Yoma, Chin Hills and Naga Hills. The second zone is located along the Sagaing facet, the third zone is situated along the northern edge of Shan plateau south of Mogok. These belts are closely related to the tectonics of Myanmar (Fig. 1).

The seismotectonics of Myanmar is shown in Figure 1. Earthquakes in Myanmar have resulted from two main causes: (1) the continued subduction (with collision only in the north) of the northward-moving

Indian Plate underneath the Burma Platelet (which is a part of the Eurasian Plate) at an average rate of 4-6 cm/ yr, (2) the northward movement of the Burma platelet from a spreading centre in the Andaman Sea at an average rate of 2.5 – 3 cm/yr (Bertrand et al., 1998). Very large overthrusts along the Western Fold Belt have resulted from the former movement, and the Sagaing fault and related faults from the latter movement. Intermittent jerks along these major active faults have caused the majority of earthquakes in Myanmar. The well-known and seismologically very active Sagaing Fault deserves a brief special mention. The Sagaing fault is a major dextral strike-slip right lateral continental fault that extends over 1200 km and connects to the Andaman spreading center at its southern termination. The linear Sagaing fault was also initiated 5 Ma ago with the Andaman spreading center, when deformation was localized on a single boundary from Vigny et al. (2001). These seismotectonic processes are still going on.

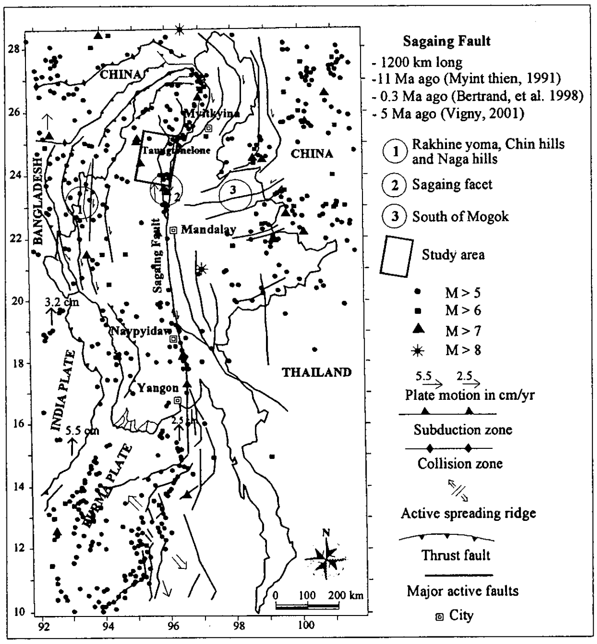

(Modified from Dr. Maung Thein and U Tint Lwin Swe)

Fig. 1 Seismotectonic map of the Myanmar region (Earthquake data: NEIC for the period 1964-2004; from other sources for 1912 - 1963. Tectonic boundaries and fault locations are mainly based on GIAC reports (1997, 2000)).

Seismicity is associated with major lineaments. Relationship between earthquakes and the geological structure of the area of earthquake due to the study of lineaments was studied by a number of authors. For example, Cotilla-Rodriguez and Cordoba-Barba (2004) studied the morphotectonic structure of the Iberian Peninsula and showed that the main seismic activity is concentrated on the first and second rank lineaments, and some of important epicenters are located near the lineament intersections (Stich et al., 2001).

Tectonic faults are often associated with characteristic geomorphological features such as linear valleys, ridgelines and slope breaks that can be identified as lineaments in remotely sensed images of digital terrain models. It supposes that lineaments are able to detect, at least partially, the presence of ruptures deep in the Earths crust (Jordan, G., 2004). The lineament features and stripe density fields caused by seismic activity (Arellano-Baeza, et. al, 2006). Lineament is used in a variety of applications, such as fault line and fracture system analysis in geology and many innovative topographic and lithographic ones.

Lineaments are any linear features that can be picked out as lines in aerial or space imagery. Geologically, these are usually faults, joints, or boundaries between different formations. Others causes for lineaments include roads and railroads, contrast emphasized contacts between natural or man-made geographic features.

Most of lineaments were attributed either to faults or to fracture systems that were controlled by joints. Lineaments are well-known phenomena in the Earth's crust. Clear lineaments are often used as indicators of major fractures in near-surface. Lineament detection of early stage was made from aerial photographs. Recently, geologists have been interested in tracing lineaments from satellite images which have broad coverage under the uniform conditions.

The lineament reflects the geological structure such as faults or fractures. In this sense, the lineament extraction is very important for the application of remote sensing to geology. The nature of lineaments is related to the presence of faults and dislocations in the crust, situated at different depth. If a dislocation is situated close to the surface, the fault appears as a clear singular lineament.

The principal objective of the study is to determine whether there is a relationship between lineament density and earthquake. This can provide a valuable tool for earthquake study, complementing other ground based and satellite studies.

2. Satellite data and processing

A lineament map was prepared using stereo pair image of ASTER (Advanced Spaceborne Thermal Emission and Reflection Radiometer) image, Landsat 7ETM+ image, the Shuttle Radar Topography Mission (SRTM) 90-meter resolution DEM image. A variety of image processing techniques are used to highlight linear features of images. Known techniques such as color composite, Pseudo color DEM shade relief and 3D stereo anaglyph have been applied to enhance images for visual interpretation. The lineaments were extracted and adjusted circle plan by TNTmips and AutoCAD softwares. And then using Excel, the number and lengths of lineaments were calculated. The lineament density result compared and confirmed with horizontal ground acceleration (HGA) map of Myanmar. It is computed from various seismic events, using known earthquake data set for the period 1912-2004 (Dr Maung Thein and Tint Lwin Swe, 2006). Acceleration at a particular site is related to the distance from the site to the epicenter. In addition, acceleration is related to earthquake magnitude – the greater the earthquake, the bigger the acceleration at all locations (Seekins and Boatwright, 1994). Ground motion expressed as a fraction of the acceleration of gravity (1g = the acceleration of gravity = 9.8 m/sec^2).

2.1 Data Preprocessing of Digital Elevation Model

Moellering & Kimerling (1990) used multi-image operation of false color composites, RGB color model in morphotectonic studies to simultaneously analyse three Digital Elevation Model. The similarly the study area used this method in RGB and interpreted the lineaments. RGB shade relief images sun direction created 270:325:360 (R:G:B) pseudo color shade relief image (Fig. 2). Pseudo color representation can increase the contrast of hill shade image.

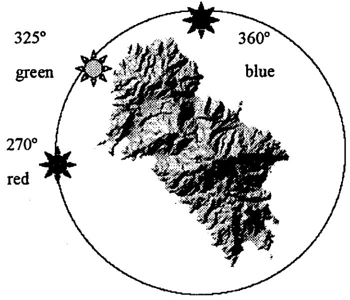

Fig.2 Pseudo color shade relief image model (modified from Moellering & Kimerling, 1990).

2.2 Anaglyph Image Generation

The stereoscopic images have been prepared from the available ASTER data that has the stereoscopic sensor performing nadir viewing (3N) and simultaneous backward viewing (3B) in VNIR Band 3. The glasses had a red colour for the left eye and cyan colour for the right eye was used to observe the 3D effect of the terrain.

2.3 Color Composite

The human eye can only distinguish between certain numbers of shades of gray in an image however, it is able to distinguish between much more colors. Therefore, a common image enhancement technique is to assign specific digital number (DN) values to specific colors to increase the contrast of particular DN values with the surrounding pixels in an image. An entire image can be converted from a gray scale to a color image, or portions of an image that represent the DN values of interest can be colored.

2.4 The Final Lineament Map Generation

The above mentioned techniques are used to extract lineaments from the satellite image. There is not a commonly accepted method to prepare the final lineament map. Although any of these techniques can be used to extract lineaments, three different techniques are applied here in order to be sure that no lineament is missed in the study area. The reason for this is that the area is not homogenous in terms of the surface characteristics, and it is believed that each method may enhance on aspect of the surface.

2. 5 Lineament Length Density Analysis

The purpose of the lineament density analysis is to calculate frequency of the lineaments per unit area. This is also known as lineament-frequency (Greenbaum, 1985). This analysis will produce a map showing concentrations of the lineaments over the area. The procedure of density analysis is shown in

Figure 3. First a unit area (a circular area with a search radius) is defined by the user. Every time, the frequency of the lineaments is counted and the number is recorded in an ASCII file for the center of corresponding unit area. The resultant text file that contains X, Y and Z values (Easting, Northing and frequency, respectively) and is stored to be processed for preparing density (contour) map of the area.

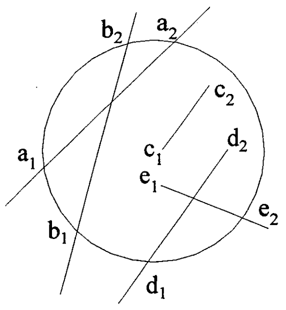

- Lineament Length density

= Sum of lineaments length within circle / Area of circle

= $(a_1a_2 + b_1b_2+c_1c_2+d_1d_2+e_1e_2) / \pi r^2$

- Counts density

= Number of lineament within circle / Area of circle
= $5 / \pi r^2$

- Cross-points density

= Number of lineament cross-points within circle / Area of circle
= $2 / \pi r^2$

Fig. 3 The calculation method of lineament density values using the circular method (the center of the circle is one of the grid points).

A grid system was used to obtain the data for lineament density values: the length density of lineaments, the numerical density of lineaments and the cross-points density of lineaments within the unit circular cell. The length density of lineaments is the total length (in km) of lineaments per cell area (km^2), the number of lineaments is the total number of lineaments per cell area (km2) and the cross-points density is the total number of cross points of lineaments per cell area (km2) existing within the unit circular cell (Fig. 3).

3. Result and Discussion

Analytical relief shading is the computer based process of deriving a shaded relief from a digital elevation model (DEM). Shade relief images created from digital elevation model (DEM) was helpful in identifying faults in rugged mountains. Unlike airphoto interpretation, the method enhanced lineaments by simulating topographic illumination under varied light direction. RGB shade relief images sun direction created 270:0:325 (R:G:B) pseudo color shade relief image (Fig. 4A). Pseudo color representation can increase the contrast of hill shade image.

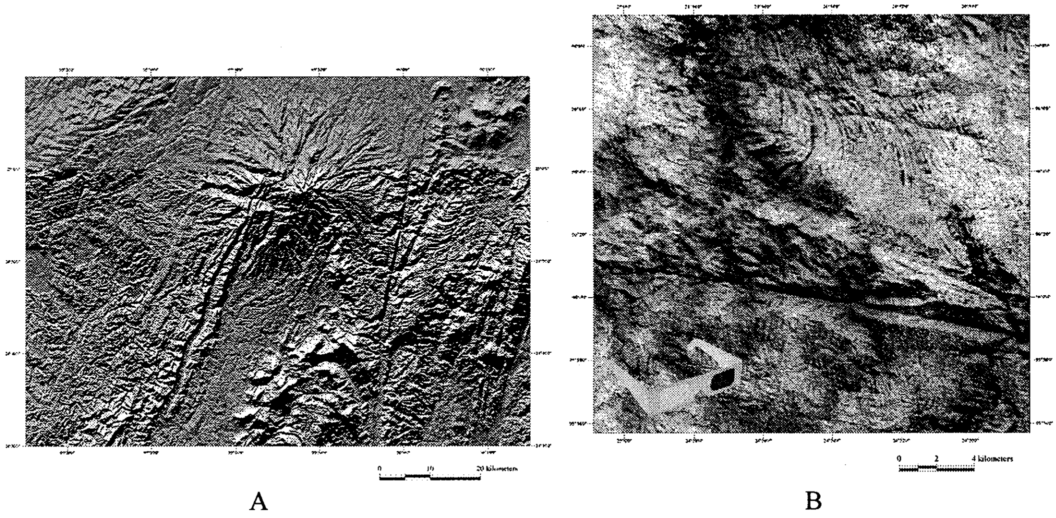

Fig. 4 (A) Pseudo color shade relief image created 270:0:325 (R:G:B) of Taungtonelone area, (B) The 3D anaglyph image of ASTER stereo pair. Use anaglyph glasses to see the three-dimensional aspect of the terrain and part of sagaing fault.

Anaglyph images were generated and found as the most suitable method. Anaglyph images have been generated using ASTER stereo pair image (15 meter resolutions). The image requires red/cyan anaglyph glasses for viewing in 3D and is in colour. The image has been orthorectified so can be used for purposes requiring spatial accuracy. 3D topographic surface views such as these provide an excellent tool for interpretation of surficial lineaments and bedrock geological features (Fig. 4B).

False color images are produced for manual lineament extraction because they increase the interpretability of the data. Different combinations of three bands are examined and the best visual quality is obtained with a false color image bands 7, 5 and 4 (in blue, green and red respectively) (Fig. 5). Although any of these techniques (or combination of more than one) can be used to extract lineaments, three different techniques are applied here in order to be sure that no lineament is missed in the area. The reason for this is that the area is not homogenous in term of the surface characteristics. It is believed that each method may enhance one aspect of the surface. Each process will generate a GIS layer that can be linked to other layers easily. Presence of multiple lineament maps, however, may result in confusion and complexity. To overcome this problem a single lineament map should be generated from the results of all these methods.

Fig. 5 Lineament interpretation result draped on Landsat 7ETM+ false color image bands 7, 5 and 4 (in blue, green and red respectively).

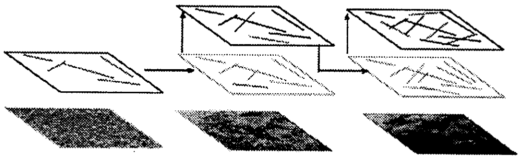

Fig. 6 Steps of combining the lineament maps generated by different methods.

The procedure for combining the lineaments obtained from all methods into one map is shown in Figure 6. Accordingly, here is always one output file which is overlaid every time on a different processed image. Following steps are applied for the generation of final map: (1) manually extracted lineaments are overlaid onto the same map, one map at a time. The order of the overlay analysis is not important during this process. The order used in this study is applied for this step. (2) Duplicated lineaments are erased from the map every time a new layer is added. Erasing of duplicated elements is performed by manual interpretation. In case of different lengths, the shorter lineaments and the roads are deleted. Lineaments patterns have been summarized using rose diagram, when lineament processing is completed, the final geological lineament file is also converted to a vector format (Fig. 7B). The stress vectors were used to predict orientations of different faults types for each model in accordance with the Andersonian theory of faulting (Park, 1988) (Fig. 7C).

According to image interpretation, lineaments with North and South orientations are longer and more distinct along the Sagaing fault and Igneous rocks. This direction coincides with the Sagaing main fault and they are right-lateral fractures. Lineament distribution and its general orientation are shown in Fig. 7. Major lineament trend can be summarized as NS, N50-70E, and N10-40E, under considering exaggeration due to imaging orientation. N50-70E lineament structure widely distributes and might be old structure before Tertiary sedimentation in the study area. N-S structure is the most dominant orientation, and is common to occur as longest lineaments more than 60 km. This structure concentrates especially around the central portion close to N-S trending Sagaing fault. N 10-40 E structure usually occurs as an aggregate of short lineaments less than 10 km and tends to accompany with longer N-S trending lineament. Some of these structures can be identified as dilational fault jog related to strike-slip faulting. Dilational fault jog is an aggregate of open fissure and/or sheared fracture. The lineaments described above are the younger lineaments covering most of the eastern part of the Wuntho massif. Lineaments with northwest and southeast orientations can be seen mainly in the southeastern region of Kawlin-Wuntho area. This orientation coincides with the direction of extensional fractures attended by the right lateral strike slip fractures and they are generally a normal fault.

The test points were selected using the grid system with equal distances of 16.5 km latitudinally and 16.5 km longitudinally. Figure 7A shows the grid model circle plan of lineament density calculation. The total number of grid points was 110, which appeared sufficient for a statistical analysis. The area of a unit circle is 855 km^2. After calculation of the lineament density values for each radius, the graphs for the relation between lineament density values and radius of the unit circles were constructed, from which the representative elementary area point was determined.

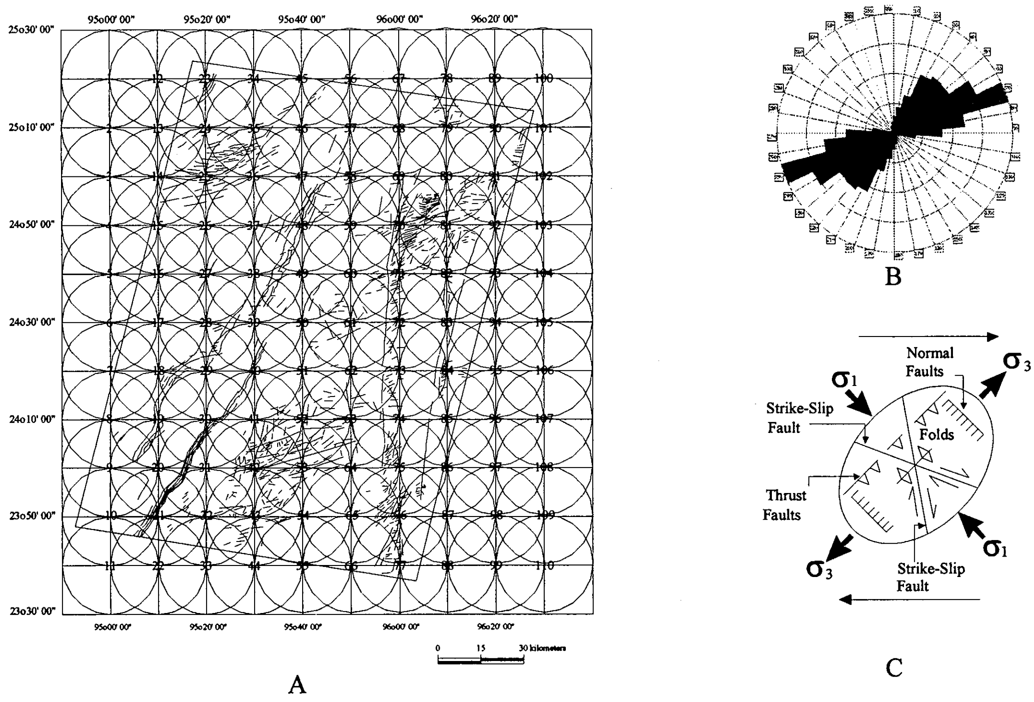

Fig 7. (A) The arrangement of circle plan for lineament density calculation (Actual 110 test points used to calculate) map for Taungtonelone area, northern Myanmar, (B) Rose diagram of the mapped lineament of Taungtonelone area, (C) Diagram representing the structural pattern produced by dextral simple shear (after Park, 1988).

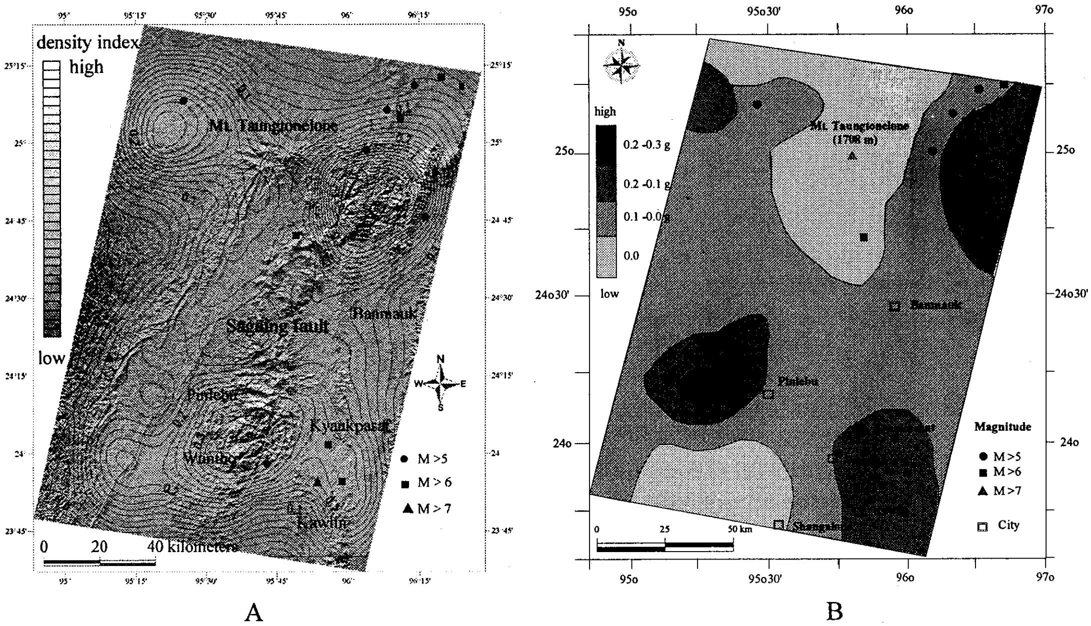

Fig. 8 (A) lineament density contour draped on shade relief image, (B) Horizontal ground acceleration earthquake hazard level map of Taungtonelone area, using known earthquake data set for the period 1912-2004 (modified from Dr. Maung Thein and U Tint Lwin Swe, 2006).

Figure 8 shows the lineament density contour for the lineament analysis of Taungtonelone area. The zone showing highest lineament density contour lies along the Wuntho-Kawlin massive area, Kyaukpasat area and east of Mt. Taungtonelone area. Lineament density contour also showed good correspondence with horizontal ground acceleration earthquake hazard level map computed from various seismic events of these areas. Eastern part of Mt. Taungtonelone area, there are high lineament density contour level and this region was high frequency and heavily affected by the earthquake.

4. Conclusion

The lineament density map can be used for the quantitative evaluation between lineaments and the earthquake risks monitoring for the future. If the average lineament density values for the whole study area are known, better or more accurate earthquake monitory map can be drawn using satellite image data. The lineament analysis can be convert one of power tools for earthquake study, complementing other ground based and satellite studies in the future. This could significantly increase the reliability of the earthquake forecast. The using of anaglyph image produced from ASTER image in the visual interpretation of the identification of the structural elements and the geomorphic characteristic has been found to be the most suitable method in this study. The using of the false color image of Landsat 7ETM+ and the pseudo colour shade relief images produced by the SRTM DEM also gives good results. It is possible to identify clearly the effects of the extensional tectonic on the satellite images by visual interpretations based on experience and knowledge.

This study is to be used for new recognition of seismic hazards and is expected to increase the awareness for disaster prevention. Fortunately, the proposed method does not require any special satellite program and can use any multi-spectral high-resolution images, such as obtained by ASTER, Landsat, etc., which makes it a very low cost. T. The lineament density method could be used not only for earthquake zone but also for mineral exploration. This observation also can be applied to other seismic fracture zone of mountainous area. The study has proved that the lineament high density areas are closely within seismic zones. Thus lineament density map can be used for the quantitative evaluation between lineaments and the earthquake risks monitoring for the future.

5. Acknowledgments

This paper was prepared for the 13rd CEReS International Symposium on Remote Sensing "Disaster Monitoring and Mitigation in Asia", held 29-30 October 2007, Chiba, Japan. The author would like to sincerely thank the organizing committee. We wish to thank the Editor and the reviewers of this manuscript. We are grateful to Dr Maung Thein and U Tint Lwin Swe, Myanmar Earthquake Committee. Mr. Paul Moiya Kia, Graduate School of Engineering and Resource Science, Akita University for detail and insight comments that greatly improved the original manuscript. The authors would like to thank Professor Ryutaro Tateishi and his students, Center for Environmental Remote Sensing, Chiba University, for discussions and the developing of image processing knowledge skills. The Consortium for Spatial Information (CGIAR-CSI) provided SRTM DEM data. The authors would like to thank the Global Land Cover Facility (GLCF) which kindly provided the Landsat 7ETM+ data of the study area.

Reference:

Arellano-Baeza A.A, Zverev, A.T, Malinnikov V.A. 2006, Study of changes in the lineament structure, caused by earthquakes in South America by applying the lineament analysis to the Aster (Terra) satellite data, Advances in Space Research 37, pp 690-697.

Bertrand, G. et al., 1998, The Singu basalt (Myanmar): new constraints for the amount of recent offset on the Sagaing Fault, Earth & Planetary Sciences, 327, pp 479-484.

Cotilla Rodriquez, M. O., Cordoba Barba, D. 2004, Morphotectonics of the Iberian Peninsula, Pure and Applied Geophysics, 161(4), pp 755-815.

Dr Maung Thein and Tint Lwin Swe, 2006, Seismic Zone Map of Myanmar (Revised Version, 2005), Prepared under the auspices of Myanmar Earthquake Committee)..

GIAC, 2000, Final Report of GIAC project.

Greenbaum D. 1985, Review of remote sensing applications to groundwater exploration in basement and regolith. Brit Geol Surv Rep OD 85/8, 36 pp.

Jordan, G. 2004, Terrain Modelling with GIS for Tectonic Geomorphology Numerical Methods and Applications, pp 18-24.

Moellering, H., and Kimerling, A.J. 1990, A new Digital Slope-Aspect Display Process, Cartography and Geographic Information Systems, 17(2): pp 151-159.

Park, R.G. 1988, Geological Structures and Moving Plates. Chapman & Hall, New York, 337 pp.

Seekins, L.c., and Boatwright, J. 1994, Ground motion amplification, geology and damage from the 1989 Loma Prieta earthquake in the city of San Francisco. Bulletin of the Seismological Society of America, 84: pp 16-30.

Stich, D., G. Alguacil, Morales J. 2001, The relative locations of multiplets in the vicinity of the Western Almeria (southern Spain) earthquake series of 1993-1994, Geophysical Journal International, 146(3), pp 801-812.

Vigny, C., Rangin, C., Socquet, A., 2001. GPS network monitors Sagaing fault, Myanmar. Eos Transactions Supplement 82 (20).

Validation of urban boundaries derived from Global population density data, MODIS and nighttime lights satellite imagery

* Alimujiang Kasimu A. Shalaby, and R. Tateishi

Center for Environmental Remote Sensing (CEReS), Chiba University 1-33, Yayoi-cho, Inage-ku, Chiba 263-8522 Japan
Tel (81)-43-290-2964; Fax: (81)-43-290-3857
E-mail: Alimkasim@gmail.com

Abstract

Global population density data compiled on a 30" X 30" latitude/longitude grid. Census counts were apportioned to each grid cell based on likelihood coefficients, which are based on proximity to roads, slope, land cover, nighttime lights, and other information. Population density data integrated with MODIS and nighttime light DMSP data have been proposed as a useful tool for monitoring urban expansion around the world, but determining appropriate thresholds for delineating cities remains a challenge. In this study we present a new approach. We used coarse resolution satellite data to delimit urban boundaries for cities with different level of urbanization and economic development, and compared the results against boundaries derived from fine-resolution Landsat ETM+ imagery and other existed continental scale urban map. Our comparison highlights population density data integrated with MODIS and nighttime lights DMSP data are good source for global urban mapping.

Key word: Urban mapping, population density data, MODIS, DMSP, Landsat ETM+

1. Introduction

Approximately half of the World population lives in urban areas. Urban areas are expanding rapidly in many parts of the world. 90% of urbanization is occurring in low-income countries, however, it is difficult to measure accurately rates of urban growth. While such information is more readily available for high-income countries, maps of settlements in low-income countries are often outdated, inaccurate or nonexistent.

Satellite remote sensing has long been a useful alternative for mapping the expansion of urban uses. However, common approaches remain problems. Imagery from fine-resolution sensors such as Landsat or SPOT provides a level of detail sufficient to distinguish urban from non-urban land uses in most cases. Unfortunately these sources are too expensive for most university researchers to acquire and process at continental scales. Imagery from coarse resolution sensors such as the nighttime lights DMSP data, are poorly registered, and exhibit "blooming" effects that inflate city boundaries (Elvidge et al., 1996). Recent coarse resolution global urban mapping from MODIS and GLC2000 were unsatisfactory, because of tedious process of training data collection. Population density data integrated with MODIS and nighttime lights DMSP offer a opportunity for easily and correctly mapping urban areas (Alimujiang et al., 2006) .

A major challenge for applying population density data with MODIS and DMSP imagery to delineate urban area is choosing appropriate thresholds. This paper describes ongoing efforts to produce reliable representations of urban areas at 1 km resolution, as part of a larger project of GLCNMO (Global Land Cover National Mapping Organization). The primary goal of this paper is to map GLCNMO urban land cover at 1km spatial resolution by Population density data, DMSP and MODIS-NDVI data. Three major tasks were involved in this study. First threshold population density data and MODIS – NDVI data based on continents with the reference of fine-resolution Landsat ETM+, then classified urban and not-urban class. The second task was to combine urban derived from population density with DMSP data and MODIS-NDVI data. Third task was to validating the final urban mapping with Landsat ETM imagery also other existed continental scale urban maps. Our objective is to contribute to the development of rules for deriving more accurate urban boundary information from population data, MODIS and DMSP. If such a rules can be developed, it will be more useful in monitoring the rate of urbanization around the globe.

2. Data and methods

2.1. Data

(1) Population density data: Global population data compiled on a 30" x 30" latitude/longitude grid. Census counts were apportioned to each grid cell based on likelihood coefficients, which are based on proximity to roads, slope, land cover, nighttime lights DMSP, and other information. This data downloaded following website (www.ornl.gov/sci/landscan/index.html).
(2) DMSP-OLS data: The files are cloud-free composites made using all the available archived DMSP-OLS smooth resolution data for calendar years. The products are 30 arc second grids, spanning -180 to 180 degrees longitude and -65 to 65 degrees latitude. A number of constraints are used to select the highest quality data for entry into the composites. (http://www.ngdc.noaa.gov/dmsp/maps.html)
(3) MODIS-NDVI data: MODIS/Terra Nadir BRDF Adjusted Reflectance 16 Day L3 global 1km SIN grid product (MOD43B4NBAR) data (MODIS) with seven bands (band 1-7) were used. MODIS data in 2003,starting from 3 December 2002 to 16 December 2003, were acquired from USGS in 10d x 10d of Sinusoidal format. These data were then mosaic and reproject into Geographic Latitude/Longitude. NDVI was calculated using following formula.NDVI= (NIR-Red) / (NIR+Red). A Maximum Value Composition (MVC) was then applied to all NDVI images with the aim of selecting pixels less affected by clouds and other atmospheric perturbations (Holben, 1986).
(4) Validation data: Landsat Enhanced Thematic Mapper (ETM+) images, which were reasonably close in date to the time frame of the Population data imagery, were acquired from Global Land Cover Facility at the University of Maryland (http://glcfapp.umiacs.umd.edu/). Visually interpolate ETM data was compared with 1km resolution GLCNMO urban map.
(5) Other urban map: Three global urban maps were obtained for comparing. The Digital Chart of the World's (DCW) populated places was developed originally for the US Defense Mapping Agency (DMA) using DMA data. DCW coverage is represented as polygons at 1:1000000 scales(Danko, 1992). A global land cover classification at a spatial resolution of 1 km, using 14 years of imagery from the NASA/NOAA Pathfinder Land (PAL) Advanced Very High Resolution Radiometer (AVHRR) data set (Hansen et al., 1998) was downloaded from the Global Land Cover Facility, University of Maryland (URL: http://www.glcf.umiacs.umd.edu/data/landcover/), and the "urban" land cover class extracted. GLC2000 (Global Land Cover 2000) at a spatial resolution of 1km was obtained from the website (http://www-gvm.jrc.it/glc2000/Products/)

2.2. Methodology

2.2.1 Delineating Urban lands in Landsat ETM+ data

We identified urban lands in our study areas by performing the commonly used supervised maximum likelihood classification on each. Performing this classification without the use of a priori probabilities, we initially produced as many as 10 classes of land cover. We then drew on our knowledge of the study areas and additional published maps to merge these classes into urban and non-urban land use classes.

2.2.2 Processing population density data, MODIS and DMSP

Different thresholds were given population density data, MODIS-NDVI and DMSP, respectively based on continents and regions with the reference of fine resolution Landsat ETM+. When using population density data, higher threshold area required with higher levels of population density continents. Lower thresholds are required lower levels of population density with higher levels of economic development places. When applying NDVI data, higher threshold are given to the urban with low vegetation cover, lower thresholds are given to the urban with higher vegetation cover.

2.2.3 Integrating population density, MODIS and DMSP

Nighttime lights DMSP data used to exclude small villages area in the urban map derived from population density data. MODIS-NDVI applied to exclude large parklands amidst urban areas (i.e. Golden Gate Park or Mount Tamalpais in San Francisco and Kamakura area in Tokyo) or mixed agricultural–industrial zones (Fig. 1).

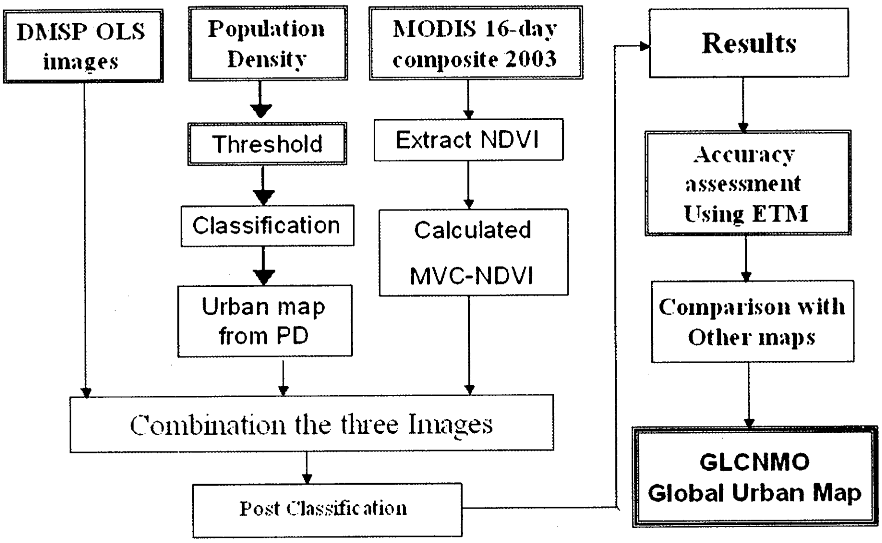

Fig. 1 Flow chat of methodology

3. Result and discussion

Using the ETM-derived urban land use classes as a standard, we performed an accuracy assessment on the GLCNMO urban boundaries images to produce confusion matrices summarizing the GLCNMO urban by integration population density data with MODIS and DMSP is acceptable or not. We also compared the overall land area falling within the GLCNMO urban boundaries with the Landsat ETM-derived area, to draw attention to difference in shape and position. The result of these comparisons urban derived from ETM with GLCNM urban are summarized in fig.2.

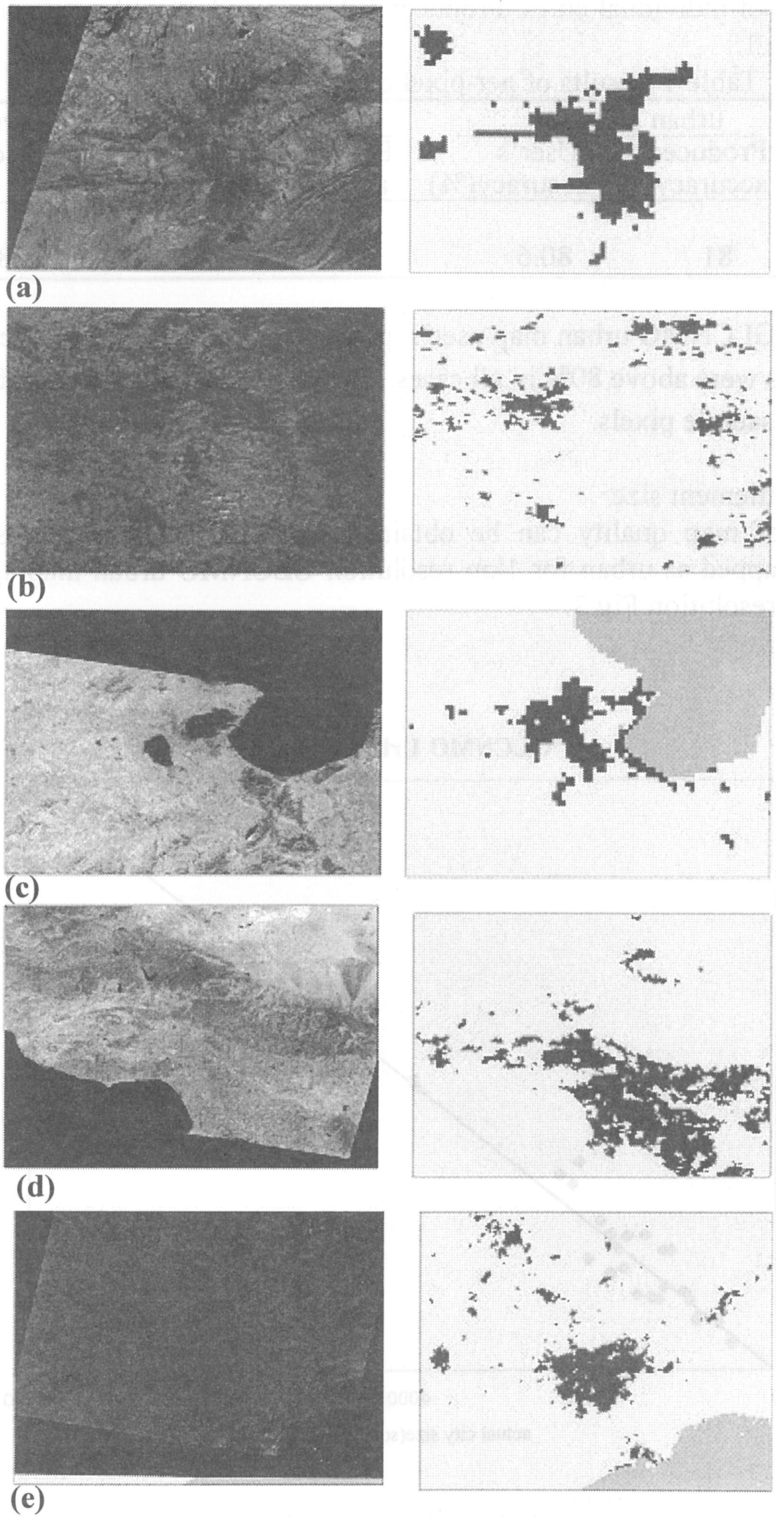

Fig.2 Landsat ETM images and urban boundaries derived from GLCNMO
(a) Urumqi, China in Asia. (b) Birmingham, UK in Europe. (c) Tunis, Tunisia in Africa (d) Los angels, USA in North America. (e) Sao Paulo Bazil in South America

3.1 per-pixel comparison

The per-pixel agreement between the Landsat ETM+ data and GLCNMO urban land cover was examined at the level of individual cities. Producer's, User's and overall accuracies were calculated and displayed in table.1.

Table.1 Results of per-pixel comparison

Urban map	urban class		Non-urban class		overall Accuracy (%)
	Producer's accuracy(%)	User's accuracy(%)	Producer's accuracy(%)	User's accuracy(%)	
GLCNMO	81	80.6	93	93.2	89.8

Table.1 result shows GLCNMO urban map user's, producer's and overall accuracies for both urban and non-urban classes were above 80% in all cases. This indicates accurate classification of both urban and non-urban sample pixels.

3.2 Comparison of settlement size

A second measure of map quality can be obtained from estimates of city size. This method compares the area mapped as urban for 1km resolution GLCNMO urban map against the Landsat ETM+ data at a 30m resolution Fig.3.

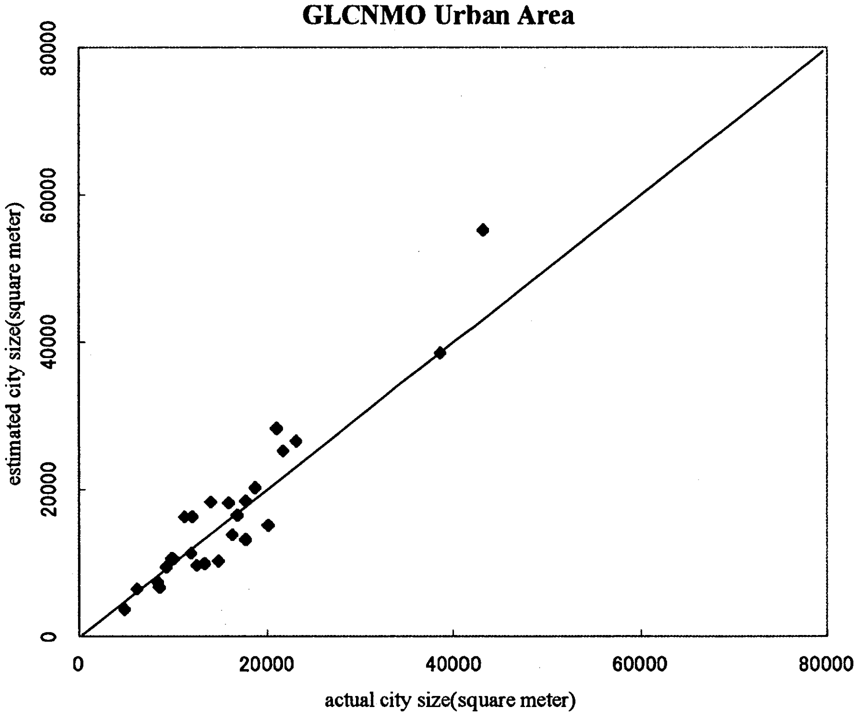

Fig.3 a comparison Landsat ETM-estimated settlement size against estimated settlement size by GLCNMO

The location of each of the points above or below the one-to-one line on the scatterplots indicates whether an urban area has been overestimated or underestimated. Fig.3 shows that urban area is estimated accurately for many areas, there is overestimated in some cases and underestimated in others by GLCNMO.

4. GLCNMO urban map comparison with other urban map

Effective use of classified maps requires thorough analysis and quantification of map quality. Each raster 1 km urban map (DMSP-OLS, GLC2000, DCW, GLCNMO) was coregistered to uniform Goode`s Interrupted Homolosine projection. Fig 4 shows a subset of each of the four maps under test for Cheng du China.

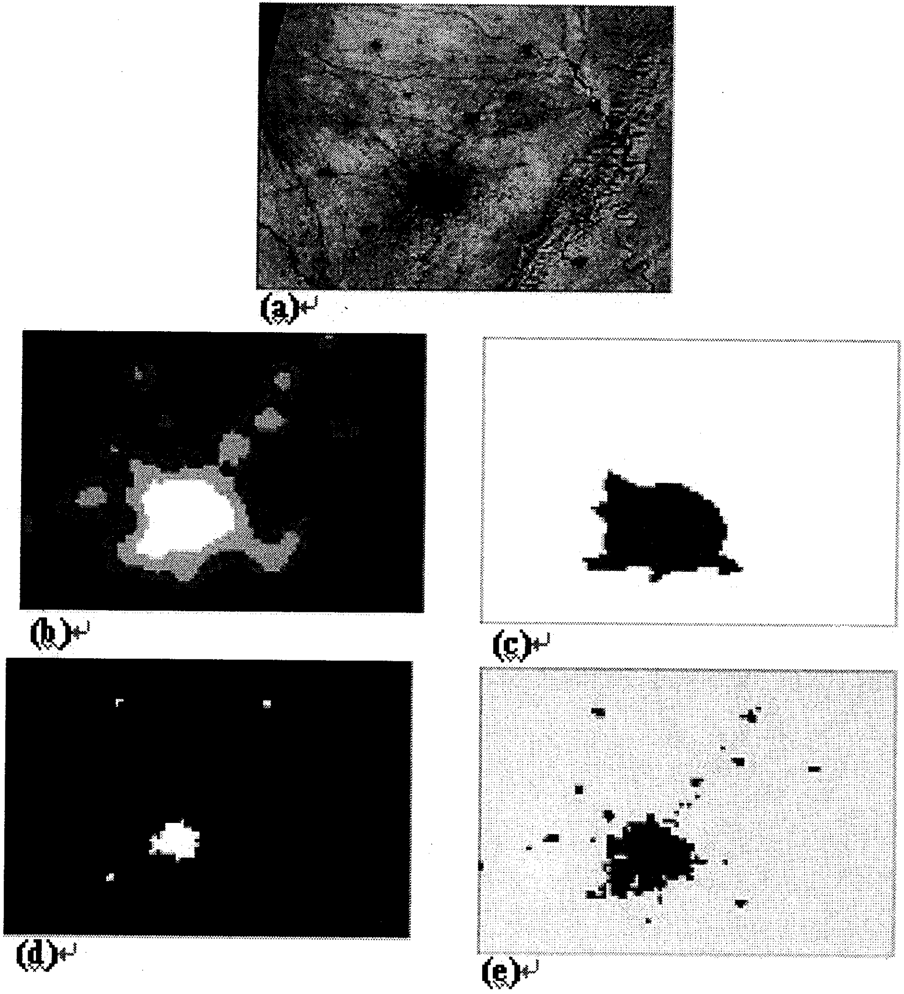

Fig.4 Chengdu mapped by the four settlement maps under test, with the high resolution Landsat ETM. The Chengdu area showing (a) 30m Landsat imagery (urban areas appear purple); (b) the nighttime lights DMSP data (blue boundary represents commonly used threshold); (c) the urban data from the GLC2000; (d) the urban map from DCW; and (e) GLCNMO Urban map produced in this research

Fig.4 shows that nighttime lights DMSP data overestimate urban area (fig.4-b), the GLC2000 data, overestimated some area and underestimated other (fig.4-c), the DCW data underestimated urban area. And GLCNMO urban map achieves the closest and least biased fit to the "true" city size.

4. Conclusion

These results demonstrate that, for cities at different levels of development, quite different thresholds are required when using population density imagery to delineate areas that approximate the urban areas seen in Landsat TM imagery. Higher thresholds are required with higher levels of population density continents. Lower thresholds are required lower levels of population density with higher levels of economic development places. We have shown that it is not possible to settle upon a single threshold that can be used to delineate urban boundaries across the board, it leaves open the possibility that thresholds can be chosen for continents at comparable levels of Population density, development and urbanization.

Compared with any other existed 1km resolution continental scale urban map, GLCNMO is more accurate. The population density data integrate with nighttime lights DMSP and NDVI offers a useful perspective for monitoring the extent and level of urbanization at a global scale.

Reference

[1] Alimujiang Kasimu Ryutaro Tateishi 2006 Experimental survey in China for global urban mapping. Proceedings of the 41th Conference of the remote sensing society of Japan, pp.180-181.

[2] Danko,D.M. , 1992 The digital chart of the world project. Photogrammetric Engineering & Remote Sensing,58,pp.1125-1128

[3] Elvidge,C.D.,K.E.Kihn, and E.R.Davis, 1996. Mapping city lights with nighttime lights DMSP data from the DMSP-OLS operational linescan system, Photogrammetric Engineering & Remote Sensing,63,pp.727-734

[4] Hansen,M., DeFries, R., Townshend, J.R.G., & Sohlberg, R. 1998. 1km land cover classification derived from AVHRR. College Park, Maryland; The Global Land Cover Facility.

[5] HOLBEN, B.N. , 1986: Characteristics of maximum value composite Images from temporal AVHRR data. International Journal of Remote Sensing., 7,pp. 1417-1434.

Measurement of NO_2 and aerosol in the atmospheric pollution using differential optical absorption spectroscopy (DOAS) with an obstruction flashlight

Ippei Harada[1], Masashi Miyazaki[2], Daisuke Kataoka[3], Hiroaki Kuze[4]
Toshiaki Ichinose[5]
[1,2,3,4] Center for Environmental Remote Sensing , Chiba University, Chiba, Japan
[5] National Institute for Environmental Studies, Tsukuba, Japan
E-mail: [1] ippei@restaff.chiba-u.jp, [4] hkuze@faculty.chiba-u.jp

Abstract

The Cheong-gye stream flowing from west to east in the city center of Seoul was functioned during about half a century as a busy highway after it had been covered with concrete in 1950's. However, the problem of safety by the aged deterioration was pointed out, and the conversion to the space of water and green was tried. The restored river was opened by the common people in October, 2005 after about two years of the restoration construction. During the execution of a large-scale city environmental improvement business that doesn't see the example in the world where an old river in the Seoul city is restored and a water and green space creates it, the purpose of this study is twofold. First, we compare the long-path result with the point data simultaneously measured at ground-based monitoring stations. Second, we analyze quantitative evaluation of the effect of Cheong-gye stream restoration on air quality.

We report on the atmospheric pollution monitoring in Tokyo of Japan and Seoul of South Korea during the summer 2007. By means of the differential optical absorption spectroscopy (DOAS), average concentrations of NO_2 particles in the atmospheric pollution have been measured. The air quality standards of NO_2 around Cheong-gye stream was more than 50 ppb during 2001 to June 2005. However, it is worth observing atmospheric pollutant species, since the value of NO_2 around Cheong-gye stream has been low after restored a Cheong-gye stream.

1. Introduction

In recent years, the atmospheric pollution in Japan, as a whole, has been improved as compared with situations couple of decades ago. However, we still have problems in places such as urban roadside areas, where the environmental standards have not been achieved. In this respect, efforts are required for monitoring anthropogenic air pollution, especially the combustion products such as nitrogen oxides and particulate matters.

The main pollution species in urban areas in Japan is the nitrogen dioxide (NO_2) and suspended particulate matter (SPM), usually referred to as PM_{10}. In the monitoring of such species, conventional point sampling at ground stations leads to concentrations for local environments. It is also valuable to obtain additional information of regional concentrations measured over a certain distance, e.g., several hundred meters to several kilometers. Differential optical absorption spectroscopy (DOAS) in the visible and near-UV region is more suitable to monitor horizontally averaged concentrations of pollutants (Edner *et al.*, 1993).

In the conventional long-path DOAS method, a continuously emitting light source is employed, and the source (or occasionally a retroreflector) is placed at a certain distance from the observation site. The use of aviation obstruction lights makes it possible to employ a simple detection system that consists of a telescope and a compact CCD spectrometer. Our group in Center for Environmental Remote Sensing, Chiba University (CEReS) reported a novel DOAS method that is based on a white flashlight source and a compact CCD spectrometer.(Yoshii *et al.*, 2003). In Japan, it is mandatory for tall constructions (higher than 60m) to operate highly illuminant (more than 2×106cd) white flashlights during the daytime that are detectable in every direction from several kilometers away.

The purpose of this study is twofold. First, we compare the long-path result of DOAS measurement with the point data simultaneously measured at nearby ground-based monitoring stations. We report on the recent results in Tokyo and Seoul. Both measurements were performed as part of air-monitoring campaigns of a National Institute for Environmental Studies (NIES) team. Second, The aim of the Seoul measurement was to evaluate the effect of Cheong-gye stream (Cheonggyecheon) restoration on the regional air quality.

2. Study area and Experiment

2.1 Study area

Seoul City is composed of 25 administrative districts. The area of the city is about 605km^2. The scale of Seoul City is equal to Tokyo City that is about 621 km^2. The population of Seoul City is about 10 million, and which is more than the population of the Tokyo by 2 million in 2000. The highway over the Cheong-gye stream was removed and the stream was finally restored on October 1st, 2005. The study area located near Cheong-gye stream. In two years time from then, the total number of visitors to the restored Cheonggycheon area has exceeded 56 million. An average of 53,000 a day visited the stream on weekdays and 125,000 during weekends and holidays.

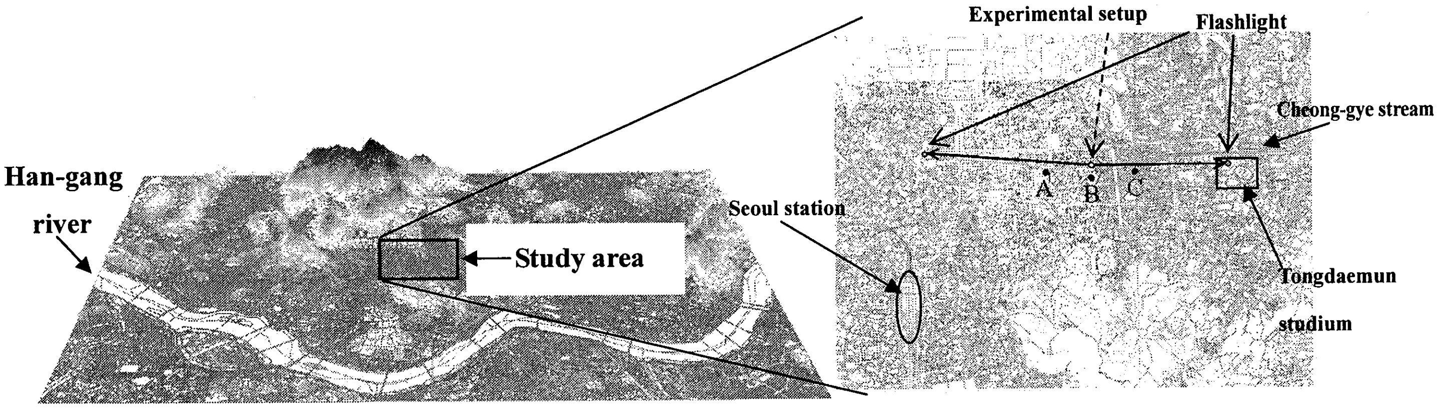

Fig. 1　Study area (Seoul city)

2.2 Experimental method

Fig. 2 shows a schematic of the experimental setup in the central Tokyo. An astronomical telescope (Meade, DS-115), with an aperture diameter of 115 mm and a focal length of 910 mm, is employed to focus the image of a point light source located at a far distance. The image is formed near the eyepiece location (the eyepiece itself is removed from the telescope) where the entrance slit (1 mm high and 5 μm wide) of a CCD spectrometer (Ocean Optics, USB2000) is placed. The CCD consists of 2048 elements and is sensitive in a wavelength range of

200-800 nm, resulting in an average resolution of 0.3 nm/pixel. This CCD spectrometer is composed of a fixed grating and a linear CCD array with a mechanically stable, crossed Czerny-Turner design. No moving parts are incorporated, resulting in high reliability and compactness (89 mm wide × 63 mm deep × 34 mm high). The CCD gate duration is set at 300 ms in the experiment. Between successive gate periods, there exists a time lag of 7 ms, in which each spectral data is sent to a personal computer (PC) through the universal serial bus. The data acquisition can be attained successfully even when no trigger (synchronous with the flashlight) is applied to the CCD spectrometer, though this relatively long gate time as compared with the flashlight duration causes somewhat increased amount of the background skylight.

We automatically achieved the discrimination of data with and without the flash event by comparing the light intensity integrated over a wavelength region of 400 – 450 nm, used for the present NO_2 detection. The spectral difference between the flash and the no-flash events exhibits the net strobe intensity after the long-path transmission in the urban atmosphere. Fig.2 shows optical thickness of each component detected by the DOAS spectrometer. The absorption of NO_2 gas species gives a structure of the order of 0.2 in terms of the optical thickness. In order to extract the NO_2 concentration, contributions from molecules and aerosol particles can be subtracted by simply applying a linear fit to the back-ground. Another important aspect from this figure is that, by measuring the light intensity, it becomes feasible to evaluate the aerosol contribution in the DOAS signal itself.

For the measurement in the central Tokyo, we made use of a xenon strobe install at a steel tower in Jujyo as a light source. The lamp height is about 130m above the ground level. According to the regulation, the light intensity is diminished at dusk and dawn, and during the nighttime blinking red lights replace the flashlights. Thus, the DOAS measurement is limited to the daytime, around 5 a.m. to 7 p.m. during the summer. In the north direction 4.8km from the source, a DOAS system was installed in Four Seasons Hotel Tokyo at Chinsan-so. For the measurement in Seoul, we made use of projector as a light source. The lamp height is about 70m above the ground level. The DOAS measurement with the light source of projector is used during the daytime to nighttime. In the east direction 1.4km from the source, a DOAS system was installed in a Cheong-gye stream at Cheongae-3ga (Fig .1).

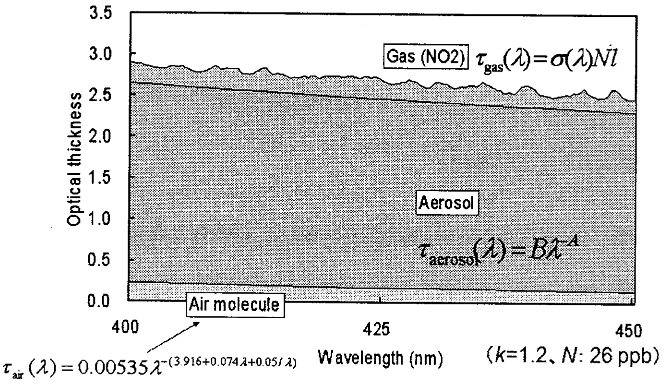

Fig. 2 Optical thickness of each component

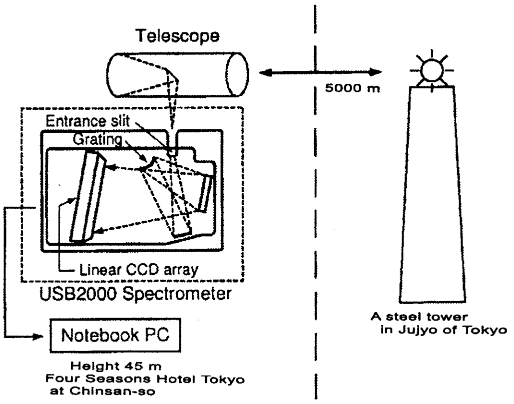

Fig. 3 Experimental setup for measuring NO_2 in the central Tokyo

3. Result

3.1 DOAS measurement with an obstruction flashlight in the central Tokyo

In Tokyo, the obstruction flashlight was used as a light source. The distance was 4.8 km from the observation site. The diurnal change of NO_2 concentration was measured during 10-13 August 2007 (Fig .4). A reasonable correlation is found between the result of the long-path measurement and the data from a ground station below the optical path. The ground data obtained every hour. The temporal resolution of the DOAS data is five minutes, much shorter than the sampling measurements. The DOAS measurement was limited to the daytime, and the resulting NO_2 concentration is obviously lower than that from the sampling measurement. Since the measurement was during hot, sunny days in August, we had expected a well-mixed boundary layer in the urban atmosphere. The present results, however, suggests that the concentration of pollution can exhibit local inhomogeneity, particularly when the exhaust from motor vehicles was the dominant cause of the pollutants. From the ground sampling measurement, it is also noteworthy that the NO_2 concentration was much higher during the nighttime. This is presumable because of the rush hour on the regional highways due to the family reunion in this particular season.

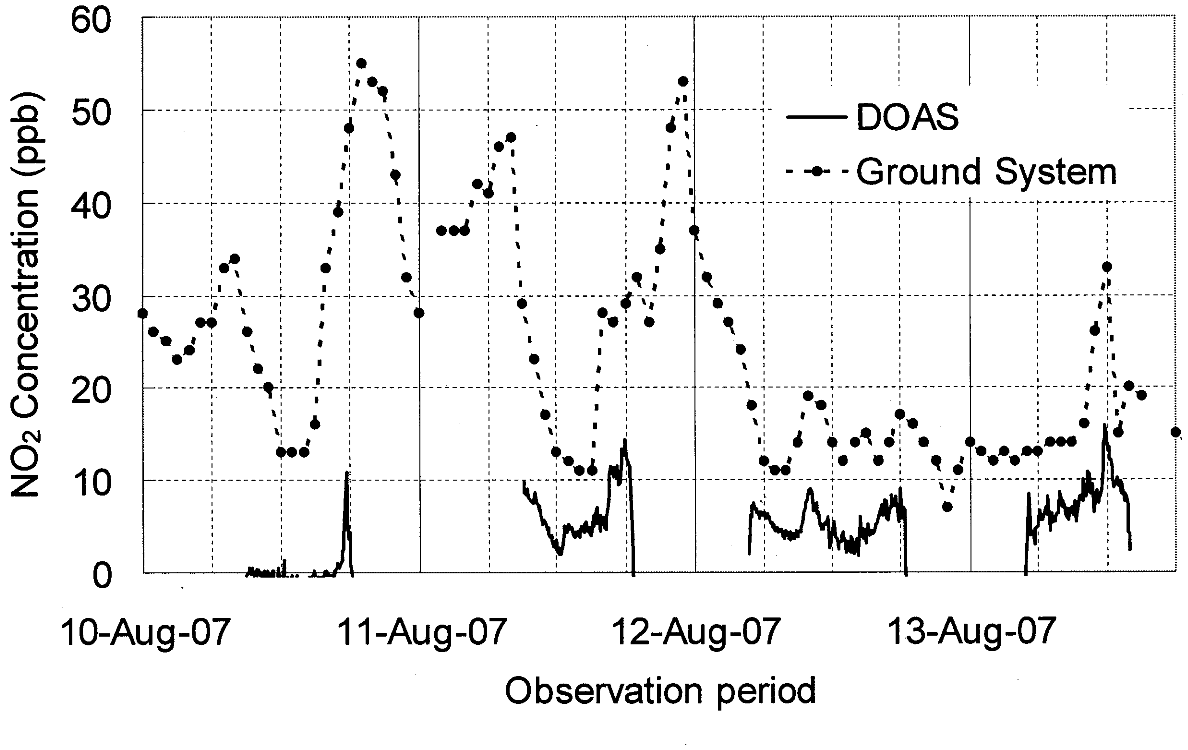

Fig. 4 The DOAS measurement in comparison with the ground sampling data in the central Tokyo

3.2 DOAS measurement with a projector flashlight in the restoration zone, Seoul

The projector flashlight was used as a light source and the distance of the light source and observation was 1.4km. Power consumption of the projector is 220 W, and the emission covers the visible wavelength. Fig. 5 shows the data from nearby ground stations (operated by the municipal environmental department and available on the Internet). The value of NO_2 is more than 50 ppb during 2001 to 2005. However, the value has decreased after the restoration of stream in October 2005.

For the observation in Seoul measurement was set up at about 30 m height. The projector flashlight was used as a light source and the distance of the light source and observation was 1.4km. The projector flashlight was set up at about 70 m height. The ground data obtained every hour. The temporal resolution of the DOAS data is five minutes. Therefore, the value of DOAS and Ground system data were same (Fig. 6).

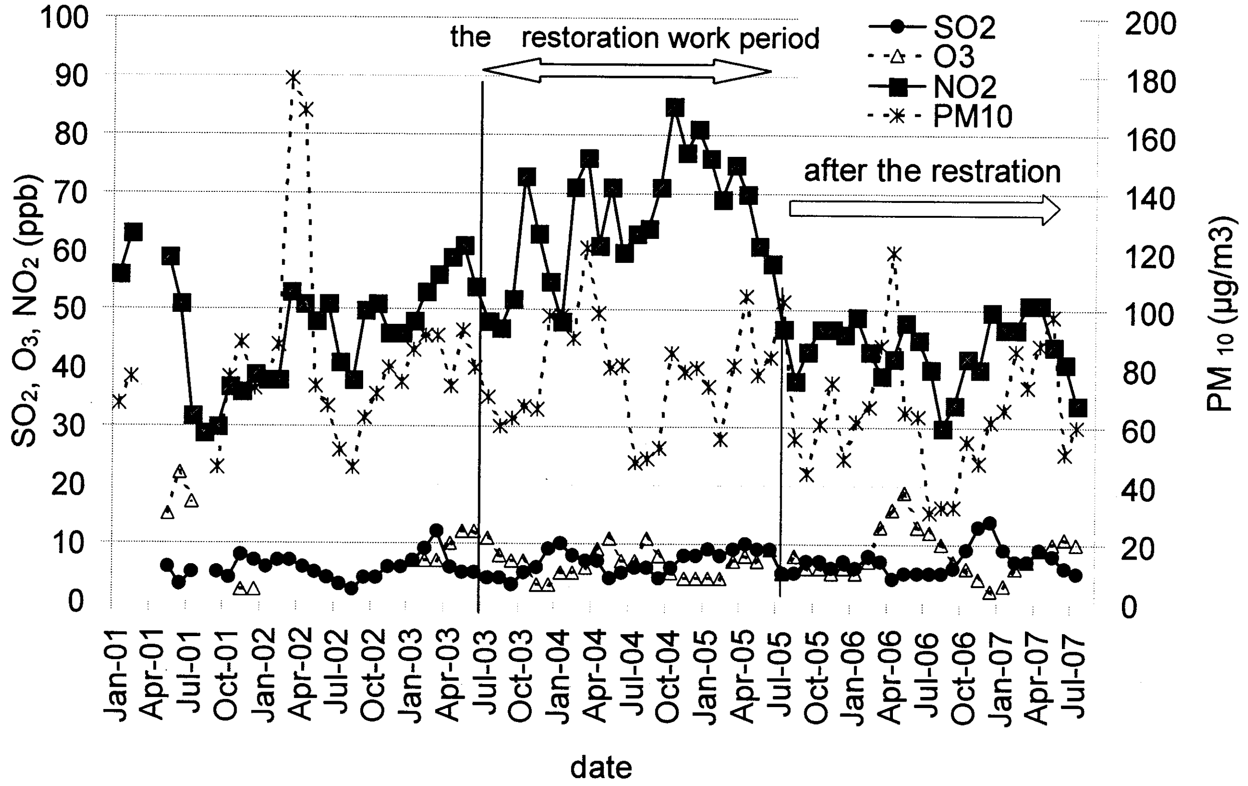

Fig. 5 Monthly average of atmospheric pollutant species around the restoration zone (Cheonggye 4ga of Ground system)

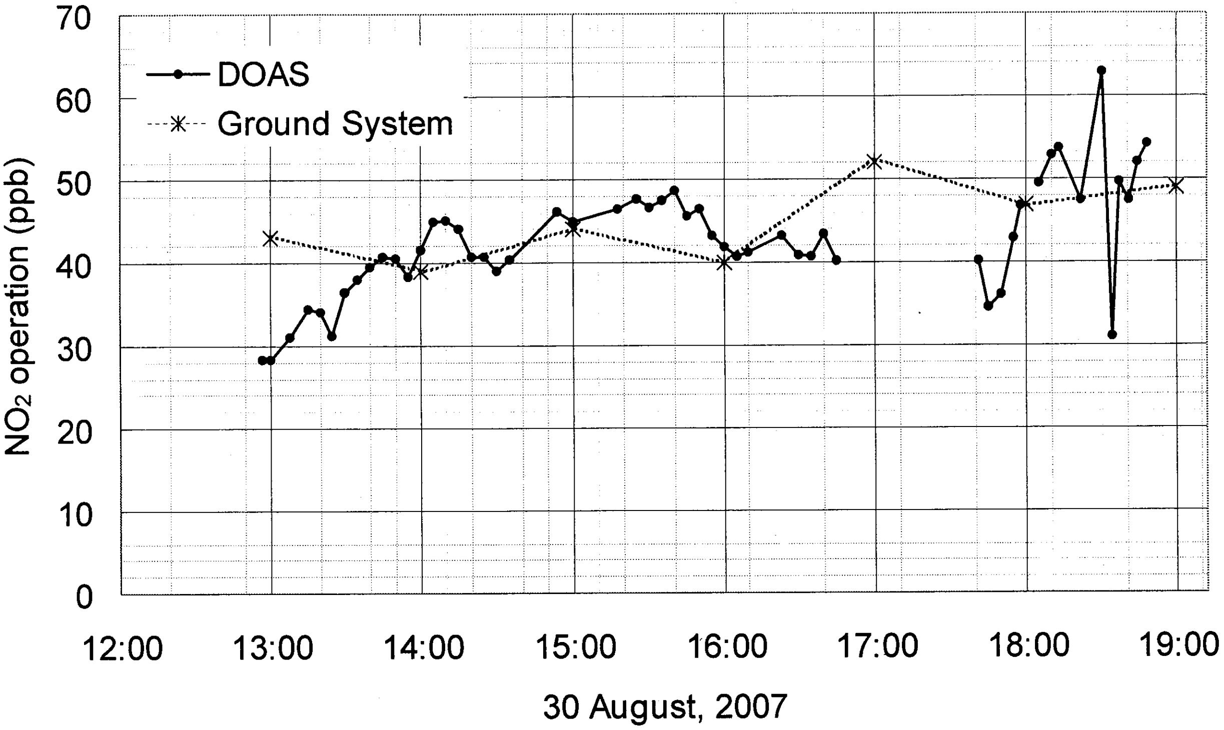

Fig. 6 The DOAS measurement in comparison with the ground sampling data in Seoul

4. Conclusions

For the observation in Tokyo, the NO_2 concentration from the DOAS measurement was much lower than the ground sampling result, though the temporal behavior of the concentration was similar between the two methods. We need further studies to elucidate the local or vertical inhomogeneity of the pollution distribution in the city areas. For the observation in Seoul measurement, we have obtained a reasonable agreement between the DOAS and ground-sampling measurements. The projector light provides a favorable light source for the DOAS measurement for both daytime and nighttime.

Further long-term monitoring is planned to study the effect of restoration.

References

Edner, H., Ragnarson, P., Spannare, S., and Svanberg, S. (1993): Differential optical absorption spectroscopy (DOAS) system for urban atmospheric pollution monitoring, Applied, Optics, 32, 327-333.

Fuqi, S., Kuze, H., Yoshii, Y., Nemoto, M., Takeuchi, N., Kimura, T., Umekawa, T., Yoshida, T., Hioki, T., Tsutsui, T., and Kawasaki, M. (2005): Measurement of regional distribution of atmospheric NO_2 and aerosol particles with flashlight long-path optical monitoring, Atmospheric Environment, 39, 4959-4968.

Yoshii, Y., Kuze, H., Takeuchi, N. (2003): Long-path measurement of atmospheric NO_2 with an obstruction flashlight and a charge coupled device spectrometer, Applied Optics, 42, 4362-4368.

Application of JERS-1 SAR Data for Tropical Forest Cover Mapping

M. Mahmudur RAHMAN[1] and Josaphat Tetuko Sri SUMANTYO[2]
[1, 2] Microwave Remote Sensing Laboratory, Center for Environmental Remote Sensing, Chiba University
1-33, Yayoi, Inage, Chiba 263-8522 Japan
E-mail: [1]mahmud@restaff.chiba-u.jp (Corresponding author)

Abstract

Monitoring of tropical forest cover is important because it is changing in many parts of the world. Synthetic Aperture Radar (SAR) is a useful tool to delineate the forest, as it can penetrate cloud, which often hinders the use of optical remote sensing in the tropics. The study area is located in the tropical forest region of south-eastern Bangladesh. The research used Japanese Earth Resource Satellite 1 (JERS-1) Synthetic Aperture Radar (SAR) imageries of 1997. Landsat Enhanced Thematic Mapper Plus (ETM+) imagery of 1999 assisted the interpretation procedure. Filed verification was done in 1998-1999. SAR imageries were geo-coded using previously rectified Landsat ETM+ pan image. Speckle noises on the imageries were removed by Lee-Sigma Filter. Three SAR scenes (Path/row: 144/264, 144/265, 145/264) were mosaiced. Relative image-to-image radiometric normalization was used to reduce the anomaly due to the differences in brightness before making the mosaic. The use of both SAR- intensity and texture image could separate forest from agriculture, shrimp farms, water and bare soil. Field-verification and the use of ETM+ optical image could differentiate eight different forest types (primary and secondary forest, bamboo, shrubs, plantation with indigenous species, Teak, Rubber and Acacia) but the use of only JERS-1 SAR image this was not possible. Finally, forest cover map prepared for the study area.

Key words: SAR, Tropical forest, Classification, Mapping

1. Background

Forest is the source of wood for energy, construction material, pulp and paper and many other versatile uses over centuries. Since the beginning of industrial revolution forest has been cleared in many parts of the world for industrial input and building materials. Population growth has also adversely affected the forest area; settlements and agricultural farmlands have replaced many forests. Until the late nineteenth century deforestation and forest degradation mostly took place in the temperate regions. Today, forest cover in the developed countries is still increasing slightly; between 1980 and 1995, there was an average increase of 1.3 million ha per year (FAO 1999). In the recent decades, many temperate forest stocks are expanding through the establishment of plantations, the re-growth of forests on abandoned agricultural lands, and increased growing stock of forest biomes. In contrast, tropical forests are dwindling; the rate of tropical deforestation is estimated to be 15.5 million per year in the period of 1980-1995 (FAO 1999).

As a consequence, periodic monitoring of forest is important. Application of optical sensor for continuous forest inventory often faces difficulties due to cloud coverage. On the other hand, Synthetic Aperture Radar (SAR) is a useful tool for monitoring of forest cover since it can penetrate the cloud. The objectives of this investigation are to (i) prepare forest cover map using Japanese Earth Resources Satellite-1 (JERS-1) SAR data and (ii) develop visual interpretation key for land cover interpretation using SAR data for south-eastern Bangladesh. Studies were conducted to prepare forest map using optical data (i.e. Rahman and Csaplovics 2001).

2. Literature Review

Many studies have used SAR for land cover and landuse mapping. Shuttle Imaging Radar-A (SIR-A) in association Landdsat Multispectral Scanner (MSS) data have been used to prepare a thematic map of south of Tianjin, north China (Jiyuan *et al.* 1986). The investigation interpreted nine different land covers and landuses: irrigated land, dry land, vegetable plot, orchard, pond, river and canals, residential area, railway and highway. Visual interpretation map was prepared from SIR-A data of Pensacola, Florida (Lo 1988). The investigation could separate cropland, built-up area and highway.

Forest was separated from non-forest area using multi-temporal C-band European Resource Satellite (ERS) SAR data on a range of test sites in the United Kingdom, Finland and Poland (Quegan *et al.* 2000). The study applied a threshold value for backscatter coefficient (dB) to distinguish forest from non-forest area. A knowledge-based classification using a hierarchical decision rule was applied to classify four different types of vegetation (Short Vegetation, Broadleaf, Upland Conifer and Lowland Conifer) and flat surface in northern Michigan (Dobson *et al.* 1996). The investigation used ERS-1 and Japanese Earth Resource Satellite-1 (JERS-1) data. The classification result was compared with classification based on air-photo interpretation.

Multidate three-frequency polarimetric AIRSAR data was applied for forest type mapping in the Tanana river flood-plain, interior Alaska using a maximum-a-posteriori Bayesian classifier (Rignot *et al.* 1994). Open water of rivers and lakes and five vegetation types were separated, dominated by White Spruce, Balsam Poplar, Black Spruce, Alder/Willow Shrubs and Bog/Fen/Non-forest Vegetation. Forest cover of East Kalimantan was mapped from L-band Shuttle Imaging Radar-B (SIR-B) data (Ford and Casey 1988). Five cover types: Tidal Forest, Swamp, Coastal Lowland Forest, Wetland and Clear-cut Areas were mapped but there was no attempt to prepare forest map with microwave data in the region.

3. Study Area

The study area is located at southern Chittagong, which is in the south-eastern part of Bangladesh. The area corresponds to the selected parts of three scenes (144/264, 144/265 and 145/264) of JERS-1 SAR image. The size of the study area is about 3000 sq. km (62 km x 47 km). It covers 21°24′to 21°50′ N Latitude and 91°48′ to 92°15′ E longitude (Figure 3.1).

The area is characterised with a sub-tropical monsoon climate with three distinct seasons per year: the pre-monsoon hot season from March through May, rainy monsoon season which lasts from June through October, and a cool dry winter season from November through February. Summer temperatures range from 26° to 32° C and winter temperatures 18° C to 29° C. Monsoon season starts in June and ends in October and accounts for 80% of the total rainfall. The average monthly rainfall varies from 400-500 mm in the monsoon period (June to October) to 100 mm in the dry period.

The forests of the study area are classified as tropical wet evergreen forests and tropical semi-evergreen forest (Champion *et al.* 1965, Figure 2). In the regional context the Chittagong flora differs from the Eastern Himalayan flora by the absence of Sal (*Shorea robusta*) and that from Myanmar by the absence of Teak (*Tectona grandis*). The outstanding feature of the forest vegetation is the frequent occurrence of the general Dipterocarpus, Quercus and Eugenia (*Syzygium* spp) (Baten 1969).

Since all the accessible areas were transformed to shifting cultivation, virgin forests are seldom noticed. Present crop mostly consists of secondary re-growth, which is still in the process of succession to the climax evergreen type. This process of succession is often influenced by the continuous human disturbance and thus leads to a drier scrubby forest or to a savannah in many areas (Khan 1979).

The Dipterocarps are the characteristic feature of evergreen stratum. A certain amount of deciduous species like Anacardaeous, Swintonia is often predominating. Sterculiaceae, Artocarpus and Sygigium those generally form an important part of the upper canopy are often present. Sometimes bamboo appears in several places when upper canopy is disturbed. Bamboo is typically absent in the virgin forests where canes and palms are the main woody monocotyledons. Tree ferns sometimes occur but epiphytes and ground-ferns are frequent. In certain areas, the gregarious occurrence of several Dipterocarpus species is common in top canopy with a seldom occurrence of any other species (Khan 1979).

The main characteristic of semi-evergreen forest is the dominance of appreciable proportion of deciduous species in the top canopy. The canopy is correspondingly lighter during the period of minimum rainfall (November to March) because of shedding leaves. Epiphytes, climbers and bamboos are often present in the lower canopy, which later in some extent are replaced by canes and palms in climax evergreen formation.

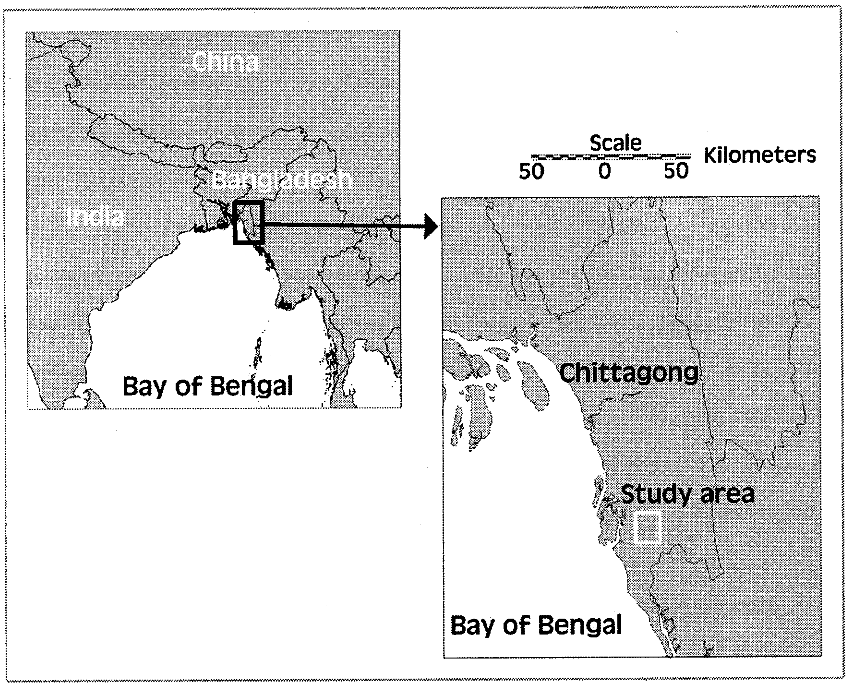

Figure 1. Location of the study area

Figure 2. Tropical wet evergreen and semi-evergreen forest of the study area (photograph was acquired during 2002-2003)

4. Methodology

The study used (i) JERS-1 SAR data of path/row: 144/264 (08-02-1997), 144/265 (08-02-1997) and 145/264 (09-02-1997) and (ii) Landsat ETM+ images of 135/045 (14-02-2000) and 136/045 (19-12-1999). Level 0 JERS-1 SAR data was procured from Remote Sensing Technology Center (RESTEC) of Japan and was converted to 1.1 intensity image using the software provided by Japan Aerospace Agency (JAXA). Speckle noise on the imageries was reduced by 3x3 Lee-sigma filters. SAR images were geo-rectified with geo-coded Landsat ETM+ pan image mosaic using polynomial function 1. The RMS errors of geo-rectification were 1.6, 2.9 and 1.1 pixels for 144-264, 144-265 and 145-264 scenes respectively. Three scenes were joined to make a continuous image mosaic. A sub-scene from the mosaic was selected for mapping.

On the SAR image forest, degraded forest (scrubby vegetation associated with forest re-growth), agriculture, shrimp-farming, urban and water-body could be interpreted on the SAR image. Visually interpreted SAR image was digitized on-screen and forest (land) cover map was prepared. Field verification was done in several times during 1998-2004.

5. Results and Discussion

Radar imagery is the result of radar signals, depends upon system parameters (wavelength, polarization and incident angle) and terrain parameters (complex dielectric constant, surface roughness, terrain geometry, and surface and volume scattering). Tone, texture, shape, size, shadow, pattern and association assisted in radar image interpretation. Land-cover characteristics and corresponding forest interpretation for the study area is presented in Table 1. Forest mosaic prepared from three JERS-1 SAR scenes is presented in Figure 3 and different land covers and landuses are indicated by a white square. Visual interpretation of SAR scene is presented in Figure 4.

Table 1. JERS-1 SAR interpretation keys for southern Chittagong, Bangladesh

Land cover / landuse type	Physical characteristics	Interpretation keys
Forest	•Tropical wet evergreen and semi-evergreen forest	•Medium tone •Rough texture
Degraded forest	•Formed after removal of primary forest by extreme human interference	•Medium tone (darker than forest)
	•Composition: re-growth and scrubby type of vegetation	•Terrain on the image is more vivid than forest class due to removal of tree coverage

Coastal plantation	•Planted with mangrove species (major species- *Sonneratia apetala*) on the newly accreted lands	•Medium tone •Smooth texture
Agriculture	•Agriculture area contains a mixture of different land cover / landuse: paddy crops; bare (both wet and dry) soil and flooded soil	•Heterogeneous (random mixture of dark and bright) tone
Shrimp farms	•Rectangle sized small pond like structure, used for the production of shrimps. It has shallow depth of water	•Appears as dark tone, a large number of white and thin lines are seen due to strong return echo (high reflectance) from the forward side (radar sensor) of the ridges
Urban	•Residential and official area mostly occupied by impervious surface (buildings and roads)	•Very bright tone
Rivers	-	•Irregular shaped dark line, sandwiched by two of bright lines especially near the coast
Sea	-	•Dark tone

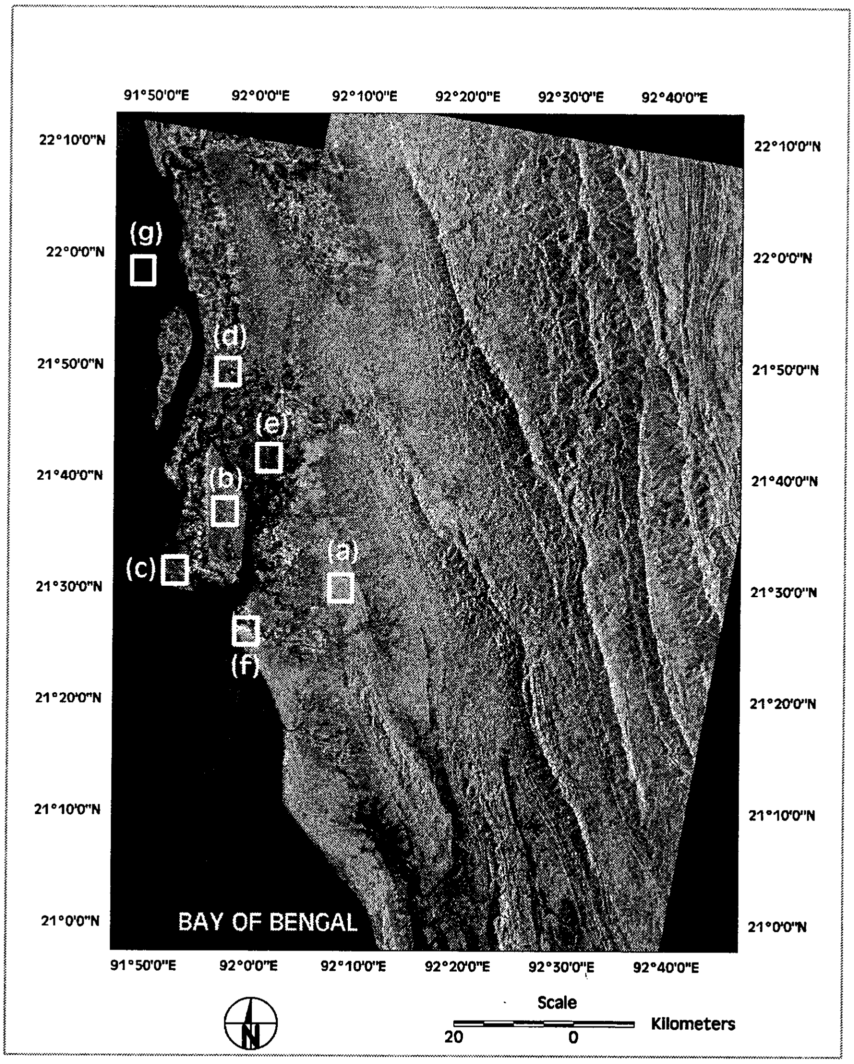

Figure 3. Mosaic of three JERS-1 SAR scenes (a) forest (b) degraded forest (c) coastal plantation (d) agriculture (e) shrimp farms (f) urban (g) water

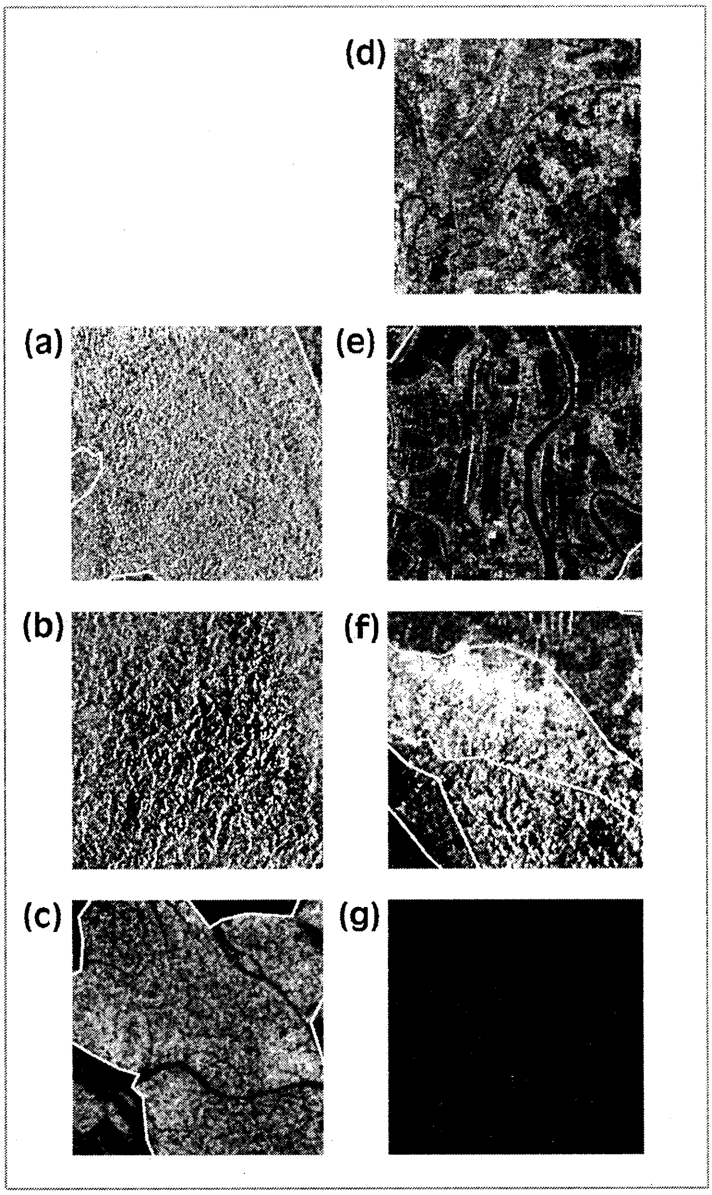

Figure 4. Visual interpretation of JERS-1 SAR image (a) forest (b) degraded forest (c) coastal plantation (d) agriculture (e) shrimp farms (f) urban (g) water

Forest cover map prepared from visual interpretation and on-screen digitizing is presented in Figure 5. The land cover and landuse on the map is separated from west to east direction. The western area is covered by sea, at the middle agriculture and eastern-side is forest; north-eastern part is degraded forest and south-eastern is forest. Statistics shows that forest area is distributed on 27 054 ha of area (9.2%).

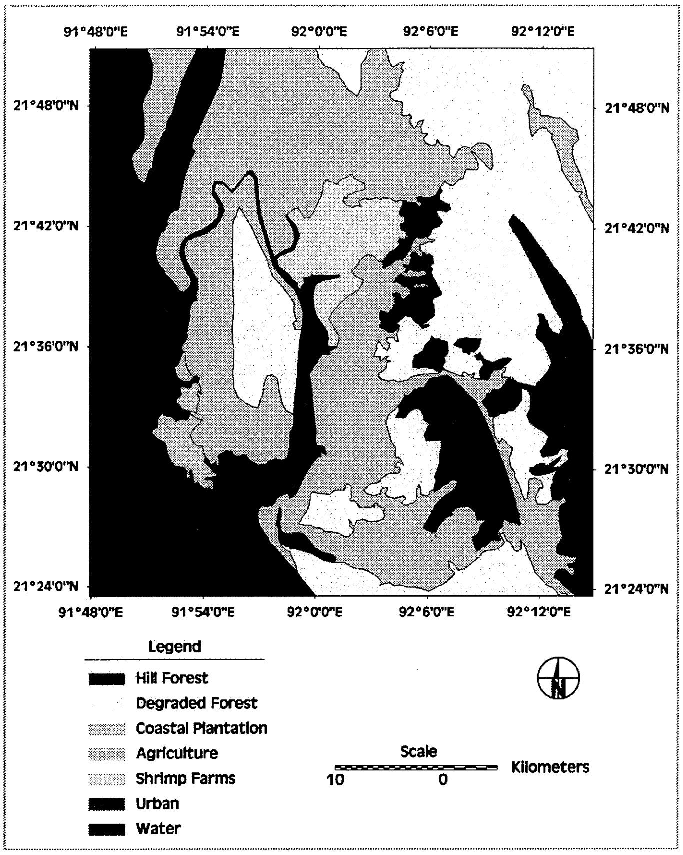

Figure 5. Forest (land) cover map of southern Chittagong using JERS-1 SAR data

Table 5. Land cover and landuse type in the study area

Landcover / Landuse	Area (ha)	Percentage
Forest	27 054	9.2
Degraded forest	95 364	32.6
Coastal plantation	2 558	0.9
Agriculture	89 454	30.6
Urban	625	0.2
Water	69 549	23.8
Shrimp farms	8 086	2.8

Radar image is suitable to separate forest from non-forest class. Forest can be separated based on the intensity and texture image. Degraded forest is also distinguishable from well-stocked forest in most of the cases. However, multispectral optical image (i.e. Landsat ETM+) could separate eight different vegetation types (primary and secondary forest, bamboo, shrubs, plantation with indigenous species, Teak, Rubber and Acacia) in the study area (Rahman *et al.* 2004). In contrast, further distinction of different forest types is not possible on the radar image.

Terrain features and urban classes are more separable on SAR image in compare with optical images (i.e. Landsat). Topographic feature is more vivid on the SAR image in compare with the optical images. The topographic features and slopes are easy to detect on the SAR image. SAR has a high intensity on the urban areas because of corner reflection, when two smooth surfaces form a right angle facing the radar beam, the beam bounces twice off the surface and most of the radar energy is reflected back to the radar sensor and appear in very bright tone on a radar image.

This study has developed an interpretation key for tropical landscape using SAR data. Such a key is available in the other regions of the world (i.e., Jiyuan *et al.* 1986) but not in this study region. However, interpretation key for vegetation of the study region has been developed using optical sensors (see Rahman *et al.* 2004).

6. Conclusion

This study has developed (i) forest cover map in southern Chittagong, Bangladesh and (ii) interpretation key to identify and delineate forest coverage in the study region. The investigation has failed to prepare a forest cover map based on digital classification with the assistance from intensity and texture-based forest classification because it often inter-mixed with many other classes. Further study should be carried out to overcome this problem.

Acknowledgement

Japan Society for the Promotion of Science (JSPS) for granting fellowship to the first author. Landsat ETM+ Satellite imageries were downloaded from http://glcf.umiacs.umd.edu/index.shtml website. The authors would like to acknowledge Luhur Bayuaji, Microwave Remote Sensing Laboratory, CEReS, Chiba University to assist in processing of SAR image from level 0 to 1.1

Reference

Baten, S. A. 1969. Revised working plan for the forests of the Chittagong Division for the period from 1968-69 to 1977-78. Forest Department, Government of East Pakistan, Dhaka.

Champion, H. G., Seth, S. K. and Kattak, G. M. 1965. *Forest types of Pakistan.* Pakistan Forest Institute, Peshawar. 238 p.

Dobson,, M. C., Pierce, L. E. and Ulaby, F. T. 1996. Knowledge-based land-cover classification using ERS-1/JERS-1 SAR composites. *IEEE Transactions on Geoscience and Remote Sensing.* 34(1): 83-99.

FAO. 1999. State of the world's forests. FAO, Rome.

Ford, J. P. and Casey, D. J. 1988. Shuttle radar mapping with diverse incidence angles in the rainforest of Borneo. *International Journal of Remote Sensing* 9(5): 927-943.

Jiyuan, L., Xuyan, T. and Jinkai, X. 1986. Application of Shuttle Imaging Radar data for land use investigations. *Remote Sensing of Environment* 19: 291-301.

Khan, S. A. 1979. Revised working plan for the forests of Chittagong Division (for the years 1978-79 to 1987-88). Volume 1. Forest Department, Government of Bangladesh, Dhaka.

Lo, C. P. 1988. Comparative evaluation of the Large Format Camera, Metric Camera and Shuttle Imaging Radar-A data content. *Photogrammetric Engineering & Remote Sensing* 54(6): 731-742.

Quegan, S., Toan, T. L., YU, J. J., Ribbes, F. and Floury, N. 2000. Multitemporal ERS SAR analysis applied to forest mapping. *IEEE Transactions on Geoscience and Remote Sensing* 38(2):741-753.

Rahman, M. M. and Csaplovics, E. 2001. Integrated Application of Remote Sensing and GIS for Assessing Tropical Deforestation in Southern Chittagong, Bangladesh. In: M. F. Buchroithner (ed). A Decade of Trans-European Remote Sensing Cooperation. 20th EARSel Symposium, 14-16 June, Dresden, Germany, pp 59-64.

Rahman, M. M., Csaplovics, E., Koch, B. and Köhl, M. 2004. Interpretation of Tropical Vegetation Using Landsat ETM+ Imagery. In. M. O. Altan (ed.) International Archives of the Photogrammetry, Remote Sensing and Spatial Information Sciences, Vol XXXV, Part B-YF, Istanbul, pp 157-162.

Rignot, E. J. M., Williams, C. L. and Way, J. and Viereck, L. A. 1994. Mapping of forest types in Alaskan Boreal Forests using SAR imagery. *IEEE Transactions on Geoscience and Remote Sensing* 32(5): 1051-1059.

Application of satellite remote sensing technique to wetland conservation in Hokkaido, Japan

Masayuki TAKADA[1] and Takashi INOUE[2]
[1]Hokkaido Institute of Environmental Sciences, [2]Hokkaido University
E-mail: mtakada@hokkaido-ies.go.jp

Abstract

We studied the usefulness of satellite remote sensing and GIS in estimating wetland vegetation classification, changes, structure and physical environment, and in evaluating the spatial characteristics of wetland environmental factors. We started by examining a method of using Landsat data to classify the existing wetland vegetation of Sarobetsu Mire in Hokkaido and of extracting temporal changes in the vegetation there. In this study, we used a classification method based on discriminant analysis to create a vegetation classification map that has high concordance rate. Vegetation classification maps for 1991 and 2000 were created using satellite images, and a comparison between those years showed that it is possible to quantitatively show the vegetation changes between those years.

Next, for Bibai Bog in Hokkaido, we estimated spatial distribution of the vegetation structure (i.e., the height of dwarf bamboo) and soil moisture through a multiple linear regression analysis using images from ASTER, ALOS, and IKONOS. To obtain spatial parameters for a hydrological change model, we analyzed characteristics of environmental factors' spatial distribution in Sarobetsu Mire. The analysis found correlations among some factors, and we found that it is useful in accurately to estimating spatial factors through multivariate analysis using groundtruth data, satellite images and GIS data.

1. Introduction

A wetland is a unique ecosystem whose existence relies heavily on the interactions between water, soil and vegetation. Conservation efforts have been made for many wetlands because of their environmental importance. Wetlands' importance from the global environmental viewpoint has been pointed out, because undecomposed plant residues in wetland soil are able to store carbon in large amounts. In recent years, however, human-induced aridification and invasion by non-wetland plants have progressed. As a result, some wetlands have become targets of nature restoration. In wetlands, because environmental factors such as topography, vegetation, hydrology, soil change in adjacent and non-adjacent areas, localized environmental surveys are not sufficient for effective wetland conservation and management. It is important to predict environmental changes using models that incorporate data on spatial distribution of environmental factors (Kellner and Halldin, 2002; Petrone et al, 2004)

Remote sensing technology is very useful for obtaining knowledge on the spatial distribution of environmental factors and changes in them. In this study, we first used remote sensing and GIS technologies and extracted data on vegetation classification and vegetation changes, and estimated structures of vegetation and spatial distribution of soil moisture. Next, to obtain parameters necessary for creating a model of environmental change (i.e., a hydrological model), which is used in conservation and management of the wetland ecosystem, we analyzed the relationship among topography, physical properties of the surface peat layer, hydrologic conditions, vegetation, and satellite spectral image data, and clarified the characteristics of the regional environment.

2. Study sites

The study sites are Sarobetsu Mire and Bibai Bog (Figure 1). Sarobetsu Mire is a wetland in the towns of Toyotomi and Horonobe, northern Hokkaido. The mire measures 27 km north-south and 5 to 8 km east-west. Designated as a national park and Ramsar site, it is Japan's largest lowland bog. We studied an area of about 1,500 ha in the northern part of the mire, where the major issues are invasion by dwarf bamboo and the impacts of construction of artificial ditches built between the mire and agricultural land. Bibai Bog is within the Test Field of the National Agricultural Research Center for Hokkaido Region. The bog is a remnant of what used to be the Ishikari Peatland (55,000 ha). Ditches run along the fringe of bog. The area of wetland vegetation has been decreasing because dwarf bamboo has invaded most of the bog. The analyzed area was 21 ha in the southern half of the bog.

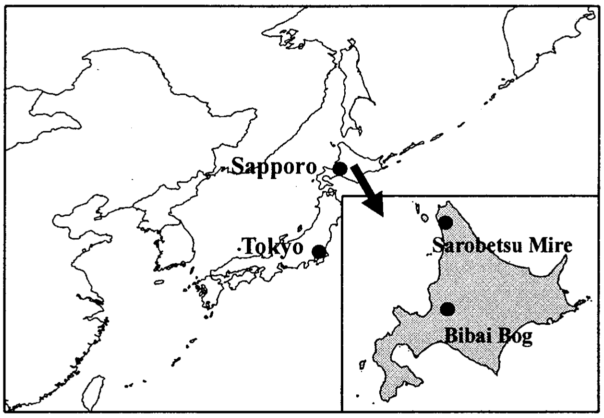

Figure 1 Study sites

3. Methods

3.1 Vegetation classification and analysis of changes

To obtain groundtruth data, vegetation was surveyed at 84 points in Sarobetsu Mire. Next, geometric and atmospheric corrections were done for Landsat ETM+ (2000.6.24) data to obtain spectral information for the points of the groundtruth data survey. Using the groundtruth data and corrected data, stepwise discriminant analysis based on Mahalanobis generalized distance was performed. Kappa statistics were obtained based on the vegetation survey data for 40 points, and the accuracy of the vegetation classification was examined. The vegetation classes for the survey area were sphagnum, sedge, dwarf bamboo, reed, and three mixed classes. A vegetation classification map was created from the satellite images using a discriminant function obtained through discriminant analysis. Next, using the same method, another vegetation classification map was created from the Landsat ETM+ (1991.6.24) data. Changes in the area of each vegetation class during a nine-year period were calculated by tallying and comparing the number of pixels for each vegetation class.

3.2 Estimation of dwarf bamboo height and soil moisture

Surveys on vegetation, height of dwarf bamboo and soil moisture were performed five times at 60 points in a 50-m mesh in the study area in Bibai Bog. Spectral information was obtained for each surveyed point using satellite images from IKONOS (2002.9.16), ALOS/AVNIR-2 (2006.7.4), and Terra/ASTER (2004.9.23). Multiple linear regression analysis were performed for these data, and distribution estimation maps for dwarf bamboo and soil moisture were created by using the obtained regression equation and images from these satellites. Estimation accuracy was verified by comparison with field survey data.

3.3 Spatial analysis for environmental factors

At Sarobetsu Mire, a field survey for environmental factors was performed at 23 to 89 points depending on the survey item (e.g., groundwater level, vegetation class, dwarf bamboo height, water quality, soil moisture, carbon content, C/N ratio, bulk density.) We processed GIS data on topographic factors, including surface elevation, slope gradient, peat depth, distance to the former river channel, the presence of natural ditches and watercourses around the surveyed area. By using these data, relationships among the factors were obtained through cross tabulation, correlation analysis, and principal component analysis. Spectral information for each survey point was obtained from ALOS/AVNIR-2(2006.5.21, 7.2, 7.21) data, and the possibility of estimating the spatial distribution for each factor was examined through multiple regression analysis.

4. Results and Discussion

4.1 Vegetation classification and analysis of changes

A vegetation classification map created from Landsat ETM+ (2000.6.24) data is shown in Figure 2. High accuracy (Kappa statistic of 0.819, significance level of 99.9%) was shown in vegetation classification based on the field survey of vegetation data (Takada et al, 2006).

Next, the vegetation changes of 9 years were obtained by comparing two vegetation classification maps created from Landsat images for 1991 and 2000 (Figure 3). The sphagnum class and dwarf bamboo-sphagnum class decreased and the dwarf bamboo class and sedge-sphagnum class increased. The result shows that there is a clear tendency of increase in dwarf bamboo vegetation and decrease in sphagnum vegetation in the entire study area.

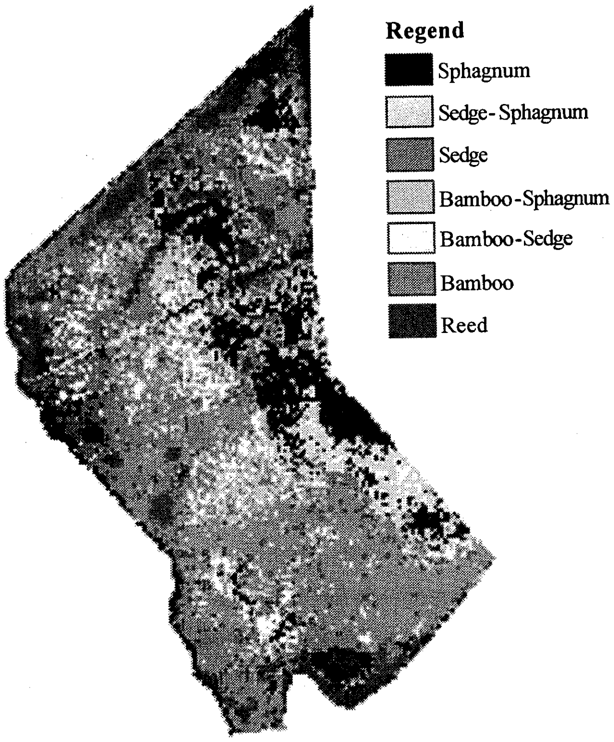

Figure 2 Vegetation classification map from Landsat ETM+ (2000.6.24)

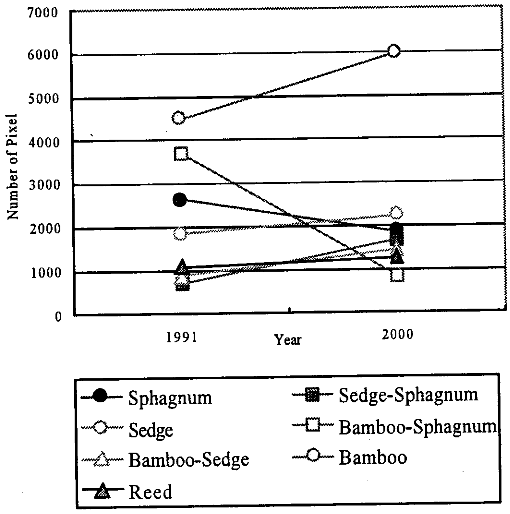

Figure 3 Vegetation changes (1991→2000)

4.2 Estimation of dwarf bamboo height and soil moisture

Multiple regression analysis was performed to estimate dwarf bamboo height. The multiple regression coefficients for IKONOS, ALOS, and ASTER data were high values of 0.785, 0.746, and 0.844, which showed that dwarf bamboo height estimation using satellite multiband data is effective. The dwarf bamboo height distribution map produced from ALOS using the obtained regression equation is shown in Figure 4. Verification using the field survey data found that the estimated values lie roughly within a 95% confidence interval for variance. The average differences between the measured and estimated values are between 4.1 cm and 5.2 cm, and the standard deviation of the differences falls between 8.7 cm and 18.6 cm. The measured values for ALOS are compared to estimated values in Figure 5 (Takada et al, 2007).

Estimation of soil moisture for each vegetation class was performed using multiple regression analysis. Multiple regression coefficients for IKONOS, ALOS, and ASTER were 0.667- 0.864, 0.708- 0.965, and 0.697, which shows that estimation of soil moisture using satellite multiband data is accurate. Verification using the field survey data found that the estimated values are roughly within a 95% confidence interval for variance. The average differences between the measured and estimated values are between 0.1% and 0.9%, and the standard deviation of the differences falls between 2.8% and 8.0%. The soil moisture distribution map produced from ALOS using the obtained regression equation is shown in Figure 6, and the relationship between the measured and estimated values is shown in Figure 7 (Takada et al, 2007).

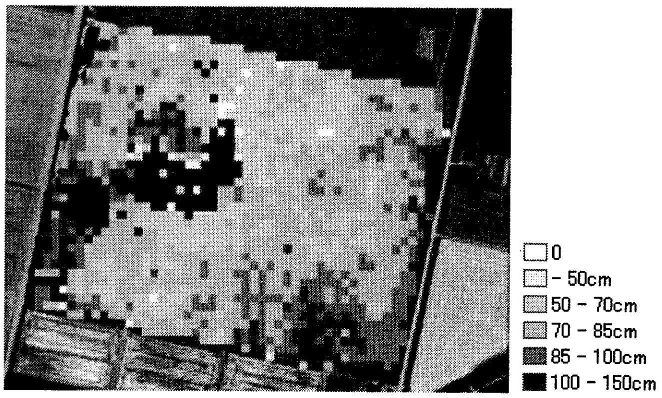

Figure 4 Dwarf bamboo height distribution map from ALOS

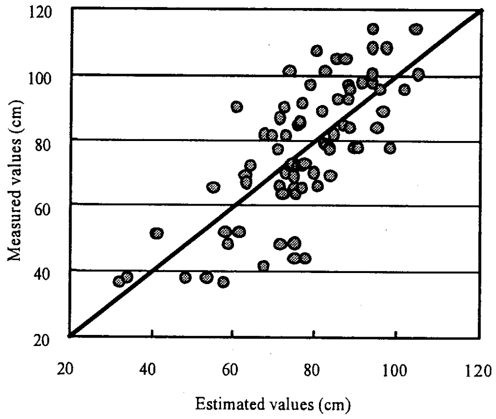

Figure 5 Verification in estimation of dwarf bamboo height for ALOS

Figure 6 Soil moisture distribution map from ALOS

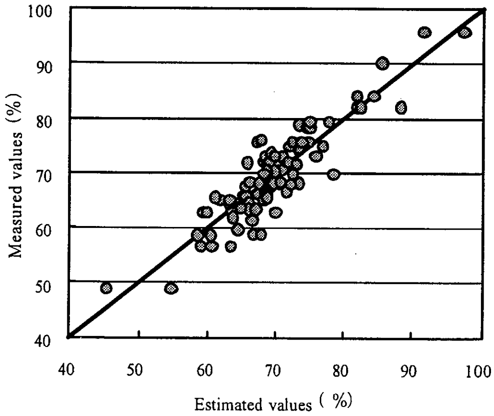

Figure 7 Verification in estimation of soil moisture for ALOS

4.3 Spatial analysis for environmental factors

Correlation analysis performed for each factor revealed that there are some factors that have high correlation coefficients and high significance levels. Some examples are shown in Figure 8. Cross tabulation using the GIS data was performed, and close relationships between topographical factors, distance from watercourses and vegetation were found (Figure 9). For example, dwarf bamboo vegetation was found in areas close to natural ditches and away from the former river channel.

Next, principal component analysis was performed using the groundtruth data and GIS data. The first component represents the physical properties of the surface peat layer, height of dwarf bamboo, and elevation. The second principal component represents the groundwater level. The third principal component represents the spatial factors such as slope gradient and distance from the former river channel. Cumulative contribution until the third principal components accounted for 85.5%. Estimation of bulk density, an important parameter for a hydrological model, was performed by multiple regression analysis. It was clarified that estimation of bulk density was possible using groundtruth data and GIS data (multiple regression coefficient of 0.94) and spectral data of ALOS (multiple regression coefficient of 0.76)

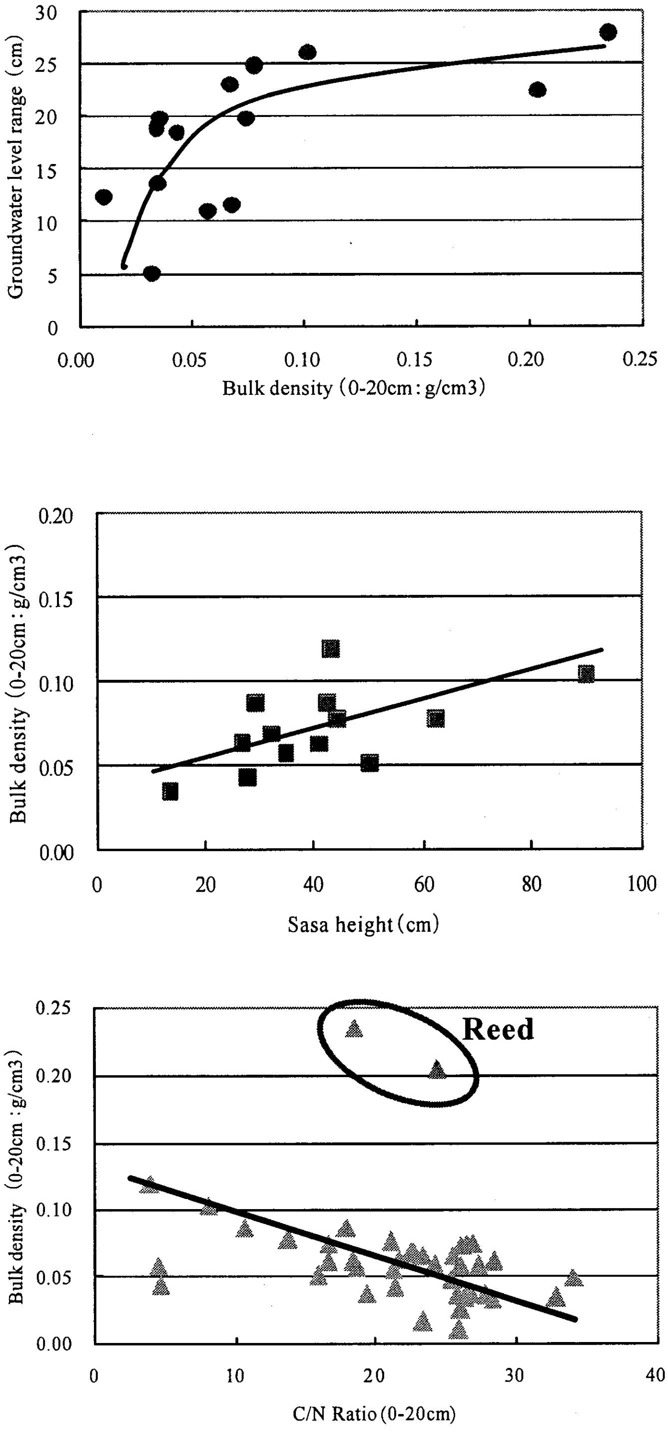

Figure 8 Examples of correlation analysis for each factor

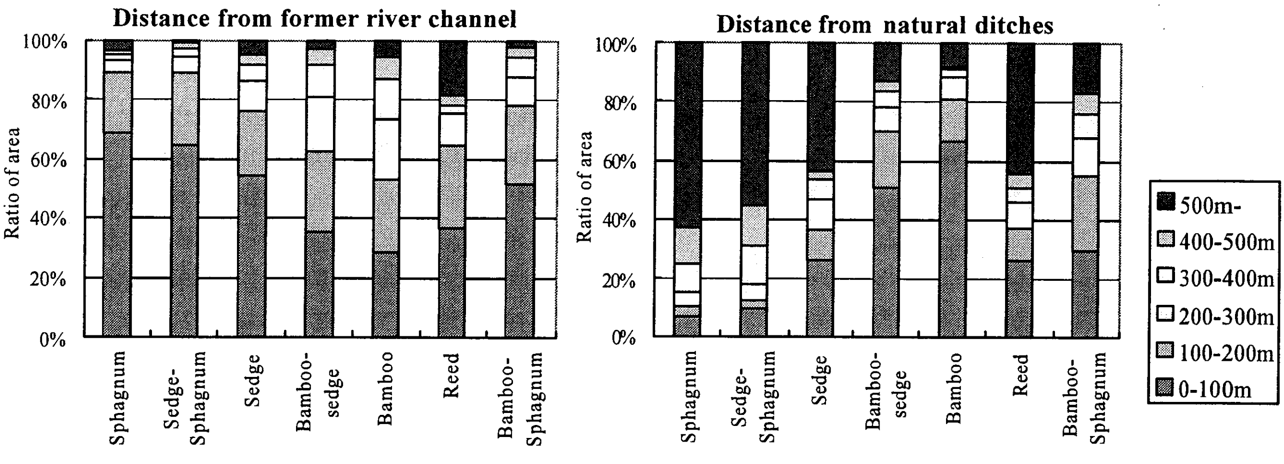

Figure 9 Cross tabulation between distance from watercourses and vegetation

5. Conclusions

This study clarified that estimation of vegetation classification and changes, vegetation structure (height of dwarf bamboo), and physical environment (soil moisture) using satellite images was accurate for wetlands, where there are particularly interactions among hydrology, soil, and vegetation closely.

Interactive relationships between the groundtruth data (groundwater level, water quality, carbon content, bulk density, etc.), the GIS data (topographical factors and distance from watercourses) and satellite data was confirmed, and it was found that it may be possible to use those relationships to determine which parameters are necessary to a model of environmental change. It will be necessary to increase the number of data and further improve the accuracy of the analysis.

Acknowledgements

We sincerely thank the Japan Aerospace Exploration Agency, the Remote Sensing Technology Center of Japan, and Japan Space Imaging Co., Ltd. for providing satellite images, and Nobuhiro Sasaki of the Ministry of Environment, Toshihiro Shimazaki of NPO Sarobetsu Eco Network, Yoshio Mishima and Tomotaka Kato of the Hokkaido Institute of Technology, Akane Kagemoto of Hokkaido University, Osamu Nagata of the National Agricultural Research Center for Hokkaido Region, and Shosuke Natsume and Rie Kitagawa of the Hokkaido Institute of Environmental Sciences, for providing great technical and logistical assistance.

References

Kellner, E. and Halldin, S. 2002. Water budget and surface-layer water storage in a *Sphagnum* bog in central Sweden. Hydrological Processes 16: 87–103.

Petrone, R.M., Price, J.S., Carey S.K. and Waddington, J.M.. 2004. Statistical characterization of the spatial variability of soil moisture in a cutover peatland. Hydrological Processes 18: 41-52.

Takada, M., Buhe, A., Natsume, S., Saito, K. and Kato, K. 2006. Classifying the vegetation at Sarobetsu Mire, Hokkaido, using satellite remote sensing. Landscape Ecology and Management 11(1): 3-14. (In Japanese with English summary)

Takada, M., Natsume, S., Kagemoto, A. and Nagata, O. 2007. Estimations of spatial distributions for vegetation and physical environment in wetlands using ALOS/AVNIR-2. Journal of the Japan Society of Photogrammetry and Remote Sensing 46(4): 20-25. (In Japanese)

Spectral discrimination of hydrothermal minerals by using ASTER data: Case Study in Um Nar area, Egypt

Nehal SOLIMAN[1], Adel SHALABY[2], Thomas NGIGI[3] and Ryutaro TATEISHI[4]
[1, 2, 3, 4] Center for Environmental Remote Sensing, Chiba University
E-mail: nehal_narss@yahoo.com

Abstract

ASTER data are attractive to many geological researchers due to their high spatial and spectral resolutions. This work examines ability of ASTER data to map hydrothermal minerals in an arid area in Central Eastern Desert, Egypt, using spectral analysis techniques. Visible, near infrared and short wave infrared reflectance data (first 9 bands) are utilized. Minimum noise fraction (MNF) transformation is executed on the data and then pixel purity index (PPI) run on the new data set. N-dimensional visualization is carried out on the PPI to extract pure pixels. Extreme pure pixels are identified from the pure pixels. Spectra of these extreme pure pixels are compared with NASA JPL spectra of minerals available in the study area, by both spectral angle mapper (SAM) and spectral feature fitting (SFF) giving two lithological maps. Against reference lithological data, the overall accuracies of the two maps are 78.85%, 70.33% respectively, Proving applicability of ASTER data in lithological mapping.

Keywords: Aster, Hydrothermal Minerals, Um Nar,

1. Introduction

The Neoproterozoic basement complex of Egypt is composed mainly in the Eastern Desert as a ~ 800 km long belt that parallels the Red Sea coast. It presents ~10% of the total area of Egypt and forms part of the Nubian Shield, which is the western segment of the Arabian-Nubian Shield. The study area represents the south most banded iron formations (BIF) occurrence in the Central Eastern Desert of Egypt. It is bounded between latitudes 25° 14′ 45″N and 25° 16′ 18″N and longitudes 34° 15′ E and 34° 17′ 27″E and represents one of more than fifteen BIF occurrences in The Eastern Desert. The mineable reverse of the Um Nar BIF is evaluated at 13.7 Mt. (El Ramly et al, 1970). Up to date, no commercial mining operation has taken place in Um Nar because of the high silica content of the ore (El Habaak, 2004). The Um Nar BIF proved to be gold and silver bearing with gold contents with average of 0.82 ppm. The type of gold associated with the Um Nar BIF is classified by as stratabound gold deposits associated with Alogma-type BIF. The source of gold in Um Nar is suggested to be associated with ancient oceanic crust represented by the serpentinites of Gabal El Mayit. The gold content has been found to be higher in the highly deformed areas because the resulting shear zones and tectonic fractures have acts as channel ways and depositional loci for the gold –bearing fluids and that the hematite bands of the Um Nar BIF are slightly richer in gold than the magnetite.

2. Data used

The ASTER data used in this study are two cloud free level <u>1A</u> data scenes acquired on Febrauary 18, 2007. The images have been pre-georeferenced to UTM Zone 35 North projection with WGS-84 datum. To preserve the spectral characteristics of the SWIR bands, the VNIR bands were Spatially resized (nearest neighbor algorithm) to match the spatial resolution of the SWIR bands. and then clipped to the study area. The SWIR bands were corrected for the crosstalk effect (Rowan and Mars, 2003) by using the crosstalk correcting software provided by (ERSDAC 2001).

MODTRAN4 software was used to calculate the solar irradiance and to convert ASTER data into surface reflectance images.

2.1. SWIR Pre-processing

SWIR crosstalk is an offset or additive error in radiance due to the leakage of photons from one detector element to another (Iwasaki et al., 2001). So it was corrected by using the crosstalk effect software provided by the Japanese ASTER Ground Data System (GDS), solar irradiance values were calculated by using MODTRAN4. And the images were calibrated to reflectance values. To be able to analyze spectral responses of surface cover types, it is necessary to apply residual log residual algorithm on SWIR bands to reduce noises from Topography and sun illumination.

3. Methodology

Analysis of ASTER data for lithologic mapping is based on determination of the relationship between spectral reflectance and spectral emittance and the mineral composition of the rock units of interest. The Spectral Angle Mapper (SAM) technique (Kruse et al., 1993) was applied to test the similarity between pixel spectra and mineral reference spectra for 7 minerals and by using the Spectral feature Fitting method (SFF) "Absorption features" to measure the absorption depth. The reference spectra were extracted from the National Aeronautics and Space Administration/Jet Propulsion Laboratory/ (NASA/JPL) spectral library, and were re-sampled to the same ASTER bands widths, using filter functions. Similarities between image spectra and reference spectra were calculated. Small SAM angles indicate great similarity between pixel spectra and reference spectra. To enhance variations in the depth of the 2200 nm absorption bands on a per-pixel basis, the continuum removal method (Clark, 1999) was applied on bands 5 to 8. For endmember selection, a semi-automatic procedure, based on the sequential use of the minimum noise fraction (MNF) and pixel purity index (PPI) techniques, was applied to the surface reflectance values of the ASTER VNIRSWIR bands (Boardman and Kruse, 1994). End members were selected from the inspection of extreme pixel spectra extracted from PPI and projected as points in *n*-dimensional scatter plots of the higher-order four MNF images.

4. Summaries and Conclusion

The paper has investigated the usage of the ASTER data for mapping the geology for an arid area in Egypt. Several spectral image-processing techniques were used. In general, not one spectral analysis procedure is consistently superior to others judged by the comparison of our analysis results with the reference data. Each of the three-hyperspectral classification techniques has its unique strengths and limitations. The spectral analysis method based on MLH has a relative advantage in terms of better definition of the intercalation nature of layered rocks. However, in terms of overall classification accuracy, SAM and SFF procedures seem to yield classification results closer to the reference data, with total accuracies of 78.85%, 70.33% respectively. SAM and SFF proved to be effective techniques in mapping lithological units in an arid area and their results can be improved further if data calibration can be applied with the support of atmospheric information. SAM demonstrated strength in mapping distribution detail for lithological units, while SFF was good at achieving the best balance of classification accuracy among different rock types.

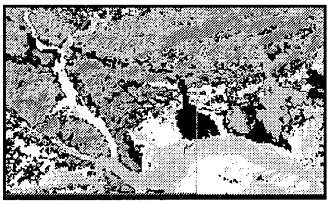

CLASSICIFATION OF ISO DATA

CLASSICIFATION OF MLH

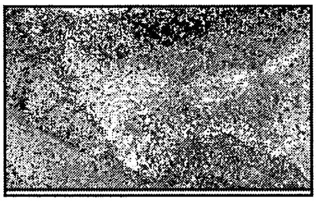

CLASSICIFATION OF SFF

CLASSICIFATION OF SAM

Reference

Boardman, J.W., and Kruse, F.A., 1994, Automated spectral analysis: a geological example using AVIRIS data, north Grapevine Mountains, Nevada. Proceedings of the Tenth Thematic Conference on Geologic Remote Sensing, 9-12 May 1994 (Ann Arbor, MI: ERIM), vol. 1, pp. 407-418.

Clark, R.N., 1999, Spectroscopy of rocks and minerals and principles of spectroscopy. In Remote Sensing for the Earth Sciences, edited by A.N. Rencz (New York: Wiley), pp. 3-58.

El Habaak, G.H., 2004. Pan-African skarn deposits related to banded iron formation,

Um Nar area, central Eastern Desert, Egypt. Journal of African Earth Sciences 38 (2004) 199–221.

El Ramly, M.F., Ivanov, S.S., Kochin, G.G., 1970. General review of the mineral potential of Egypt. In: Moharram, O. (Ed.), Studies on Some Mineral Deposits of Egypt. Geological Survey, Egypt, pp. 3–27.

ERSDAC (2001). Earth Remote Sensing Data Analysis Center (ERSDAC), 2001, The crosstalk correction software: user's guide. Mitsubichi Space Software CO., LTD. 17 pp.

Iwasaki, A., Fujisada, H., Akao, H., Shindou, O., & Akagi, S. (2001). Enhancement of spectral separation performance for ASTER/SWIR. Proceedings of SPIE, The International Society for Optical Engineering, 4486, 42- 50.

Kruse, F.A., Lefkoff, A.B., Boardman, J.W., Heidebrecht, K.B., Shapiro, A.T., Barloon, P.J., and Goetz, A.F.H., 1993, The Spectral Image Processing System (SIPS) - Interactive visualization and analysis of imaging spectrometer data. Remote Sensing of Environment, 44, 145-163.

Rowan and Mars, 2003) Rowan, L.C., and Mars, J.C., 2003, Lithologic mapping in the Mountain Pass, California area using Advanced Spaceborne Thermal Emission and Reflection Radiometer (ASTER) data. Remote Sensing of Environment, 84, 350-366.1787

A study on the Mitigation of Meteorological Hazard using a Multi-factor in the Nackdong Basin

Youngjoo KWAK [1] and Akihiko KONDOH [2]
[1] Graduate school of Science, Chiba University
E-mail: kwak_yj@graduate.chiba-u.jp
[2] Center for Environmental Remote Sensing, Chiba University
E-mail: kondoh@faculty.chiba-u.jp

Abstract

The earth's climate will become hotter over the coming century than in the past. We can see changes in the climate and increases in greenhouse gases. The climate changes will be much more significant over the next 100 years. As a result, floods have increased due to rapid urbanization and human activity in pyramid areas and lower lands comparing to the Mean Sea Level. Therefore, regular river flood control is essential for embankments and the need for maintenance of the river is out of safety concerns as well as keeping them functional. In order to determine the geomorphological effectiveness of the floods, we used the present flooding data in 2002 and Landsat TM image. With Normalized Difference Vegetation Index (NDVI), we found useful data and could assess the relation of distribution between plantation and water. In this study, we have conducted a comparative research on the geomorphologic basin of disaster areas. Moreover, we recognized that land cover classification determined physical aspects on the relation of urbanization between plain areas and mountainous areas near rivers. This study's purpose is to extract not only the risk parameter but also geomorphologic relation, which we then analyzed to generate multiple criteria such as water level, DEM, aspect, slope and image analysis of Landcover, NDVI in Nackdong basin.

Keywords: Geomorphological basin, Flood information, Spatial analysis, Multi factor.

1. Introduction

1.1 Background

The earth's climate will become hotter over the coming century than in the past. We can see changes in the climate and increases in greenhouse gases. The climate changes will be much more significant over the next 100 years. As a result, floods have increased and inflict a great deal of damage. So governments and civilians demand readjustment of embankment and river control information in basins. In Korea, flash floods often happen in a localized torrential downpour due to rapid urbanization and human activity in pyramid areas and lower lands compared to the Mean Sea Level. Therefore, regular river flood control is essential for embankments and the need for maintenance of the river is out of safety concerns as well as keeping them functional. For example, Nakdong River Flood Control Office[7] announces flood forecasts for the main areas of each river and provides information in real-time to the public about rainfall and water level transmitted from monitoring stations which are set up in the Nakdong river basin in Korea. However, due to lack of hydrologic, hydraulic and geomorphic data the geomorphic effectiveness of such high-magnitude floods is often difficult to compute in terms of the distribution of stream power per unit boundary area (ω) over time [3].

FEMA(Federal Emergency Management Agency) reports that floods are one of the most common disasters in the United States. Flood effects can be local, impacting a neighborhood or community, or very large, affecting entire river basins and multiple states. However, all floods are not alike. Some floods develop slowly, sometimes over a period of days. But flash floods can develop quickly, sometimes in just a few minutes and without any visible signs of rain. A FIRMette is a full-scale section of a FEMA Flood Insurance Rate Map (FIRM) including floodplain management, flood insurance, and enforcement of mandatory flood insurance purchase requirements[2].Therefore, regular river flood control is essential for all embankments and the need for maintenance of the river is for safety purposes as well as keeping them functional. In order to determine the geomorphological effectiveness of the floods, we used the present flooding data in 2002 and Landsat TM image.

Antonie et al.[1] presented an example application on integration of multi criteria valuation techniques with GIS for sustainable land use in Kenya; maximizing revenues from crop and livestock production, maximizing food output, maximizing district self-reliance in agricultural production and minimizing environmental damages from erosion. Lee traces the flood inundation area around rural small streams by using RADARSAT images because it has the ability of acquiring data during storm periods irrespective of rain and cloud[6]. The inundated area was at the joint area of two streams, thus the floodwater overflowed bounding discharge capacity of the stream in Korea.

1.2 Purpose

This study's purpose is to extract not only disaster parameters but also geomorphologic relation, and which we then analyzed to generate multiple criteria such as water level, DEM, aspect, slope and image analysis of Landcover, NDVI in Nackdong river basin. Moreover we consider the weight of these variables in order to predict and reduce a natural disaster such as floods.

2. Effects on Rivers as Natural Systems

2.1 Study area

The area of the Nakdong basin is a second largest basin in S.Korea and surrounded by mountain ranges. Its length is 521.5km and area is 23,817km2. It is centered in Gyeongsang Province and is located between north latitude 127°29′ to 129°18′ and east longitude 35°03′ to 37°13′. It makes up approximately 24.1% of South Korea's entire area[8].

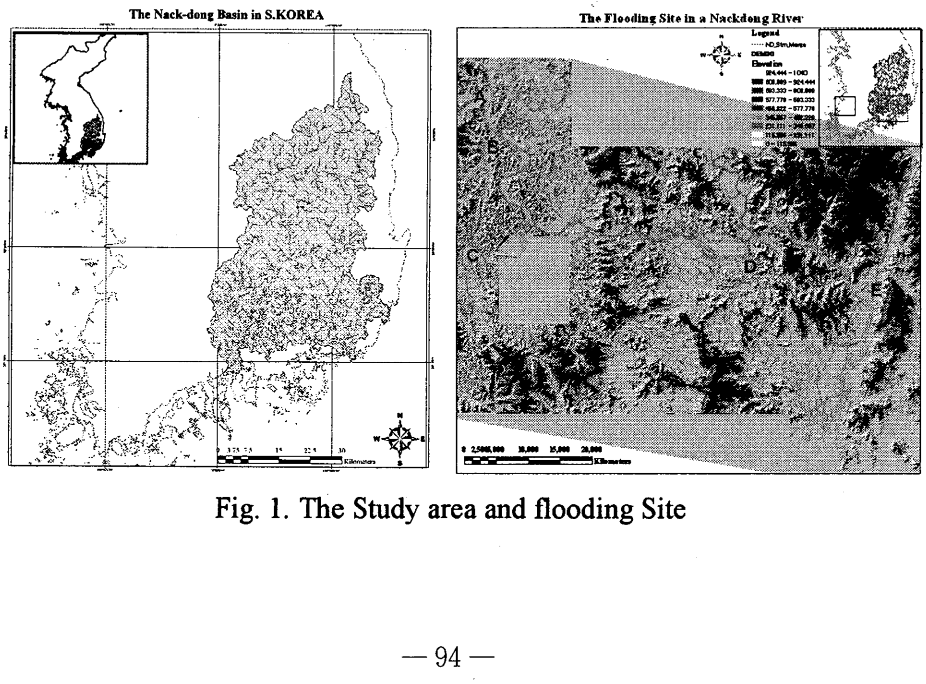

Fig. 1. The Study area and flooding Site

2.2 Previous Occurrence of flood

In Nackdong basin, if the typhoons pass through the east path, as opposed to the west, the damage is more extensive. These typhoons have caused flooding of the Nackdong basin 16 times in the period between 1987 to 2002. Natural occurrences, such as heavy rain, weather systems, and typhoons, can cause floods. Late in the summer of 2002, remarkable flooding which occurred twice that August, brought by RUSA killed about 262 people and caused more than $60 billion in property damage. Table 1 shows more detailed damages[4].

Table 1. Damage of the flood plain (KOWACO,2002)

	1st Flood	2nd Flood(RUSA)
Death	16 person	246person
Cause	Long time inundation	Flood and landslide caused by typhoon
Area	Along the Nackdong river	Nackdong river and East coast
Max. rainfall	405mm/24hr	880mm/24hr
Mean rainfall	400mm(13days)	157mm(3 days)
Damage	$920,000,000	$ 5,114,790,000
Occurred date	3. Aug~15.Aug (heavy rainfall)	30.Aug ~1.Sep (Typhoon)

Table 2 illustrates flooding area, rainfall and cause during August 2002[4]. At that time the water level reaches over 5m above msl. Generally NRFCO[7] alert river residents to prepare for flooding at 70% level of planning flooding and operate all over the district. In the case of the flooding area represented in the diagram as (E), present water level is 2.0m.

Table 2. A representative flooding site in Nackdong basin

Site	Flooding Location	Area	Participation	Cause
A	Hapchun-gun chugduk-myun	100 ha	814.5mm	Collapse of banks
B	Hapchun-gun gahyun-ri	100 ha	814.5mm	Collapse of banks
C	Haman-gun bupsu-myun	320 ha	760.1mm	Collapse of banks
D	Kimhae-si hanrim-myun	720 ha	1,114mm	Collapse of banks
E	Yangsan-si mulgum-up	520 ha	695 mm	Flooding of banks

2.3 Data used and methodology

For the multiple criteria valuation technique, we choose multiple factors and determine their relation and how they impact the flooding areas(table3). Then, we make the layers of a thematic map, which is a raw data acquisition, and transfer to appropriate GIS layers. GIS environments consist of ArcGIS9, ERMapper and establish a GIS data table of flood information.

Table 3. Raw data to make the multiple factors

Criteria	Data type
Geomorphology	Terrain map unit Previous occurrences of flood
Topography	Digital Elevation Model Slope change Slope direction
Hydrology	Discharge Meteorological data(precipitation) Water level
Remote sensing	Normalized Difference Vegetation Index Water area Land Cover

3. Result and discussion

3.1 Geomorphology

Geologically the Nackdong Basin represents part of the Archeozoic era, which is comprised of granite, sedimentary rocks and plutonic/hypabyssal rocks. Nackdong river flows a gneiss system in its upper-stream and a Mesozoic formation in its mid-stream. Finally, it flow a melaphyre in its lower-stream. Flows, therefore, get wider and slower as the gentle slope of discharge increases. Nackdong river flows through geo-morphologically and tectonically stable regions which are affected by frequent flood-producing heavy rain[7]. Table 4 shows a characters of Nackdong Basin. In the summer of 2002, the main causes of floods were heavy rainfall and typhoon RUSA. Flash floods frequently occur due to its local geological and topographic features and climatic conditions in the nearby mountainous area.

Table 4. Characters of 6 rivers in a Nackdong Basin

River	Nackdong	Hyengsan	Taewha	Suyeng	East	West
Area	23,702.0	1,139.99	660.9	865.4	2,895.0	2,448.6
Perimeter	1,097.1	19.73	162.3	341.6	792.2	2,101.6
Height.ave	291.2	177.30	188.4	130.2	237.9	121.4
Height.max	1,911.9	849.64	1,227.1	901.0	1,135.0	836.3
Gradient.ave	32.3	27.39	27.7	24.1	36.2	29.8

3.2 Topography

Using a digital map on a scale of 1:25,000, it is possible to extract and examine the contours of the geography. Utilizing this map we can produce a 3D DEM(Digital Elevation Model) which is established from a TIN; with primary topographic attributes by 30m, such as mean elevation[5]. DEM data represents that there is not only a gentle slope but a few flood plains like the Kimhae plains. The height of a study area is between 0 and maximum value of 359.9m.

3.3 Hydrology

Nackdong river Basin is influenced by monsoonal rains. The average annual rainfall in the Nackdong river Basin is 1,231 mm/hr. Compared to the average annual rainfall in Korea, it is approximately 1274mm. About 64% of the annual rainfall occurs during the monsoon months from June to October[7].

3.4 Landsat TM Image Analysis

We produce the thematic map and data from TM image analysis using ERMapper 7.0 and ArcGIS9.0. The NDVI, a simple numerical indicator that can be used to analyze remote sensing measurements, typically assess whether the target being observed contains live green vegetation or not. When examining Landsat's images, we can concentrate on the images that separately show the levels of NDVI and the water distribution separately. However, it is important to consider the connection between NDVI and the water distribution present in the flooding. Hence, in the case of the lower NDVI values, we can make an estimate of the location of higher risk that flooding cause more than any place.

Unsupervisor Classification using ISODATA(Iterative Self-Organizing Data Analysis Technique) clustering method was used in order to examine multiple possible criteria data extraction. To focus on a weak point of flooding in the basin, 6 classes were included in the scheme: forest, urban, road, soil, water and barren land. The spatial distribution of all 6 classes was extracted from Landsat TM in April 2002. The class areas in this study were a forest of 4238.453km2(37.30%), urban area of 1295.598km2(11.40%), road area including concrete and asphalt area of 461.684km2(4.06%), soil area including agriculture area of 1060.624km2(9.33 %), water area of 23504.209 and an area of barren land of 803.996km2(7.07 %).

3.5 Vulnerability map

In order to get a good grasp of flash flood mechanisms, we extracted multiple factors from the flood information. The selected factors were composed of four main parameters. The value of Geomorphology(G) ranges from 0 to 1, the value of Topography(T) ranges from 0 to 10, The value of Hydrology(H) ranges from 0 to 5, The value of Image Analysis(I) ranges from 0 to 6. P(x) value indicates a flooding index in the rate of occurrence in basin and Σ An value totally indicates 1.0 in equation (1). In detail, the weight of the parameter are equally 0.25 respectively for the history of flooding, water level, Landcover, monthly rain fall, gradient of main drainage, NDVI and width of stream. The calculated and extracted data were converted to a 30m pixel, spatial resolution, and ArcGIS grid type for analyzing.

$$P(x) = A_1G(x_1)+A_2T(x_2)+A_3H(x_3)+A_4I(x_4) \quad (1)$$

We process and overlay multiple criteria from a training data, field data and large scale 1:5,000 digital map. We produce a vulnerability map to overlay and Calculate the following: existing history of flooding, a water level of over 5m msl, gradient of main drainage about 0, monthly rain fall of 700 mm/month, Landcover of soil and urban Landcover, NDVI of less than 0.2 and width of stream more than 50 degree.

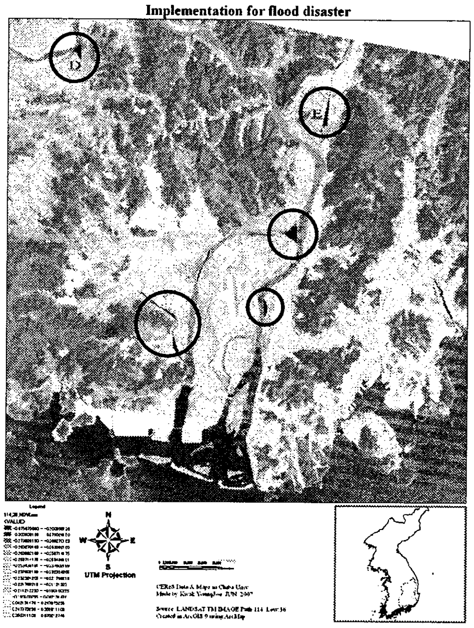

Fig. 2. Implementation for flooding disaster

The circle segments of Nackdong river are an isthmus which poses danger and regular flooding of about 20km surround E site(Fig.2).

Although loss of life in floods during recent occurrences has declined, mostly because of improved warning systems, economic losses have continued to rise due to increased urbanization. As we know, there are many land classes such as urban, agriculture and barren. Useful land is the most important resource for human activity. For the government, the management of a river is primarily concerned with human livelihood without considering nature. Analysis of urban flooding and natural disaster in a basin must be analysed differently. Particularly, urban flooding has more variety and requires more consideration of time and spatial analysis than natural disasters. In this study, it fairly known that sub-stream meets a main stream and flows backward against high speed energy of main stream. We are evaluating floods from previous occurrences and natural disasters in order to prevent future occurrences.

4. Conclusion

We suggested determining a methodology for diminishing floods using spatial analysis and image analysis in the Nackdong river basin, but we approach decreasing hazard from a geomorphologic point of view, rather than a regional one. This method, we can conclude the location of utmost danger. This study can be summarized as follows:

1) Topolocially and geologically, it is difficult for water to flow through the gentle and lower valleys at the lower stream(flooding site E). Moreover, flooding occurs at a bend against the main stream and respectively at an isthmus. An isthmus of sub-stream meets a main stream and flows backward against high speed energy of main stream.

2) According to the characteristics of a river system and the Nackdong basin GIS information data from the flooding field, we can conclude the location of higher risk in the Nackdong basin. We extract not only the risk parameters but also geomorphologic relation, which we then analyzed to generate multiple criteria such as water level, DEM, aspect, slope and image analysis of Landcover, NDVI in Nackdong basin. We then produced a Vulnerability map.

3) The vulnerable areas of a flood in the study were evaluated in near river and lower urban areas. The results can be realistic only for specific conditions. Furthermore, using a high resolution image and field survey during flooding time, will be more useful in producing a hazard map. We have suggested a basic function and risk management of GIS data and image analysis of a flood, but viewed from a different standpoint, we must develop a monitoring technique which will control a real-time GIS image and hazard map of pre, present and post-flooding.

References

1. Antonie, J., Fischer, G. and Makowski, M., 'Multiple criteria land use analysis', Applied Mathematics andComputation. Vol.85 pp.195-215, 1997.
2. FEMA, Federal Emergency Management Agency, http://www.fema.gov/hazard/flood.
3. Kale and Hire, 'Effectiveness of monsoon floods on the Tapi River, India: role of channel geometry and hydrologic regime', *Geomorphology* 57, pp. 275–291, 2004.
4. KOWACO, Korea Water Resources Cooperation, http://www.wamis.go.kr.
5. Kwak Youngjoo, Jang Yonggu, Kang Injoon, 'Web GIS Management and Risk Evaluation of a Road Slope Using a Terrestrial LiDAR', International Conference on W2GIS 2005, LNCS 3833, pp.256-266, 2005.
6. Lee Misun, Park GunAe, Kim Sungjun, "A study on the extraction of flood inundated scar of rural small stream area using RADARSAT SAR images", Journal of Korea Water Resources Association, Vol.39 No.11 pp.969-976, 2006.
7. NRFCO, Nakdong River Flood Control Office, http://www.nakdongriver.go.kr/
8. PWRI, 'Estimation of Cut Slope using GIS', Joint-Research Report, Public Works Research Institute, 2004

Monitoring Kashiwa City Using Remote Sensing

Katsumi Ohyama[1], Luhur Bayuaji[2] and Josaphat Tetuko Sri Sumantyo[2]
[1]Center for Environment, Health, and Field Sciences, Chiba University
[2]Center for Environmental Remote Sensing, Chiba University
E-mail: k_ohyama@faculty.chiba-u.jp

Abstract

Remote sensing measurements are widely used in various fields such as monitoring underground resources, environment, agricultural information, and volcanic activity. The purpose of this study was to monitor the development of Kashiwa-no-ha Campus Station and its surrounding area. This was done using visible and near-infrared images (VNIR: 0.52–0.86 μm), short-wave infrared images (SWIR: 1.60–2.43 μm), and thermal infrared images (TIR: 8.125–11.65 μm) acquired by the Advanced Spaceborne Thermal Emission and Reflection Radiometer (ASTER)—an optical sensor mounted on the Earth observation satellite TERRA (EOS AM-1) launched in 1999. Continuous monitoring of the target area, where land use has been changing dramatically due to the introduction of the railway (Tsukuba Express line) and the construction of buildings, will contribute toward sustainable development of the target area as well as increase the quality of life for the people living in this area.

1. Introduction

Regional sustainable development requires a balance among diverse social goals, for instance environmental conservation and/or improvement vs. economic development (Zhang and Guindon, 2006). The fulfillment of single factor is not sufficient to improve regional sustainability, and thus, comprehensive investigation with respect to the social goals is essential. A comprehensive investigation is more important in a developing region than in a developed region because of possible alterations in its development plans. For further improvement in the regional sustainability, transitions in the land use and environmental indicators (e.g., vegetation index and surface temperature) between the past and present need to be compared quantitatively. The objective of this study is to demonstrate that satellite remote sensing can be used for determining land use, and thus, for evaluating regional sustainability at a low cost.

2. Materials and Methods

2.1 Target Area

Images of an area neighboring Tsukuba Express (railway) in Kashiwa City (northwest region of Chiba Prefecture, Japan; Fig. 1 and Table 1) acquired by the Advanced Spaceborne Thermal Emission and Reflection Radiometer (ASTER) on the Earth observation satellite TERRA (EOS-AM1) were used. In Kashiwa City, especially in the area neighboring Tsukuba Express line, land use has been changing dramatically. The introduction of the railway increased accessibility to Tokyo, resulting in rapid construction of buildings (e.g., shopping malls and houses), increase in the population, and decrease in the cultivation area and/or green area. Hence, Kashiwa-no-ha Campus Station (35°53'34"N, 139°57'9"E) and its surrounding area (radius: 5 km) was intensively analyzed.

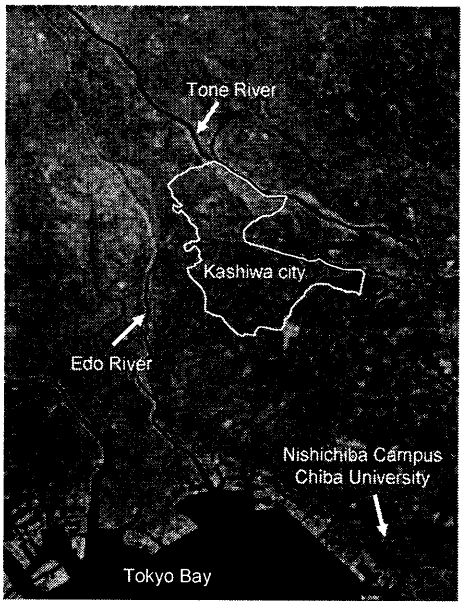

Fig. 1 Location of Kashiwa City.

Table 1 Profile of Kashiwa City

Area:	114.9 km^2
Location:	35°46'41"N–35° 55' 58"N 139°54'59"E–140°06'55"E
Altitude:	0–32 m
Population:	386,050 (as of April 1, 2007)

2.2 Data Acquisitions

The Earth observation satellite TERRA, which was launched on December 18, 1999 and began to operate on February 24, 2000, employs a radiometer complex called ASTER. ASTER consists of three radiometers: a visible and near-infrared radiometer (VNIR: 0.52–0.86 μm), a short-wave infrared radiometer (SWIR: 1.60–2.43 μm), and a thermal infrared radiometer (TIR: 8.125–11.65 μm). The surface resolutions of VNIR, SWIR, and TIR are 15, 30, and 60 m, respectively (Earth Remote Sensing Data Analysis Center, 2001). The Observation data acquired by ASTER were provided by the organization ASTER Ground Data Service (GDS) for the public. In addition, the cost for obtaining the image data acquired by VNIR, SWIR, and TIR (Level 1B) is 10,450 Japanese Yen (approximately US $90).

For evaluating land use in the city, VNIR, SWIR and TIR images acquired by the ASTER wherein the scene cloud coverage was less than 10% were used (Table 2). Based on the analyses of the images, transitions of land use and environmental indicators [i.e., normalized difference vegetation index (NDVI) and the surface temperature] were tracked.

Table 2 The ASTER images used in this analysis.

No.	Product Name	Scene cloud coverage	Date
1	ASTL1B 0005160148350606220620	3%	05/16/2000
2	ASTL1B 0104010143480607220615	0%	04/01/2001
3	ASTL1B 0106040142330106111171	5%	06/04/2001
4	ASTL1B 0109240139240606220619	0%	09/24/2001
5	ASTL1B 0210130134190606220617	0%	10/13/2002
6	ASTL1B 0309300133060607220598	0%	09/30/2003
7	ASTL1B 0404250133210605310528	0%	04/25/2004
8	ASTL1B 0509030132280605130005	0%	09/03/2005
9	ASTL1B 0605010132470605050465	1%	05/01/2006
10	ASTL1B 0611090132430611090018	0%	11/09/2006

2.3 Data Analyses

2.3.1 NDVI

In order to find the NDVI value using ASTER data, the following formula from Stafanov *et al.* (2005) was applied.

$$NDVI = \frac{Band3N - Band2}{Band3N + Band2} \qquad (1),$$

where *Band 3N* is the near infrared in nadir off, and *Band 2* is the visible red reflectance.

2.3.2 Surface temperature

In order to retrieve temperature information, an algorithm for brightness temperature was employed to convert the radiance value observed by the sensor to the temperature value. As described in Alley *et al.* (2001), the most straightforward method was to rely on the central wavelength λ_i of each channel i (i = 10 – 14). The brightness temperature T_i in degrees Celsius was calculated as follows:

$$T_i = \frac{c_2}{\lambda_i \log\left(\dfrac{c_1}{\lambda_i^5 \pi L_i} + 1\right)} - 273.15 \qquad (2),$$

where c_1 is the first radiance constant (3.741775 × 10^{-22} W m^3 μm^{-1}), c_2 is the second radiance constant (0.0143877 m K), and L_i is the radiance observed for the ith channel. The radiance L_i could be derived from the digital number (DN_i) as follows:

$$L_i = k_i(DN_i - 1) \qquad (3).$$

The unit conversion coefficient k_i and central wavelength λ_i of each TIR channel are listed in Table 3. Based on our ground sampling, the composition of hot mud was 70% water and 30% particles. In view of this, here we employed the following empirical algorithm to derive the land surface temperature (*LST*):

$$LST = 1.16 - 1.07T_{10} + 0.49T_{11} + 1.13T_{12} + 0.78T_{13} - 032T_{14} \qquad (4).$$

Here, T_{10}, T_{11}, T_{12}, T_{13}, and T_{14} are the brightness temperature of channels 10, 11, 12, 13, and 14 of ASTER, respectively. The coefficients in equation (4) were derived from the mud surface type described by Matsunaga *et al.* (2002).

Table 3 Central wavelength and conversion coefficient for TIR channels of the ASTER sensor.

Band	Central wavelength (μm)	Conversion coefficient (10^{-3})
10	8.30	6.822
11	8.65	6.780
12	9.10	6.590
13	10.6	5.693
14	11.3	5.225

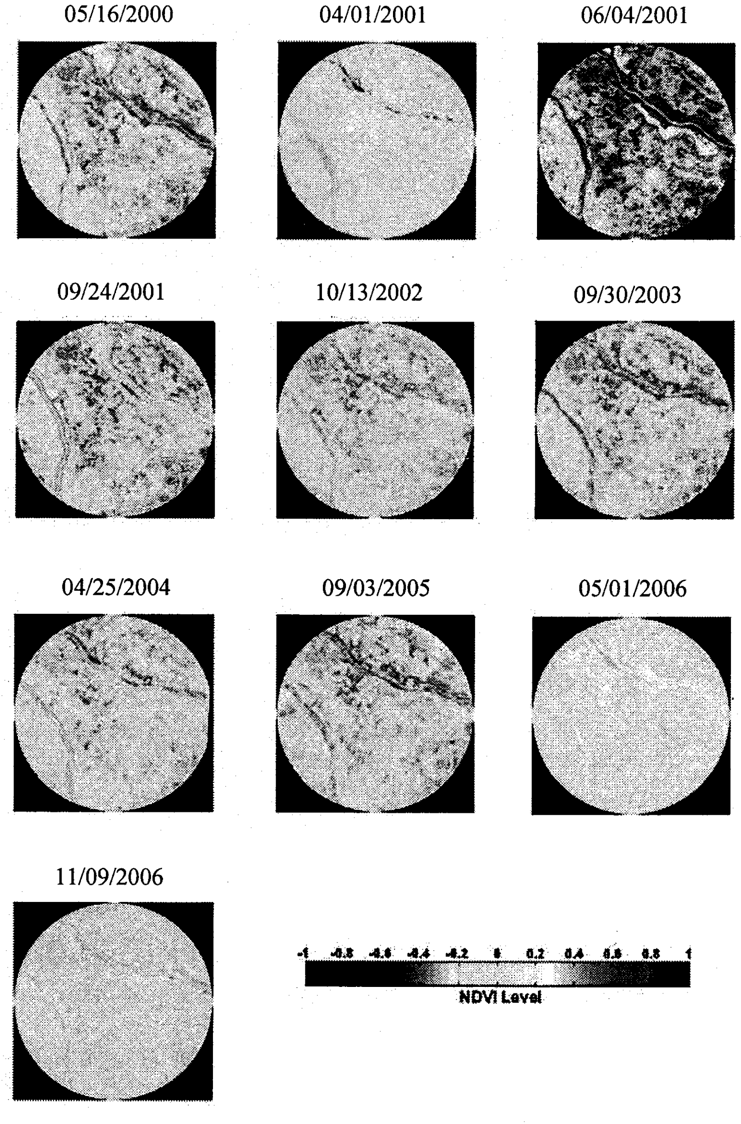

Fig. 2 Time course of NDVI around Kashiwa-no-ha Campus Station.

2.3.3 Data processing

The data were processed using a program called "ITTVIS ENVI" written with IDL programming language in order to select the region of interest (ROI), process the temperature brightness from the digital number, and calculate the NDVI value. The plot was determined using the software MATLAB from The Mathworks Inc. because this software is more flexible and is equipped with more functions than VIS ENVI.

3. Results and Discussion

Profiles of NDVI and LST around the Kashiwa-no-ha Campus Station are shown in Figs. 2 and 3, respectively.

Around the Kashiwa-no-ha Campus Station (center of the images in Fig. 2), the NDVI was higher in 2000 than in 2006. While the campus station previously contained a golf course and a forest, drastic changes in land use occurred after the introduction of the railway. Thus far, most of the vegetation has been destroyed. Further, buildings are continually being constructed.

Although obvious differences among the LST images were not observed (Fig. 3), the surface and air temperatures around the Kashiwa-no-ha Campus Station can increase in the near future due to the decrease in vegetation, which facilitates sensible and latent heat exchange. To prevent the increase in the air temperature in the area, i.e., the so called "heat island phenomenon," the amount of vegetation should be maintained or increased while simultaneously striking a balance between vegetation and city development.

For practical purposes, air temperatures in Kashiwa City were essential for evaluating thermal environment of the people living there. However, in this research, only information regarding LST was obtained. We plan to measure meteorological data in Kashiwa City at a resolution of 1–2 km. Combining and/or comparing the meteorological data observed on the ground and the data acquired by ASTER will clearly show the effect of city development on the climate around Kashiwa-no-ha Campus Station.

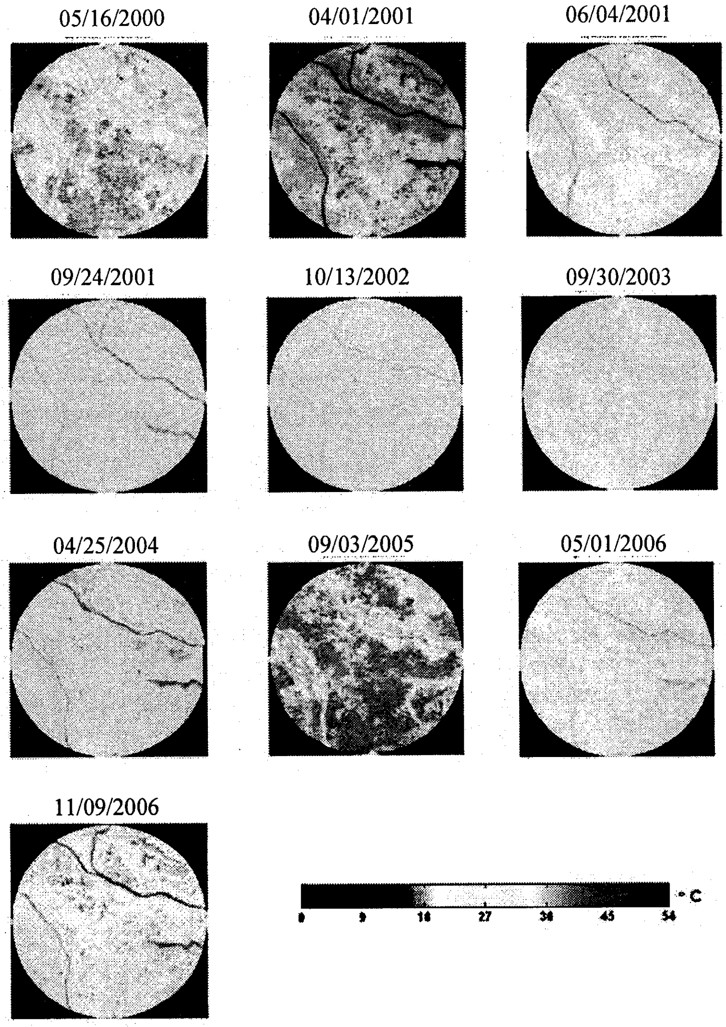

Fig. 3 Time course of LST around the Kashiwa-no-ha Campus Station.

4. Conclusion Remarks

The normalized difference vegetation indexes (NDVI) and land surface temperatures (LST) around the Kashiwa-no-ha Campus Station (Tsukuba Express line) were obtained from the images acquired by ASTER on the Earth observation satellite TERRA. As we mentioned above, in Kashiwa City, especially in the area neighboring Tsukuba Express line, land use has been changing dramatically. Hence, some diagnostic tool for evaluating the land use was required for the sustainable development of the city. Continuous monitoring of the target area using remote sensing will contribute to sustainable development of the city as well as increase the quality of life of the people living in this area.

References

Alley, R.E. (2001) ATBD-AST-02 Algorithm Theoretical basis document for brightness temperature. Standard Product AST04 Report, The Jet Propulsion Laboratory, California Institute of Technology, Los Angeles, CA.

Earth Remote Sensing Data Analysis Center. (2001) ASTER LEVEL 1 data products specification (GDS Version) Ver. 1.3, AG-E-E-2209-R03

Matsunaga, T., T. Ueki, M. Naya and T. Tachikawa (2002) Validation of ASTER water surface temperature algorithm using in-situ water temperature data in Tokyo Bay, Remote Sensing Society of Japan, pp. 191–192

Stefanov, W.L. and M. Netzband (2005) Assessment of ASTER land cover and MODIS NDVI data at multiple scales for ecological characterization of and arid urban center, Remote Sensing of Environment, pp.31–43

Zhang and Guindon (2006) Using satellite remote sensing to survey transport-related urban sustainability Part 1: Methodologies for indicator quantification. International Journal of Applied Earth Observation and Geoinformation 8: 149–164

DEVELOPMENT OF CIRCULARLY POLARIZED SYNTHETIC APERTURE RADAR ONBOARD MICROSATELLITE

Chiba University ・ ○J. T. Sri Sumantyo, Nihon University ・ H. Wakabayashi, Tokyo University ・ A. Iwasaki, JAXA ・ F. Takahashi, Sentencia Corporation ・ H. Ohmae, NIES ・ H. Watanabe, Chiba University ・ R. Tateishi, Chiba University ・ F. Nishio, Chiba University ・ M. Baharuddin, and Chiba University ・ P. Rizki Akbar

ABSTRACT

Previously, several types of synthetic aperture radar (SAR) sensor have been developed for many applications. These sensors work in linear polarization, high power, bulky system, and sensitive to Faraday rotation effect. To solve these problems, recently, we are developing a new type of microsatellite onboard synthetic aperture radar sensor called Circularly Polarized Synthetic Aperture Radar (CP-SAR) to improve the quality of conventional type of SAR images. The interest in the earth observation technologies is expected to increase with the CP-SAR in the coming years. In this paper, the specification of CP-SAR system is discussed.

I. INTRODUCTION

Synthetic Aperture Radar (SAR) is a multi purpose sensor that can be operated in all-weather and day-night time. Recently, the SAR sensor is operated in linear polarization (HH, VV and its combination) [1] with limited retrieved information. The characteristics of the conventional SAR sensor is bulky, high power, sensitive to Faraday rotation effect etc. Recently, we are developing the Circularly Polarized Synthetic Aperture Radar (CP-SAR) onboard microsatellite to retrieve the physical information of Earth surface, especially the Asian disaster area in the future.

In this research, the CP-SAR sensor is developed to radiate and receive circularly polarized wave. The sensor is designed as a low cost, simple, light, strong, low power or safe energy, low profile configuration to transmit and receive left-handed circular polarization (LHCP) and right-handed circular polarization (RHCP), where the transmission and reception are working in RHCP and RCHP+LCHP, respectively. Then these circularly polarized waves are employed to generate the axial ratio image (ARI). This sensor is not depending to the platform posture, and it is available to avoid the effect of Faraday rotation during the propagation in ionosphere. Therefore, the high precision and low noise image is expected to be obtained by the CP-SAR.

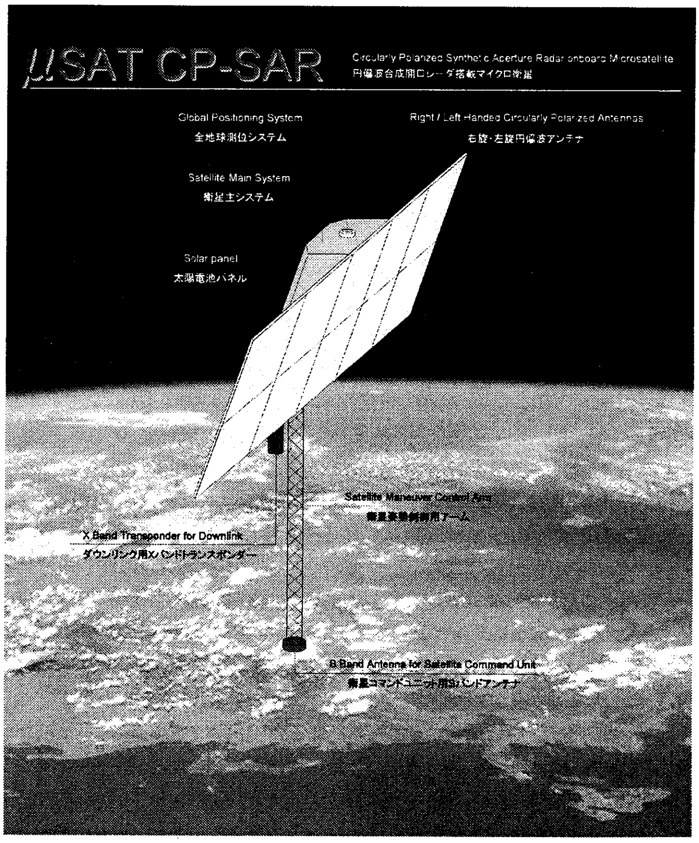

Fig. 1. Illustration of CP-SAR onboard microsatellite

The illustration of CP-SAR onboard microsatellite and its specification are shown in Fig. 1 and Table I, respectively. This satellite is composed by RCHP and LHCP antennas for CP-SAR sensor subsystem, telemetry subsystem that constructed by S band telemetry and X band transponder to transmit CP-SAR signal to ground station, and altitude controller subsystem (GPS, magnetic torque and reaction wheel assembly).

This satellite planned to be launched in 2012 with altitude between 500 km and 600 km. As shown in the specification of CP-SAR, this sensor is operated with center frequency 1.27 GHz (L band) and 10 MHz of chirp pulse bandwidth. The gain in main beam is set higher than 30 dBic to obtained received signal higher than -20 dB (equivalent backscattered noise level). The axial ratio is set lower than 3 dB to obtained ideal circular polarization. The antenna size is 1 m and 4 m for range and azimuth directions, respectively, to obtain the beamwidth 13.5° (range) and 3.4° (azimuth). The off-nadir angle is set 23°~ 35°, where the detail calculation to find this off-nadir angle will be discussed in the next Section. The transmittion antenna is RHCP, and reception is RHCP+LHCP. Fig 2 shows the developed circularly polarized antennas: (a) microstripline type, (b) microstrip type (Japan patent No. 2003-014301, International patent No. PCT/ JP03/05162, Japan patent No. 2006- 023701)

The ARI is expected to retrieve various information of Earth surface accurately and high precision. i.e. up-lift and subsidence, biomass, vegetation height and age, soil and snow physical characteristics based on the relationship between axial ratio and each characteristic. In the near future, CP-SAR is expected to improve the characteristics of conventional SAR system, especially to improve the application for disaster monitoring.

TABLE I

SPECIFICATION OF CP-SAR ONBOARD MICROSATELLITE

Parameter	Specification
Altitude	500 km ~ 600 km
Frequency f	1.27 GHz (L band)
Chirp bandwidth Δf	10 MHz
Polarization	Transmitter : RHCP Receiver : RHCP + LHCP
Gain G	> 30 dBic
Axial ratio AR	< 3 dB (main beam)
Antenna size	4 m (azimuth) 1 m (range)
Beam width	3.4° (azimuth) 13.5° (range)
Ground resolution	35.5 m
Swath width	55 km
Off nadir angle	23° ~ 35°
Power	300 W

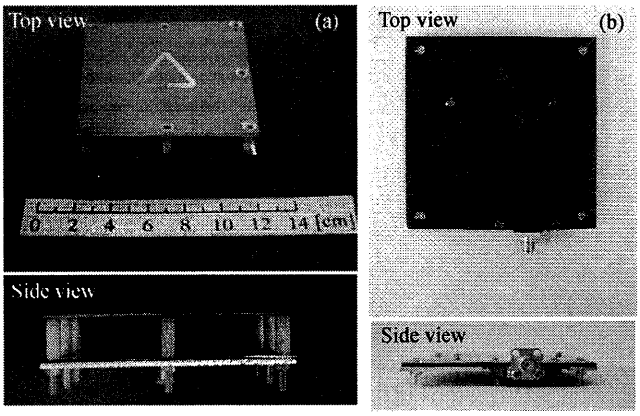

Fig. 2. Developed antennas for CP-SAR

II. PRF CALCULATION

Base on the CP-SAR hardware specification shown in Table I, especially the antenna size, altitude (500 km to 600 km), off-nadir angle 20° to 35°, and swath width 55 km; the satisfied PRF was calculated by procedure :

(1) Minimum frequency of Pulse Repetition Frequency (PRF) is decided by Doppler bandwidth employed in azimuth compression. Here, we must consider over sampling ratio to control the azimuth ambiguity to be low.

(2) Maximum frequency of PRF is reciprocal number of total time of transmission pulse width, reception gate time and transmission-reception switching time.

(3) All scattered wave from the target in swath area must be received in reception gate.

(4) SAR sensor transmits microwave to off-nadir direction, but scattered wave from nadir (nadir echo) is very high. Therefore, nadir echo received time must be set out of reception gate time.

Base on the above conditions, the result of PRF calculation for CP-SAR sensor is obtained as below.

(1) Azimuth Doppler frequency 3,830 Hz is obtained base on azimuth antenna size. Over sampling ratio is empirically set as 1.2 to control azimuth ambiguity. Therefore, low frequency PRF is obtained about 4,600 Hz and Signal-to-Ambiguity ratio S/A at azimuth direction is obtained 22.4 dB.

(2) Maximum PRF frequency obtained 5,556 Hz by considering transmitted pulse width $30\mu S$, reception gate $140\mu S$ to realize 21 km (slant range) swath width, transmission-reception switching time $5\mu S$. Finally, scattered waves from observed area (swath area) are captured during reception gate time by considering minimum and maximum PRF frequencies. The results of PRF for altitude 500 km and 600 km are shown in Fig. 3.

(3) Fig. 4 shows the PRF distribution by avoiding nadir echo to be observed in reception gate time.

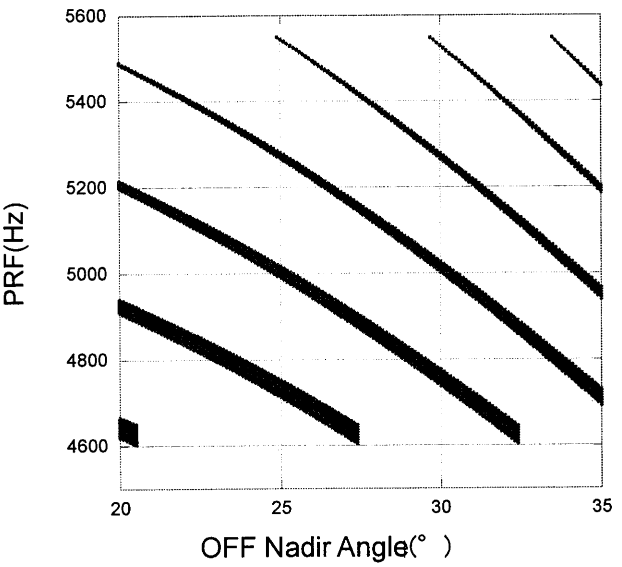

Fig. 3 (a). Satisfied PRF range (Altitude 500 km)

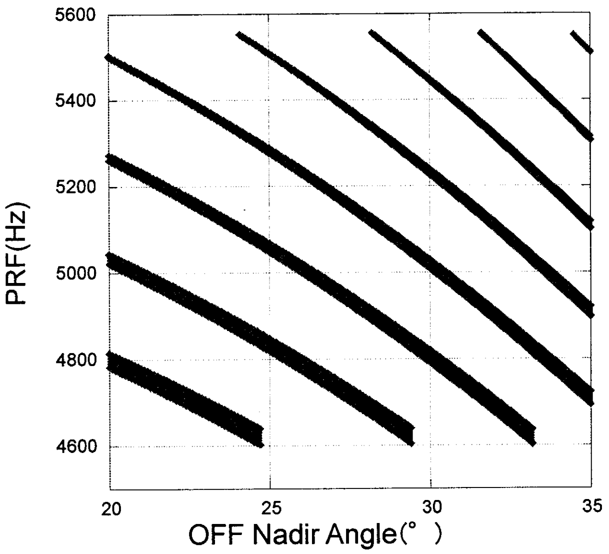

Fig. 3 (b). Satisfied PRF range (Altitude 600 km)

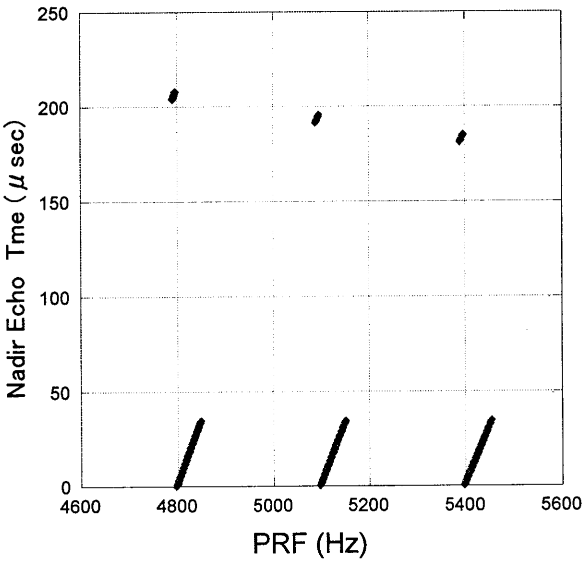

Fig. 4 (a). Nadir echo received time (altitude 500 km)

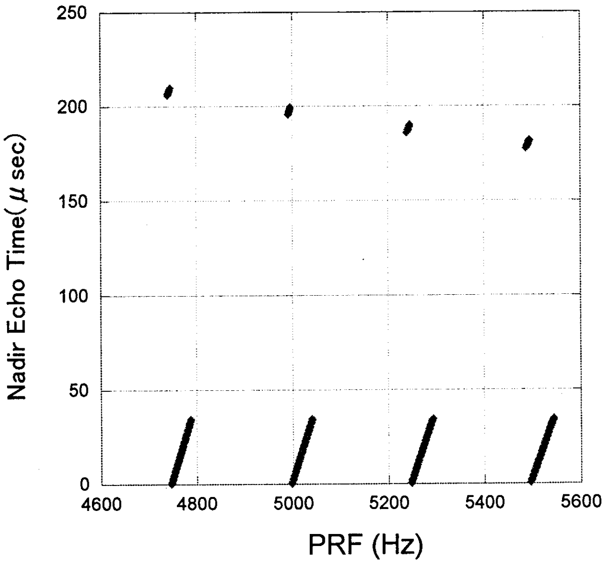

Fig. 4 (a). Nadir echo received time (altitude 600 km)

Figs. 3 and 4 show the relationship between altitude and off-nadir angle and satisfied PRF to secure the CP-SAR performance. The increasing of PRF will increase the average transmission power, data rate of CP-SAR and range ambiguity. Therefore the low PRF is must be selected to secure the CP-SAR performance. Base on Figs. 3 and 4, PRF 4,790 Hz ~ 4,850 Hz and 4,740 Hz ~ 4,790 Hz are the solutions for altitude 500 km and 600 km, respectively. Then off-nadir angle for altitude 500 km is 23°, 29° and 34°, and for altitude 600 km is 22°, 27°, 31° and 35°.

III. CP-SAR SYSTEM

Fig. 5 shows the CP-SAR sub-system that composed by signal generator unit to generate the chirp pulse with bandwidth 10 MHz. Then this signal flows to RF circuit to be coupled -10 dB as reference signal to derive the In-phase (I) and Quadrature (Q) signal. The 300W output signal is generated by antenna controller then transmitted by right handed circular polarization (RHCP) antenna (TX). For the experiment, both RHCP and left handed circular polarization (LHCP) will be employed together, but only RHCP will be employed in microsatellite onboard CP-SAR. The reception (RX) is constructed by LHCP and RCHP antenna. The dipole antenna that working with center frequency 1.27 GHz is employed for calibration and validation.

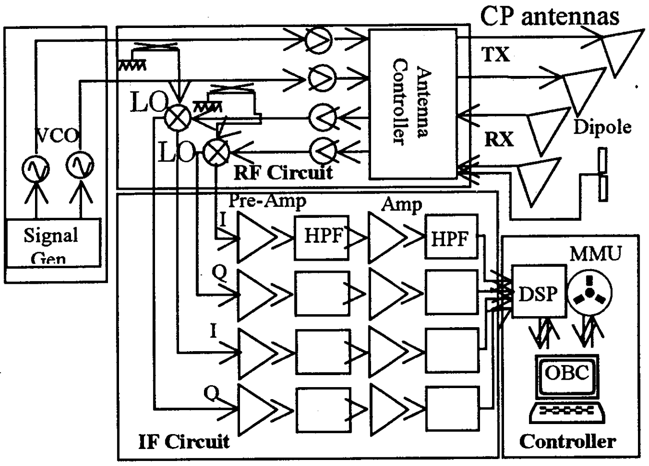

Fig. 5. CP-SAR Sub-system

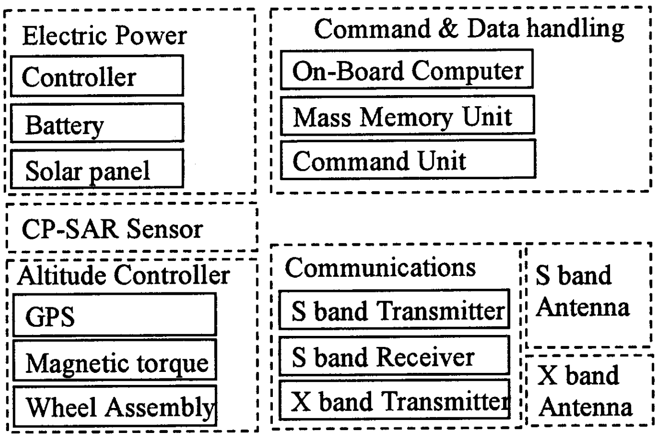

Fig. 6. CP-SAR onboard Microsatellite System

The received signal is amplified by Pre-Amp to obtain the satisfied intensity level. Then target signal is filtered by high pass filter (HPF). Then this signal is processed by DSP and On-Board Computer (OBC) in microsatellite. Temporary the signal is saved in Mass Memory Unit (MMU) before transmit to the ground station.

Fig. 6 show the CP-SAR onboard microsatellite system. This system is composed by CP-SAR sensor, electric power, altitude controller, command and data handling, and communications subsystems. Electric power subsystem supplies the electricity for CP-SAR sensor and other sub systems. In this sub system, the electricity collected by 3 m^2 solar panel then it charges the battery. The altitude of microsatellite is controlled by magnetic torque and wheel assembly. The information of microsatellite location is collected by GPS. This information is saved in the MMU add to the CP-SAR signal. These saved data transmit to ground station by using X band communication sub-system.Telemetry is held by using S band transmitter and receiver. Command and data handling subsystem is composed by MMU, Command Unit and On-Board Computer (OBC). The OBC is center to control the CP-SAR and other sub-systems in microsatellite. The received LHCP and RHCP signal will be processed to derive axial ratio image (ARI) to retrieve the physical information on the Earth surface. Fig. 7 shows the flow chart of CP-SAR signal processing.

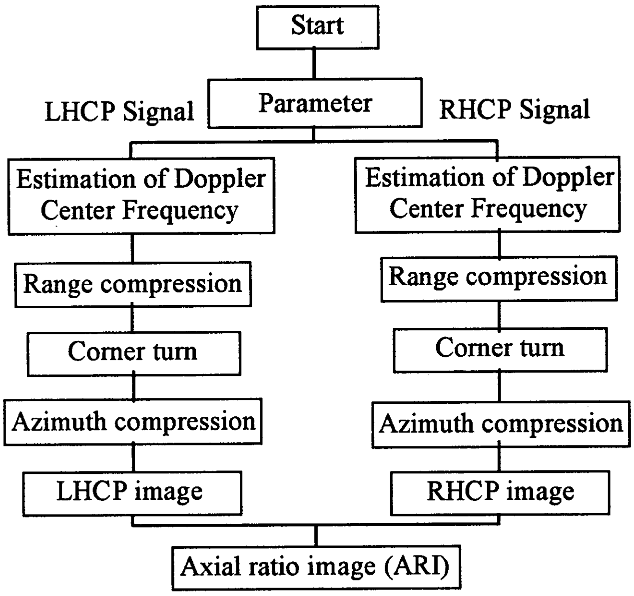

Fig. 7. CP-SAR Signal Processing flow chart

IV. CONCLUSION

In this paper, recently our laboratory developed the Circularly Polarized Synthetic Aperture Radar (CP-SAR) onboard microsatellite to retrieve the Earth surface. This sensor is developed to monitor the disaster, especially in Asian countries, i.e. forest fire, earthquake, flood, ice berg etc. The CP-SAR sensor is developed to radiate and receive circularly polarized wave. The sensor is designed to transmit and receive left-handed circular polarization (LHCP) and right-handed circular polarization (RHCP). These circularly polarized waves are employed to generate the new type of SAR image called axial ratio image (ARI).

REFERENCES

[1] http://www.asf.alaska.edu/reference/reference_docs.html

Urban Sprawl Phenomenon Detection Using Spectral Mixture Analysis (SMA) from Multitemporal Landsat Satellite Images: A case study in Bandung Basin, Indonesia

Ketut WIKANTIKA[1], Ivan PRATAMA[2], Akhmad RIQQI[2], Ibnu SYABRI[3], Y. Ihya ULUMUDDIN[1],
Syams NASHRRULLAH[1] and Firman HADI[1]
[1] Center for Remote Sensing, Institut Teknologi Bandung
[2] Geodetic and Geomatics Engineering, Institut Teknologi Bandung
[3]Urban and Regional Planning Engineering, Institut Teknologi Bandung
E-mail: wikantika@yahoo.com

Abstract
Bandung was a rapid developed city in Indonesia. However the development was unplanned and sporadic. It was urban sprawl phenomenon that was most found in developed countries. Our study was using Spectral Mixing Analysis (SMA) to detect the phenomenon using multitemporal Landsat satellite images. The most difficult process and crucial of the method was determination of end-member. The study could determine two end-member for one band of image and its were used to detect the urban sprawl phenomenon. The application of determined end-member could detect the urban sprawl and it shown that the pattern of residential land distribution is around primary road connecting Bandung and other cities around.

1. Introduction

Urban sprawl is defined as continues growth of urban areas, expanding to peripheral, sporadic and unplanned, and its always produce land use change from rural to urban use. The phenomenon emerges as response of spatial needs in rural for residential land, commercial and service areas, industrial areas, transportation, communication and utility land use and other public facility land use. Rapid population growth and urbanization were causes of sporadic and unplanned residential land development in rural areas. It is urban sprawl phenomenon that is found in Indonesia and other developed countries.

One of big cities that are rapidly developing in Indonesia is Bandung that has a unique magnetic power (Kompas, 2004). Bandung is one of center for mode in Indonesia. Textile and garment industries were spreading out in peripheral areas of Bandung City and it is supported by shop and store tourism for clothing and shoes. Culinary tourism is also supported the shop and store tourism. It could be unique magnetic power for tourists-most of them come from Jakarta-particularly after toll road Cikampek-Purwakarta-Padalarang corridor (connecting Jakarta and Bandung) has been opened. Not only it is making easy to access to Bandung from Jakarta, but also it could be magnetic effect for somebody, which is working in Jakarta, to live in Bandung and around. In addition, Bandung has many universities; there are three governmental universities and many non-governmental universities. Therefore many students from overall of Indonesia are interested in Bandung. All of them are making rapid urban growth in Bandung and it towards urban sprawl phenomenon.

Since 1970s, Bandung's decision-makers have known the phenomena mentioned-above. To solve the problem, Bandung and small cities around have been planned in "Bandung Raya Development" concept. But it is never being and to be far away from the concept; establishment of Cimahi City is the sign of the failure (Kompas, 2003). Unplanned urban growth is pictured on some spots such as Kopo, Setia Budhi, Ujungberung and Cimahi.

In our study will be investigated the using of multitemporal Landsat satellite images to detect width and distribution of residential land on the spots mentioned-above. Satellite images are time series data and it could be used for monitoring purposes. To achieve the aims of study, Landsat images (that has medium resolution in spatial) must be proceed by using particular methods. Thus the medium resolution satellite images could produce residential land map more accurately. Therefore Spectral Mixture Analysis will be developed in the investigation to produce the map.

2. Study area

The spots of residential land mentioned-above are in Bandung Basin. The areas include Bandung City, Kabupaten Bandung, Cimahi City and part of Kabupaten Garut and Sumedang. Fig. 1. is Bandung Basin map. :

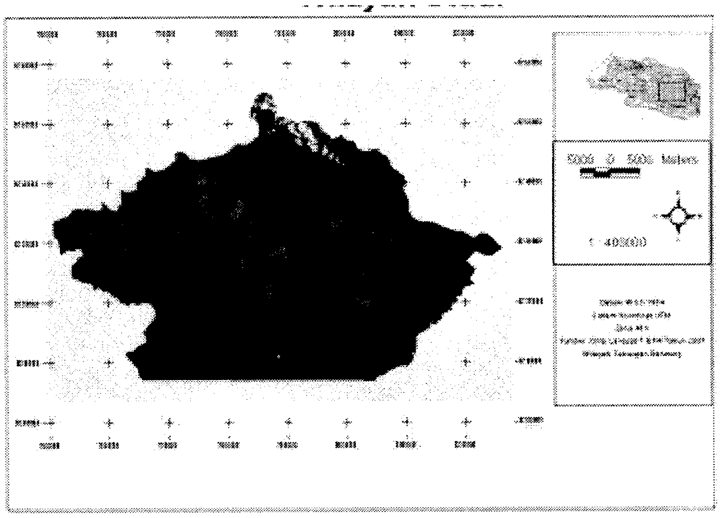

Figure 1. Bandung Basin

3. Data and Methodology

The study uses images of Landsat TM 1994, Landsat ETM 2001. The Landsat images are composite data, 6 bands (1-5 and 7). It is used WGS'84 for datum reference and SUTM 48 zone for projection system. The images are proceed through the stages which is shown in flowchart below:

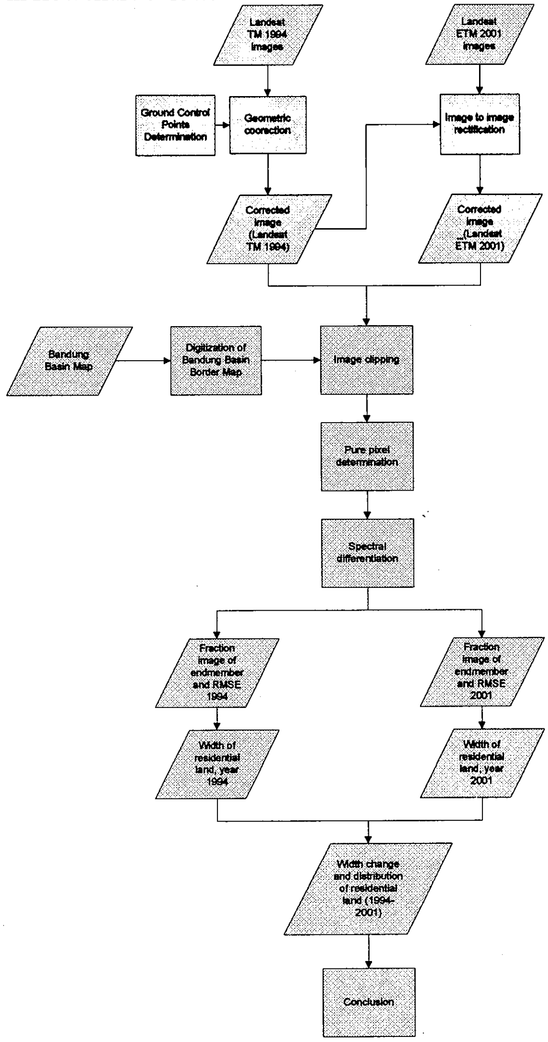

Figure 2. Flowchart of methodology

4. Spectral Mixture Analysis

Spectral Mixture Analysis (SMA) is a process or method to identify the different objects in one pixel of medium and low spatial resolution images. For example: Landsat and MODIS imagery respectively are 30x30 m and 250x250 m in spatial resolution. One pixel may contain more than one object, but one pixel has only one brightness value. By using SMA method, the proportion of the objects in one pixel can be identified and determined. Identified and determined the objects are defined as end-member.

The first process in SMA is determination of pure pixel. The pure pixel is pixel that contains brightness value of one object. Pure pixel determination is proceed through creating training sample end-member. The next process is calculation of each end-member fraction of images. The fraction of each end-member is inverse of matrix below (Peng and Uchida, 1999):

$$\begin{pmatrix} d_{i1} \\ d_{i2} \\ \cdots \\ d_{im} \end{pmatrix} = \begin{pmatrix} r_{11} & r_{12} & \cdots & r_{1p} \\ r_{21} & r_{22} & \cdots & r_{2p} \\ \cdots & \cdots & \cdots & \cdots \\ r_{m1} & r_{m2} & \cdots & r_{mp} \end{pmatrix} x \begin{pmatrix} f_{i1} \\ f_{i2} \\ \cdots \\ f_{ip} \end{pmatrix} \ldots\ldots\ldots\ldots\ldots\ldots\ldots\ldots (1)$$

or

$$D_i = R \times f_i \ldots\ldots\ldots\ldots\ldots\ldots\ldots\ldots\ldots\ldots\ldots\ldots\ldots\ldots\ldots\ldots (2)$$

where,

d_{im} = brightness value of pixel i and band m
r_{mp} = brightness value of end-member p and band m.
f_{ip} = fraction of end-member p and pixel i
n = pixel total of overall image

with requirements:

$f_{ik} \geq 0$, and
$f_{i1} + f_{i2} + f_{i3} + \ldots + f_{ik} = 1, \quad where\ i = 1, 2, 3, \ldots, n \ldots\ldots\ldots\ldots\ldots\ldots\ldots\ldots (3)$
and requirements of matrix to make its inverse matrix.

5. The Result of Spectral Mixture Analysis Application

According to the requirement of spectral differentiation matrix in eq (1), it was chose three cases for end-member determination, two end-member one band, three end-members two bands, and four end-members three bands. From three cases, two end-members one band was selected to detect residential land change in width and urban sprawl phenomena. The end-member determination is the most crucial process because probably pixels with the same brightness value (they have the same object) have different fraction magnitude. It can produce error in interpretation to define direction and magnitude of the changes. The result of selection of the cases is used to investigated urban sprawl phenomena on some spots in Bandung Basin: Kopo, Setia Budhi, Ujungberung and Cimahi.

5.1. *Urban Sprawl* in Kopo

Kopo areas are passed by Jalan Kopo as primary collector road collecting transportation from and to Bandung City (Fig 3). It is connecting Bandung hinterland around. It enhances the growth of residential land around Jalan Kopo (Kristiani, 2004).

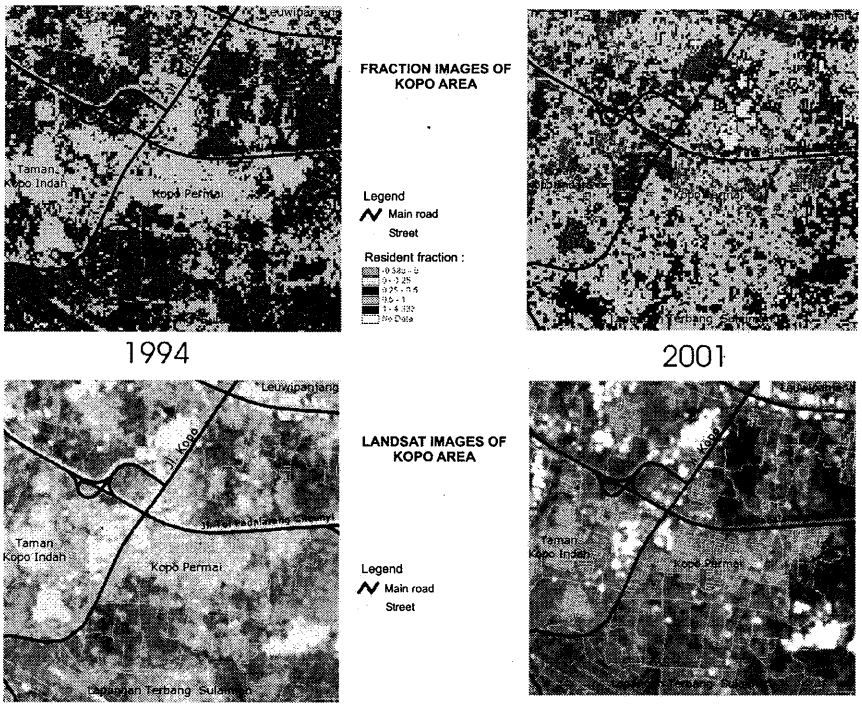

Figure 3. Fraction Images of Kopo Area

5.2. *Urban sprawl* in Ujungberung

Governmental Role number 16, 1987 (PP No. 16, 1987) gives a role of rural development in Bandung toward east. Unfortunately, residential land expansion is not only toward east but also toward west or center of Bandung City (Budianto, 2001). Residential land spreads out following primary road that the purpose of the road is as artery road connecting Bandung and others (Fig. 4).

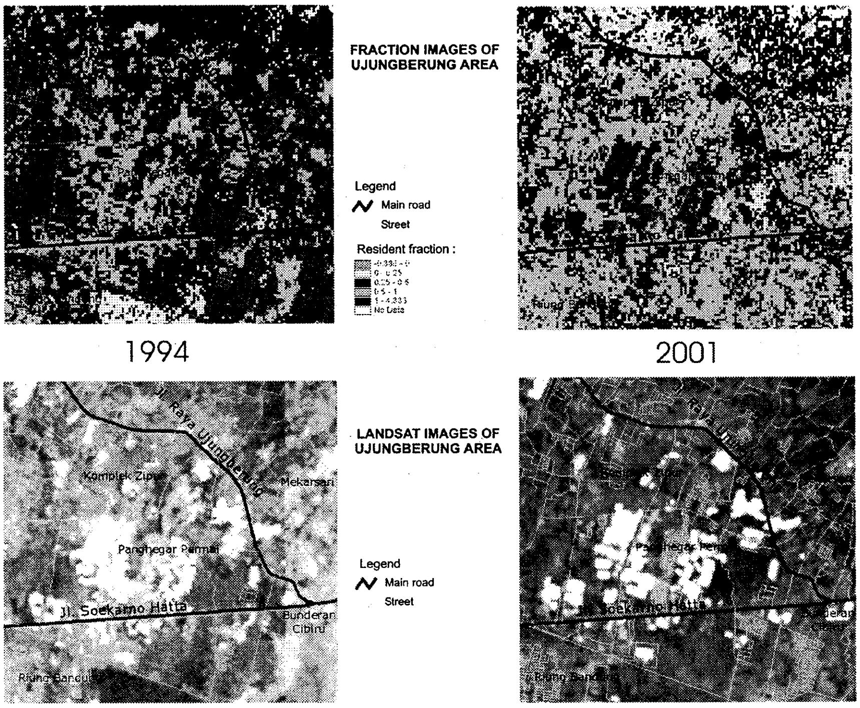

Figure 4. Fraction images of Ujungberung Area

5.3. *Urban sprawl* in Setia Budhi

The residential land of two spots above growths rapidly because it is supported by the road connected Bandung and others. Residential land expansion in Setia Budhi follows Jalan Setia Budhi, the easier access to governmental facilities and commercial and service facilities (Fig. 5). In addition, mountain air-fresh (ten years before) in Setia Budhi areas is one of reasons to build houses. Jalan Setia Budhi is also as primary road connected to tourism areas in Lembang and Kabupaten Subang.

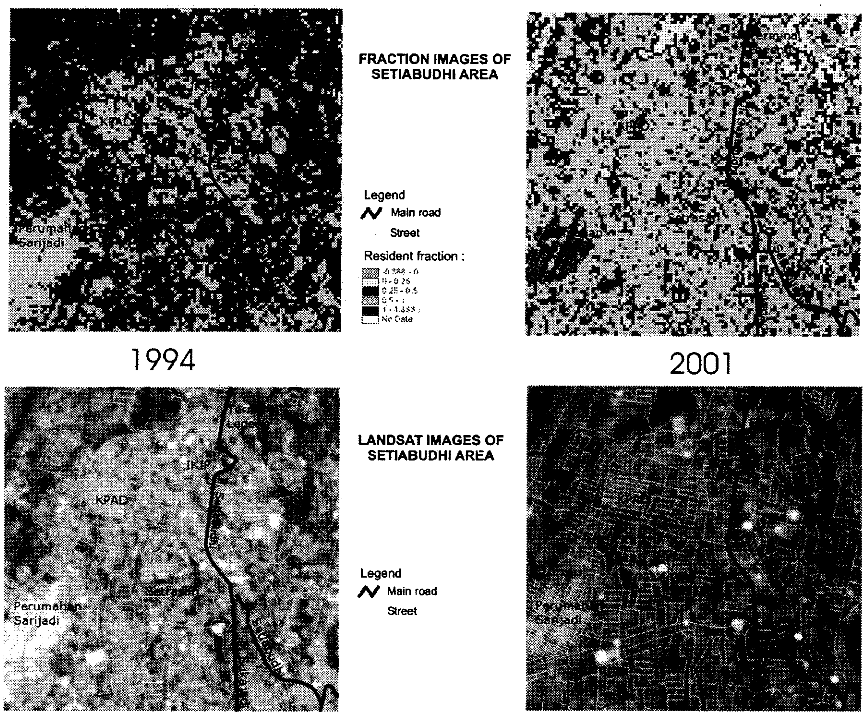

Figure 5. Fraction Images of Setia Budhi Area

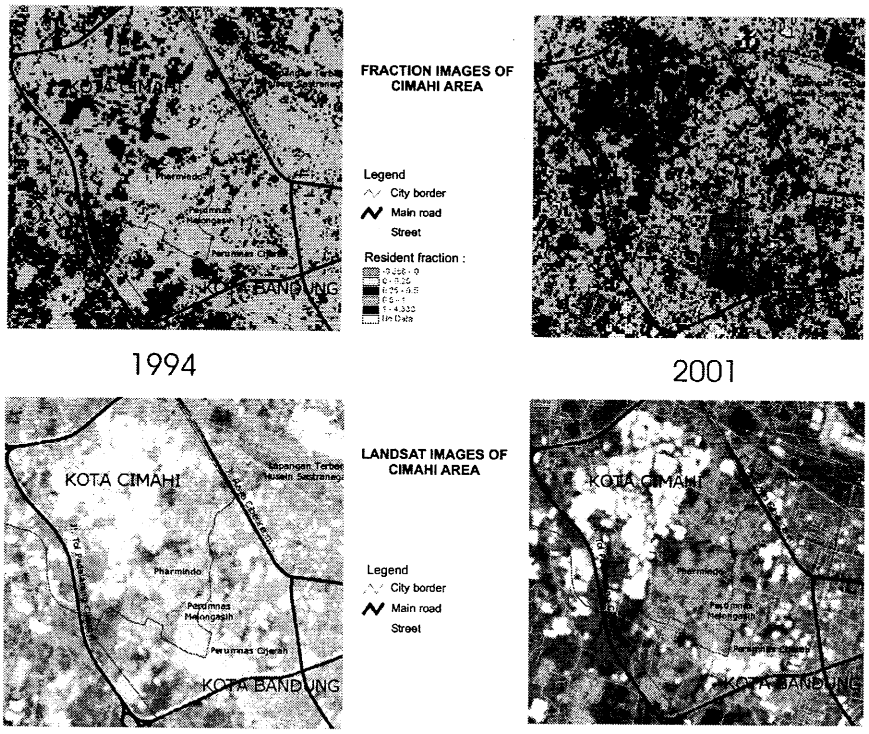

Figure 6. Fraction images of Cimahi Area

5.4. *Urban sprawl* in Cimahi

Different from three spots above, residential land expansion in Cimahi follows the rural growth as center for military training and education and industrial areas to improve the income of Kabupaten Bandung (before being Kota Cimahi). Residential land growth in the spot overlaps with the two activities. Population growth in Cimahi enhances development of commercial and service areas that its placement also overlaps with other land use. The development is enhanced by strategic position as a gate of Bandung City in the south (Fig. 6).

6. Conclusion

The use of Spectral Mixture Analysis method has difficulties on end-member determination. From three cases end-member determination, two end-members, one band was selected to detect residential land growth in Bandung Basin. In general, residential land growth on the spots investigated follows road development, particularly the roads connected to other city.

References

Budianto, F. 2001. Karakteristik Perjalanan Penghuni Perumahan Formal dan Pengaruhnya Terhadap Tingkat Pelayanan Jalan Raya Timur Bandung. Kasus Perumahan Formal di Kawasan Ujungberung Bandung. Departmen Teknik Planologi. Institut Teknologi Bandung. Bandung. Indonesia

Kristiani, L.A. 2004 Kajian Perubahan Tingkat Pelayanan Jalan Kopo Bandung dengan Pengelolaan Lalu Lintas. Skripsi. Departemen Teknik Planologi. Institut Teknologi Bandung. Bandung. Indonesia

Layuck, J. R. 2003. __________________. Kompas, 30 November 2003. Jakarta. Indonesia

Suganda, H. 2004. Bandung Raya, Apakah masih relevan?. Kompas, 6 Desember 2004. Jakarta. Indonesia.

Peng, Y and Uchidas. S. *The Use of Linear Spectral Unmixing Model for Improving Estimation Accuracy of Winter Wheat Acreage – A Case Study in Shunyi County*. Beijing. China.

Feature extraction and analysis of properties of NOAA-AVHRR data for geometric correction

Yoichi KAGEYAMA, Yoshiaki SHOJI, and Makoto NISHIDA
Department of Computer Science and Engineering, Faculty of Engineering and Resource Science, Akita University
E-mail: kageyama@ie.akita-u.ac.jp

Abstract

NOAA (National Oceanic and Atmospheric Administration)-AVHRR (Advanced Very High Resolution Radiometer) data are available on a daily basis and have been frequently used for global observations. Akita University, Japan, has been receiving the NOAA-AVHRR data since 2001. For a long-term analysis or monitoring in Asia, geometric correction is very important as a preprocessing technique.

Therefore, this paper essentially examines the features of the NOAA-AVHRR data acquired at Akita University for the geometric correction. First, the change information of the coordinates between before and after the geometric correction was analyzed by using the positional information of Japan Isl. Second, we analyzed the properties of three elements: fractal dimensions, run-length matrix, and co-occurrence matrix, as the indices to automatically extract ground control points (GCPs). The results suggest that the regions set by the study are useful to understand the features of geometric correction, and the run-length matrix is useful to extract the GCPs.

1. Introduction

Remote sensing serves as a powerful technique for monitoring environmental changes. Presently, various remotely sensed data are being used according to the required purpose. With land-use/land-cover changes in global regions, low spatial but high temporal resolution satellite output signals are being widely used. Two or more satellite data with poor resolution such as those obtained by NOAA-AVHRR are available on a daily basis and have been frequently used to understand global events. Many studies have been conducted with the help of the NOAA-AVHRR data(1)-(4).

In the database of the remotely sensed data, the amount of cloud per scene is used as one of the effective search indices. However, the operator is required to manually distinguish the amount of cloud in each data and register the value into the database(5). In order to perform an automatic evaluation of the amount of cloud by the reduction of work and the same standard of operators, it is necessary to automatically estimate the cloud amount with sufficient accuracy under the following conditions: (i) the range acquired in the NOAA-AVHRR data is different per data, although the receiving point is the same, (ii) the amount or location of cloud per data varies, and (iii) land- and sea-cover conditions are variable due to seasonal conditions. That is, the geometric correction based on the properties of NOAA-AVHRR is a very important preprocessing technique for various analyses.

In the conventional method for the geometric correction of the remotely sensed data, many GCPs are set to statistically determine the geometric transform of the equation because a 4–10 pixels of error arises in the geometric correction based on just the system information(6). For an automatic selection method of the GCPs, a scheme of geometric correction that focuses on the features of the coastline was developed(6)-(9). When clouds exist at the boundary of water and land, the boundary information becomes obscure and results in an error. It is therefore necessary to select the GCP by considering other features such as texture information. A new geometric correction method that directly determines the optimum geometric transform equation without choosing the GCPs was developed(10). Although the optimization on two parameters (scene center displacement) is sufficient for the relatively narrow area (18 km × 18 km) in the landsat thematic mapper (TM) images with a resolution of 30 m, the method is simply not applicable to the NOAA-AVHRR data with a resolution of 1.1 km; the ground resolution of the Landsat TM is considerably different from that of the NOAA-AVHRR.

The more precise the knowledge of the features obtained by the geometric correction, the more useful is the data. Therefore, this paper is concerned with the basic studies of the properties of the NOAA-AVHRR data acquired at Akita University for the geometric correction. First, change information on the coordinates between before and after the geometric correction processing was analyzed by using the positional information of Japan Isl. Second, we analyzed the properties of three textures: fractal dimensions, run-length matrix, and co-occurrence matrix, as the indices to automatically extract the GCPs.

2. Methods

2.1 Features of NOAA-AVHRR data

Akita University, Japan, has been receiving the NOAA-AVHRR data comprising five spectral bands since 2001. Due to the large width of the data (approximately 2800 km)(11), the range of observations corresponding to

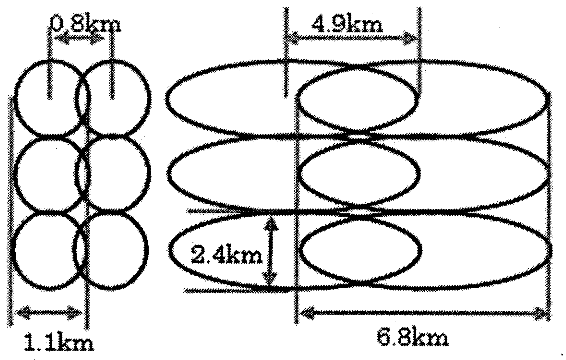

(a) Below the satellite (b) Ends of the observation

Fig.1 Relation between a pixel and the observation width.

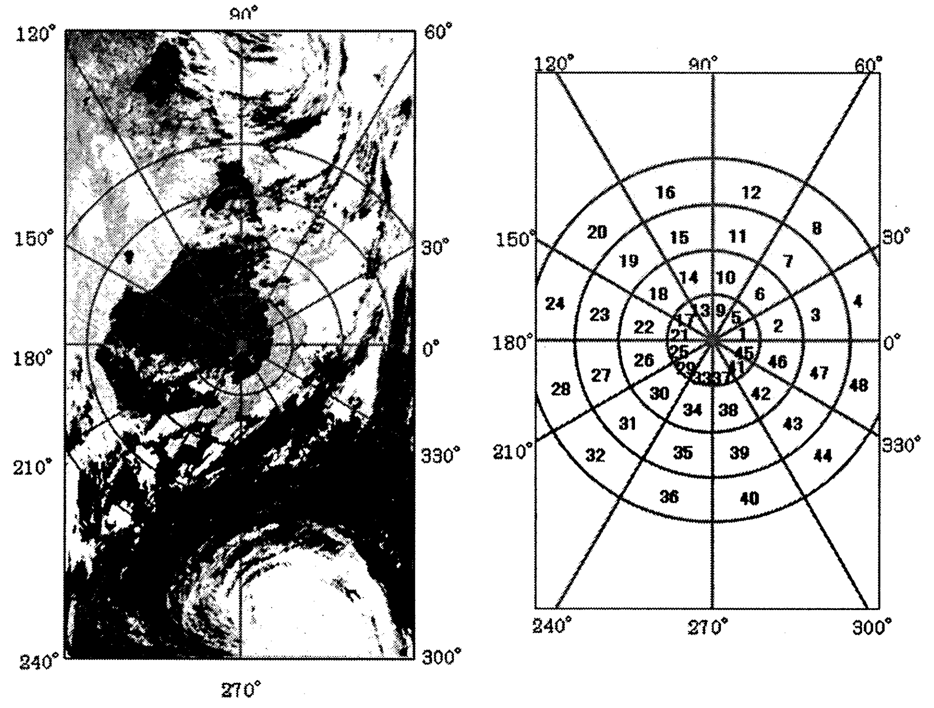

Fig.2 48 areas set in the study.

one pixel is variable. Figure1 shows the relation between a pixel and the observation width. The ground resolution of the data is 1.1 km immediately below the satellite on a horizontal scale; at both the ends of the observation width, a long axis serves as an ellipse of approximately 6.8 km(9). Also, the range of images acquired by NOAA-AVHRR is different per data, although the receiving point is the same as that for Akita University. Therefore, geometric correction is required for conducting data analysis with sufficient accuracy.

2.2 Change information of coordinates (Experiment 1)

This paper aims to examine the features obtained by geometric correction; the NOAA-AVHRR images are classified into the following three cases: (i) left (case 1), (ii) center (case 2), and (iii) right (case 3) by using the positional information of Japan Isl. per image. Then, the change information of coordinates, which are computed between before and after the geometric correction in the same point, is studied. The logical latitude and longitude of both the coordinates immediately below the satellite and four corners on a horizontal scale were set up manually by using the range of observations computed from the orbital information of NOAA in order to perform the geometric correction. The procedure consists of the following three steps:

Step1: In order to analyze the coordinates' change information in all the directions, focusing on the earth as a sphere, the domain was set every 30 deg from the central pixel of the image, and the image data was divided into the 12 directions.

Step2: Four concentric circles per 300 pixels were set from the image center. Then, 48 areas, namely area 1 through area 48, were set by combining the resulting four circles and the domain set every 30 deg, as mentioned in step 1. (See Fig.2)

Step3: The ratio of the digital number (DN) of the X coordinates of the image in the same points, which were computed between before and after the geometric correction, and the value acquired in each area was used as the change value in the area. Figure 3 shows an example of selecting the points from the images acquired before and after the geometric correction.

2.3 Features used for position specification (Experiment 2)

The width of the NOAA AVHRR output signals is approximately 2800 km and earth is a sphere; hence, the geometric correction is required to be improved using nonlinear interpolation. In order to perform the nonlinear interpolation process with sufficient accuracy, it is necessary to automatically extract the GCPs from a NOAA image while the conventional GCP method uses the manually acquired GCPs. Therefore, a fundamental examination is conducted for the feature that can be utilized as an index to extract the GCP. The following three elements are examined: fractal dimensions (12), run-length matrix (12), and co-occurrence matrix (12). In this experiment, we selected the Oga Peninsula (40N, 140E) near the receiving ground (Akita University) as the study site.

(1) Fractal dimension processing in consideration of occupancy of land area

First, the image including the Oga Peninsula is obtained in the size of 200 × 200 pixels after binary processing. Second, the window size that measures a fractal dimension is set as m × m pixels, and the fractal dimension of the neighboring eight images, shifted by eight pixels in four directions, is also measured (see Fig.4). Here, we set m = 32 after trial and error. Third, four occupancies of the land area located in the neighborhood of the central image are also computed. By using the abovementioned features, i.e., nine fractal dimensions and four occupancies of the land area, extraction of the Oga Peninsula is performed.

(2) Run length matrix processing

The run length was measured after binary processing. In order to compare the run length with the other features, the window size that measures a single run length is set as 32 × 32 pixels.

(3) Co-occurrence matrix processing

A NOAA image is transformed into 16 gray scales, and the area including the Oga Peninsula is extracted in the size of 200 × 200 pixels. Then, the co-occurrence matrix is measured in the window sizes of 9 × 9 and 16 × 16.

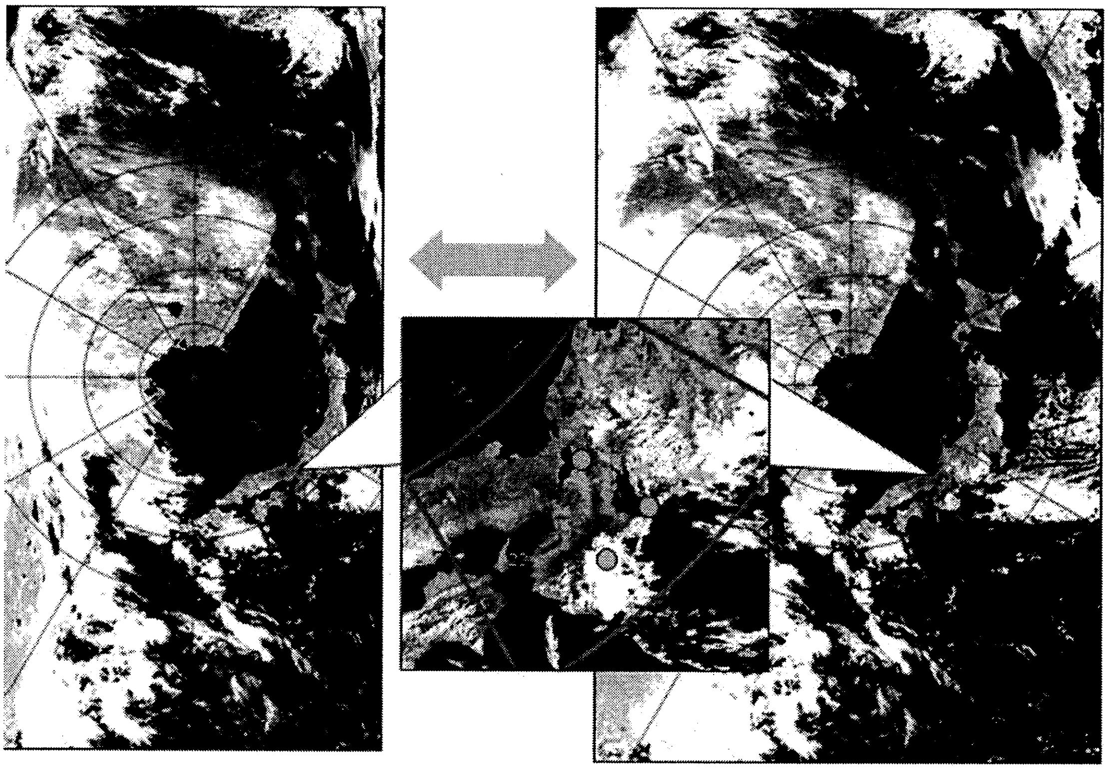

(a) Before geometric correction (b) After geometric correction

Fig.3 An example of selecting the points from the images acquired before and after geometric correction.

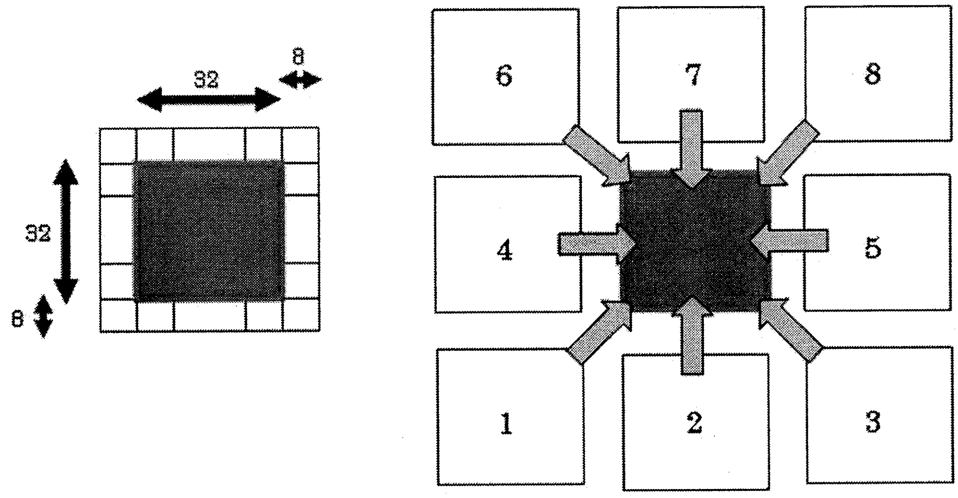

Fig.4 Calculation of fractal dimension.

Table 1. The calculation results of change value (Case 2)

degree	area	data6	data7	data8	data9	data10
0 - 30	1	1.22	1.24	1.25	1.25	1.24
	2	1.18	1.16	1.16	1.17	1.17
	3	1.19	1.17	1.17	1.17	1.18
	4	1.21	1.23	1.22	1.23	1.25
30 - 60	5	1.26	1.25	1.26	1.23	1.25
	6	1.19	1.18	1.19	1.19	1.19
	7	1.16	1.15	1.16	1.15	1.15
	8	1.18	1.18	1.18	1.17	1.17
60 - 90	9	1.26	1.31	1.31	1.29	1.31
	10	1.24	1.26	1.25	1.25	1.28
	11	1.25	1.23	1.28	1.22	1.23
	12	1.26	1.19	1.22	1.21	1.21

3. NOAA-AVHRR data

NOAA-AVHRR data received at Akita University were used in this experiment. For Experiment 1 regarding the features of the geometric correction by the positional information of Japan Isl., five images were selected per case (i.e., three points on Japan Isl., located in the left, center, and right), i.e., a total of 15 images.

On the other hand, for Experiment 2 regarding the features of position specification, 42 images were selected for the study.

4. Results and Discussion

4.1 Change features of coordinate's information (Experiment 1)

Table 1 shows the calculation results of the change value regarding the area under the conditions that Japan Isl. is located in the center of the image (case 2; 0–90 deg). For five images (i.e., data6 through data10), the change features in the coordinates at a given area exist, respectively. The information of the coordinates' changes presents the same features with the same angle (i.e., 90–360 deg as well as 0–90 deg). The same result was also accepted at different given cases; the average value of the coordinates' change per area is calculated from five scenes, and the calculation results are summarized in Fig.5.

When focusing on the transverse direction with a large distortion, the values acquired from the center are different from those of the horizontal direction; the areas located on the right-hand side of the images possess a smaller range of fluctuation of coordinates' change, unlike the areas located on the left-hand side of the images. For example, area 45 possesses a fluctuation of 1.24, while area 25, 1.48, as shown in Fig.5 (a). The change value appears to be similar on the basis of the X-axis; both areas 7 and 43 possess a fluctuation of 1.15, as shown in Fig.5 (b). The change values of the areas located on the left-hand side increase as the area moves away from the central area. On the other hand, the change values of the areas located in 60 to 90 deg and 270 to 300 deg reduce under identical conditions. For 300 to 360 deg and 0 to 60 deg, the central areas such as areas 2 and 3 possess smaller change values in comparison with the end areas such as areas 1 and 4.

The calculation result of the coordinates' change according to the angle in the three cases (left, center, and right) is shown in Fig. 6. When focusing on the left-hand side of the NOAA-AVHRR image, the influence of the geometric correction is computed to be greater than that on the right-hand side; consequently, the distributions in the left-hand side of the areas are also larger than those in the right-hand side of the areas. Additionally, the influence of the geometric correction on the right-hand side of each image also changes due to the positional change of Japan Isl. (See Fig.6 (a)–(c) in the 300–330 deg, 330–360 deg, and 0–30 deg). The relation between the change of values in each degree and the position of Japan Isl. is obtained; the area, which has the value of 1.19 or 1.20, is appeared to be changed when the position of Japan Isl. changes.

The above results demonstrate that the features and tendency differ from each other by the set areas and the positional information of the Japan Isl.

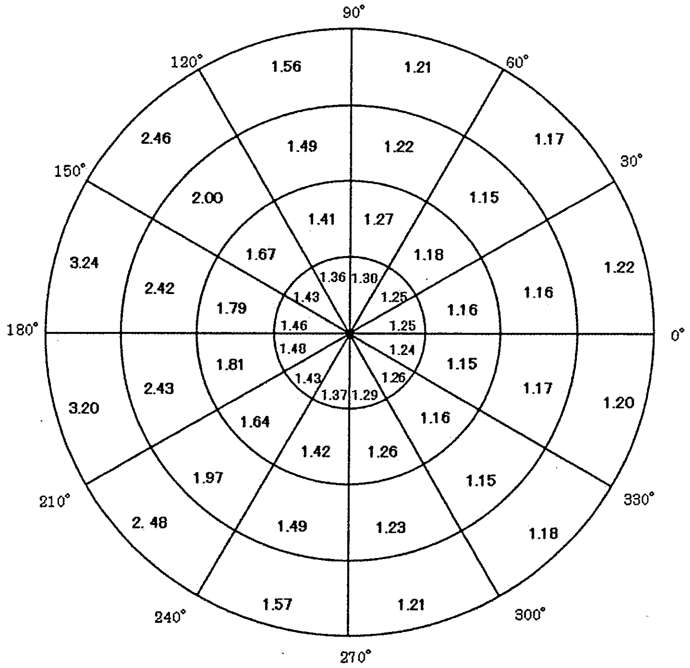

(a) Change values in case 1

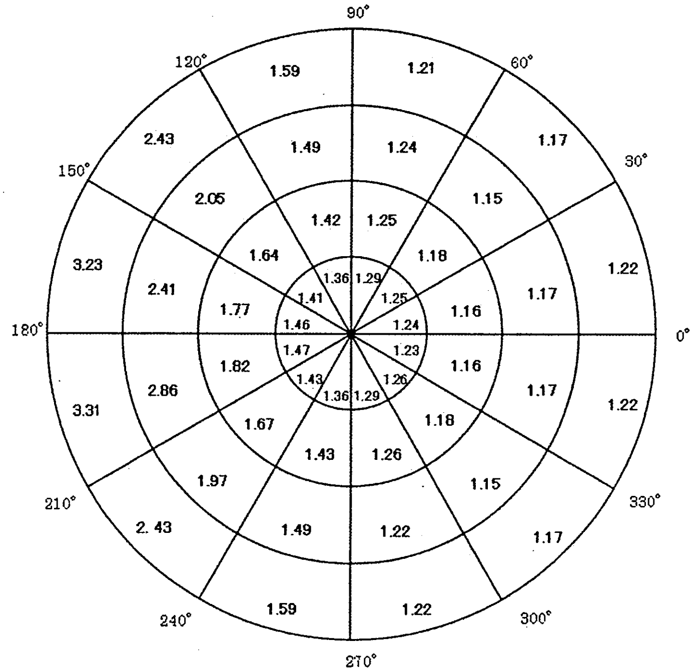

(b) Change values in case 2

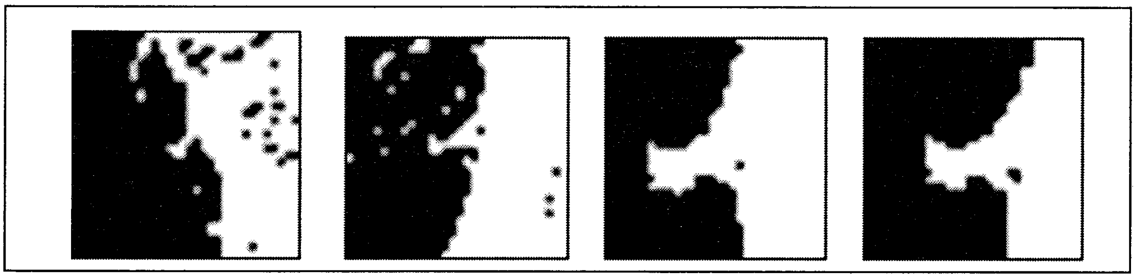

Fig.7 Examples of binary images for computing fractal dimension.

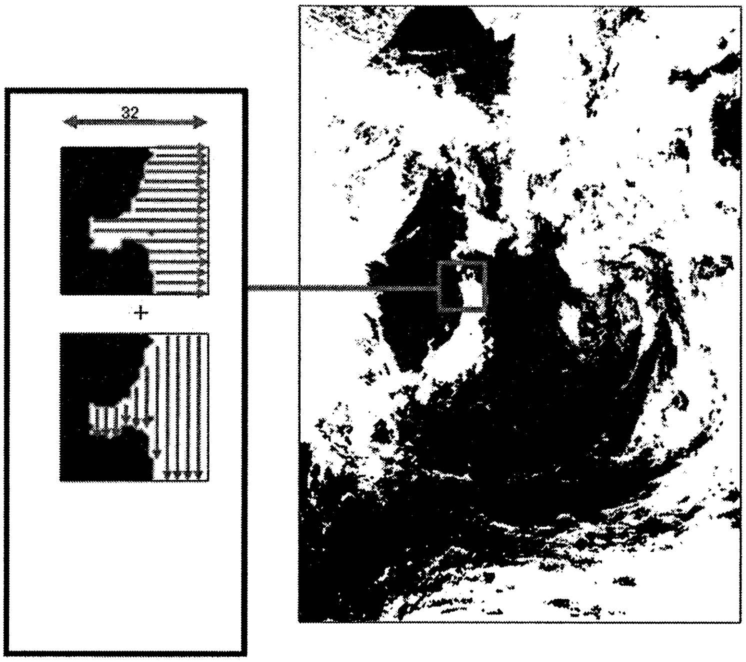

Fig.8 An example of extracting the target point by the run-length matrix.

References

(1) C. A. D. Sannier and J. C. Taylor: “Real-time monitoring of vegetation biomass with NOAA-AVHRR in Etosha National Park, Namibia, for the risk assessment”, Int. J. Rem. Sens., Vol.23, No.1, pp.71-89 (2002)
(2) J. Cihlar, H. Ly and Q. Xiao: “Land Cover Classification with AVHRR Multichannel Composites in Northern Environments”, Rem. Sens. Env., Vol.58, pp.36-51 (1996)
(3) J. A. Sobrino, N. Raissouni and Zhao-Liang Li: “A Comparative Study of Land Surface Emissivity Retrieval from NOAA Data”, Rem. Sens. Env., Vol.75, pp.256-266 (2001)
(4) Y. Kageyama and M. Nishida: “A Method for Retrieving Sea Surface Temperature in Local Regions Using NOAA AVHRR: A Case Study in Japan Sea”, J. Geography, Vol.114, No.5, pp.739-750 (2005)
(5) RESTEC’s Web Site: http://www.restec.or.jp/
(6) Y. Chang and M. Takagi: “Accurate Geometric Correction for Meterogical Satellite NOAA’s AVHRR Data,” J. JSPRS, Vol.34, No.2, pp.25-35 (1995)
(7) M. Takagi, T. Hiyama, M. Sone and M. Onoe: “Automatic Correcting Method of Geometric Distortion in Meteorological Satellite NOAA image,” IEICE Tarns., Vol.J71-D, No.5, pp. 883-893(1988)
(8) M. Sone, M. Sakauchi and M. Takagi: “A Fast Technique for Registration Processing between Meteorological Satellite NOAA Image and Coastline Image,” J. Institute of Television Engineers of Japan, Vol.43, No.9, pp.957-966(1989)
(9) Y. Chang and M. Takagi: “A Method for Geometric Correction of AVHRR Data,” J. RSSJ, Vol.15, No.1, pp.16-39 (1995)
(10) Y. Iikura: “Optimization of Geometric Correction of Landsat TM Images using Digital Elevation Model,” J. RSSJ, Vol.22, No.2, pp.189-195 (2002)
(11) NOAA’s Web Site: http://www.noaa.gov/
(12) M. Takagi and H. Shimoda: “Handbook of Image Analysis [Revised Edition]”, University of Tokyo Press (2004)

Extraction of water bodies and shoreline using MODIS data

*A. Shalaby, Alimujiang Kasimu and R. Tateishi

Center for Environmental Remote Sensing (CEReS), Chiba University 1-33, Yayoi-cho, Inage-ku, Chiba 263-8522 Japan
Tel (81)-43-290-2964; Fax: (81)-43-290-3857
E-mail: Adelnan@yahoo.com

Abstract

The application of remote sensing for extraction of water bodies and shoreline has long been used in water resources assessment and coastal management. In this paper MODIS data have been used to map water bodies on global scale. Unsupervised classification K-means and ISODATA was performed on MODIS data of 2003 to extract water bodies and shoreline. The accuracy of the classification was assessed using reference data such as TM and Google earth. The result showed that the accuracy of water bodies of the produced map was higher than that of GLC (Global Land Cover 2000).

1. Introduction

Mapping water bodies and shoreline at global scale can only be done using remote sensing imagery. The importance of water and shoreline mapping is that it has many applications such as coastline erosion monitoring, coastal-zone management and evaluation of water resources.

Following the increase in the availability of satellite images, the development of tools for geographic data analysis and image processing techniques, numerous research studies have attempted to extract and delineate water bodies from these images (Smith 1997). The extraction of features such as coastlines and water bodies directly from satellite images overcomes the problem of matching available coastline/shoreline datasets with the image dataset studied. There are various methods for the extraction of water information from remote sensing imagery, which, according to the number of bands used, are generally divided into two categories, i.e. single-band and multi-band methods. The single-band method usually involves choosing a band from a multi-spectral image to extract open water information (Rundquist et al. 1987). A threshold is then determined for the band to discriminate water form land. However, the subjective selection of the threshold value may lead to an over- or under-estimation of open water area and the extracted water information is often mixed with shadow noise. The multi-band method takes advantage of reflective differences of each involved band. There are two ways to extract water information using the multi-band method. One is through analyzing signature features of each ground target among different spectral bands, finding out the signature differences between water and other targets based on the analysis, and then using an if-then-else logic tree to delineate land from open water (Yu et al. 1998). The other one is a band-ratio approach using two multi-spectral bands. One is taken from visible wavelengths and is divided by the other usually from near infrared (NIR) wavelengths. As a result, vegetation and land presences are suppressed while water features are enhanced. However, the method can suppress non-water features but not remove them, and therefore the normalized difference water index (NDWI) was proposed by McFeeters (1996) to achieve this goal. Nevertheless, the NDWI cannot efficiently suppress the signal from built-up land so that enhanced or extracted water features are still mixed with built-up land noise.

The objective of this study is to map water bodies at global scale using MODIS data through examining different methods. In this study an unsupervised classification was performed in order to separate water from other land cover types. The NDWI was calculated and integrated with other bands for classification.

2. Methodology

2.1. Geometric accuracy inspection

After mosaicking and re-projection had been done, a geometric accuracy checking for all output images was done, for this purpose Landsat ETM+ images were used and considered as a reference. Landsat ETM+ images were downloaded from Global Land Cover Facility Earth Science Data Interface of University of Maryland. The results indicate that the RMSE is less than half pixel of global MODIS 2003 data

2.2. Clearing Cloud Pixel Contamination

Cloud cover is the major factor limiting the use of optical remote sensor for various applications. Clouds contaminate many pixels of the original MODIS data and might have cloud pixel contamination on a series of all (16-day) 23 periods. For each of the five continents (North America, South America, Africa, Eurasia and Oceania), and in order to verify the cloud-cover continuation, an analysis of cloud-cover has been performed for each pixel of each band for all (16-day) 23 periods. Cloud -cover analysis revealed that, for the same continent, different parts of the all-23 periods of all 5 continents might have cloud-contaminated pixel on a series of 16-day data (i.e. from period 1 start on January 1 to period 23 end on December 31). Therefore, and in order to use MODIS data of 2003 a clearing of a cloud-contaminated pixel is very important. For this purpose, a method has been developed at Tateishi Lab. of CEReS, Chiba University using MODIS data of 2002 (a year before) and 2004 (a year after).

2.3. Unsupervised classification

Unsupervised classification was performed on MODIS data of 2003 to extract water bodies and shoreline. Both K-means and ISODATA were used for the classification. A number of trials were performed with different number of classes ranging from 10 to 120 classes for both K-means and ISODATA for three periods (May, July and August for northern hemisphere and November, January and March for southern hemisphere) for each continent. To avoid overestimation of water surface area, the class is considered water if it is classified as water in at least two of the three periods.

2.4. Normalized Difference Water Index (NDWI)

The NDWI is expressed as follows (McFeeters 1996):

$$\mathrm{NDWI} = \mathrm{Green} - \mathrm{NIR} / \mathrm{Green} + \mathrm{NIR}$$

This index is designed to (1) maximize reflectance of water by using green wavelengths; (2) minimize the low reflectance of NIR by water features; and (3) take advantage of the high reflectance of NIR by vegetation and soil features. As a result, water features have positive values and thus are enhanced, while vegetation and soil usually have zero or negative values and therefore are suppressed (McFeeters 1996). The NDWI was calculated and integrated with other bands for classification. Flow chart of the methodology is shown in figure 1.

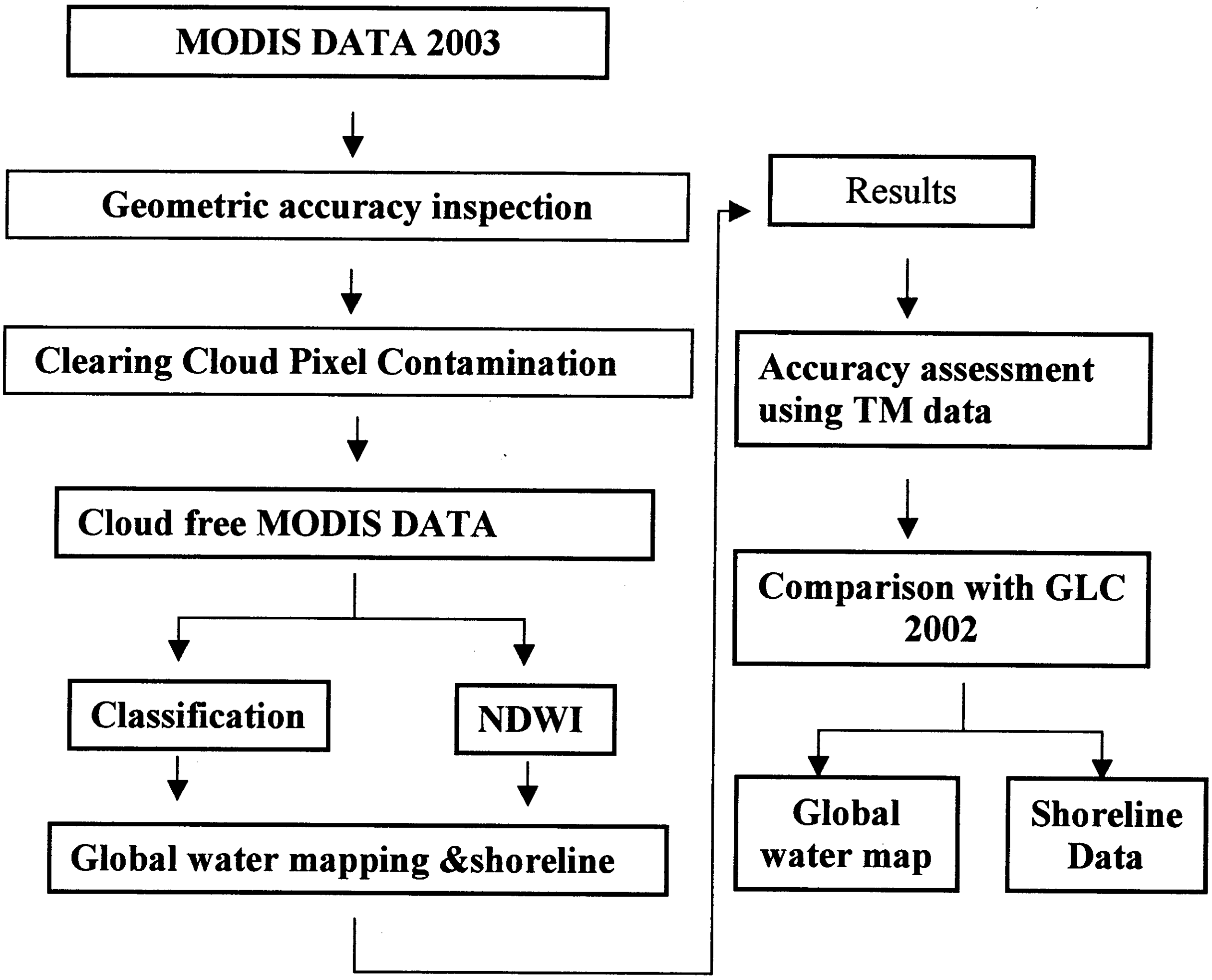

Figure 1. Flowchart of the methodology

3. Result and discussion

After supervised classification was performed, the classes which represent water were grouped in two classes, first class for deep water and the second class for shallow water, while the other classes were grouped in one class as non-water. The result of unsupervised classification for the five continents were carried out, examples are shown in figure 2 and figure 3.

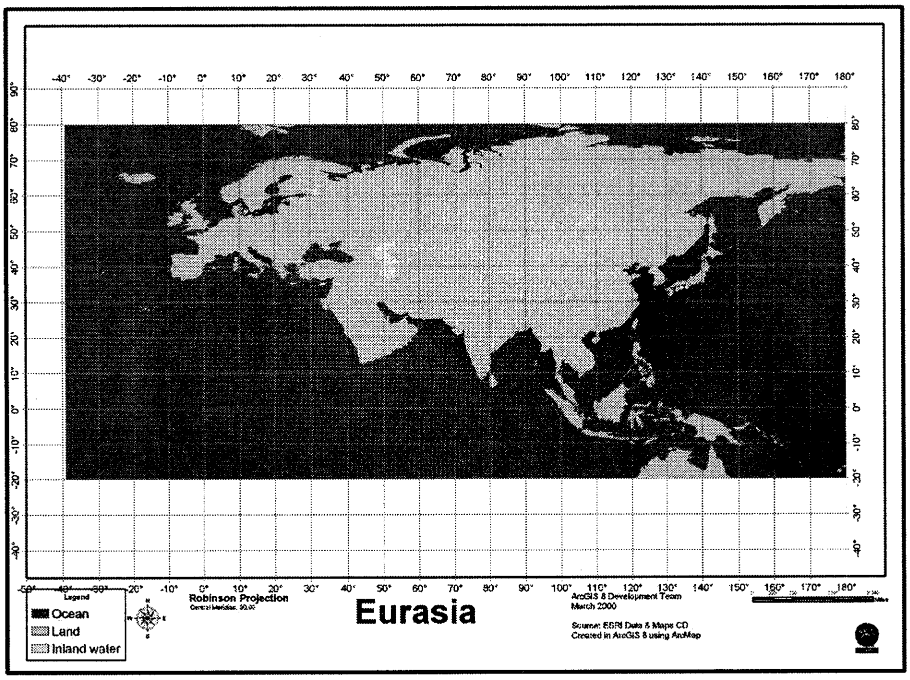

Figure 2. Water map of Eurasia

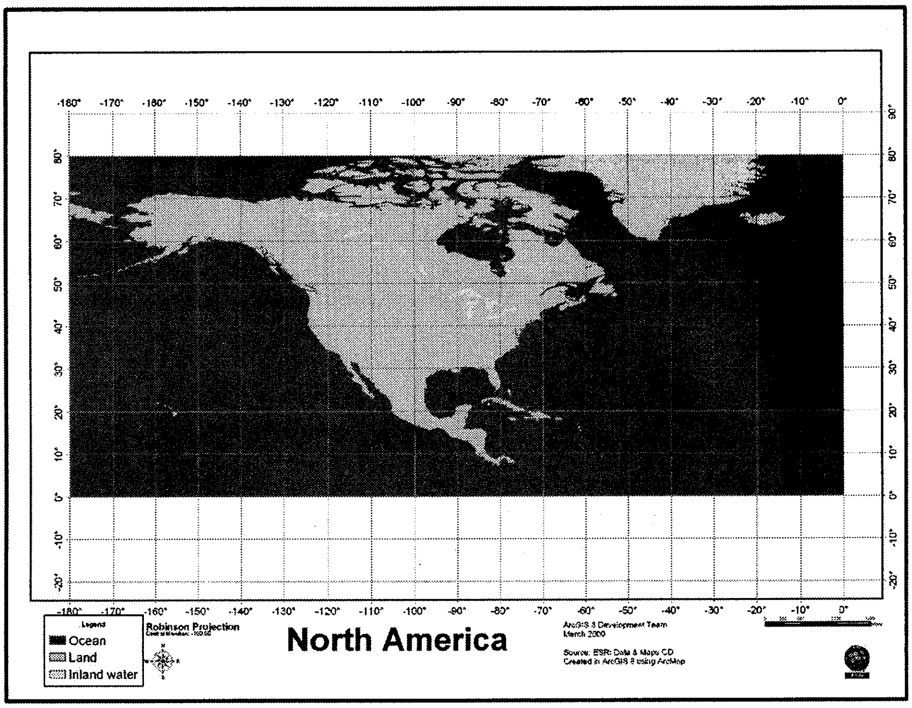

Figure 3. Water bodies of North America

Water bodies were classified with high accuracy (more than 95 percent). This could be explained by its unique spectral pattern which has a very low reflection in the infrared region compared to vegetation and other land cover types.

The use of the NDWI alone gave a lower accuracy compared to the use of MODIS bands. It is also noticed that the integration of the NDWI with MODIS bands did not improve the accuracy of the classification.

Accuracy assessment

Accuracy assessment was carried out using TM and ETM+ data. The accuracy was more than 95 percent for all of the five continents. Comparison between the classified results of MODIS data with TM images is shown in 4, 5 and 6.

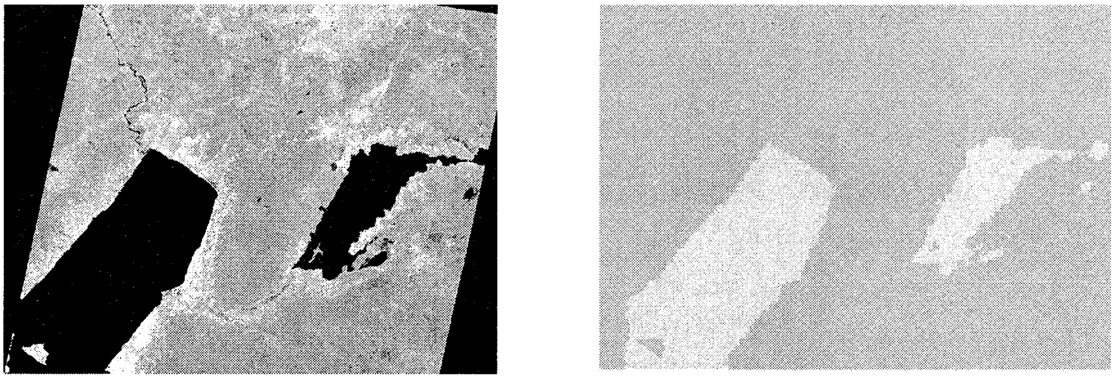

Lake Mweru, located on the border between Zambia and Democratic Republic of the Congo

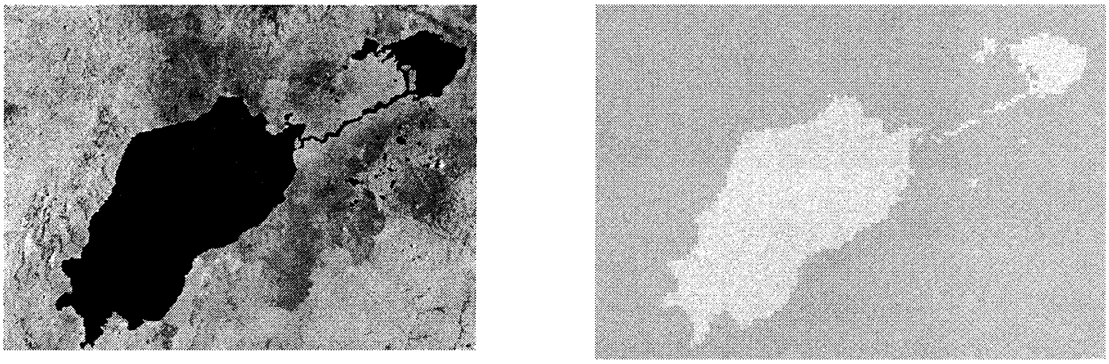

Lake Edward, located on the border between the Democratic Republic of the Congo and Uganda

Figure 4. Subset of some lakes in Africa

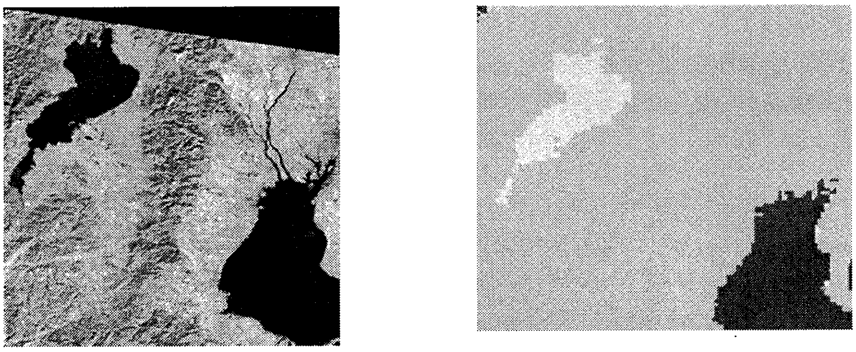

Lake Biwa, Japan

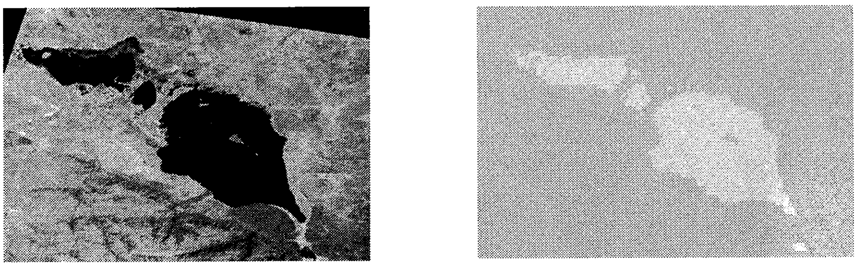

Lake Alakol,

Figure 5. Subset of some lakes in Eurasia

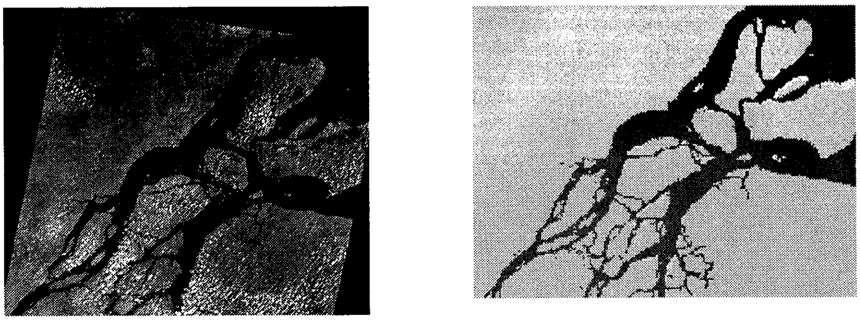

Amazon river, Brazil

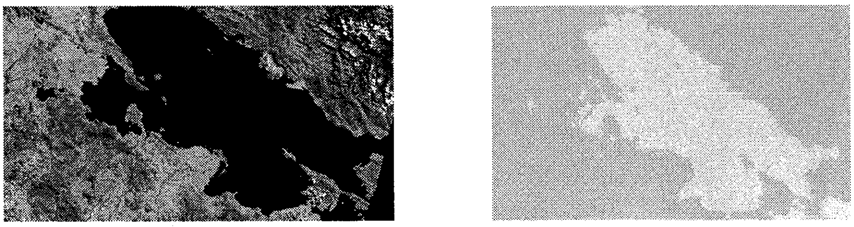

Lake Titicaca located on the border between Peru and Bolivia

Figure 6. Subset of some lakes in South America

4. Conclusion

Unsupervised classification can be used for mapping water bodies from MODIS data on global scale with acceptable accuracy. Including other water indexes could further improve the accuracy of mapping water bodies and shoreline. The use of NDWI alone is not the ideal case for water mapping because it gave much lower accuracy compared with the use of MODIS bands.

References

MCFEETERS, S.K., 1996, The use of normalized difference water index (NDWI) in the delineation of open water features. International Journal of Remote Sensing, 17, pp. 1425–1432.

RUNDQUIST, D., LAWSON, M., QUEEN, L. and CERVENY, R., 1987, The Relationship between the Timing of Summer-Season Rainfall Events and Lake-Surface Area. Water Resources Bulletin, 23, pp. 493–508.

SMITH, L.C., 1997, Satellite remote sensing of river inundation area, stage, and discharge: a review. Hydrological Processes, 11, pp. 1409–1413.

YU, J., HUANG, Y. and FENG, X., 2001, Study on water bodies extraction and classification from SPOT image. Journal of Remote Sensing, 5, pp. 214–219.

Flood Monitoring (2007) in Bangladesh Using Terra MODIS Satellite Imageries

M. Mahmudur RAHMAN[1] and Josaphat Tetuko Sri SUMANTYO[2]
[1, 2] Microwave Remote Sensing Laboratory, Center for Environmental Remote Sensing, Chiba University
1-33, Yayoi, Inage, Chiba 263-8522 Japan
E-mail: [1]mahmud@restaff.chiba-u.jp (Corresponding author)

Abstract

Bangladesh, a low-lying delta is located in the South-Asian Monsoon System. The intense monsoon rain often creates flooding in the country. Moderate Resolution Imaging Spectrometer (MODIS) on NASA's Terra satellite image on the 5th August 2007 image was classified to prepare flood map and administrative boundary was overlaid to create the statistics. The result shows nine districts of the country were severely affected (more than 50% of area remained under water). Overall, this investigation found that about 22% of the country was under water though cloud coverage (about 22%) obscured part of the country to create accurate statistics.

1. Introduction

Bangladesh is located at the confluences of Bhramaputra, Meghna and Ganges Rivers. The rivers are the part of the Himalayan drainage systems and empty into the Bay of Bengal through the largest river delta in the world. The annual discharge through these rivers is the second largest after the Amazon in the world. Normal flooding during the monsoon periods is a common phenomenon in Bangladesh. Floods make the cultivable land fertile, but excessive flooding sometimes becomes catastrophic evens. Floods have created devastation in Bangladesh throughout the history, especially during the recent years: 1987, 1988, 1998, 2004 and 2007. The flatland within the country is very fertile and criss-crossed by many rivers. All the river-plains are densely populated. As a consequence catastrophic flooding in any region of the flood-plains creates severe impact to many people.

Since the inception of remote sensing, the technology has been using for flood detection, monitoring, damage assessment and forecasting. Several studies have been carried out in many parts of the world using both the optical and microwave sensor data. The flooding events have been investigated in the many parts of the world., i.e. Senegal River Valley in West Africa (Sandholt *et al.* 2003), Limpopo Basin in southern Africa (Asante *et al.* 2007), Mackenzie River Basin in Canada (Temimi *et al.* 2005), Yellow River Basin in China (Liu and Yan 2005), Ganges-Bhramaputra Delta in Bangladesh (Rasid and Pramanik 1990, Rasid and Pramanik 1993).

The objective of this research was to (i) delineate the extent of flooding in the Ganges-Bhramaputra Delta in Bangladesh during July-August 2007 and (ii) generate flood statistics for each district (local administrative units) of the country.

2. Study Area and Remote Sensing Data

The study area is located in the lower Ganges-Bhramaputra basin covering the administrative boundary of Bangladesh. It covers from 22^0 to 26^0N latitude and 89^0 to 92^0 E longitudes. The area enjoys a sub-tropical monsoon climate with three distinct seasons per year: the pre-monsoon hot season from March to May, rainy season June to October and cool dry season from November to February. The average annual rainfall varies from a maximum of 5690mm in the northeast of the country to minimum of 1110 mm in the west. Most rainfall is concentrated in the monsoon season (about 80%).

The research used Moderate Resolution Imaging Spectrometer (MODIS) satellite imagery of 2nd May and 5th August, 2007, Shuttle Radar Topographic Mission (SRTM) elevation data and administrative (districts) boundaries of Bangladesh. Satellite imageries were downloaded from http://rapidfire.sci.gsfc.nasa.gov/ website. Processed image of 2nd May in jpg format was only available on the website and used in this study for display. Geo-rectified three-bands (1, 2 and 7) were available in tiff format and were downloaded (detailed band descriptions in Table 1). SRTM data was downloaded from Global Land Cover Facility (GLCF). Administrative boundaries were used from Bangladesh Space Research & Remote Sensing Organization (SPARRSO) archive.

Table 1. Terra MODIS selected band descriptions

Primary use	Band	Bandwidth (nm)	Resolution (m)
Land/Cloud/Aerosols Boundaries	1	620-670 (Visible red)	250
	2	841-876 (Near-infrared: NIR)	250
Land/Cloud/Aerosols Properties	7	2105-2155 (Mid-infrared)	500

3. Methodology

Terra MODIS satellite image of 5th August was visualized on computer screen; three bands 1, 2, and 7 into red-green and blue color. Clear water appears in dark blue and water with sediments in light blue. Bare-soil or

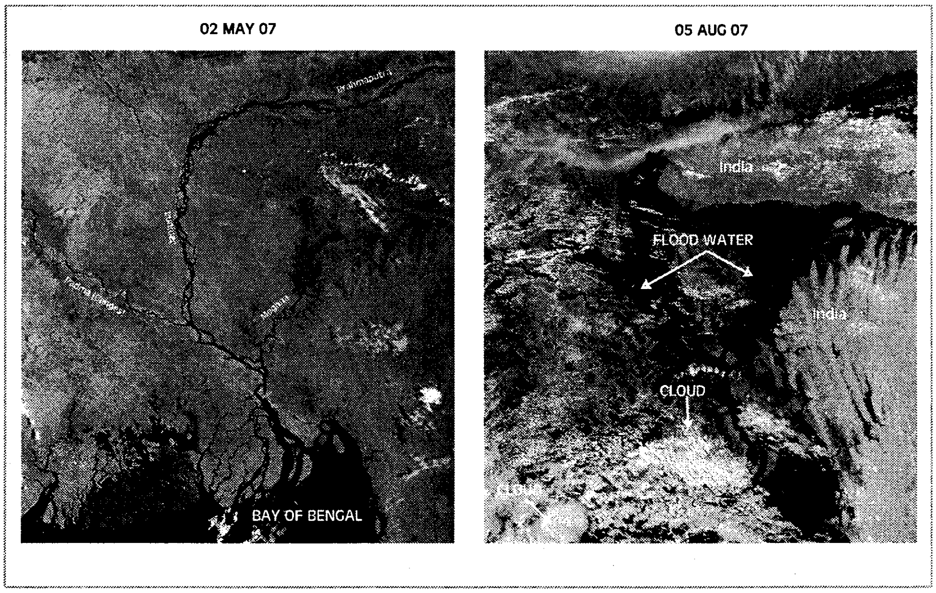

Figure 1. Comparison of inundation level (left image before monsoon and right image during flooding

lightly vegetated area appears as tan, vegetation as bright green, cloud as white (with pink and blue tone). The image was classified using supervised method. First training samples were collected from seven classes: water, vegetation and cloud- two categories in each class and exposed soil class. Care was taken to collect only the homogenous pixels as training samples. In the second step all these seven classes were merged to water, land and cloud. Maximum likelihood algorithm was used in classification. The classification accuracy was computed from training set of pixels and presented in an error matrix. The local administrative unit (district) boundaries were overlaid on the classified imagery to assess the extents of flooding in each district.

4. Results and Discussion

4.1 Monsoon Flooding 2007

Before the on-set of monsoon the rivers and the water bodies in Bangladesh are in the dry months' inundation level and the course of each river is clearly defined on the satellite image (Figure 1, left image). Due to the intense monsoon rain in these regions as well as in the upper catchments the rivers and water bodies were filled with water, over-flowed and submerged many low-lying areas, agricultural fields, villages and cities and created catastrophic flooding. The swollen water-level is shown in Figure 1 (right image).

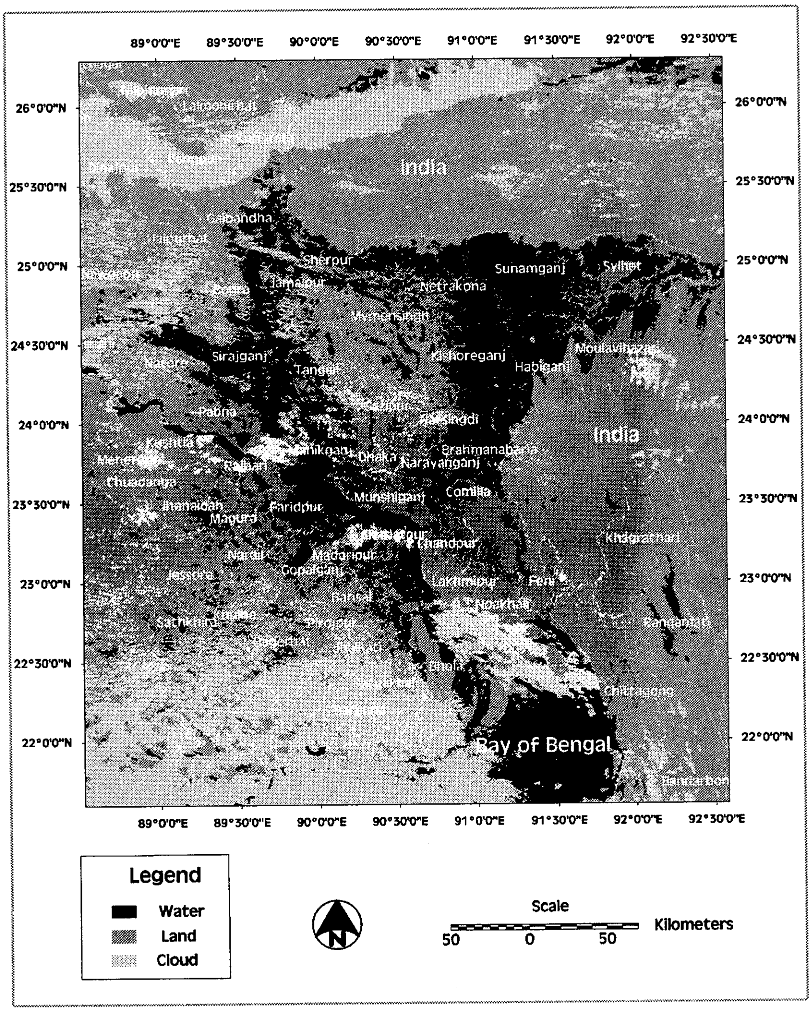

Figure 2. Flood map of Bangladesh (05 August 2007)

Flood map shows that the central and northern region is the most affected part of Bangladesh (Figure 2). Among the 64 districts of the country, nine districts (Sunamganj, Sirajganj, Brahmanabaria, Kishoreganj, Netrakona, Faridpur, Habiganj, Manikganj and Sylhet) were most affected (more than 50%, Table 2). Overall 22% of the country is inundated by 2007 (July-August) flood though cloud coverage (22%) obscures to compute for an accurate statistics and 56% of the country were not affected.

Table 2. Flood water inundation in different districts of Bangladesh (5th August 2007)

Flood Damage	District	Coverage (%)			Area (ha)		
		Water	Land	Cloud	Water	Land	Cloud
>50%	Sunamganj	85	15	-	311 558	54 956	122
	Sirajganj	77	18	5	187 619	43 305	12 813
	Brahmanabaria	75	23	2	144 488	43 230	4 211
	Kishoreganj	71	29	-	179 900	72 177	110
	Netrakona	70	30	-	202 778	85 977	215
	Faridpur	62	38	-	126 680	79 234	12
	Habiganj	58	42	-	150 041	107 734	-
	Manikganj	52	32	15	73 031	44 705	21 444
	Sylhet	50	50	-	174 743	171 554	105
30-50%	Shariatpur	46	39	16	57 971	48 852	19 724
	Jamalpur	43	42	15	88 196	86 547	29 761
	Madaripur	40	50	9	44 368	55 491	10 199
	Munshiganj	40	60	-	37 666	55 915	6
	Sherpur	36	62	2	48 492	82 341	2 294
	Comilla	33	67	-	103 367	209 365	732
	Tangail	33	51	16	113 107	176 932	53 800
	Dhaka	32	59	9	47 801	89 590	13 266
	Chandpur	31	68	2	51 919	115 262	2 840
10-30%	Narayanganj	29	68	3	23 128	53 533	2 132
	Pabna	29	64	7	69 227	155 192	16 582
	Barisal	29	64	8	65 992	147 264	17 471
	Narsingdi	28	59	13	32 607	69 471	15 281
	Mymensingh	26	72	2	110 470	306 209	7 911
	Gaibandha	26	60	14	56 310	131 658	29 755
	Natore	25	57	17	48 759	110 319	33 431
	Gopalganj	25	72	3	39 112	110 999	4 490
	Magura	22	77	-	23 494	81 145	412
	Moulavibazar	20	76	3	55 502	207 436	9 078
	Rajbari	20	66	14	22 129	73 850	15 821
	Bogra	19	51	30	55 833	149 640	86 064
	Narail	11	84	6	10 600	81 917	5 512
	Kushtia	10	74	16	17 238	123 649	27 164

The overall effect of flooding in 2007 is lower than 1955, 1987 and 1988 floods, when 37%, 40% and 57% of the country were affected by flooding respectively (BWDB 1987, Rashid and Pramanik 1990). Considering the elevation gradient from the northern Himalayan Mountain to the southern Bay of Bengal two depressed pockets are vivid in the north-eastern and north-western part of the country (Figure 3). These pockets often become inundated during the monsoon season and results normal flooding every year. But excessive rain in addition to the melting of the Himalayan snow sometimes creates catastrophic flooding and inundates vast areas of northern and central parts of the country, where the elevation is often lower than 20m above mean sea level.

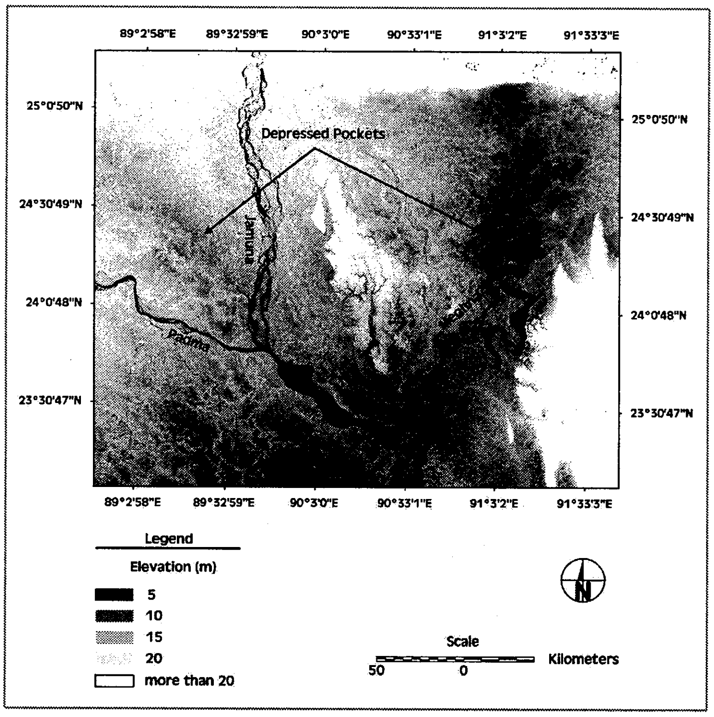

Figure 3. Elevation map of the flood affected region (2007) of Bangladesh

Table 3. Classification error matrix for flood mapping using Terra MODIS satellite imagery

		Training Pixels			
		Water	**Land**	**Cloud**	**Total (classified)**
Classified Pixels	Water	38 437	0	0	38 437
	Land	19	12 410	0	12 429
	Cloud	1	0	28 025	28 026
	Total (training)	38 457	12 410	28 025	78 892

4.2 Classification Accuracy

The overall accuracy of classification computed from the training pixel-sets is almost 100%. This happens because of the large difference of the optical properties between water, land and cloud in bands 1, 2 and 7. The columns and rows of the error matrix show the training and classified pixel-sets respectively (Table 3). The training pixel sets those are accurately classified are located along the diagonal of the error matrix (running from upper left to the lower right). The upper-right cell of the diagonal represents the commission errors and the lower-right cells the omission errors. Omission errors mean this category has been omitted from the class and commission error is the opposite.

5. Conclusion

This investigation concludes that (i) about 22% of the country was affected by this flooding event though cloud coverage on the image (22%) obscures to compute for an accurate country-level statistics (ii) nine districts among the 64 districts of the country were severely affected (more than 50% inundated). In recent decades catastrophic floods in Bangladesh are becoming common within a few years` interval. Intense rainfall is one of the main reasons of flooding. Further studies should be carried out to investigate whether climate change is affecting the South Asian Monsoon System and rainfall patterns, and often creating catastrophic flooding in this region. The result of this study will be useful for the policy makers to make plan for the post-flood agricultural and reconstruction activities.

Acknowledgement

Terra MODIS satellite imageries and SRTM data were downloaded from http:// rapidfire. sci. gsfc. nasa. gov/ and http: //glcf.umiacs.umd.edu/index.shtml websites respectively.

Administrative boundaries are used from SPARRSO database.

Japan Society for the Promotion of Science (JSPS) is acknowledged for granting the fellowship to the first author.

References

Asante, K. O., Macuacua, R. D., Artan, G. A., Lietzow, R. W. And Verdin, J. P. 2007. Developing a flood monitoring system from remotely sensed data for the Limpopo Basin, *IEEE Transactions on Geoscience and Remote Sensing,* 45 (6), 1709-1714.

BWDB (Bangladesh Water Development Board) 1987. Flood in Bangladesh 1987. Ministry of Irrigation, Water and Development & Flood Control, Dhaka, Bangladesh.

Liu, L. and Yan, J. 2005. MIPPR 2005: The application of MODIS data on ice flood monitoring of Yellow River. SAR and Multispectral Image Processing. Zhang, L; Zhang, J; Liao, M. (Eds.) Proceedings of the SPIE, Vol. 6043, 780-785.

Rasid, H. and Pramanik, M. A. H. 1990. Visual interpretation of satellite imagery for monitoring floods in Bangladesh, *Environmental Management* 14(6), 815-821.

Rasid, H. and Pramanik, M. A. H. 1993. Areal Extent of the 1988 flood in Bangladesh: How much did the satellite imagery show? *Natural Hazards* 8, 189-200.

Sandholt I., Nyborg L., Fog B., Lô M., Boucoum O., Rasmussen K. 2003. Remote Sensing techniques for flood monitoring in the Senrgal River Valley, *Danish Journal of Geography,* 103(1), 71-81.

Temimi, M. Leconte, R., Brissette, F. and Chaouch, N. 2005. Flood monitoring over the Mackenzie River Basin using passive microwave data, *Remote Sensing of Environment,* 98 (2-3), 344-355.

Monitoring areas at risk of desertification in Xinjiang Uyghur Autonomy Region, China based on integrated analysis of SPOT VEGETATION imagery and Geophysical data

* Alimujiang Kasimu, T. Ishiyama and R. Tateishi

Center for Environmental Remote Sensing (CEReS), Chiba University 1-33, Yayoi-cho, Inage-ku,
Chiba 263-8522 Japan
Tel (81)-43-290-2964; Fax: (81)-43-290-3857
E-mail: alimkasim@gmail.com

Abstract

Abstract: Monitoring of desertification processes by satellite remote sensing is an important task in Xinjiang and other arid regions of the world. We used a full year 2006 time-series of SPOT VEGETATION imagers with 1km special resolution to produce a land cover map with emphasis on sparse vegetation as an indicator of areas at risk of desertification. The best classification results were obtained by integrating topographical (elevation) and climate (precipitation and temperature) information with multi temporal VGT imagers. The areas at risk of desertification were modeled and the result suggests that more than 20% areas at risk of desertification and mainly distributed desert-oasis ecotone. Integrated analysis of SPOT VEGETATION imagers and geophysical data should be very useful to detect larger scale dynamics of environmental changes and desertification processes.

1. Introduction

Desertification represents one of the most threating environmental hazards. It is estimated that desertification directly affects one-third of the Earth's land and 250 million people, most of them in developing countries. The United Nations Convention to Combat Desertification (UNCCD) defines 'desertification' as land degradation in arid, semi-arid and dry sub humid areas resulting from factors including climatic variations and human activities. Degradation is defined as the reduction or loss of biological or economic productivity and complexity in croplands, pastures, and woodlands (Tsunekawa, 2000). Nowadays, in China land characterized by total desertification amounts to about 3.34×106 km^2, and the rate of annual desertification accelerated from 1560 km^2 in the 1960s to 2100 km2 in the 1980s and then 2460 km^2 in 1990s (Wang, 2003). Desertification caused a direct economic loss estimated around US$ 2-3 billion, while the associated indirect loss is 2 to 3 times more. Xinjiang Uyghur Autonomous Region is the most seriously affected area in China, particularly in the Tarim River Basin and Ebinur Lake Basin. To combat desertification, continuous monitoring is required to understand the processes leading to desertification.

Remote sensing has been applied to monitor desertification in Asia, to map land cover/land use and to ascertain indicators of desertification (Tsunekawa, 2000). Many authors have experienced a wide range of indicators in order to map the occurrence and severity of desertification (Mabutt 1986, Mouat et al. 1997). Many of these indicators were unsatisfactory, because of their high costs and tedious process of data collection, however vegetation cover proves to be a more popular criterion. Vegetation status can sensitively reflect the environment variation caused by desertification, especially the sparse vegetation area are likely at risk of desertification.

In this paper, the integration of multi-temporal VGT data and information affecting vegetation distribution directly or indirectly is presented with the aim of extracting sparse vegetation cover to detect area at risk of desertification in Xianjing Uyghur Autonomy Region. The objective of the study was first to generate a 1km spatial resolution land cover map of Xinjiang for desertification monitoring, and then to identify area at risk of desertification, investigating the integration multi-temporal VGT data with geophysical datasets could be used in a multi-scale desertification monitoring system.

2. Material and methods

2.1. Study area

Xinjinag Uyghur Autonomous Region, Lat: 34° 25' N, Lon: 73°40' E and Lat: 49°10' N, Lat: 96°23' E, is situated in the northwest of China and covers an area of more than 1.6 million Km^2. As China' s largest province, its area is equal to one-sixth of the entire territory of China. Xinjiang has a vast land area with a very complicated landscape (Fig.1). There are several huge mountain ranges running east and west across Xinjiang. On its northern border loom the Altay Mountains, and on the southern border lie the Rarakorum Mountains, the Kunlun Mountains and the Altun Mountains. The mammoth Tianshan Mountains in the middle part of the region cover its entire length, dividing it into northern and southern Xinjiang. Two enormous basins, the Tarim Basin in the south, the Dzungar Basin in the north, spread out from Tianshan' s foothills. The Xinjiang province elicits an explicit geographical differentiation with several mountain ranges. The altitude variation is quite high ranging from –140 to 7600 meters. Situated deep in the interior of Asia and not penetrated by the air currents from the oceans, the Xinjiang Uygur Autonomous Region has typical continental climate. The average annual rainfall in Xinjiang is about 150 millimeters. Because of the "blocking effect" of the Himalayan Range, moist air currents from the Indian ocean fail to reach xinjiang, resulting in the vast expanse of arid terrain. Hydrologically, there is a progressive increase of precipitation from south to north, with the Altai region receiving the highest annual precipitation. Due to the unique geography, climate and natural resources, Xinjiang is characterized by special oasis and irrigation agriculture.

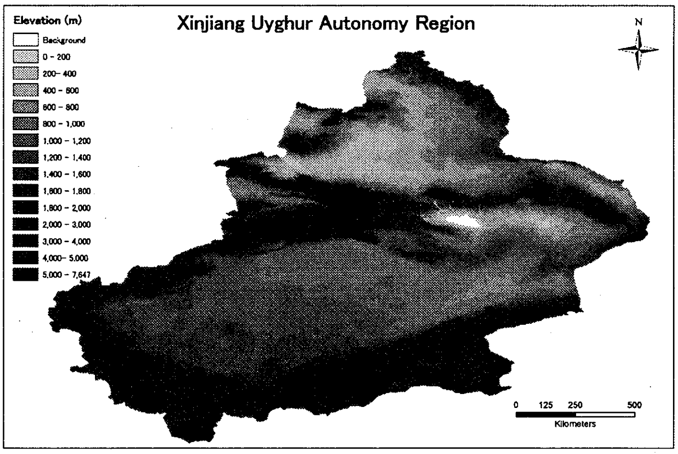

2.2. Data and pre-processing

2.2.1 VGT data set

The VGT instrument is a recent space-borne optical sensor, optimized for global terrestrial vegetation and land surface monitoring. Muti-temporal VGT-S10 (10-day synthesis product) radiometric data for January 1, 2006 to December 31,2006 were downloaded from the free VGT products website (http://free.vgt.vito.bez). The VGT products are pre-processed by the VGT image pre-processing Center (CTIV). Data processing includes navigation and geo-correction, calibration and atmospheric correction for water vapor, ozone and aerosol horizontal and vertical distribution. The final VGT-S10 product is produced based on the maximum value NDVI composite (MVC). The information of a VGT-S10 HDF image includes B0, B2, B3, SWIR and NDVI. All the bands were coregistered to an uniform geographic Latitude/Longitude projection based on WGS84 spheroid with a pixel size of 0.0089285714 degrees.

Two indices were selected to quantify the vegetation status in our study. The NDVI in Eq (1) is the most used vegetation index. The Normalized Difference Water Index (NDWI) in Eq. (2) is used to represent vegetation water content (Gao, 1996).The NDWI is used as well to identify snow and ice (Xiao et al., 2002). NDWI values cumulated from April to October are calculated and present seasonal vegetation water content. The five months during winter are removed to reduce the effect of snow cover.

$$NDVI = \frac{NIR - R}{NIR + R} \qquad \text{Eq(1)}$$

$$NDWI = \frac{Green - NIR}{Green + NIR} \qquad \text{Eq(2)}$$

2.2.2 Ground truth data from ASTER images

Ground truth data were selected based on the geo-referenced Advanced Spaceborne Thermal Emission and Reflection (ASTER) imagery. Most of the ASTER imagery was acquired during May till September between 2002-2004. The information extraction is based on interactive visual interpretation with the help of existing land use map. We transformed the Albers equal-area project into a Geographic Latitude/Longitude projection and re-sampled pixels from a spatial resolution of 15 meters to a 0.0089285714-degree resolution.

2.2.3 Geophysical datasets

A number of geophysical datasets were collected and organized for this study, including elevation, precipitation, temperature, and land cover maps. The GTOPO Digital Elevation Model (DEM) at 1 km spatial resolution was obtained from USGS (http://eros.usgs.gov/products/elevation). For climate data we used precipitation and temperature raster data set. The National Land Cover Dataset (NLCD) is composed of 25 land-use and land-cover types and was used as the main reference for signature training and consistency checking. GLCNMO urban mapping derived from Population density, DMSP and MODIS data (Alimujiang, 2007) used to identify urban area for xinjiang Land cover classification.

2.3 Classification method

Land cover was classified in three steps:

1. Vegetated and non-vegetated area was separated based on threshold value. We determined these thresholds by visual comparisons of the annual maximal NDVI with high resolution ASTER imagery.
2. Non-vegetated areas were classified into urban, stone desert (Gobi), sand-desert, water and wetland, permanent snow and ice based on SPOT VEGETATION imagery (Fig.2).
3. Vegetated areas were classified based on the seasonal variation of the NDVI and geophysical datasets (Fig.2). To separate forest and grasslands, we applied decision tree classification method. The NDVI and DNWI, elevation, precipitation and temperature are calculated for each landscape patch. All the landscape patches are then classified into forest and grassland types (table.1).

Figure.2 Flow chat of methodology

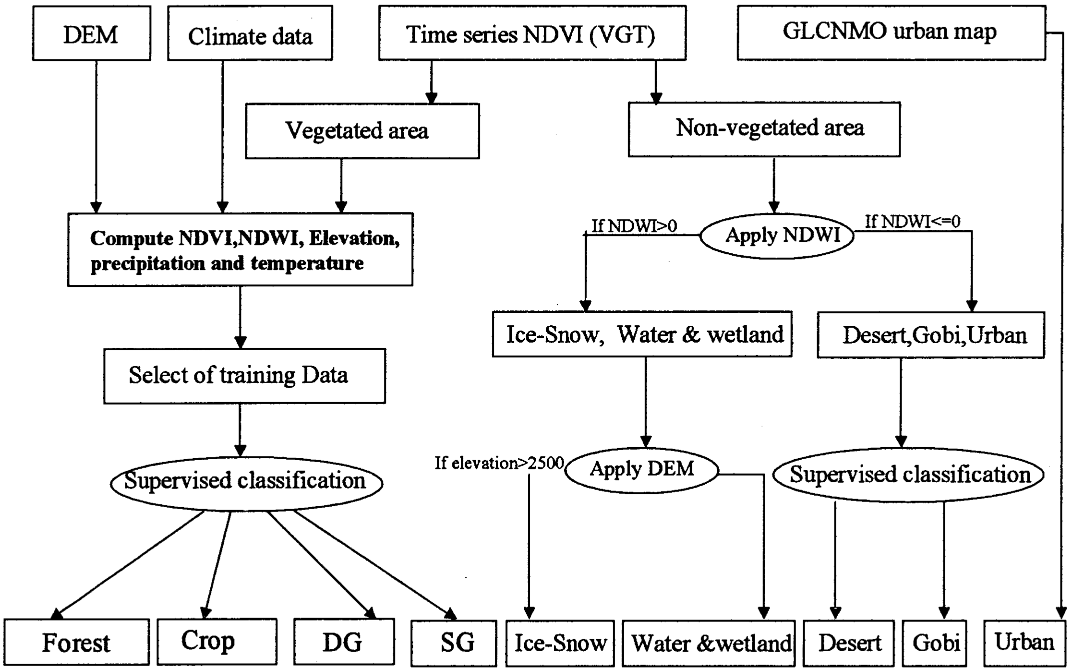

3. Result and discussion

3.1 vegetation index

Fig.3 shows that large areas of xinjiang are desert. Large area in Tarim basin and Junggar basin had very low NDVI values indicating the Taklimakan, Kurbantungkut desert. High NDVI values were found in the Altay and Tianshan mountain ranges and oases in south and north xinjiang. We found that the NDVI of sparse vegetation varied with the seasonal change of photosynthetic activity, increasing at the beginning of June, peaking in August and decreasing again in September, while non- vegetated areas did not show such a temporal pattern.

3.2 Land cover classification map

Fig.3 shows the result of Xinjiang land cover classification. Here mainly focus on sparse vegetation class type. Sparse vegetation are mainly distributed the fragile ecosystem desert-oasis ecotone. The monthly maximum NDVI values are very low and less than 0.2. The monthly average NDWI values for sparse vegetation are negative and close to –0.1. This spatial pattern, i.e. the gradual increase of vegetation density from deserts to sparse and dense vegetation suggests that the sparse vegetation might be a buffer against the invasion of the desert into agricultural area. While dense grassland covers an area of lower part of Tianshan and Altay Mountain area. It shows higher monthly maximum NDVI value. During June to September it shows positive monthly average NDWI values.

Figure.3 Land Cover classification of Xinajing

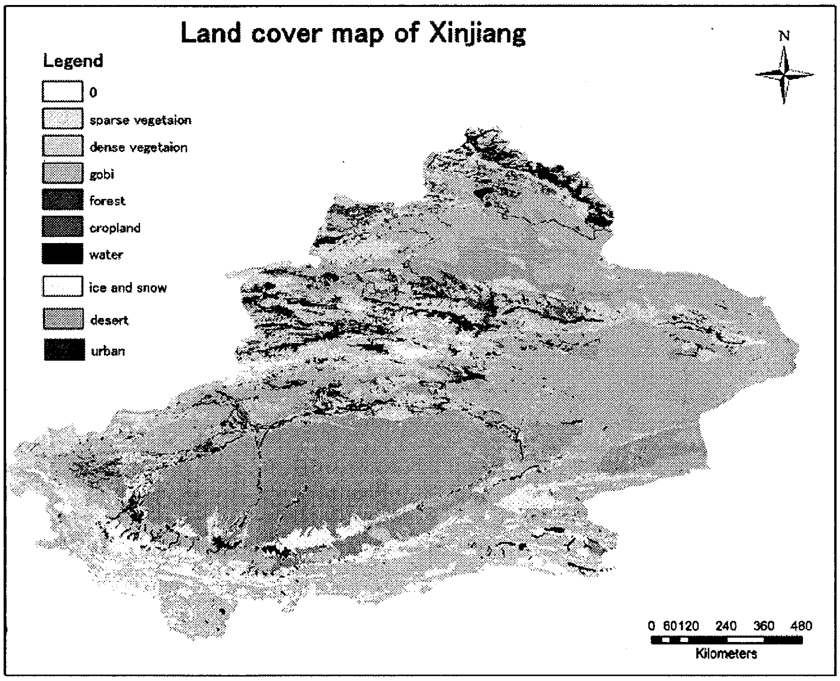

3.3 Areas at risk of desertification

Areas at risk of desertification were defined as all sparsely vegetated area of the class of sparse grassland in xinjiang land cover map. Due to highly variable rainfall events and increasing human pressure the landscapes covered by sparse, drought-adapted vegetation are most serious affected by desertification. Three major risk areas were potentially of the interests: (1) Oasis-desert ecotone, which is easily damaged by human activities. (2) The lower reaches of Tarim river, which is affected by inappropriate water utilization. (3) The overgrazing land in semi-arid regions

4. Conclusion

1.Vegetation cover is a common criterion to assess desertification. The NDVI is an useful parameter to assess the land cover in arid regions. Compared with the mono-temporal NDVI of August, which is critical month during growing season, the annual maximal NDVI proved to be more useful to detect sparse vegetation because vegetation growth in arid and semi-arid environments is usually highly rainfall dependent and peaks in NDVI values coincide with vegetation response to occasional rainfall events (Schmidt et al 2000).

2. Desertification around oasis is the major obstacle for sustainable development of oases in Xinjiang Uyghur Autonomous Region, China. An effective way maintaining the stability of oases is to recover the relatively stable ecological zone between an oasis and desert from destroyed.
3. Geophysical data, used in conjunction with SPOT VEGETATION imagery, can improve the presentation of driving factors (climate, soil, etc) and the spatial patterns of sparse vegetation distribution. This helps to improve the interpretation of images and contributes greatly to increase accuracy and higher efficiency of remote sensing classification for detecting area at risk of desertification. Climate and DEM were applied in this work to reduce the confusion among land cover types belonging to different regions. The result of classification indicates that this is feasible way for large-scale land cover characterization in Xinjiang. For further improvement of the classification, the following work is required: (1) acquisition of new and more detailed geophysical data; and (2) investigation in relationships among geophysical data and land cover types.

Reference

Alimujiang Kasimu, Ryutaro Tateishi GLOBAL URBAN MAPPING USING COARSE RESOLUTION REMOTE SENSING DATA WITH THE REFERENCE OF LANDSAT IMAGERS 28TH Asia Remote Sensing Conference, Kuala Lumpur Malaysia 2007
Gao, B. (1996) NDWI - a normalized difference water Index for remote sensing of vegetation liquid water from space. Remote sensing of Environment, 58, 257-266
MABBUTT, J.A. (1986): Desertification Indicators. Climate Changes., 9: 113-122.
MOUAT, D., LANCASTER, J., WADE,T., WICKHAM,J., FOX,C. KEPNER,W. and BALL, T. (1997): Desertification evaluated using an integrated environmental assessment model. Environment Monitoring and Assessment., 48: 1388-1391.
Schmidt, H., Karnieli, A., 2000. Remote sensing of seasonal variability of vegetation in a semi-arid environment. Journal of Arid Environments 45, 43-59
Tsunekawa, A. (2000): Methodologies of desertification monitoring and assessment. In: Workshop of the Asia Regional Thematic Programme Network on Desertification Monitoring And Assessment (TPN1) (provisional edition), 28_30 June 2000, UNU, Tokyo, Japan, pp. 44-55.
WANG, T. (2003): Desert and Desertification in China (ShiJiaZhuang: Hebei Science and Technology Publishing House).
Xiao X., Moore,B., Qin, X et al. (2002): Large-scale observation of alpine snow and Ice cover In Asia: using multi-temporal VEGETATION sensor data. International journal of Remote Sensing, 23:2213-2228.

Cropland characterization of Asia using MODIS data

Ts. Enkhzaya and R. Tateishi
Center for Environmental Remote Sensing (CEReS), Chiba University
1-33, Yayoi-cho, Inage-ku, Chiba 263-8522 Japan
Tel (81)-43-290-2964; Fax: (81)-43-290-3857
E-mail: tse_enkhzaya@graduate.chiba-u.jp

Abstract

Remote sensing images have been widely used in agricultural application for estimating cropland areas and crop production from region to global scale. Despite its widespread use, crop type separation from satellite images still poses problems and various techniques are developing to improve crop identification.

In this paper, we present our investigation on only two classes: paddy and other cropland area using 1 km MODIS data for Asia. We evaluated Normalized Difference Vegetation Index and Normalized Difference Water Index from MODIS images for describing the temporal and spatial dynamics of surface greenness and moisture. 16-day composite cloud free data and multi-temporal NDVI and NDWI images used for generate agricultural area mapping using supervised classification algorithm. This study indicates that the combination of multi-spectral data, multi-temporal NDVI and NDWI data are effective tool in analysis of cropping types and cropping pattern, even there have limitation at the 1 km resolution for heterogeneous landscape.

Key words: agricultural area, paddy area, MODIS data, NDVI, NDWI

1.Introduction

Asian agricultural population densities on rice producing lands are the highest in the world and rice presents a significant portion the amount of daily caloric intake. Updated information on rice planting of paddy fields and its distribution is needed to quantify the impacts from paddy to atmospheric chemistry and climate. Because paddy rice grows on flooded soil and contributing over 10 % of the total methane flux to the atmosphere, which may have substantial impacts on atmospheric chemistry and climate. Asian cropland has a wide range of landscape types and contains a wide variety of climatic conditions, ranging from the temperate to the tropical zones. Such large variations in the cropland region, makes the generation of a timely and spatially explicit cropland dataset a challenging task.

Recently, remote sensing images have been widely used in agriculture for estimating cropland areas and crop production. Despite its widespread use, crop type separation from satellite images still poses problems due to wide difference between transplanting and harvesting time of crops, cropping condition and cropping patterns. In this paper, we present our investigation on only two classes: paddy and other cropland area using 16-day composite cloud free MODIS data for Asia. We evaluated Normalized Difference Vegetation Index and Normalized Difference Water Indices for describing temporal and spatial dynamics of surface greenness and moisture Our objectives of this paper were 1. to assess the potential of MODIS data for land cover classification, 2. accurately discrimination of paddy rice and cultivated area and its characterization at large spatial scales.

2.Study area

The study area encompasses South and South-East Asia ranging from east 65 to 180-east longitude and south 10-to 70-north latitude. Asia has large differences of landscape types and climatic conditions including tropical and subtropical zones in the southeast, temperate zones in the northern. Most of the dry and temperate zone have one rice or other crops per year because of high dictation of temperature and precipitation while in the tropical zone two rice crops per year is common, and in some area three crops are grown.

The population is almost 3.4 billion or half of the world population and most of the population are dependent on agriculture sector. Rice is the most important production in this part and top nine paddy rice producer countries are located: China, India, Indonesia, Bangladesh, Vietnam, Thailand, Myanmar, Philippines, Japan.

3. Analysis

3.1 Used data

For analyze and distinguish the paddy fields from other cultivated area, we used 16-day composite multi-temporal MODIS images for 2003. The spatial resolution is 1 km and has 7 spectral bands. Cloud contamination is removed in Tateishi laboratory using the MODIS data for 2002 and 2004 year. MODIS derived NDVI and NDWI (McFeeters 1996) images were visually examined to describe the temporal and spatial characteristics of surface greenness and moisture and then used for supervised classification.

$$NDVI_{MODIS}=(NIR+RED)/(NIR-RED)$$

$$NDWI_{MODIS}=(Green-NIR)/Green+NIR)$$

Training data is collected from GLC 2000 global map. Agricultural areas are divided into two classes; paddy and cultivated area. Training data for paddy and cultivated area are collected from existing paddy field maps (Takeuchi, Okamoto, Surassawadee) at regional and county level and polygons checked on the Landsat scenes (Maryland university) and Google earth. Administrative boundary vector map is then used to visually analyze the classification results within the country.

3.2 Training data analysis

Time series data of NDVI and NDWI used to visually examine and describe the characteristics of agricultural area. Cultivated and paddy rice fields in different environment had different cropping pattern and cropping phenology. Most of the north and northeastern part observed the peaks of NDVI from late May/June to August/September (single cropping), while a few sites had 2 peaks (multi-cropping). South and southeastern parts are experienced mostly double and triple crops. The cultivating periods have large differences for whole year and generally can be divided into three crops: winter-spring, autumn and rainy season.

The main characteristic of paddy area is, it grows on the flooded soil and completes their life cycle within 110-120 days in the tropical zone, while in temperate zone completes 140-150 days. For separate paddy fields from other cultivated area, we made simple assumption based on the NDVI and NDWI curves of agricultural training sites. 1. if the NDVI value is higher than 0.4 and this peak continues 2.5 to 3 months at least, and 2. if NDVI have lower value in the beginning and end of this peak, and at the same time have opposite curves of NDWI value, then it can be count as paddy fields.

4.Results.

Composite image of original multi-temporal 7 spectral bands and NDVI and NDWI images used for generate agricultural area mapping using maximum likelihood algorithm.

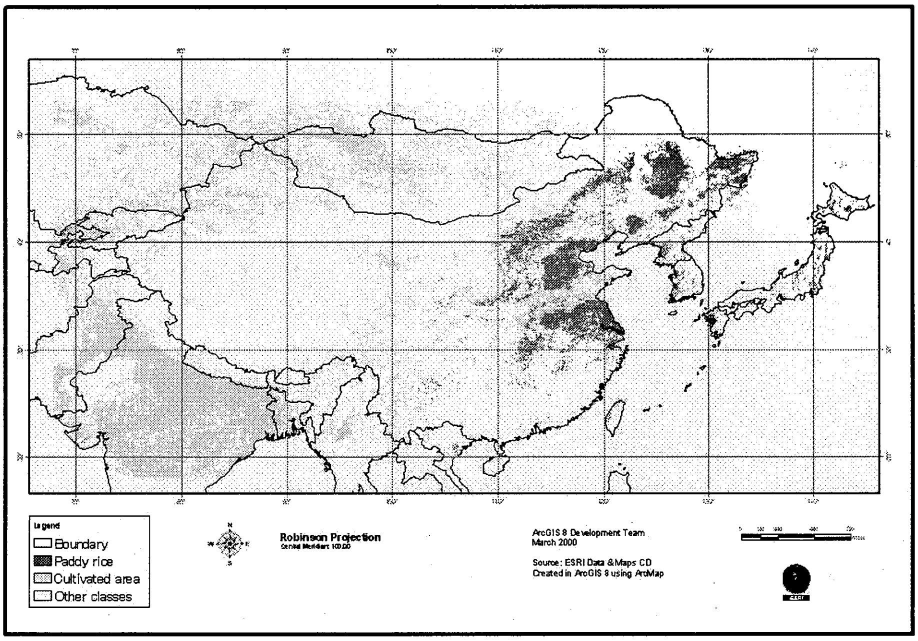

Figure1. Agricultural area map, in 2003

The false color composite image (Figure 1) shows the spatial extent of only two agricultural classes in the study area. According to the classification map, overall accuracy was 90.4%. The cultivated and paddy rice area accounts 2.9% and 4.13 % of the total area and user accuracy was 96.4% and 69.4%, respectively.

5. Conclusions

This study indicates that the combination of multi-spectral data, multi-temporal NDVI and NDWI data are effective tool in analysis of cropping types and cropping pattern and extraction of paddy fields from other cultivated area, even there have limitation at the 1 km resolution for heterogeneous landscape. Therefore, we need to make additional examination on agricultural area extent in each country level and to combine with country and county level agricultural census data.

6.References

Le Toan, T., Ribbes, F., Fluory, N., Wang, L., Kong, J., Kurosu, T., and Fujita, M, 1997 Rice crop mapping and monitoring using ERS-1 data based on experiment and modeling results. IEEE Trans Geoscience and Remote Sensing, 35 (1), 41-56.

McFeeters, S, K., 1996, The use of the Normalized difference water index (NDWI) in the delineation of open water features. International Journal of Remote Sensing, 17, 1425-1432.

Okamoto, K., and Kawashima, H., 1999, Estimation of rice-planted area in the tropical zone using a combination of optical and microwave satellite sensor data International Journal of Remote Sensing, 20 (5), 1045-1048

Surassawadee, P., 2004, Rainfed Rice Mapping using RADARSAT Nakhon Nayok case study, In proceedings of 25th Asian conference on Remote sensing

Takeuchi, W., Yasuoka, Y., 2005, Mapping of fractional coverage of paddy fields over East Asia using MODIS data. Journal of the Japan Society of Photogrammetry and Remote Sensing 43 (6) 20-33

Effect on ocean color after gigantic earthquake in Indonesia in recent times

Sisir Kumar Dash [1] & Tasuku Tanaka [2]

[1, 2] Department of Mechanical Engineering, Faculty of Engineering
Yamaguchi University, 2-16-1, Tokiwadai, Ube, 755-8611, Japan
Email: skdash@yamaguchi-u.ac.jp

Abstract:

Several earthquakes triggered to tsunami, devastated Indonesia and become one of the seismic active regions in the world, changes oceanic environment in recent times. Changes in chlorophyll were studied after the earthquakes using MODIS-Aqua satellite data. Chlorophyll concentration estimated using SeaWiFS chl-a algorithm (OC4V4). The initial result shows high concentration of chlorophyll after the earthquake in the west coast of Sumatra and Java regions. The epicenter mostly located in the bottom of ocean, so there is a counter assumption that due to large magnitude there is a significant increase in suspended sediment due to intense ground shaking and causes to sudden upwelling which reflects in both sea surface height anomaly and chlorophyll images. The increase of the primary production in the coastal water certainly due to upwelling occured during 2004-2007. It is difficult to assume the existence of upwelling prior to earthquake. In few occasions, comparison studies were made in pre and post earthquake events. The comparison is significant to know the temporal variability of ocean color particularly in Sumatra regions prior to earthquake. In coastal waters, the changes are largely affected by vertical mixing of waters compared to open ocean. Due to thick cloud cover in the tropical areas like Java and Sumatra, satellite images failed to detect ocean color information in some cases.

Keywords: Ocean color, Tsunami, Chlorophyll, SSHA

1. Introduction

Indonesia archipelago that is affected by earthquakes and tsunami takes thousand of lives since 2004. Despite 26th December 2004 earthquake with a magnitude of 9.3, every year the subcontinent experiences earthquake with more than 6.0 magnitudes. Due to frequent earthquakes the Australia plate moves north-northeast with respect to the Sunda plate at about 59 mm/year (USGS, 2006). Recently, there are three big earthquakes in the year 2006 and 2007. The detail about their position, magnitude is shown in Fig.1 and described in Table-1. After a massive earthquake, the casualties caused by either tsunami or landslide or any means become a serious threat to human being. Besides this, the marine environments get distrubed and largely affected to oceanographic life in this region. So far, there have not many studies reported on ocean color (Chlorophyll concentration) variabilty during pre and post earthquake events in these areas. Due to limitation for the in-situ observation, satellite remote sensing has provided an alternative to study the oceanographic conditions in the Java-Sumatra regions.

There are several ocean colors sensors like MODIS, MERIS, SeaWiFS which provide Chlorophyll-a (chl-a) concentrations and used as the relative measure of phytoplankton abundance and biomass in the ocean (Martin, 2004). In the open ocean or case-1 waters, all of the optical properties in the ocean are determined by phytoplankton concentration. However, in coastal waters so called case-2 waters, suspended sediment, colored dissolved organic matter (CDOM) and phytoplankton concentration are mixed. Satellite altimeter also provides sea surface height anomaly (SSHA) information on regular basis.

The December 26, 2004 tsunami caused vast destruction to the marine ecosystem (UNEP, 2005). High sedimentation caused by backwash resulted in overestimation of the chl-a concentration during the massive tsunami event(Tan et al, 2007). But the chl-a bloom at the upwelling area at Malacca Straits did not exhibit any significant changes in relation to the tsunami wave. Mostly all these upwelling caused by north-east monsoon wind. Based on the above observation, it is clear that suspended sediment dominance were observed significantly in pre and post tsunami event. Due to large cloud cover, it become difficult to estimate chl-a concetration during this period. Simliar obeservation were reported in Gujurat earthquake during 2001. Singh et al, 2001 reported that the increase of chl-a and suspended sediment concentration is clearly seen in the creek regions of the Gujurat coast and along the west coast of India immediate after earthquake using IRS-P4 OCM data. They also proposed that the significant increase in chl-a and suspended sediment concentration after the earthquake can be attributed to the upwelling of subsurface water and vertical mixing (Uz et al, 2001).

The main objective of this study is to examine the tsunami effects on the chl-a and SSHA variations using MODIS Aqua sensor and altimeter data during pre and post earthquake. We are fortunate to get the cloud free data in this period except at E3 location. Due to lack of sufficient in-situ data and the suspended algorithm we failed to show suspended sediment concentration information in this region. The SSHA and chl-a depicts the tsunami features as most of the data were processed immediate after earthquake.

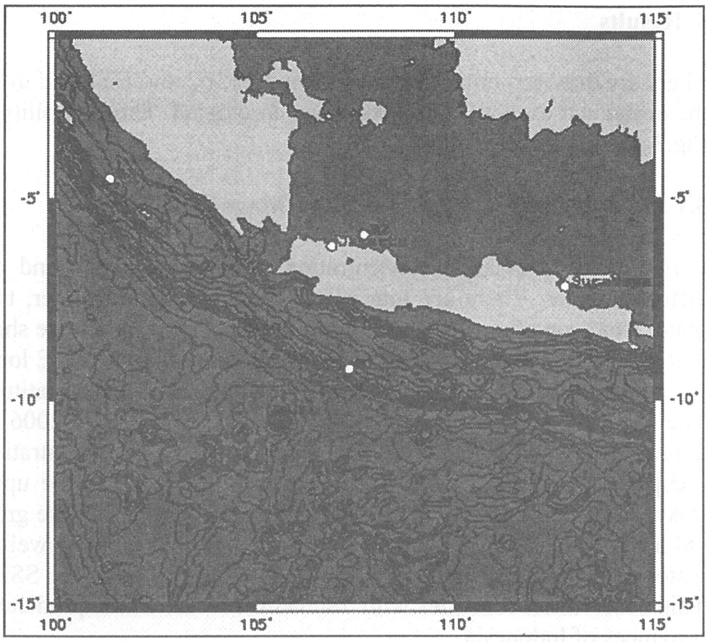

Fig.1 Study area. The white dot with number shows the epicenter of earthquake on three different location and three different time shown in Table -1.

2. Material methods

The study area covers the earthquake epicenter and tsunami affected areas at the Indonesia Sea within area between 100°E - 115°E longitude and 1°S - 15°S latitude comprising eastern Indian ocean and Java sea. Fig.1 shows the bathymetry and geographical locations of major earthquakes (http://www.aquarius.geomar.de/omc/make_map.html).

2.1 Satellite Data

The spatial and temporal changes of ocean color and SSHA during pre and post tsunami event were studied using MODIS-Aqua and Altimeter data respectively. MODIS-Aqua images are produced from both the Level 2 and Level 3 data from Ocean Color Web (http://oceancolor.gsfc.nasa.gov/). The Level 2 data is used to provide near realtime images, though it is replaced by the Level 3 data once it becomes available. The chl-a images were processed using standard MODIS chl-a algorithm (OC4V4). Sea surface anomaly data are produced from Jason, TOPEX/POSEIDON(T/P), Geosat Follow-On(GFO), ERS-2 and Envisat altimeter data processed in near real-time, usually within 12 to 36 hours of over flight. The data were processed online using Colorado university website (http://argo.colorado.edu/~realtime/welcome/). An analysis product is based on the latest 10 days of Jason and T/P, 17 days of GFO and 35 days of ERS-2 and Envisat sampling, if available.

SL. No.	Date and Time (UTC)	Place	Latitude	Longitude	Earthquake Magnitude	Tsunami Forcast (USGS)	Casualty*
E1	2006-07-17 08:19:28	South of Java	9.23S	107.33E	7.7	Yes	403
E2	2007-08-08 17:04:56	Java	5.90S	107.69E	7.5	No	4
E3	2007-09-12 11:10:26	Southern Sumatra	4.50S	101.36E	8.4	Yes	25
* Report from USGS, Yahoo News							

Table - 1: showing the location of major earthquakes and other parameters

3. Results

There are three major earthquakes named E1, E2 and E3 listed in Table.1. All these epicenter are bottom of the ocean and except E2, tsunami were forecasted. The variability of chl-a concentration is shown in Fig.2, Fig.3 and Fig.4 respectively.

3.1 17th July 2006 Earthquake (E1) – Magnitude 7.7

Large variation of chl-a concentration is observed in pre and post earthquake shown in Fig.2 in three different plates. There are four plates describes the epicenter, two days prior to earthquake (in separate plate) and soon after earthquake respectively. Plate b and c are shown to identify the upwelling phenomena that caused due to strong wind or monsoon wind. At 107.33°E longitude the upwelling merely visible prior to earthquake observed on 16th and 17th of July 2006 and its latitudinal extent varies between 11°S to 14°S. The exact time of earthquake is 08:19:28UTC of 17th July 2006 and the satellite pass of MODIS-Aqua is approximately 06:00:00UTC. The changes in chl-a concentration is found by the 18th July 2006 pass compared to previous days. This change is attributed to the upwelling of subsurface water and vertical mixing caused by tsunami. It is difficult to predict the intense ground shaking cause high concentration of chl-a but certainly significant change is observed as weak upwelling. To find out the movement of surface water caused due to tsunami, altimeter observation shows the SSHA and the contour moves northeastward. This observation coincides with Tsunami forecast which predicted to Cilacap, Kebuman and Tasikmalaya provinces of Indonesia.

3.2 8th August 2007 Earthquake (E2) – Magnitude 7.5

The epicenter of 08th August 2007 earthquake (E2) was 110km north of Jakarta, Indonesia. Before the earthquake (07th and 08th August 2007), the spatial distribution of chl-a concentration of around 0.1-0.5mg/m3 mostly in Java sea is shown in Fig.3 plate b and c. High concentration of chl-a observed in Jakarta and Semarang coast. Since the epicenter was 280km below the sea bottom, its effect was very small. Hence a drastic change in chl-a concentration was not found on 09th august 2007 satellite data as appeared in Fig.3 plate d. The SSHA remain unchanged during these days. Tsunami was not forecasted and the devastation was small.

3.3 12th Sept 2007 Earthquake (E3) – Magnitude 8.4

Due to large amount of cloud cover prior to 12th Sep 2007 earthquake (E3), it become difficult to estimate chl-a concentration. However, Fig.4 plate b shows the image of high concentration of chl-a along Sumatra region at 101.36E 4.50S and moves southwards. This epicenter was similar to E1 epicenter and significant changes were observed along sumatra and Java coastal areas. Very high chl-a concentration (> 10.0mg/m3) were observed at north-western sumatra. Chl-a also increased near Bengkulu and Sumatra Barat. A tsunami with a wave height of 90 cm was measured at Padang (USGS, 2007). After the tsunami, the clould exists and failed to depict the chl-a concentration. SSHA moves southward and remain unchaged for one week at 6.0°S. The chl-a plume moves from 4.0°S to 6.0°S and the reason of movement remain unknown.

Based on these three case studies, it is evident that the chl-a concentration varies depending on tsunami and epicenter depth. Though in some cases cloud become a major threat to depict chl-a concentration, altimeter data can provide the movement of surface water mass based on its contour plotted with chlorophyll. If information from chl-imageries failed, then overlaying SSHA data reveals much more information.

4. Discussion

4.1 Chlorophyll-a concentration variation

Immediate after earthquake, tsunami generated in Open Ocean and the wave migrated towards coastal regions possibly stirred up by bottom sediments and other constituents. During this vertical mixing process, the possible high concentration of chl-a sometimes overestimates with MODIS algorithm. Regional algorithm for chl-a concentration in the turbid coastal water is needed in order to understand the actual chl-a variation in this area.

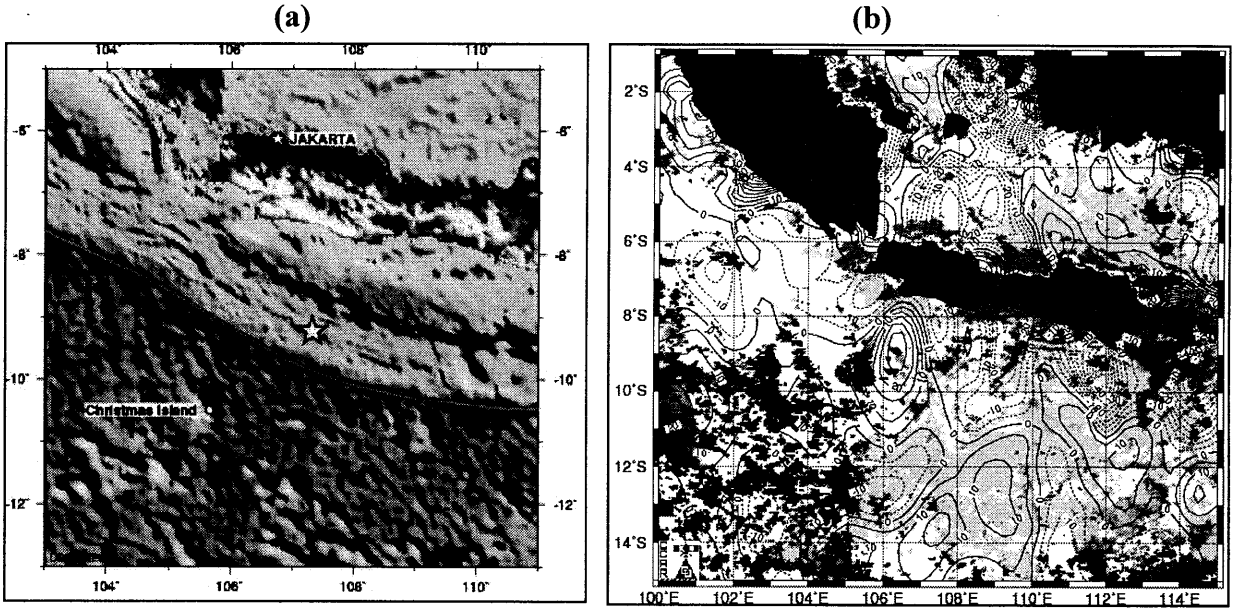

Earthquake Location: South of JAVA, Indonesia
2006 – 07 – 17 08:19:28 UTC
9.23S 107.33E, Depth: 34m, Magnitude: 7.7

16th July 2006

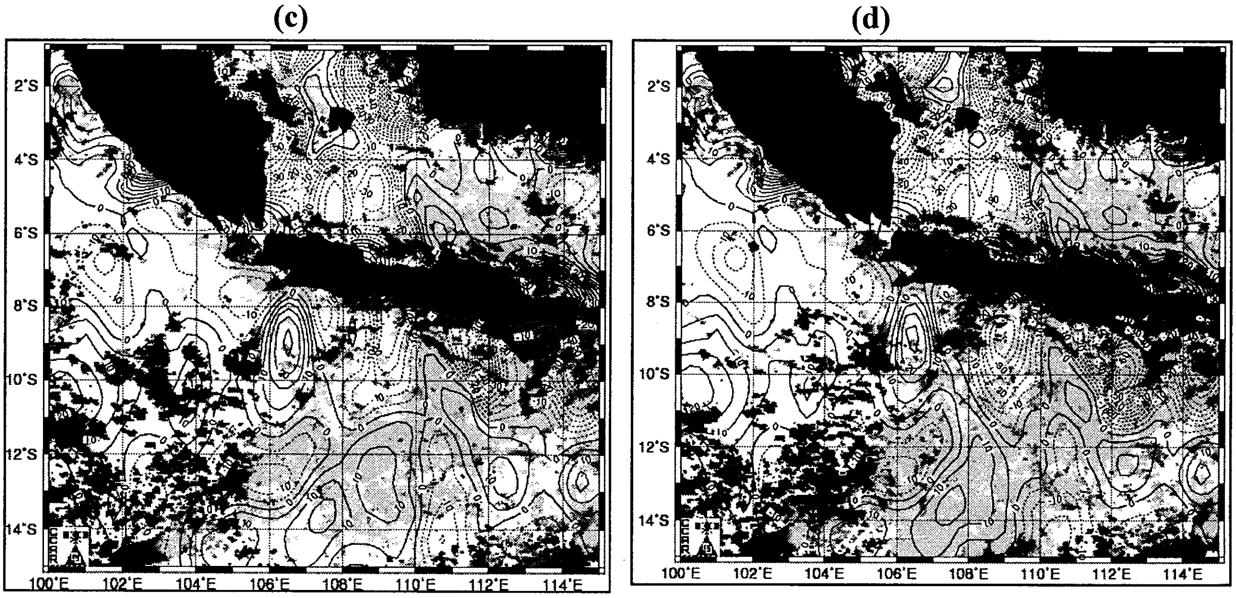

17th July 2006

18th July 2006

Fig. 2 Real time SSH (cm) and Chlorophyll concentration (mg/m3)

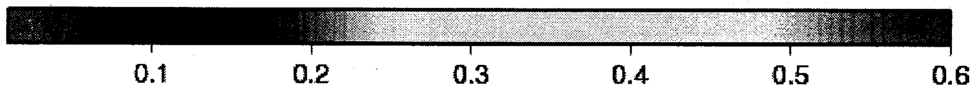

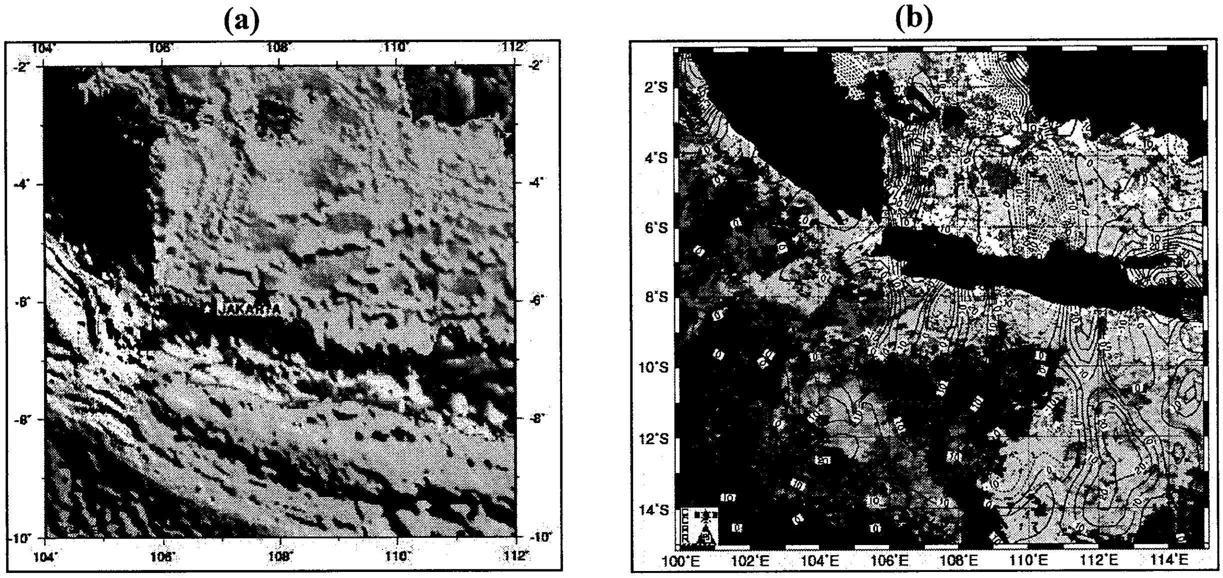

Earthquake Location: Java Indonesia
2007 – 08 – 08 17:04:56 UTC
5.90S 107.69E Depth: 280km, Magnitude: 7.5

7th August 2007

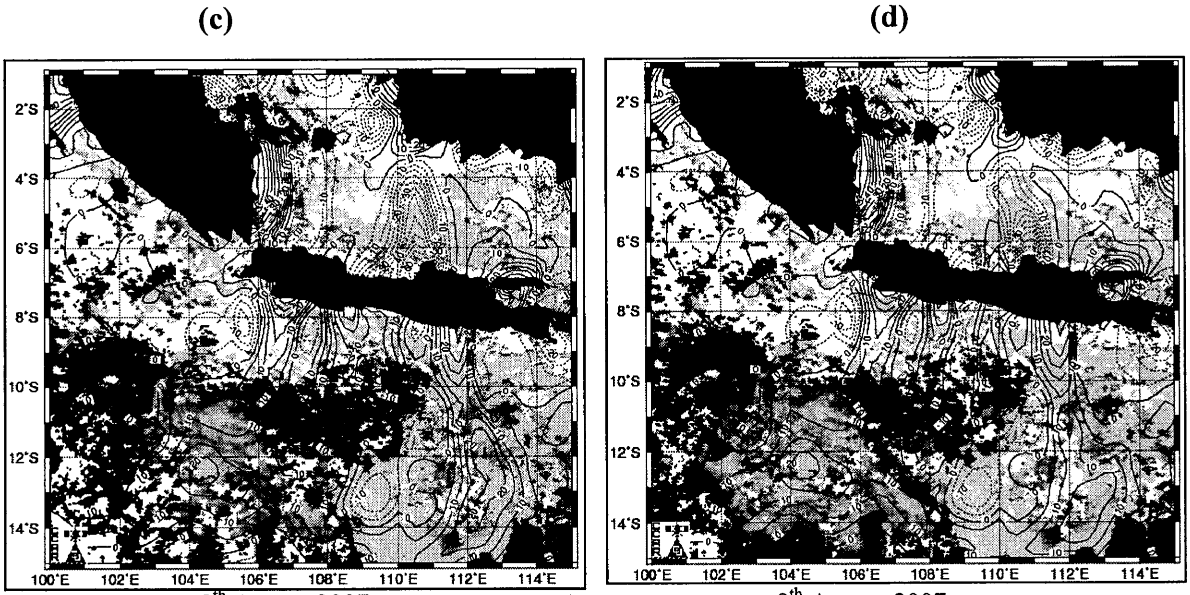

8th August 2007

9th August 2007

Fig. 3 Real time SSH (cm) and Chlorophyll concentration (mg/m3)

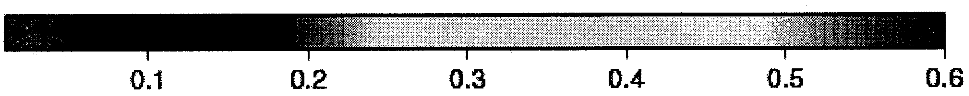

There are various algorithms available to quantify chl-a concentration. SeaWiFS chl-a algorithm (OC4V4) is relatively good for chl-a estimation in both case-1 and case-2 waters. In the present study, a large increase in chl-a concentration after the tsunami event is discussed. The increase of chl-a in the tsunami-affected coastal waters could possibly be due to the increase of turbidy where chl-a values were overestimated. It may be due to the presence of suspended sediment which affect on the chl-a concentration mainly in coastal waters. In some cases, coastal chl-a values were ignored and treated as black pixel.

We are investigating the chlorophyll variability during pre and post tsunami event caused by gigantic earthquake. In 17th July 2006, the chl-a varies from 0.5 mg/m3 to > 10.0mg/m3 at the epicenter of earthquake and migrated towards Cilacap, Kebuman and Tasikmalaya coast. This clearly indicates that during propagation of tsunami wave, the ocean productivity increases significantly and caused upwelling. The ocean color signatures either in form of chl-a or suspended sediment reveals upwelling.

(a)

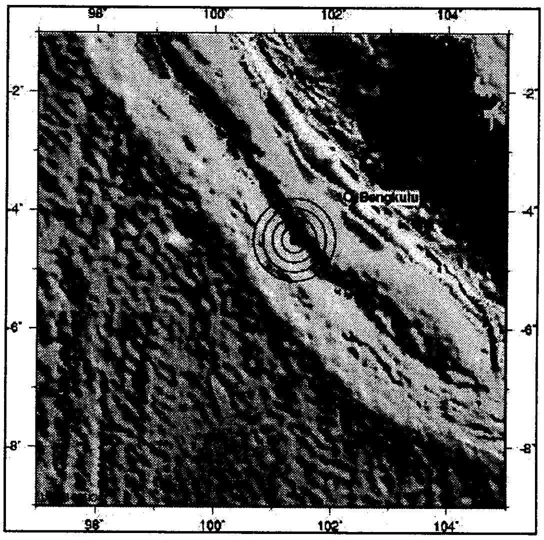

Earthquake Location: Southern Sumatra, Indonesia, 2007-09-12 11:10:26 UTC 4.50S 101.36E Depth: 34km, Magnitude: 8.4

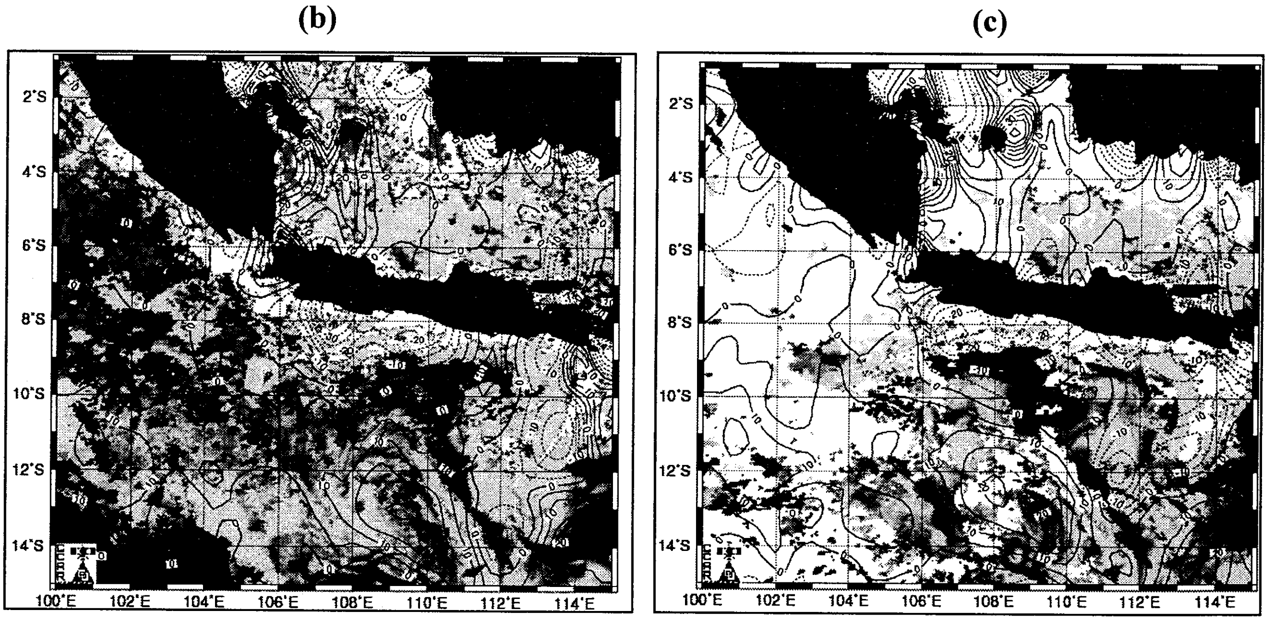

7th September 2007

13th September 2007

Fig. 4 Real time SSH (cm) and Chlorophyll concentration (mg/m3)

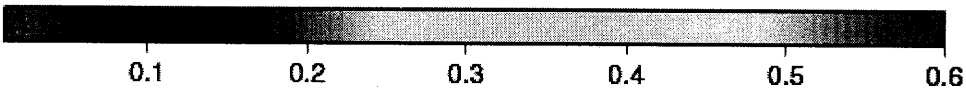

There is no tsunami forecasted in 08th August 2006 earthquake in the north of Java, Indonesia. However, an upwelling at 6°S was observed. The upwelling mechanism at the northern Java is caused by monsoon wind-driven Ekman pumping. The concentration of chl-a varies from 0.3-0.6mg/m3 remain unchaged after the earthquake. This confirm that the high magnitude earthquake did not affect the turbidity significantly in the upwelling area. The gigantic earthquake on 12th September 2007 with an magnitude of 8.4 and its associated tsunami show wide variation on chl-a concentration along southwest of sumatra. The intense of tsunami may cause vertical mixing and probably an upwelling may appear soon after the earthquake. Satellite image failed to show sufficient evidence due to thick cloud cover after the tsunami forecasted in the westcoast of sumatra.

4.2 SSHA anomaly

The combination of ocean color and SSHA data can predict the evolution of small scale eddies and upwelling in world ocean (Martin, 2004). SSHA data shows significant water mass movement followed by tsunami. The cloud cover threat in MODIS data is compensated by satellite altimetry when SSHA is superimposed on chl-a concentration images.

5. Conclusions

Indonesia archipelago experiences several gigantic earthquakes every year and suffers from vast destruction by tsunami in both land and ocean environment. This study has revealed that the effect of tsunami on chl-a and vertical mixing process is rapid and spontaneous. If it can be monitored, then several rapid assessment on fisheries can be done for the upliftment of nature resources. Because phytoplankton variation effect pelagic fisheries as a food and global climate change. Besides chl-a, suspended sediment estimation is needed to know about the local circulation caused by tsunami.

References:

1. Martin, S., An Introduction to Ocean Remote Sensing, Cambridge: Cambridge University Press, 124-165, 2004
2. Significant changes in ocean parameters after the Gujurat earthquake, Current Science, vol. 80, No.11, 1376-1377, 10 June 2007
3. Tan.C.K., Ishizaka, J., Manda, A., Siswanto, E and Tripathy, S.C., Assessing post-tsunami effects on ocean color at eastern Indian Ocean using MODIS Aqua satellite, International Journal of Remote Sensing, 28:13, 3055-3069, 2007.
4. UNEP (United Nation Environment Programme), After the Tsunami: rapid environmental assessment. Available online at: www.unep.org/tsunami/tsunami_rpt.asp (last accessed on 20 October 2007)
5. USGS Available online at: http://earthquake.usgs.gov/regional/world/historical.php (last accessed on 20 October 2007)
6. Uz, B.M et al, Nature, 409, 597-600, 2001

Annual Variation on Ice Flow by Using Satellite Images in Shirase Glacier, Antarctica

Tomoaki KITAYAMA[1] , Kazuki NAKAMURA[2] and Fumihiko NISHIO[3]
[1, 3] Center for Environmental Remote Sensing, Chiba University
Advanced Industrial Science and Technology
E-mail: tomotomo@graduate.chiba-u.jp

Abstract

In 1998, shiase glacier floating ice tongue broke (Fig.1). same time, Sea Ice discharged from Lutow-Holm Bay in Antarctica (Ushio, 2006). But we have not understood it changes, because observations are very difficult in this area. For the understanding of Shirase Glacier detailed changes, especially Velocity of Floating ice tongue using satellite images from 1990 to 2006. Using satellite is acquired by MOS-1, MOS-1b, JERS-1, ERS-2, and Terra.

The result from that, the velocity of floating ice tongue had not constant and had changed for the past 17 years. Particularly, after the floating ice tongue broken in 1998, it was clarified that the velocity of the glacier had increased greatly when it was compared with the average year value.

1. Introduction

In the present climate condition, the melt in the cryosphere is remarkable. Result it is thought that the sea level rises. The 90% ice on the earth exists in the Antarctica. When thinking about the sea level change related to the climate changes, it is very important to think about the mass balance on the Antarctic ice sheet. In this area, the amount of consumption is decided by the glacier. So study of glacier is very important

In this study, using satellite images that velocity of shirase glacier floating ice tongue calculated. Annual variation on Ice flow velocity was presumed of 17years from 1990 until 2006.

2. Study Area

Shirase glacier located about 100km southwest of syowa station at east Antarctica (Fig.2). It flows to the Lutow-Holm Bay. Front of this glacier is floating ice tongue.

3. DATA

For the long term observation, using some satellite images. MOS-1 (sensor name is MESSR), MOS-1b (MESSR), JERS-1 (SAR), ERS-2 (AMI) and Terra (ASTER).

For the Geometric correction, Used RAMP (Raderasat Antarctic Mapping Project Digital Elevation Model Version2) Data Set by NSIDC (National Snow and Ice Data Center).

4. Method

All satellite images have difference information about Longitude, Latitude, resolution and others. There information should be made same. So I did Geometric Correction. Second, Reading coordinates of corresponding point between images with different time. And glacier velocity is requested by using coordinates value by using the following expression.

$$V_{year} = \frac{365}{\Delta T}\sqrt{(x_2 - x_1)^2 + (y_1 - y_2)^2}$$

Flow velocity is calculated like this.

5. Result

It understand that the average velocity (1990~2006, 17years) is 2750m/a in left bank and 2350m/a in right bank (Fig.3). There is 400m difference in left and right velocity. It is thought that the thickness of Ice in left and right is cause in it (Nakamura et al., 2007). It understands that velocity is not constant and has variation every year. Especially, velocity in 1990 and 1998 was faster than Average. At the same time, shirase glacier floating ice tongue broken (Fig.1 and Fig.4). I think that it relate these events. When Floating ice tongue shorter Velocity of shirase glacier faster.

6. Summary and Discussion

It understand that velocity of shirase glacier floating ice tongue (1990~2006, 17years Average) are 2750m/a in left bank and 2350m/a in right bank. There is 400m/a difference in left and right velocity. And the velocity is not constant and has variation every year. Especially, velocity in 1990 and 1998 was faster than Average. At the same time, shirase glacier floating ice tongue broken (Fig.1 and Fig.4). When it broken that sea ice decreased in Lutow-Holm bay at the same time.

I think that velocity is not constant because there are possibility of influencing sea ice extend in lutow-holm bay, temperature, wind and melt water under the bed lock. But I don’t understand it. And I think that it relate velocity increase to floating ice tongue broken. When floating ice tongue is long that it velocity is decreasing. Because floating ice tongue velocity depends on the shirase glacier movement. So floating ice tongue controls glacier movements. When floating ice tongue broken that velocity is increase because there is no bar.

References

K. Nakamura, K. Doi, K. Shibuya, 2007.Why is Shirase Glacier turning its flow direction eastward? Polar Sci. (accepted)

S. Ushio., et al 2006. Sea ice variation in Lutow-Holmbukta, Antarctica, during the last fifty years. J. Japanese Soc. Snow and Ice 68, 4, 299-305

Fig.1 Collapse of shirase glacier floating ice tongue

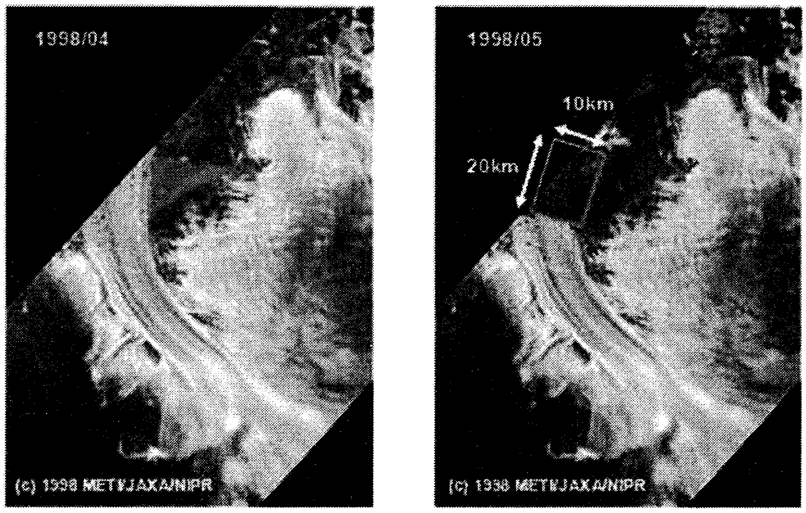

Fig.2 Shirase glacier and Antarctica

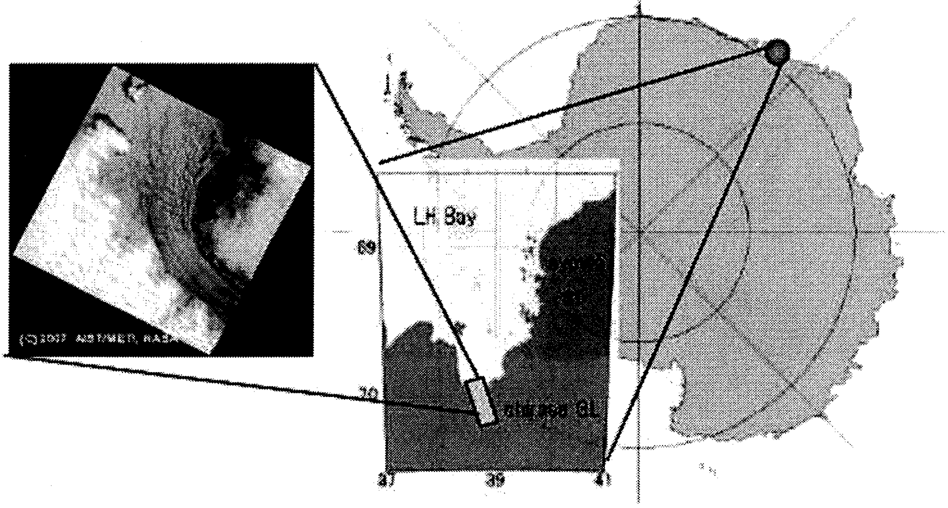

Fig.3 Velocity of shirase glacier left and right bank

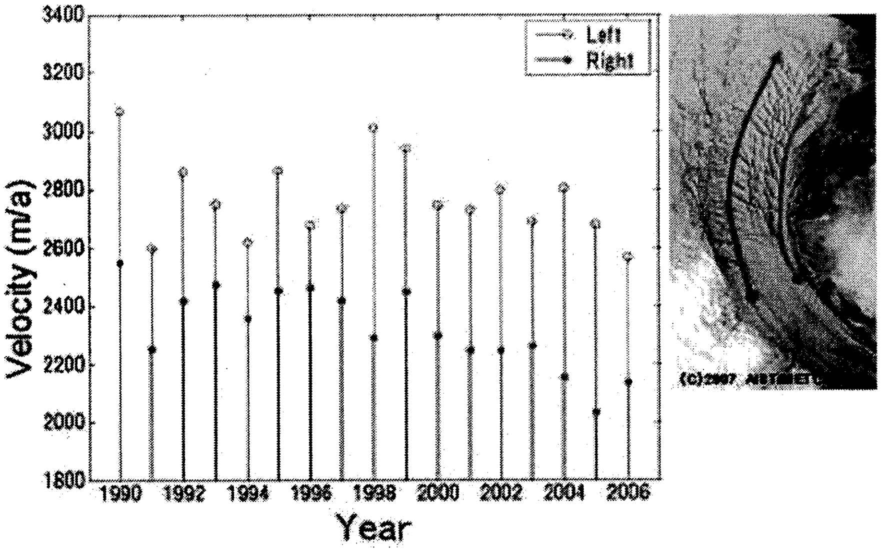

Fig.4 Distance for floating ice tongue from reference line

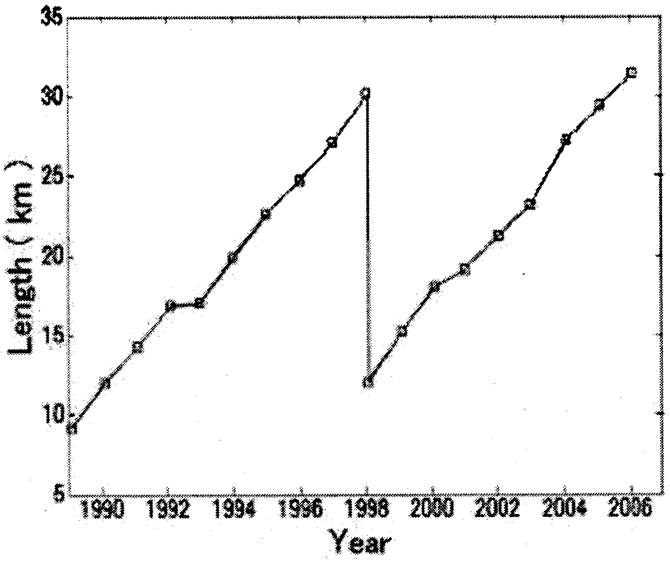

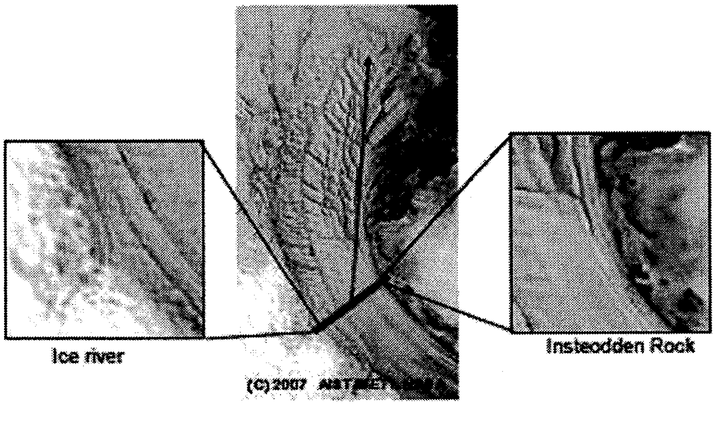

Utilization of remote sensing data for estimating damage ratio of rice crop –Part6- Examination of the yield estimation model based on kinds of agricultural weather hazard

Chiharu Hongo[1] , Kunio Takezawa[2], Akihiko Ito[3], Seishi Ninomiya[2],
Kazuhisa Tokui[4] and Toshiaki Takeshima[5]
[1]Center for Environmental Remote Sensing, Chiba University(E-mail: hongo@faculty.chiba-u.jp)
[2]National Agricultural Research Center, [3]Space Engineering Development Co., Ltd.,
[4]National Agricultural Insurance Association, [5]Japan Aerospace Exploration Agency

Abstract

The evaluation with objectivity is required by the policyholder because the estimate of damage ratio of rice crop is depending on the evaluation member's skill and also it has misgivings about the evaluation staff's aging.

In this study, the estimation of the rice yield affected by the storm and flood damage and the blast disease were conducted in Hokkaido and Miyagi prefecture, Japan. The five different models were adopted to estimate the rice yield of each damage. The predictive error of the blast disease derived from both the multiple linear regression and the ridge regression was within the range of value calculated through the external examination by the evaluation of expert staff.

The result suggested that, by the creating each yield estimation model for kinds of agricultural weather hazard, the predictive error will be improved.

***Keywords* : rice yield, storm and flood damage, blast disease, agricultural insurance**

1. Introduction

The agricultural benefit is an agricultural insurance system to protect the farm management from agricultural damages(Fig.1). The evaluation of the damage is labor intensive. For example, 83,787 assessors worked for 173,000days to evaluate damages occurred in 2.92 million cases/fields in 2003. The entire system has difficulties both to maintain the objectivity and to cope with the aging problem of the population. Our study aims at developing a damage evaluation system for rice crop based on satellite data, GIS, and ground observations.

In the previous study, the results showed that the predictive error of rice yield affected by the cool summer damage was 57kg/10a. In this study, the estimation of the rice yield affected by the storm and flood damage and the blast disease were conducted in Hokkaido and Miyagi. The five different models were adopted to estimate the rice yield of each damage.

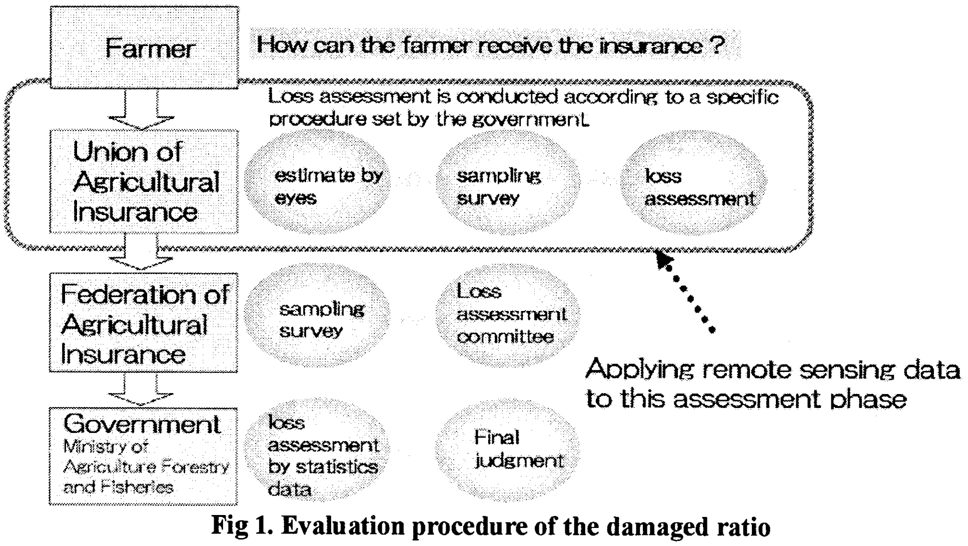

Fig 1. Evaluation procedure of the damaged ratio

2. METHODOLOGY

2.1 Study site

The study was conducted in Hokkaido and Miyagi prefecture, Japan(Fig.2). Three test sites were selected in this study. The K-district and O-district are from Miyagi and T-district is from Hokkaido.

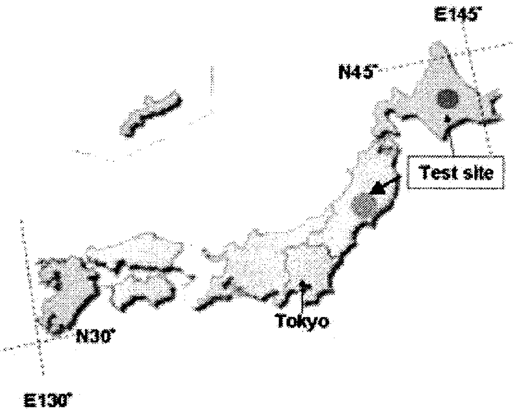

Fig 2. Study site

2.2 Ground truth data

The data of survey by reaping the plots, which is owned by agricultural insurance group, was used as the ground truth data in 2006. Eight species of rice crop were selected which are Kirara397 Hoshinoyume, Nanatsuboshi, Oborozuki,Hitomebore, Sasanishiki, Koshihikari and Miyakogane for estimating the rice yield. The numbers of ground truth samples of each damage Are: 401 fields of non-damage,47 fields of storm and flood damage and 23 fields of blast disease.

2.3 Satellite data and GIS data

The ALOS/AVNIR-2 data acquired on August 26, the SPOT5 data acquired on September 2 and September 17 of T-district were used to estimate the rice yields. The SPOT5 data acquired on September 21 of K-district and the data acquired on September 21 of O-district were used for analysis.

The GIS data of 2006 was used from the data base of Soil Improvement Organization to identify paddy fields in the satellite data.

2.4 Procedure

The image analysis procedure is described in Figure 3. The satellite data was rectified using GIS data by the nearest neighbor resampling algorithm using the selected ground control points. The shape file of paddy field was created from GIS data and overlaid on satellite data to extract paddy fields. The digital number (DN) values for selected points were extracted and the statistical models which are Multiple Linear Regression Analysis (MLRA), Partial Least Squares method (PLS), Ridge analysis(Ridge),L2 boosting(L2) and Projection Pursuit Regression Model (PPRM) were executed to estimate a rice yield. Finally, the comparison of prediction errors of each models were performed using the 10-fold cross-validation by random data partitioning.

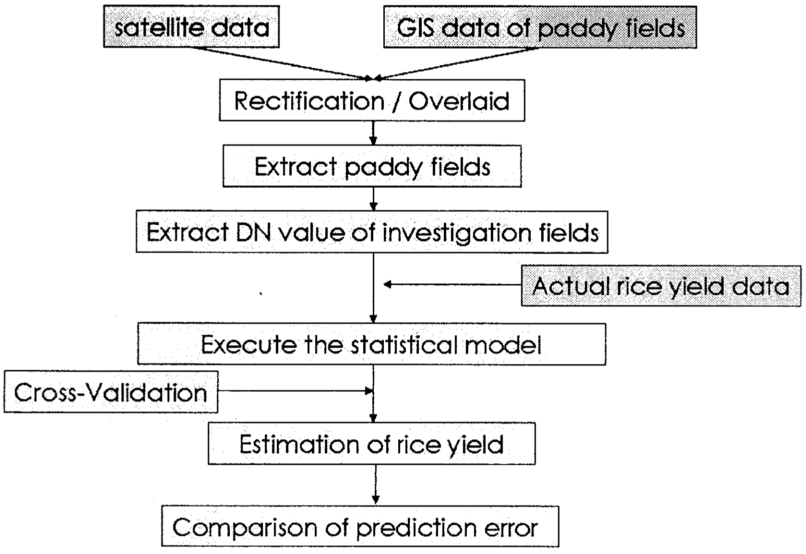

Fig 3. Procedure of analysis

3. RESULTS

The results of rice yield estimation are shown as follows.

K-district : The predictive error derived larger in the following order : Multiple linear regression analysis(85.3kg/10a)< Ridge analysis<L2 boosting<Partial least squares method<Projection pursuit regression model(123kg/10a), when adopted the combination of the storm and flood damage and the non damaged data(Fig.5). In the case of blast disease and non damaged combination data, the predictive error become larger in the following order : Ridge analysis(66kg/10a)<Multiple linear regression analysis<L2 boosting= Partial least squares method<Projection pursuit regression model(78.5kg/10a)(Fig.4).

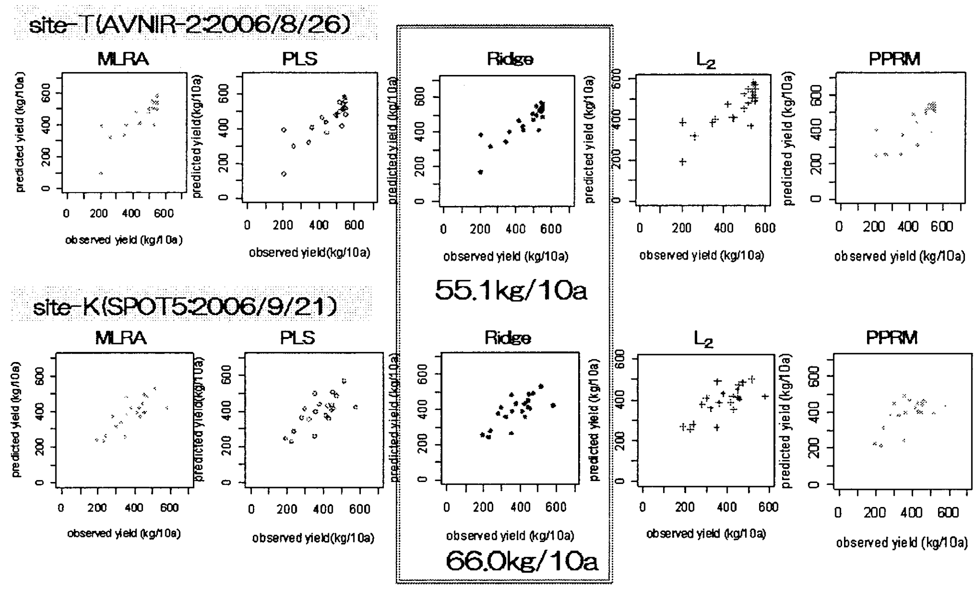

Fig.4 Predictive error of the blast disease

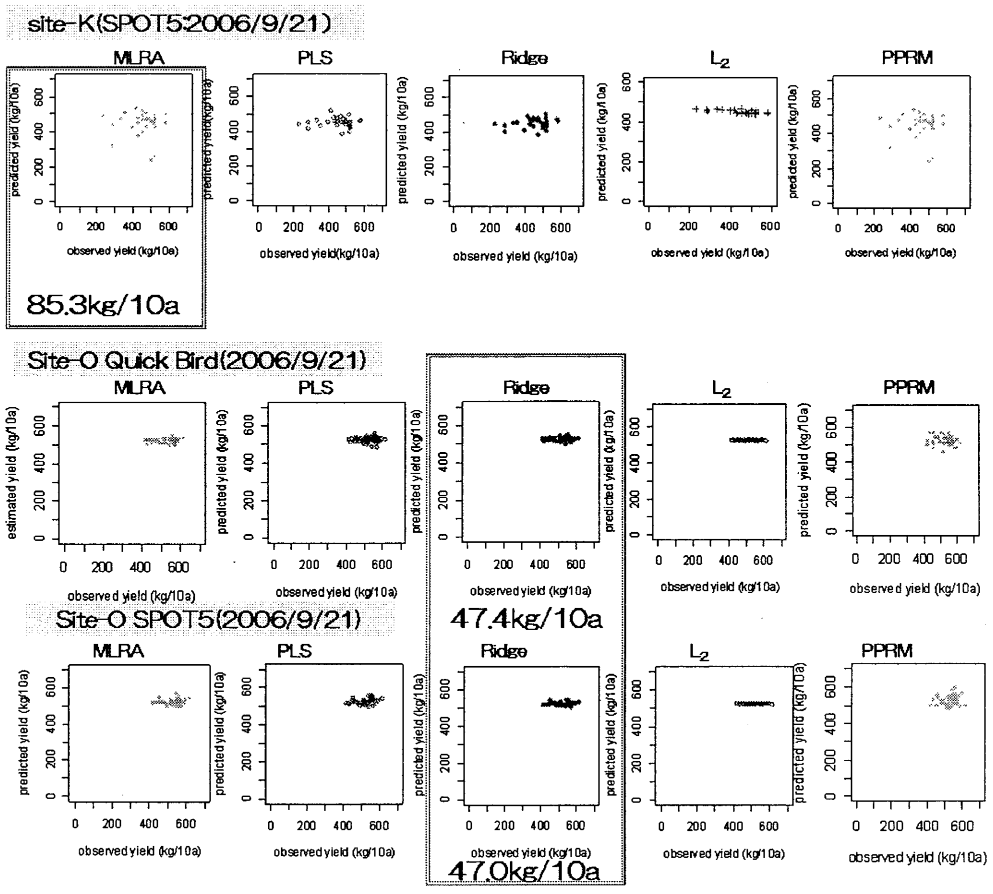

Fig 5. Predictive error of the storm and flood damage

O-district : The predictive error derived larger in the following order of Ridge analysis (47.5kg/10a)<L2 boosting <Multiple linear regression analysis<Partial least squares method<Projection pursuit regression model(54.2kg/10a), when adopted the combination of storm and flood damage and non damaged data(Fig.5).

T-district : In the case of using the ALOS/AVNIR2 data, the predictive error derived from the blast disease and non damaged combination data was larger in the following order of Ridge analysis(55.1kg/10a)<Partial least squares method<Multiple linear regression analysis<L2 boosting < projection pursuit regression model(72.9kg/10a)(Fig.4). The similar results were obtained using SPOT5 data. The error reduced from 55.1kg/10a to 54.1kg/10a when adopted Ridge analysis. The error reduced from 55.1kg/10a to 54.1kg/10a using the Ridge analysis when the observation date of satellite data was close to hervesting time.

3. DISCUSSIONS

The derivation of regression equation using remote sensing data helps us estimate the rice yield per 10a.The predictive error of the flood damage obtained through five different estimation models were not acceptable for practical use. There is a positive correlation between the degree of blast disease and the rice yield. On the other hand the rice yield of flood damage does not conform to this rule. The accuracy of predictive error was affected by this phenomenon. This is a reason why the predictive errors are bigger in the case of storm and flood damaged fields, than the blast disease damaged fields.

The results suggest that by creating each yield estimation model for kinds of agricultural weather hazard, the predictive error will be improved. The use of a specific agricultural weather hazard of rice crop leads to a beneficial regression equation. Based on the result, it may be concluded that this is an effective method for saving the expenditure and labor force. If we use such regression equations to reduce the workforce of expert staff, our simulation can play an essential role in reducing cost. We believe that the practical use of such techniques will be realized in the near future by tackling the remaining problems.

This research is supported by JAXA through the project titled : "Development for practical use of model for damage ratio calculation system of paddy rice using the remote sensing data and the ground observation".

Application of line detection method as a new approach for classifying crops

Case study: Selenge region, Mongolia

B.Erdenee[1], Ts.Javzandulam[1], Thomas G.Ngigi[1] and RyutaroTateishi[2]

[1]Graduate School of Science and Technology, Chiba University
[2]Center for Environmental Remote Sensing, Chiba University

Introduction

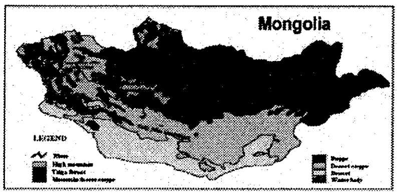

Vegetation zones	% of total land area	Annual precipitation mm	Number of growing days
Alpine zone	4.48	400-500	60-70
Taiga	3.89	300-400	65-90
Forest steppe	23.28	200-300	79-112
Steppe	25.86	125-250	112-125
Desert steppe	21.92	100-125	125-130
Desert	15.34	<100	>130

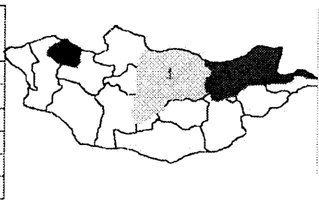

1. Central cropland region is located in north-eastern part . It covers mostly forest-steppe, steppe and rich with chernozem soil
2. Dornod region is located in west-northern part and belongs to the dry-steppe and steppe zone where dominate calcareous chestnut and fine chestnut soils.
3. Western cropland region is located in west-northern part of the mountains zone. The soil of crop land characterizes by chernozem and chestnut soil.

Background

1. Extracting straight lines (by Burns, J.B., A.R.Hanson and E.M.Riseman, 1986. Pattern Analysis and Machine Intelligence, Vol.8. pp.425-445), and
2. Standard method of sowing

Objective

To utilise line detection method on standard sowing methods (drilling, cross drilling, band sowing, etc) to develop an expert classification system of agricultural crops in Selenge region, Mongolia, using Landsat TM imagery.

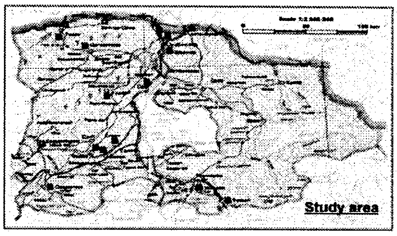

Flow diagram of line detection method-based classification by crop type

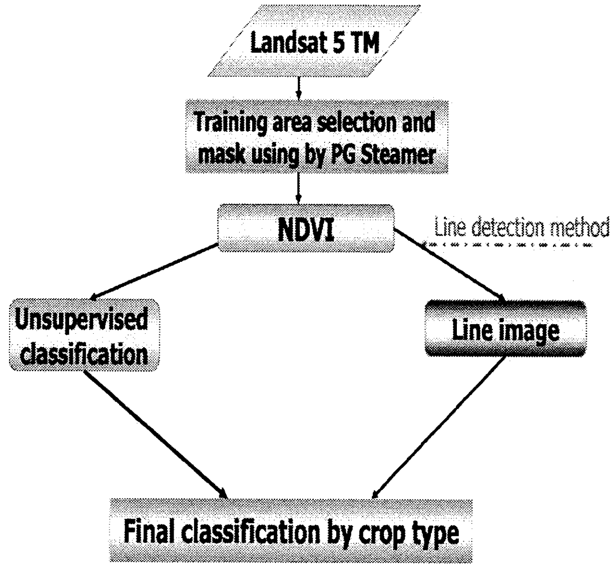

Landsat 5 TM

Training area selection and mask using by PG Steamer

NDVI

Line detection method

Unsupervised classification

Line image

Final classification by crop type

Results

Landsat 5 TM 1989.8.21

Comparison of images Unsupervised classification and NDVI 1989.8.21

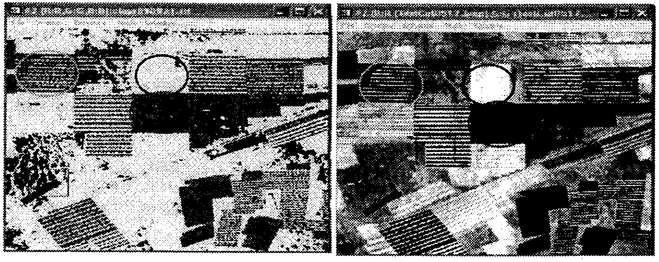

NDVI image 1989.8.21

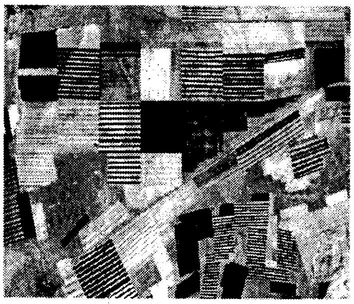

Legend

○ -Wheat

○ -Fodder

○ -Un used area in that year

Classification by crop type using line detect method

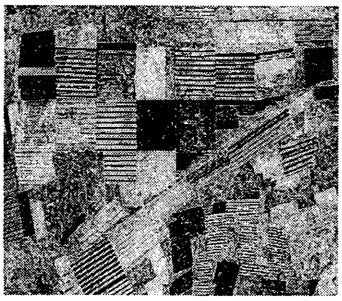

Legend

○ -Wheat

○ -Fodder

○ -Un used area in that year

Discussion

- Line detection method is applied on NDVI (30 m Landsat) data in testing area.
- It will give more accurate result from high resolution image of satellite data (Aster)
- If more RS/GIS data (e.g., contour, soil series, and etc.) are input, it is possible to use line detection method for expert classification·

Estimating sea ice mass derived from AMSR-E data

Takemasa Otosaka[1], Kazuki Nakamura[2], Kazuhiro Naoki[1] and Fumihiko Nishio[1]

(1.Chiba Univ. 2.Advanced Industrial Science and Technology(AIST))

1. introduction

1-1. background

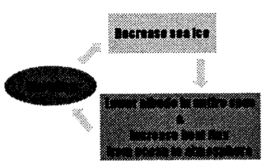

Fig.1 ice albedo feedback

When sea ice is decreased once due to warming and so on, ocean will get more heat(Fig.2(a)). Then, sea ice will be decreased again. After that, ocean will conduct more heat to atmosphere (Fig.2(b)). Finally, the global warming will make progress. This phenomenon is called "ice albed feedback". The relationship between sea ice and climate is close. Since sea ice variability can be a good indicator as a climate change, we need to monitor entire quantity of sea ice.

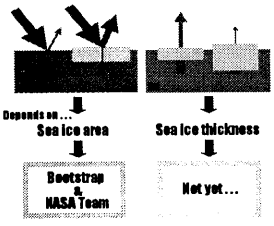

Fig.2 The two properties of sea ice for interaction between ocean and atmosphere
(a) Reflect solar radiation strongly because of high albedo
(b) High thermal insulation between ocean and atmosphere

The motion equation of sea ice

$$M_{ice}\frac{dV_{ice}}{dt}=\tau_a+\tau_w+D+G+R \qquad (1)$$

τ_a: wind stress
τ_w: ocean current stress
D: Coriolis force
G: sea surface gradient force
R: internal ice force

Based on the motion equation(equation.1), "adding a same force to two sea ice witch has different mass, a momentum of more weighted sea ice is less than of the other". In other words, sea ice mass has a relationship with sea ice motion. Therefore, we tried to estimate sea ice mass from sea ice motion.

1-2. Object

In order to estimate entire sea ice mass over a wide range , we developed the method estimated sea ice motion with the template matching with AMSR-E data. AMSR-E has a huge range of observations and high frequency observation, so it is the best for this study to use AMSR-E data. In addition, AMSR-E has a few other advantages(refer to chapter 2). The template matching has been used to estimate sea ice motion for a long time. For example, Emery 1991, Kimura and Wakatsuchi 2000 and so on. In order to solve the problem that microwave radiometer has a coarse resolution and advance accuracy of estimation, we suggest the algorithm which estimate sea ice motion down to sub-pixel.

2. About data

Data for computing sea ice motion

AMSR-E	©NSIDC http://nsidc.org/		
2003/2/18	19GHz	H pol	12.5km Grids
2003/2/19	19GHz	H pol	12.5km Grids
2003/2/20	19GHz	H pol	12.5km Grids

Data for verification

Terra/MODIS	©JAXA		
2003/2/18			1km Grids
2003/2/20			1km Grids
NCEP/NCAR Reanalysis Data	©NOAA http://www.cdc.noaa.gov/cdc/reanalysis/		
2003/2/18	sigma995	u-wind	2.5°Grids
2003/2/18	sigma995	v-wind	2.5°Grids

The characteristic of AMSR-E

- All weather
- High frequency observation (every 12h)
- Covering the earth
- Higher resolution than the other satellite microwave radiometers

3. The method of computing sea ice motion

3-1. Template matching(SSDA)

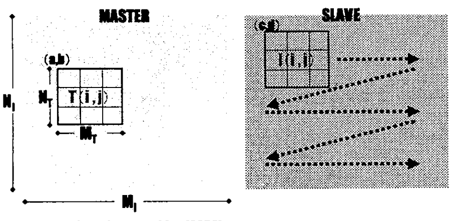

Fig.3 Template matching (SSDA)

Make a template with a focus on a certain pixel.

⬇

Calculate similarity index (Dc) with the equation (2) and Displace a template every one pixel over slave data.

⬇

Finally, the pixel which has the lowest "Dc" will be the matching point down to pixel .

$$Dc_{(c,d)}=\sum_{i=0}^{N_T-1}\sum_{j=0}^{M_T-1}\left|\,I_{(c,d)}(i,j)-T_{(a,b)}(i,j)\,\right| \qquad (2)$$

3-2. Parabola fitting

Pixel No.	...	d−1	d	d+1	...
similarity index	▪▪▪	$Dc_{(d-1)}$	Dc_{min}	$Dc_{(d+1)}$	▪▪▪

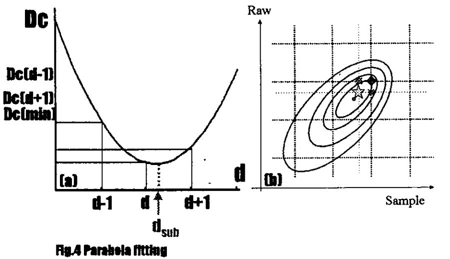

Fig.4 Parabola fitting
(a) one-dimensional fitting (b) composed matching point with two one-dimensional fittings

Implement the template matching. And calculate "Dc".

⬇

Apply a quadratic curve to Dc(min), Dc(d-1) and Dc(d+1) in a sample(or raw) direction.

⬇

The x-coordinate of the quadratic curve apex will be the matching point down to sub-pixel (d_{sub}) .

⬇

calculate "d_{sub}" in an other direction. Finally, two-dimensional matching point down to sub-pixel will be decided.

4. Computed sea ice motion

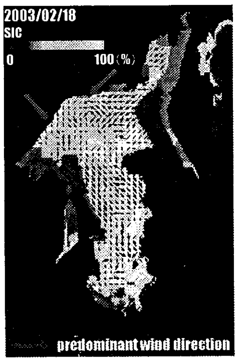

Fig.5 The result of computing sea ice motion on Feb, 18, 2003

Computed sea ice motion most probably agreed with the wind direction of NCEP/NCAR.

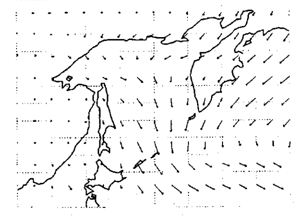

Fig.6 The wind direction near ground level on Feb, 18, 2003

5. Validation methodology

We estimated sea ice motion from MODIS data(Feb,18,2003 and Feb,20,2003) by identifying sea ice witch can be tracked through inspection. Then, we compared directions and migration length of computed sea ice motion from AMSR-E with estimated sea ice motion from MODIS.

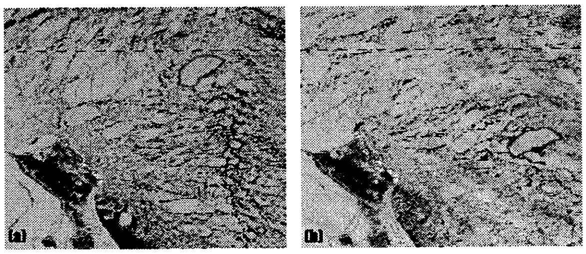

Fig.7 (a) MODIS image of the northern sea of Okhotsk on Feb, 18, 2003
(b) MODIS image of the northern sea of Okhotsk on Feb, 20, 2003

6. Results

Fig.8 Sea ice motion which was estimated from MODIS.

- Estimation regarding direction of sea ice motion was almost matching well.
- Estimation regarding migration distance of sea ice motion was not matching well. There were some miss estimation near polynya.
- Applying parabola fitting, the regression line approached 1:1 line, and the correlation coefficient was increased. However, the huge miss estimation was remained.

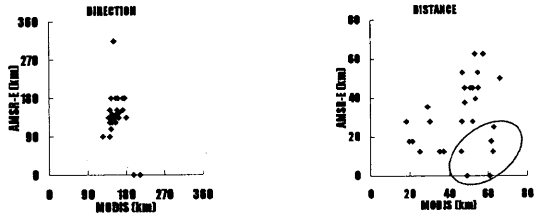

Fig.9 The scatter plot of estimated sea ice motion from AMSR-E data and MODIS data with non-parabola fitting
(a) Direction (b) Migration distance

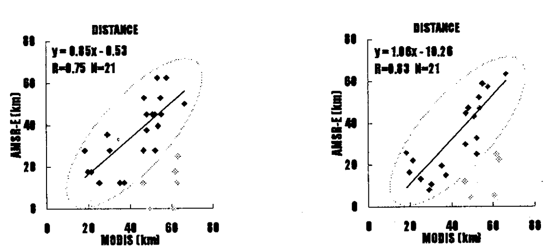

Fig.10 The scatter plot of estimated sea ice motion from AMSR-E data and MODIS data about migration distance
(a) non-parabola fitting (b) parabola fitting

7. Conclusion

- Based on momentum of sea ice, we tried to estimate sea ice mass from the relationship between sea ice mass and motion.
- In order to estimate sea ice mass, we developed the algorithm which calculate accurate sea ice motion from AMSR-E with the template matching.
- There is a miss estimation in a polynya (a polynya is a significant low concentration area).
- We was able to estimate sea ice motion by sub-pixels with the parabola fitting. As a result, the difference between migration distance estimated from AMSR-E and MODIS was decreased.

A crisis of irrigation farming by saline deposit in northern edge of Tarim basin

A.Ito : Space Engineering Development Co.,Ltd(SED),Chiba University
T.Ishiyama,K.Koutake, F. Nishio : Chiba University
S. Jalalidin :Xinjiang University , China

1.Background

The desertification area of irrigation farmland has extended in the oasis in northern edge of Tarim basin

What is the cause?

By saline deposit ?

Objective

- **Development the method for detection the saline deposit area.**
- **Understand the distribution of desertification by saline deposit.**

2.Study Area

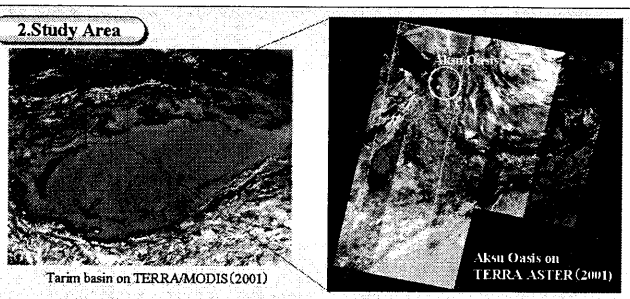

Tarim basin on TERRA/MODIS(2001)

Aksu Oasis on TERRA ASTER(2001)

4.Process of this study

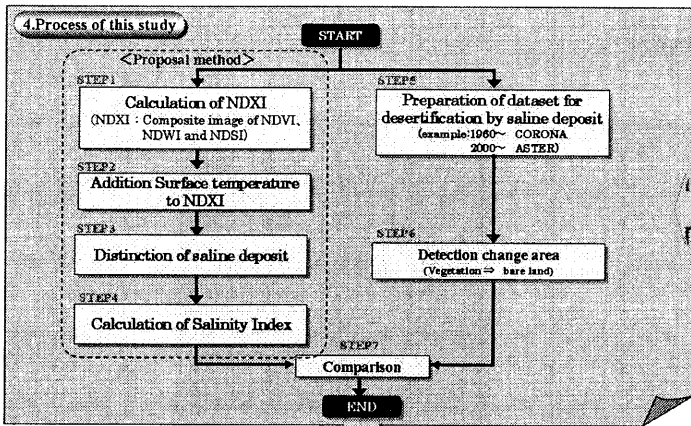

START

<Proposal method>

STEP1 Calculation of NDXI (NDXI : Composite image of NDVI、NDWI and NDSI)

STEP2 Addition Surface temperature to NDXI

STEP3 Distinction of saline deposit

STEP4 Calculation of Salinity Index

STEP5 Preparation of dataset for desertification by saline deposit (example:1960~ CORONA 2000~ ASTER)

STEP6 Detection change area (Vegetation ⇒ bare land)

STEP7 Comparison

END

3.Field Survey

Number	Soil moisture (m3/m3)	Density of Salinity(ppt)
3-A-1	0.409	12.88
3-A-2	0.453	9.30
3-B-1	0.039	37.75
3-B-3	0.030	40.60
3-B-5	0.040	44.60
4-A-1	0.477	20.10
4-A-2	0.448	4.97
4-A-3	0.441	12.84
4-A-4	0.076	9.42
4-A-5	0.492	12.09
5-A-1	0.036	10.56
5-A-3	0.454	16.34
5-A-4	0.367	20.77
5-A-5	0.404	29.16

Photograph the saline deposit in irrigation farmland

Measurement Result of Saline deposit area

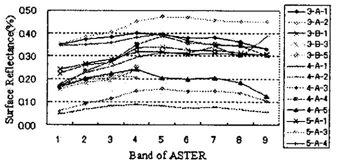

5.Result of disposal

NDVI: (band3-band2)/(band3+band2)
NDWI: (band2-band4)/(band2+band4)
NDSI: (band4-band3)/(band4+band3)

R:NDSI
G:Surface temperature (ASTER 2B03 product)
B:NDWI

15,July 2006 Terra/ASTER

STEP1 NDXI (R:NDSI G:NDVI, B:NDWI)

Composite image of Addition STEP2 Surface temperature

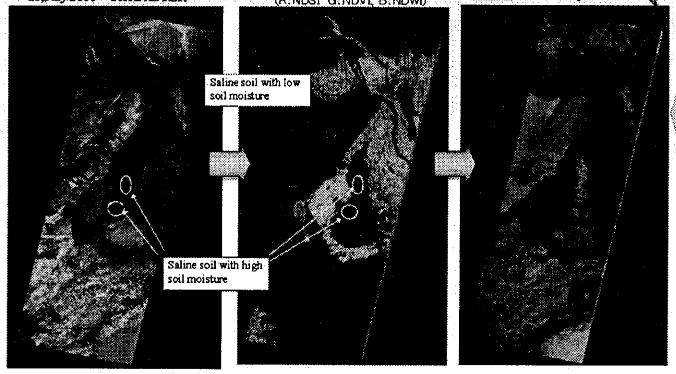

STEP3 Distinction of saline deposit

STEP4 Calculation of Salinity Index

STEP6 Detection change area

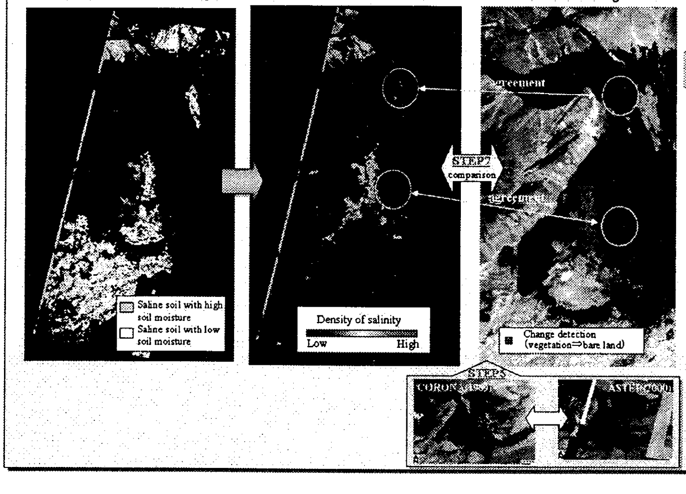

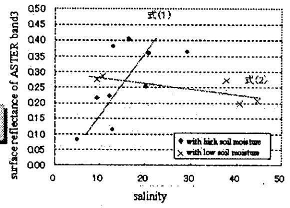

Saline soil with high soil moisture

$y=0.0107x + 0.1033(R^2=0.417)$ 式(1)

Saline soil with low soil moisture

$y=-0.002x + 0.3036(R^2=0.629)$ 式(2)

x: salinity

y: surface reflectance of ASTER band3

With high soil moisture

- ➢High soil moisture
- ➢Deposition for the surface
- ➢Color is white

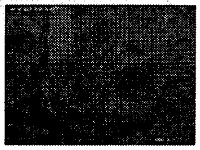

With low soil moisture

- ➢Low soil moisture
- ➢Solid soil
- ➢Color is brown or dark color.

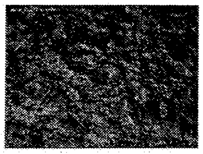

5.The Cause of saline deposit

Primary cause

An inappropriate irrigation

Deposition the salinity soil from underground

A crisis of irrigation farming

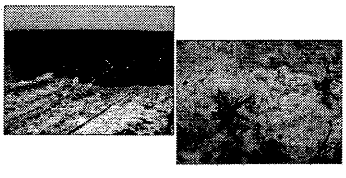

Secondary cause

Wash the salinity soil in the irrigation farmland

Accumulation for the lower reaches

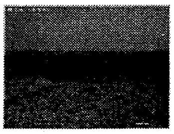

6.Conclusion

Development the method for detection the saline deposit area.
We developed the new method to detect the saline deposit area.

Understand the distribution of desertification by saline deposit.
We understood the distribution of saline deposit. Moreover we compare the saline deposit area with detection change area (vegetation ⇒ bare land). The result of comparison, we understood that the cause of desertification in northern edge of Tarim basin is saline deposit.

Extraction of the forest fire using DMSP/OLS nighttime imagery

Hiroshi YAGI*, **, Husiletu**, Shuhei OKADA*, Masanao HARA* , Fumihiko NISHIO**

*VisionTech Inc. **Chiba University

1. Introduction

The forest which is important environmental resources will need remarkable many years by the time it will restore after burned down. Once a forest fire is broken out, the fire-fighting activity is very difficult because of geographical and topological feature conditions unlike the fire of a city area, and the destructed area will become very huge widespread. And the increase of the amount of the CO_2 discharge base on the forest fire ,which is said to occupy 70～80% of greenhouse gas, influence to the global scale environment. In this research, it was tried to presume the amount of the discharge of CO_2 by the extraction of forest fires by using the artificial satellite DMSP/OLS data, and for an example the case of the forest fire which was broken out in Siberia in October, 2005 is reported.

2. Using data

- Satellite data : DMSP/OLS nighttime imagery , Oct 1,2005～Nov 3,2005 (Table 1.) (National Geo-graphical Data Center)
  : DMSP/OLS nighttime imagery Cloud Free 2003 year (Table 1.) (National Geo-graphical Data Center)
- Landuse map : MODIS 2002 (NASA)
- Reference : http://www.fire.uni-freiburg.de/GFMCnew/2005/11/1104/20051104_ru.htm [1]
  : Air purification tree-planting manual - Independent administrative agency Environmental regeneration preservation mechanism [2]

Table 1. Specs of the DMSP nighttime Imagery

	DMSP-OLS/VIS Nighttime Data Set
X_Line	43201, 180° W～180°
Y_Line	15601, 65° N～65° S
Map Projection	GEODETIC
Datum	WGS84
Pixel Size	0.008333(degree) × 0.008333(degree)

3. Methods

An satellite image observed on Oct 1, 2005～Nov 3, 2005 by a visible infrared sensor (OLS-VIS) of the Meteorological Satellite Program (DMSP) of the U.S NGDC and a Cloud Free nighttime imagery of the lights (fixed light) turned on regularly at night of the 2003 year were used. By using these images, a difference image of the fixed light of such as buildings and roads was created, and the comparison with a landuse map was performed.

3－1. Forest fire and DMSP/OLS

The MODIS imagery (Fig.1) and DMSP/OLS nighttime imagery (Fig.2, Fig.3) are shown.

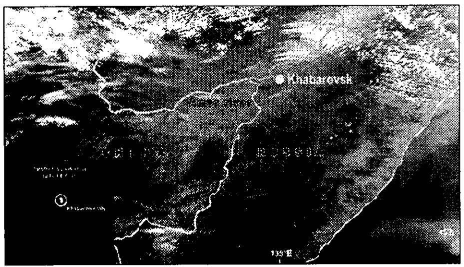

Fig.1 MODIS imagery.

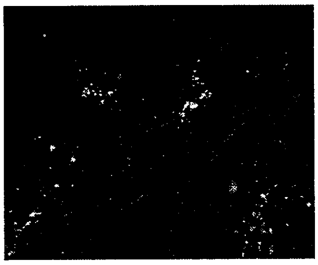

Fig.2 DMSP/OLS Oct 9,2005 19:44(JST)

Fig.3 DMSP/OLS Oct 23,2005 19:30(JST)

3－2. Extraction of Forest Fire

The Cloud Free nighttime imagery (Fig.4) and created images forest fire were extracted (Fig.5, Fig.6).

Fig.4 Cloud Free 2003 year

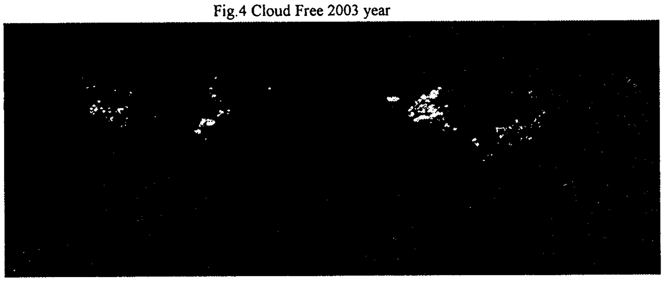

Fig.5 DMSP/OLS Oct 9,2005 19:44(JST) Fig.6 DMSP/OLS Oct 23,2005 19:30(JST)

4. Results and discussion

4－1. Presumption of forest fire

According to Global Fire Monitoring Center(GFMC)[1], the area burned down by November 3 was 12,574,863 (ha).

The result of performing area compensation in the forest fire area extracted by this research was 12,686,993.7 (ha) (Table 2).

It was the almost same result as the GFMC announcement.

Table 2. The result of fire area

Legend	Count Value	Fire Area(ha)
Evergreen needleleaf forest	2	128.888
Evergreen broadleaf forest	45	3124.998
Deciduous needleleaf forest	941	65347.17
Deciduous broadleaf forest	2727	189374.849
Mixed forest	12525	869790.971
Woodland	30007	2083817.777
Wooded grassland	51111	3549372.161
Closed shruband	544	37777.748
Open shrubland	27	1874.999
Grassland	8913	618957.838
Cropland	75851	5267426.342
Total	182693	12686993.7(ha)

3－3. Comparison with landuse map

The forest fire area was extracted from the landuse map (Fig.7) (Fig.8).

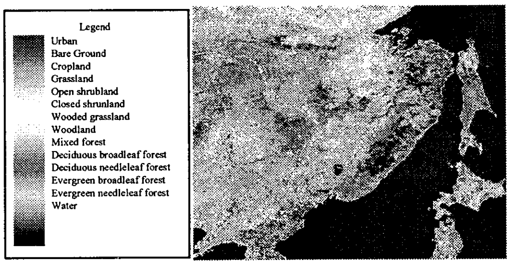

Fig.7 Landuse map

Fig.8 DMSP/OLS Oct 1 ,2005～Nov 3,2005

4－2. Presumption of the decrease of CO2 absorption in Forest fire

The decrease of the CO_2 absorption by the forest fire was presumed.

The amount WCO of the absorption of CO_2 is presumed as follows. [2]

$$WCO_2(t/year) = 1.63 \times Pn \times S$$

$$WCO_2 = 1.63 \times 18 \times 128.888 = 3.8\times 10^3\ t/year$$

where Pn is the quantity of production of a Evergreen broadleaf forest and S(ha) is its distribution area.

In the case of the forest fire, it means that the amount of CO_2 absorption of 173289×10^3 t/year becomes impossible.

5. Conclusion

- The forest fire was able to be extracted by using a DMSP/OLS nighttime imagery.
- The accuracy of fixed light and the forest fire extraction accuracy are due to be verified. Moreover, the CO_2 emissions in the forest fire are due to be presumed.

CEReS

Center for Environmental Remote Sensing,
Chiba University